UNIVERSITÉ DU
LUXEMBOURG

PhD-FTSC - 2014 - 47
The Faculty of Sciences, Technology and Communication

DISSERTATION

Defense held on 19/12/2014 in Luxembourg to
obtain the degree of

DOCTEUR DE L'UNIVERSITÉ DU LUXEMBOURG
EN PHYSIQUE
by
Helene J. MEADOWS

Laser Annealing of $CuInSe_2$ Electrodeposited Precursors as the Absorber Layer in Thin Film Solar Cells

Dissertation defence committee:

Dr. Phillip DALE, Dissertation supervisor
Associate Professor, Université du Luxembourg

Dr. Susanne SIEBENTRITT,
Professor, Université du Luxembourg

Dr. Susan SCHORR
Professor, Helmholtz Zentrum Berlin

Dr. Josh BERRYMAN
Adjoint de Recherche, Université du Luxembourg

Dr. Laurent LOMBEZ
Chargé de Recherche, Institut de Recherche et Développement sur l'Energie Photovoltaïque

1 Abstract

This thesis demonstrates a method by which a non-vacuum deposited $CuInSe_2$ precursor is transformed into a semiconductor absorber layer, suitable for completion into a photovoltaic device, using 1 s laser annealing. A final device produced using this absorber fabrication method gave a 1.6 % best conversion efficiency. This represents the first reported working device originating from electrodeposition - laser annealing. In this thesis, the steps taken to achieve this result are analysed in detail. This work is split into four parts.

Firstly, the precursor structure and the optical properties of its component materials were investigated to ensure optimal interaction between the laser beam and sample. Using the selected codeposited $CuInSe_2$ precursor it was shown that it is possible to stimulate grain growth and atomic diffusion by using a 1064 nm Nd:YAG laser with only a 1 s annealing time.

Secondly, it is shown that even on these rapid annealing time-scales the thermodynamic equilibrium reactions between the ternary $CuInSe_2$ and its constituent materials must be considered. This is proven by the formation of the first device from a laser annealed absorber only when a sufficiently elevated partial pressure of Se is supplied during the annealing process. Absorbers formed under lower Se activities led to devices which were shunted or showed negligible efficiency. A correlation was identified between the Se partial pressure and the absorber properties including its Se content, grain size and PL yield.

Thirdly, a finite element model capable of predicting the film temperature during laser annealing is demonstrated. By considering the Gaussian nature of the irradiating beam it is seen that the peak temperature of the $CuInSe_2$ film, which formed the 1.6 % device, fluctuated spatially by > 300 °C during processing. Variations in temperature led to different rates of atomic diffusion and grain growth and resulted in lateral inhomogeneities in the absorber. The low device efficiency is believed to be partially caused by these variations.

Finally, the chemical composition of the film and its effect on absorber properties is established. Increasing the Cu/In ratio of $CuInSe_2$ precursors and incorporating Na into $CuInSe_2$ absorbers is shown to increase their crystal coherence length. However, the positive effects related to these elements must be balanced against their impact on the optoelectronic properties of the absorber when present in high concentrations.

Therefore it is hoped that this initial ‘first device’ efficiency validates this fabrication route and motivates future research on this interesting topic.

Contents

2 Acknowledgements

There are so many people to acknowledge who have made a substantial contribution to this thesis and to whom I would like to express my heartfelt gratitude.

Most importantly, I thank my PhD supervisor Phillip Dale. Without his judgement, support and kindness this PhD would not have been possible. It is thanks to his persistence that I have had the opportunity to live in the best country on earth and his perseverance that I have taken 100 % out of it and enjoyed (nearly) every moment of it!

Many thanks to both Susanne Siebentritt and Susan Schorr for agreeing to be on my CET committee and for their help, support and advice over the past four years. Thank you also to Josh Berryman and Laurent Lombez for being on my defence committee.

Funding was provided for this project by Fonds National de la Recherche du Luxembourg grant MAT09/02.

This thesis contains the contribution of a large number of collaborators, as mentioned within the text. By institution, notable mentions are to:

CRP Gabriel Lippmann: Jérôme Guillot, Nathalie Valle and Thierry Girot, who measured the XPS, AES and gave assistance with XRD respectively.

IRDEP: Laurent Lombez and Elisabeth Chassaing for completion of solar cells, and the opportunity to carry out measurements at IRDEP.

HZB: Susan Schorr, Christiane Stephan and Galina Gurieva for giving me the opportunity to make detailed XRD measurements and learn Rietveld Refinement as a method for their analysis.

Universität Oldenburg: Levent Gütay and Viktor Gerliz for PL measurements.

TNO: Mirjam Theelen and Frank Grob for depositing Se caps on some of the samples.

FZ Jülich: Florian Köhler for PDS measurements.

Mike Scarpulla at the University of Utah for making the LASER project possible. Importantly to his team, in particular Ashish Bhatia, Sudhajit Misra and Brian Simonds for their help with using the laser. Brian and Ashish wrote the thermal and optical models used in this thesis. A special mention to Liz Lund for being a wonderful friend, keeping me sane and putting a roof over my head a total of six times, with Yao, Mina, Hank and April. Thank you!

Thanks to past and present members of LPV and LEM at the University of Luxembourg for their help, support and friendship. Important contributions to this thesis were from David Regesch who carried out the majority of the PL measurements detailed. Additional analyses were also carried out by Jan Sendler and Artem Malyeyev. Valerie Depredurand provided the reference samples (and friendship). João Malaquais permitted 'intelligent conversation' (in Victorian English), lab and thesis help. Diego Colombara helped with the PEC measurements and proof reading. Dominik Berg and Johannes Fischer for teaching me how to do a PhD. Maxime Thevenin made all SEM and EDX measurements and Thomas Schuler provided technical support, a mini annealing chamber and all its windows (and beer). It's been a pleasure to be part of such a great team. Particular thanks to Danielle Schoder, Katja Hönes, and Patricia Romoa.

On a personal front, there are some special mentions that must be made for their contribution to this work, on a scientific level and for keeping me sane. Firstly, and above all, I thank the

Smith Family. Sarah and Andy gave me the most amazing family and home and took on the challenge of being parents for the fifth time. My health, happiness and refound confidence is forever indebted to you and I will never forget your kindness. Thank you to all the other families I adopted; the Boelens, Meiers, Birches and finally to my ‘real’ family (last but not least).

Finally, to The Anglican Church of Luxembourg, Telstar Scouts, all my LuLu friends, a special man at work who wouldn’t ever stop asking me for help with the XRD (!) and a few other people in Luxembourg, who have been invaluable and will know to whom I refer.

3 List of Publications

1. Meadows, H. J.; Bhatia, A.; Depredurand, V.; Guillot, J.; Regesch, D.; Malyeyev, A.; Colombara, D.; Scarpulla, M. A.; Siebentritt, S.; Dale, P. J. Single Second Laser Annealed CuInSe$_2$ Semiconductors from Electrodeposited Precursors as Absorber Layers for Solar Cells. *J. Phys. Chem. C.* 2014, **118**, 1451–1460.

2. Meadows, H. J.; Regesch, D.; Thevenin, M.; Sendler, J.; Schuler, T.; Misra, S.; Simonds, B. J.; Scarpulla, M. A.; Gerliz, V.; Gütay, L.; Guillot, J.; Dale, P. J. CuInSe$_2$ Semiconductor Formation by Laser Annealing. *Thin Solid Films*, In press. 2014.

3. Meadows, H. J.; Regesch, D.; Schuler, T.; Misra, S.; Simonds, B. J.; Scarpulla, M. A.; Gerliz, V.; Gtay, L.; Dale, P. J. The Importance of Se Partial pressure in the Laser Annealing of CuInSe$_2$ Electrodeposited Precursors. *Proceedings of 40th IEEE Photovoltaic Specialist Conference 2014*, 0405–0408.

4. Meadows, H. J.; Bhatia, A.; Stefan, C.; Schorr, S.; Scarpulla, M. A.; Dale, P. J. Crystallographic Study of phases present in CuInSe$_2$ Absorber Layers Produced by Laser Annealing Co-Electrodeposited Precursors. *Proc. SPIE. 2013*, **8823**, 882302.

5. Meadows H. J.; Misra, S.; Simonds, B. J.; Regesch, D.; Bhatia, A.; Schuler, T.; Reis-Adonis V.; Scarpulla, M. A.; Dale, P. J.; Solar Cells from Electrodeposited CuInSe$_2$ Precursors Using 1 s Laser Annealing. *Submitted to Prog. Photovolt.* 2014.

6. Meadows, H. J.; Bhatia, A.; Misra, S.; Kurihara, M.; Scarpulla, M. A.; Dale, P. J.; Modelling the Laser Annealing of Electrodeposited CuInSe$_2$ Precursors. *Submitted to J. Appl. Phys.* 2015.

7. Meadows, H. J.; Malaquias, J. M.; Steichen, M.; Djemour, R.; Malyeyev, A.; Kurihara, M.; Taylor, A. A.; Mendis, B. G.; Dale, P. J.; Influence of Lateral Elemental Distribution on Cu(In,Ga)Se$_2$ Absorber Layers: from Precursor to Solar Cell. *Submitted to ChemElectroChem* 2015.

8. Simonds, B. J.; Meadows, H. J.; Misra, S.; Ferekides, C.; Dale, P. J.; Scarpulla, M. A.; Laser Processing for Thin Film Chalcogenide Photovoltaics: A Review and Prospective. *J. Photon. Energy.* 2015, **5(1)**, 050999.

9. Bhatia, A.; Meadows, H.; Crossay, A.; Dale, P. J.; Scarpulla, M.A. Continuous Wave Solid Phase Laser Annealing of Single-Pot Electrodeposited CuInSe$_2$ Thin Films: Effects of Cu/In Stoichiometry. *J. Appl. Phys.* 2013, **114**, 044904.

10. Bhatia, A.; Meadows, H.; Hlaing Oo, W. M.; Dale, P. J.; Scarpulla, M. A. Effects of Pulsed Laser Annealing on Deep Level Defects in Electrochemically-Deposited and Furnace Annealed CuInSe$_2$ Thin Films. *Thin Solid Films*. 2013, **531**, 566–571.

11. Bhatia, A.; Meadows, H.; Hymas, M. C.; Smith, E. M.; Dale, P. J.; Scarpulla, M. A.; Study of Point Defects in ns Pulsed-Laser Annealed $CuInSe_2$ Thin Films. *Proc. IEEE Photovolt. Spec. Conf.* 2012, **2**, 1–5.

12. Bhatia, A.; Karmarkar, M. A.; Meadows, H.; Hymas, M. C.; Smith, E. M.; Dale, P. J.; Scarpulla, M. A. Effects of Annealing in Sulfur Vapor on Electrodeposited $CuInSe_2$ Films. *Proc. IEEE Photovolt. Spec. Conf.* 2012, 879–883.

13. Bhatia, A.; Meadows, H.; Crossay, A.; Dale, P.; Scarpulla, M. A. Pulsed and Continuous Wave Solid Phase Laser Annealing of Electrodeposited $CuInSe_2$ Thin Films. *Proc. SPIE 2012*, **8473**, 84730F.

14. Bhatia, A.; Karmarkar, M. A.; Meadows, H.; Hymas, M. C.; Smith, E. M.; Dale, P. J.; Scarpulla, M. A. Grain Growth Study of Electrochemically Deposited $CuInSe_2$ by Rapid Thermal Annealing in a Sulfur Atmosphere. *Proc. SPIE. 2012*, **8549**, 85493B.

15. Bhatia, A.; Meadows, H.; Hlaing Oo, W. M.; Dale, P. J.; Scarpulla, M. A. Pulsed Laser Processing of Electrodeposited $CuInSe_2$ Photovoltaic Absorber Thin Films. *Proc. IEEE Photovolt. Spec. Conf.* 2011, 329–332.

4 Introduction to $CuInSe_2$-based thin film solar cells

This introduction has the aim of providing the background and motivation behind the novel topic investigated in this thesis. Initially the field of photovoltaics is introduced and then justification given as to the choice of the object of this research; that of laser annealing electrodeposited $CuInSe_2$ (CISe). This section details the current fabrication methods of thin film absorber layers based on CISe and its alloy $Cu(In,Ga)Se_2$, highlighting the important considerations involved in both the precursor deposition and annealing. Finally, the hypotheses are outlined and an overview of the thesis given.

4.1 Why Thin Film Photovoltaics?

In 2011 the Eurobarometer published what European Union citizens identified as the ten biggest threats to the world [1]. Within this list, the availability of energy ranked 5^{th} and climate change 2^{nd}. The first of these anxieties reflects the current unsustainable global situation of a population of 7 billion, which continues to grow [2], accompanied by an increase in energy consumption (predicted at 56 % between 2010 and 2040 [3]). To satisfy this higher demand, energy production must increase. Currently, 80 % of energy produced in Europe is from fossil fuels [4] (oil, natural gas and coal). Not only are these reserves finite, but their combustion releases CO_2 and other greenhouse gases into the atmosphere. High levels of these gases have been linked to a number of unwanted maleffects including acidification of the oceans, and an increase in radiative forcing (absorption of energy by the atmosphere) which increases the earth's surface temperature [5]. This leads to the second concern, that of climate change.

In contrast to these concerns, it is frequently quoted that 'the solar radiation incident on the earth during 90 minutes would meet the world energy demand for one year' [6]. Radiation from the sun offers a limitless and entirely 'green' energy supply. However, the present challenge is in how to harness this power source in an environmentally benign and economically viable way. To quantify the potential of a renewable energy source, two payback periods are considered: 1. An economic payback period, the time for the total financial value of energy produced to exceed the capital and running costs, 2. An energy payback time (EPBT) over which the energy produced has exceeded the energy costs required for the product life-cycle, including mining, manufacturing, transport, installation and end-of-life disposal or recycling. One method that has favourable payback times (EPBT $\approx$ 1 years [7][1]) is Photovoltaics (PV); the direct conversion of solar radiation into electric power. In 2012 the photovoltaic grid network surpassed 100 GW cumulative installed capacity [8] but this relates to merely 0.4 % of global power generation [4]. To increase the market share of PV, the costs involved in generating each unit of electricity must be less than the sale price of the unit to the electricity grid. This thesis aims to investigate

---

[1] Based on an 11.7 % $Cu(In,Ga)Se_2$ module, with 1700 kWh/m^2/yr irradiation), 2013

fabrication techniques that support this goal of lowering the production cost of PV panels, whilst maintaining a reasonable power conversion efficiency, by means of the following mechanisms:

1. The utilisation of a material efficient deposition technique
2. Processing conditions with a lower energy cost
3. Higher throughput via more rapid processing steps.

These sub-headings are used to guide the following discussion.

4.2 Cu(In,Ga)Se$_2$ Photovoltaics

1. Lowering material usage

The market leading PV technology is based on poly- or mono-crystalline silicon absorber layers (92 % market share in 2014 [9]). However, producing the crystalline silicon wafers is energy intensive and results in significant material wastage. Cu(In,Ga)Se$_2$ (CIGSe) devices are fabricated by growing the polycrystalline thin film directly on the substrate (commonly glass sputtered with Mo), a process consuming less energy costs and raw materials than the growth of poly- or mono-crystalline Si wafers. Figure 4.1 shows the typical structure of a substrate configuration CIGSe-based solar cell.

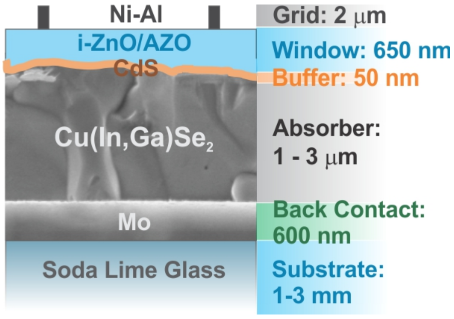

Figure 4.1: Typical structure of a CIGSe-based solar cell in substrate configuration. i-ZnO indicates intrinsically doped ZnO and AZO is ZnO doped with Al. SEM micrograph courtesy of V. Depredurand.

Si-based solar cells, are manufactured with a 200 μm thick Si wafer as the absorber layer. In comparison, CIGSe-based solar cells use only a 1–3 μm thick absorber layer, as illustrated in Fig.4.1. This thickness reduction is possible due to the ability to deposit the CIGSe layer directly onto a substrate and that it is a direct band gap semiconductor with a high absorption coefficient of 10^4–10^5 cm^{-1} [10]. The record power conversion efficiency of such a CIGSe-based device is 21.7 % [11], making it the leading thin film technology and exceeding that of multicrystalline Si (20.4 % [12]). Thin film solar cells have a further advantage stemming from the possibility of replacing the glass substrate with a flexible material such as polyimide or stainless steel allowing for novel wearable and portable applications. Further advantages of CIGSe include its high tolerance to compositional variations [13], relatively benign and easily passivated grain boundaries [14] and tunable band gap with varying group III metal content [15]. Each factor will be discussed, as appropriate in further chapters.

4.2.1 Fabrication methods

2. Lower energy process

There are a number of methods used to fabricate CIGSe absorber layers. A summary of the methods used and the record large area (submodule) efficiencies are given in Table 4.1

Method	**Process steps**	**Area [cm^2]**	**Efficiency [%]**	**Reference**
Coevaporation	1	16.0	17.4	[16]
Sputtering	2	900	17.8	[17]
Nanoparticles	2	5.0	10.1	[18]
Electrodeposition	2	12.0	13.4	[19]

Table 4.1: CIGSe technologies with the process steps: 1 - single step, 2 - precursor deposition followed by selenisation, and record module efficiencies

Vacuum fabrication technologies such as coevaporation and sputtering of CIGSe absorbers compete for the highest power conversion efficiencies both in modules and as laboratory scale devices [11][16][17][20]. Coevaporation involves the deposition of all constituent elements in a single high temperature process, whereas sputtering forms only the metallic precursor which then must be selenised in a second step. Precursor films may also be formed via a non-vacuum method, providing a route by which the energy and thus total cost of the absorber fabrication may be significantly reduced [21]. Two non-vacuum processing methods which have achieved notable efficiencies (as listed in Table 4.1) are nanoparticle deposition and electrodeposition. In this thesis precursors are fabricated using electrodeposition, which has a number of promising characteristics including:

1. Highly resource efficient (up to 98 % [22]): depleted plating solutions can be refreshed with new metal ions
2. Low cost equipment
3. Generally room temperature deposition
4. Easily up-scalable and compatible with roll-to-roll production lines [23]

It is for these reasons that manufacturers such as Solopower and Nexcis have chosen the electrodeposition method for large-scale, commercial production of CIGSe absorber layers.

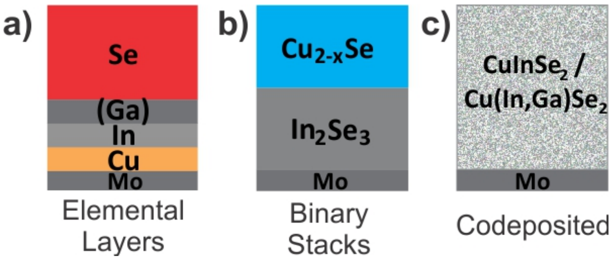

Figure 4.2: Examples of CI(G)Se precursors. a) Metallic layers, b) binary stacks, c) co-deposition.

Electrodeposition also offers a high degree of flexibility over the precursor structure. Figure 4.2 illustrates the three main CI(G)S precursor structures. Metallic Stacks (a) comprise a layer of each metal electroplated sequentially (or as a Cu-In(-Ga) alloy). Se is supplied to the precursor either as a capping layer immediately following the deposition (by evaporation or electroplating) or as an Se atmosphere during the annealing. Empirically it is found that this precursor type generally gives the largest grain size and also the highest efficiencies: 15.9 % on small area cells [24]. A second approach (b) is the deposition of the binary selenides: $Cu_{2-x}Se$ and In_2Se_3. This method has received very little research attention due to the difficulties involved in depositing In_2Se_3, where elevated temperatures and a controlled atmosphere are required [25]. This is reflected in the 5.5 % maximum achieved efficiency [26]. The most studied method is simultaneous co-deposition of all the elements (c). Whilst this method presents the most challenging electrochemistry, a record small area record device efficiency of 11.4 % has been achieved by sulphurising CISe codeposited precursors [27][28].

4.3 Annealing of Electrodeposited $CuInSe_2$

One of the drawbacks of electrodeposition is that, regardless of the deposition approach, all precursors require an annealing step. This high temperature processing step serves to (1) drive chemical reactions, (2) promote atomic diffusion, (3) induce grain growth and (4) remove structural and electronic defects. The necessity of each of these mechanisms is dependent on the precursor type, as will be discussed in detail in Chapter 5.

Traditionally, a furnace is used for annealing electrodeposited CISe due to the apparatus required being relatively cheap and simple to implement. A typical construction involves fixing the sample within a graphite box and inserting this into a quartz tube surrounded by a heating element [29]. Furnace annealed, electrodeposited pure CISe absorbers (i.e. without sulphurisation or vacuum-based deposition steps) have been fabricated into devices with efficiencies >8 % [30][31][32][33]. However, this method typically requires temperatures of 400 – 550 ^{o}C for 30 mins [34][35] up to 1 hour [36][37]. Annealing times are reduced with Rapid Thermal Processing (RTP). This technique uses halogen lamps to rapidly heat the sample (up to 200 $^{o}Cs^{-1}$) combined with a much shorter dwell time at elevated temperature e.g. 3 to 6 mins [38] and fast cooling rates. It is likely on account of such reasons that companies like Nexcis and Solopower have investigated RTP annealing for the industrial production of CIGSe-based solar cells [39][40].

To achieve even shorter annealing times, more novel heating methods are required. Examples include microwave annealing, which is shown to be capable of driving reactions and improving the crystallinity of $CuInSe_2$ precursors in time-scales from 15 s to 3 mins [41][42][43] or by applying high electrical currents to the precursor film which in addition to driving chemical reactions can control the distribution of Ga through the depth of a CIGSe film [44].

4.3.1 The Importance of a chalcogen atmosphere during furnace annealing

Initial research carried out using the 2-stage annealing method heated the CISe precursor under vacuum [45] or with a inert atmosphere (e.g. Ar, N) [46][47]. Whilst this improved the crystallinity of electrodeposited precursors, the efficiencies of devices from the resulting absorbers were negligible [48]. An important discovery was that annealing CISe precursors under high partial pressures of Se (P_{Se}) led to absorbers with improved structural and optoelectronic properties, compared to those annealed under neutral atmospheres, and produced measurable device efficiencies [49]. Prior to this, co-evaporated absorber layers had also been deposited at high

Se fluxes [50]. To explain why a P_{Se} during high temperature processing is important, one can consider a proposed thermodynamic equilibria reaction for CISe given in Eq.4.1.

$$2\ \mathrm{CuInSe}_{2(s)} \longleftrightarrow \mathrm{Cu_2Se}_{(s)} + \mathrm{In_2Se}_{3(s)} \tag{4.1}$$

Cu_2Se and In_2Se_3 may further decompose to release gaseous species including elemental Se. Some purported binary decomposition reactions are given in Eq.4.2-4.4 (See Ref[51][52]).

$$4\ \mathrm{In_2Se}_{3(s)} \longleftrightarrow 2\ \mathrm{In_4Se}_{s(l)} + \mathrm{Se}_{2(g)} \tag{4.2}$$

$$2\ \mathrm{In_2Se}_{3(s)} \longleftrightarrow \mathrm{In_2Se}_{(g)} + \mathrm{Se}_{2(g)} \tag{4.3}$$

$$2\ \mathrm{Cu_2Se}_{(s)} \longleftrightarrow 4\ \mathrm{Cu}_{(s)} + \mathrm{Se}_{2(g)} \tag{4.4}$$

Annealing at high temperatures for long times with insufficient Se activity drives each of these equilibrium reactions towards the right hand side, and the evolution of gaseous species including Se. Low levels of Se loss are accommodated by direct release of Se from the CISe lattice, forming Se vacancies, V_{Se}, and In/Ga on Cu, anti-site defects, $(In, Ga)_{Cu}$, [53]. V_{Se} is a metastable defect capable of changing the doping of the film, and may be detrimental to device performance [54][55]. If the Se activity above the CISe remains insufficient, further Se loss takes place via reactions 4.1-4.4. This Se loss decreases the volume fraction of CISe semiconductor and leaves binary or metallic secondary phases in the film, both of which are highly detrimental to device performance. In order to minimise defect formation and breakdown of the CISe semiconductor, a background partial pressure of Se exceeding the equilibrium vapour pressures of reactions 4.2-4.4 is used during annealing. This analysis highlights the importance of a sufficient P_{Se} during the annealing of CISe films.

Furthermore, high activities of vapour phase chalcogen during annealing have been observed to greatly enhance the grain size and optoelectronic properties of the resulting absorber layers [49]. In furnace annealing, a P_{Se} is created either by introducing a solid Se source, which vaporises during the annealing, or by introducing H_2Se.

4.3.2 Laser annealing of $CuInSe_2$

3. Increasing production speed

LASER is an acronym for “Light Amplification by the Stimulated Emission of Radiation”. The theory of stimulated emission was first proposed by Einstein in 1917 [56] although laser action was not demonstrated until Maiman in 1960 [57]. Lasers have become increasingly important, with their applications gaining in diversity; ranging from probing matter in basic research to mapping Mars. Lasers have made modern telecommunication possible and have lead to 19 Nobel prizes in physics and chemistry being awarded to their users [58]. The popularity of lasers is due to application-specific advantages which include precision, low cost, localised processing and high speed of operation [59]. Laser machining operations rely on the ability to use the laser beam as a heat source to rapidly increase the temperature and induce physical changes within a substrate material [59].

When compared to the more familiar methods of annealing CISe detailed in Section 4.3, laser treatment has the potential to be the most rapid. For example, femto-second laser pulses are used in the synthesis of CISe from nanoparticles [60]. For the purpose of annealing semiconductors, the energy of the irradiating radiation is chosen to be greater than the band gap of the precursor

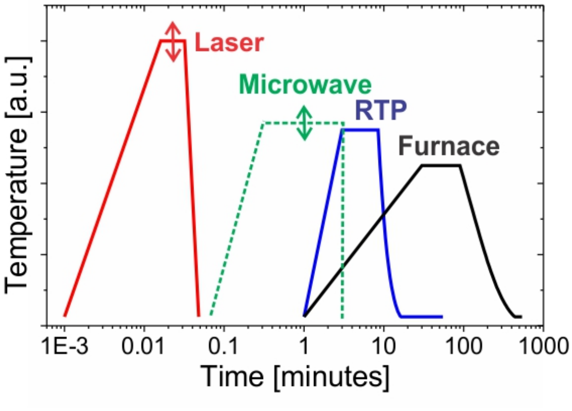

Figure 4.3: Comparison of the timescales used to anneal CISe by different methods. Annealing temperatures given for each process are purely representative. Note the log scale on the x-axis.

material, resulting in its rapid heating and annealing times from μs to 1 min [61][62]. An illustration comparing the timescales of some different annealing techniques is given in Fig.4.3. A short literature review of laser annealing is given subsequently and the theory behind the process used in this work is given Chapter 7.

The concept of laser annealing of semiconductors (summarised in ref.[63]), originated in the 1970s, and largely focused on removing the damage caused by ion implantation into Si wafers [64]. This early work used Nd:YAG lasers with wavelength λ = 1064 nm (or frequency doubled λ = 530 nm) and showed promising results with both continuous wave (CW) and pulsed laser annealing (PLA).

The first published research into laser annealing CISe, was in 1985 by the group of Laude [65][66]. Single phase CISe was formed by annealing stacked layers of Cu/In/Se with 0.7 s pulses from an Ar^+ laser. However, the 100 nm total precursor thickness, is too thin to form absorbers capable of absorbing a significant proportion of the solar radiation. Further work on Cu/In/Se precursors increased the layer thickness but as the CISe formation reaction proceeds via its binary selenides [67][68] it proved difficult to drive the reaction fully to completion and eradicate these secondary phases. PLA with 248 nm KrF lasers has been shown to reduce the defect levels in CISe absorbers [69][70][71]. However, PLA only improves the material properties of already fully-formed, crystalline CISe absorbers, produced either by vacuum deposition technique or by first annealing electrodeposited precursors in a furnace. Jost et al. used a 1064 nm Nd:YAG laser in CW mode to improve the crystallinity of co-electrodeposited CISe precursors [61]. However, the high intensity employed ($> 1x10^5\ \mathrm{Wcm^{-2}}$) resulted in melting and dewetting of the CISe film. This work was expanded on by collaborators in the LASER project[2] [62][72], who used a much lower intensity ($50\ \mathrm{Wcm^{-2}}$) to bring about a solid state annealing of co-electrodeposited CISe films. However, the low flux increased the dwell times required for crystal growth from 1 μs to $>$15 s.

Further uses of laser processing applied to CISe thin films for use in solar cells include sintering nanoparticles [73], selective ablation [74] and etching [75].

---

[2] The jointly funded project between the University of Utah and the University of Luxembourg, under which framework the research of this thesis was carried out

To summarise, previous approaches have shown structural enhancement by CW laser annealing CISe precursors, but without demonstrating optoelectronic properties of the absorber or being able to produce a functioning photovoltaic device. PLA has been shown to modify the defect levels of already formed absorber layers, potentially enhancing device efficiency, but without inducing significant structural changes. Prior to this work, there has been no systematic study of laser annealing of CISe. The unique aim of this work is to improve both the structural and the optoelectronic properties of a low cost precursor using laser annealing and to achieve absorbers of suitable quality to form devices. In order to design a method which is capable of achieving this goal, this thesis analyses a series of important considerations.

1. Precursor Structure
2. Laser wavelength
3. Annealing flux (Wcm^{-2})
4. Annealing time
5. Thermodynamic Equilibria reactions of CISe

This thesis will investigate each of these parameters and examine how, by matching the processing conditions to the precursor's properties, a successful annealing can be achieved. The merit of an annealing is determined by measuring the resulting absorber's structural and optoelectronic properties using a range of characterisation techniques. The sufficient augmentation of the sample's properties, starting from the nanocrystalline, inhomogeneous and photo-inactive precursor, will enable the fabrication of an absorber from which, when fabricated into a complete device, an efficiency can be measured.

4.4 Hypothesis and Motivation

Laser annealing offers a method by which annealing times may be reduced by 2-3 orders of magnitude when compared to furnace or RTP annealing. By combining laser annealing with the advantages of electrodeposition, including efficient material usage, ambient deposition conditions and usability in roll-to-roll processes, it is hoped that an alternative production technique with lower energy and financial costs can be demonstrated. Prior to the start of this thesis, the laser annealing of electrodeposited CISe precursors has not produced absorber layers with suitable properties for solid state devices, as detailed in Section 4.3.2. Consequently, the objective of this work is to design a laser method capable of forming device-quality CISe absorbers. To achieve this aim, a suitable precursor must be selected and undergo a solid state laser annealing process. The process must enhance the film properties in terms of homogenising atomic distribution through the depth, increasing crystallinity and eradicating secondary phases and structural and electronic defects. Having pioneered a suitable process, the precursors and the laser annealing processes are optimised. The final aim is to produce absorber layers which are fabricated into efficient devices.

The following hypotheses will be subsequently investigated:

1) By matching the optical properties of a precursor to the irradiating laser wavelength, the precursor film will strongly absorb the incident laser photons. The choice of a suitable precursor structure ensures the beneficial distribution of this energy to each of the component elements.

2) Absorption of the incident laser flux over a sufficient time-scale will heat the CISe precursor film. Using a higher incident laser flux is hypothesised to increase the heating rate of the CISe film and lead to higher peak temperatures. To transform a precursor into an absorber layer requires chemical reactions, atomic diffusion and grain growth. The rate of each of these processes is temperature dependent. Therefore, using a higher flux and thus increasing the peak temperature of the film, will increase the speed of absorber layer formation and shorter annealing times will be required. Keeping the laser power below the threshold for dewetting or melting of the precursor film will give a solid state annealing.

3) In furnace or RTP heating processes the substrate poses a limitation on the maximum annealing temperature, above which the substrate, i.e. glass, may break or bend. However, using a unidirectional and coherent heating method such as a laser is hypothesised to result in the incident photons being largely absorbed within the CISe layer. Consequently the heat generation will be concentrated predominantly in the CISe and Mo layers, with the glass only being heated indirectly and therefore reaching a much lower average temperature. Thus higher peak film temperatures should be possible without damaging the glass. One potential problem is the presence of a thermal gradient through the thick glass substrate, which could cause it to crack.

4) Section 4.3.1 presented the decomposition reactions of CISe into its binary and elemental components including gaseous Se. These reactions become increasingly favourable at higher temperatures. It is hypothesised that by increasing the activity of volatile gaseous products during the annealing, in particular Se, Se loss from the film, resulting in defects and CISe breakdown, will become less favourable. Minimising these detrimental processes is expected to lead to improvements in the structural and optoelectronic properties of the absorber.

5) Adapting the composition of the precursor is hypothesised to provide a mechanism by which to improve the structural and optoelectronic properties of laser annealed absorbers. This has a two-fold effect. Firstly, the diffusion rate of elements is compositionally dependent. Secondly, changing the Cu-content or by adding dopant ions to the precursor, alters the interaction between the material and the laser beam. The absorption pattern of the laser energy dictates the film temperature, and thus affects processes such as grain growth, atomic diffusion and defect removal, essential to convert the precursor into an absorber layer.

These hypotheses will form the basis of this thesis and will be expanded upon in subsequent chapters.

4.5 Outline of thesis

The thesis comprises the following sections:

In order to investigate the hypotheses outlined above, a number of characterisation techniques have been frequently employed. These fundamental measurement methods are outlined in Chapter 5, to give the explanatory theory for subsequent chapters.

Chapter 6 explains the theory of electrodeposition. From this foundation the deposition method for each precursor is presented, followed by an analysis of their composition and structural properties.

Using these precursor deposition methods, Chapter 7 investigates the precursor and beam interaction. Firstly an introduction to laser annealing is given from which the absorption of the laser energy by each precursor is discussed. From these investigations the most suitable laser wavelength and precursor structure combination are selected.

Chapter 8 adapts the annealing method in order to prevent breakdown of CISe during laser annealing. By forming and controlling a background P_{Se} during annealing, the structural and optoelectronic properties of absorbers are enhanced. This leads to the formation of the first laser annealed CISe device.

In order to augment the device efficiency, it is necessary to understand the laser process. Consequently, Chapter 9 proposes finite element models, FEM, capable of simulating the sample temperature during laser annealing. The effect that the calculated film temperatures have on the rates of atomic diffusion and grain growth is analysed and used to explain the observed sample properties. The effect of the precursor composition both on the heating process and atomic mobility is considered.

Chapter 10 draws conclusions and summarises the key findings of this work. Finally, in Chapter 11, suggestions are given for improvements and paths that future research work may take. The wider applicability of this processing technique is considered, in particular its utilisation in a production line of the future. To demonstrate the viability of the laser annealing method, the costs it involves, when compared to current methods, is analysed.

5 General Characterisation Techniques

This chapter briefly explains the investigative techniques which form the foundation of the analysis of thin film solar cells and that are used throughout this thesis. The basic theory behind each technique will be covered, focusing in particular on its application within this thesis, and mentioning, where appropriate, specific details of the measurement conditions used. References are given to where a more detailed explanation of each technique can be found in the literature. Firstly the structural and optoelectronic characterisation methods used for analysis of the precursor and absorber layer are discussed, followed by the measurements made on the completed device.

5.1 Precursor and Absorber layer characterisation

5.1.1 Scanning Electron Microscopy (SEM) and Energy Dispersive X-ray Spectroscopy (EDX)

The wavelengths of visible light limit optical resolution to hundreds of nm. One way to observe nano-scale dimensions is by using an electron beam. An electron beam focused onto a sample surface will interact with a specific volume of the sample and result in the emission of characteristic species. These are detected and then analysed to give information about the sample. Fig.5.1 illustrates these emissions, which include secondary electrons (SE), backscattered electrons (BSE) and characteristic X-rays along with other photons of various energies. Measurement of the emitted electrons and X-rays are used to examine the sample topography (SEM) and composition (EDX) respectively. The information given here is taken from Ref.[76][77] to which the reader is referred for further information.

EDX

When the electron beam is focused onto the sample, its electrons collide with the electrons of the sample. If this collision has sufficient energy, the incident electron can knock an inner shell electron from its orbit. This is a SE and is emitted from the sample, detected and analysed, which forms the basis of SEM analysis. The emission process leaves an electron hole in an inner orbital, for example the K shell, and the atom becomes an ion in an excited state. A higher energy electron from an outer orbital subsequently transitions down to this lower shell vacancy, releasing a quantum of energy. Due to the laws of energy conservation, this energy quantum is equal to the difference in potential energy between the outer and inner shells of the atom. As shown in Fig.5.1, this energy is either transmitted to a bound electron, which is thence emitted as an Auger electron (1), or the energy quantum is emitted as X-rays (2). As the energy quantum is equal to the potential energy difference between the shells of an atom it

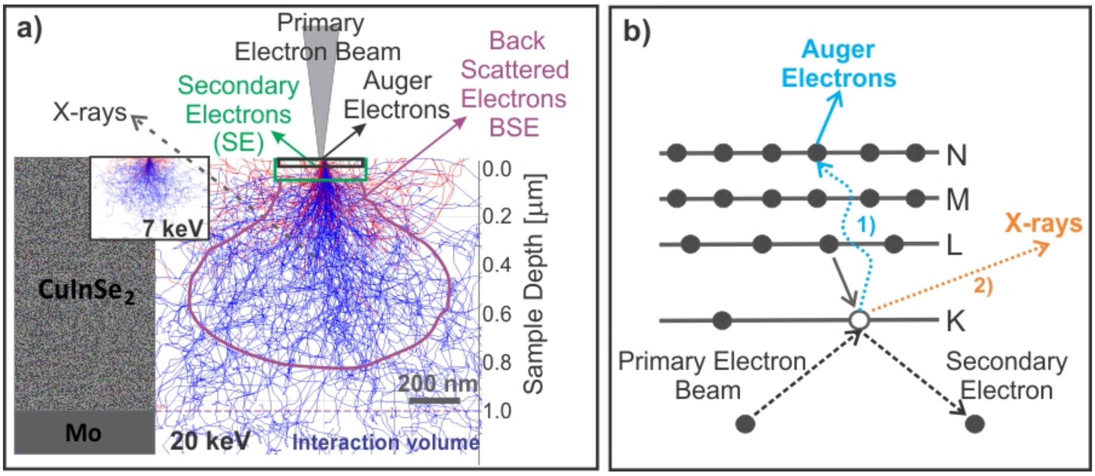

Figure 5.1: a) CASINO^a simulation of the interaction of electron beam (20 keV excitation energy) with CISe (1 μm) / Mo (0.4 μm) sample stack. The scattering of the beam energy is indicated in red and blue and the characteristic species produced and an indication of their origin within the sample are labelled. A to-scale representation of the interactions of a primary electron beam at 7 keV is shown inset for comparison. b) Schematic representation of the interaction of the primary electron beam with the electron shells of the sample, generating secondary electrons. The mechanisms by which 1) Auger electrons and 2) X-rays are created is indicated.

---

[a] CASINO V.42. A Monte Carlo Simulation programme specifically designed to calculate electron trajectory in solids.

is specific to the shell transition (e.g. L⟶K) and is characteristic of a particular element. In this way, the localised elemental composition of the film is measured. Each element may show multiple emission lines which relate to individual shell transitions. The choice of line used for evaluation depends on the primary beam acceleration voltage which must be greater than the characteristic X-ray emission. In this work, the majority of analyses were carried out at 20 keV and hence for Cu and Se the integral intensities of the K lines were compared whereas for In the L line is required. A relative elemental composition of the sample is obtained by comparing the integrated intensities of all of the emission lines. A calibration is carried out before each measurement session, which for the analysis of CISe films, was a copper foil.

SEM

In an SEM measurement, the electron beam is rastered across the sample surface. Both SE and BSE may be used for mapping the sample and the selective detection of each electron species is achieved by altering the geometry of the detection mechanism in relation to their different trajectories. SE are emitted as a result of the direct impact of the electron beam and arise only from a small volume at the sample surface and are therefore better for imaging the surface topology. BSE are beam electrons remitted from the sample by elastic scattering. Whilst BSE are not measured in the analyses of this thesis, they have the advantage over SE of giving improved visualisation of areas of elemental difference due to their energy being dependent on atomic number. Using a scintillator detector a pixelated image is formed by counting the number of electrons emitted per analysed area, the brightness of each pixel corresponding to the number of detected electrons. The resolution of this technique is dependent on the electron optical signal of the instrument as well as the electron wavelength, and whether BSE or SE are collected, but is commonly quoted as between 1 - 5 nm [77]. The resolution is also affected by the acceleration voltage (i.e. the energy) of the incident electron beam, which changes the interaction volume within the sample, as displayed in Fig.5.1a). There is a compensation between maximising the beam energy to give higher signal (and thus image contrast) and spatial resolution.

The SEM and EDX data presented in this thesis (unless otherwise stated) were measured on a combined Hitachi SU-70. SEM images were made using SE with a beam acceleration voltage of 7 keV in order to localise the beam interaction volume to the sample surface (see Fig.5.1a), and thus improve image quality. EDX measurements were made with acceleration voltages of 7 - 20 keV, depending on the analysis objective. At 7 keV, a spatial resolution down to 100 nm is achievable [76]. Using a higher energy gives a larger penetration volume, with 20 keV analysing through the full 1 μm depth of the film as well as the Mo substrate. Comparing the contribution of the signal relating to the Mo, gives a rough idea of the sample thickness.

5.1.2 X-ray Diffraction (XRD)

XRD is technique used to determine a sample's crystal-type, the phases it contains and its crystallinity. Refinement of a measured diffractogram permits determination of lattice parameters and a quantitative analysis of structural faults and stresses and strains within the crystal. The information below and further details on this characterisation method can be found in Ref.[78][79].

X-rays have a wavelength that corresponds to the inter-atomic spacing within a crystal lattice. An X-ray beam impinging on a crystal interacts with its atoms via inelastic or elastic scattering processes, the latter of these, elastic Thomson scattering, is used in XRD. The radially scattered X-rays generated from each lattice plane will then interact constructively and destructively. Due to the periodic arrangement of atoms, the angles at which constructive interference takes place can be determined analytically using rise to Bragg's law. This formula, Eq.5.1, relates the incident angle, θ, and wavelength, λ, of the impinging beam to the interplanar spacing of the crystal, d_{hkl}.

$$n_i\lambda = 2d_{\text{hkl}}\sin(\theta) \tag{5.1}$$

The integer value n_i is the reflection order (normally $n_i = 1$). The geometric derivation of this law is given in ref.[79]. All XRD analyses carried out in this thesis use Cu $k\alpha$ radiation, which has a wavelength of 0.154 nm. To measure an XRD pattern, θ is varied either by scanning the X-ray source and detector around an axis centred on the sample or by rotation of the sample itself. The scattered X-rays reaching the detector are measured as a number of counts dependant on 2θ angle, which results in a diffractogram. The most common measurement geometry is that of a $\theta - 2\theta$ scan, as illustrated in Fig.5.2a). In this measurement the X-ray source and detector move symmetrically on a circular axis around the sample. The angle, θ, formed by the beam against the planar surface of the sample (green line in Fig.5.2) is equal for both the incoming and exiting beam. In this geometry, Bragg's law is only satisfied by the diffraction of X-rays from lattice planes parallel to the sample plane. This property makes $\theta - 2\theta$ scans useful for determining texture of films. However, a drawback, particularly with thin films, is that the contribution to the measured diffractogram from the sample can be near negligible compared to that of the substrate. Thus grazing incidence (GIXRD) geometry is commonly used for the analysis of thin films. In this measurement the primary beam enters the sample at a small angle of incidence, which is fixed during the experiment, and the detector moves around the sample axis. The reduced incident angle increases the distance that the X-rays travel in the sample, localising the interactions to within the thin film. The absorption of the X-rays by the sample gives an intensity decay described by the Beer-Lambert law. Therefore, for each incident angle, θ, an X-ray attenuation distance, and therefore sampling depth, can be calculated as detailed for CISe in Fig.5.2. Using an incidence angle $\theta < 3^o$, the information depth lies dominantly within the, ≈ 1 μm thick CISe films measured in this thesis. When $\theta < 1^o$, the film's surface is selectively analysed. Reducing the incident angle further, to below the critical angle, θ_c, allows analysis of the surface few nm but will also cause a shift in the reflections from their Bragg peak position due to total internal reflection. The critical angle with Cu $k\alpha$ radiation is $< 0.4^o$ depending on the absorption coefficient of the analysed material. Consequently, GIXRD was measured in this work with incident angles between 0.75 - 3.0 ^{o}.

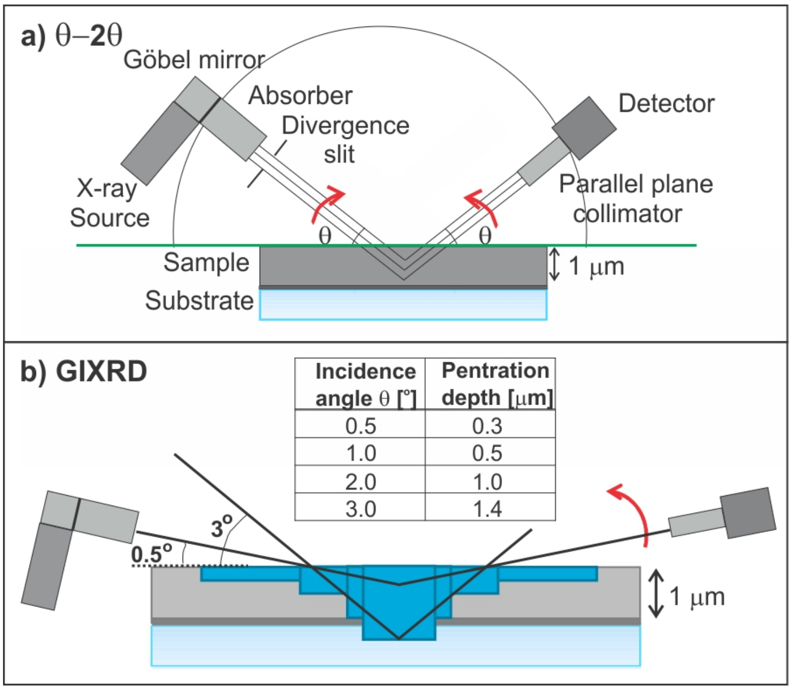

Figure 5.2: a) Experimental set-up of a $\theta - 2\theta$ XRD scan indicating the interaction of a parallel incident beam with the sample. The X-ray source and detector move around a circular measurement radius, with an angle of θ to the sample plane. b) A schematic indicating GIXRD geometry, where only the detector is scanned around the sample and the fixed angle of the incident beam determines the penetration depth of the X-rays into a CISe film. The calculated penetration volumes for typical measurement angles are represented by blue boxes and the penetration depths (attenuation of beam intensity to I_0/e) given in the inset table.

Both these measurement geometries produce diffractograms displaying reflection peaks at specific angles of 2θ. The appearance of Bragg peaks relates to constructive interference of the refracted beam, as can be calculated using Eq.5.1, and their amplitude is directly proportional to the square of a parameter termed the structure factor, F_{hlk}. F_{hkl} describes the Fourier Transformation of the electron density by summing the scattering contribution from each individual lattice site as given in Eq.5.2.

$$F_{hkl} = \sum_{c_D=1}^{C_D} f_n \exp[2\pi i(hx_n + ky_n + lz_n)] \tag{5.2}$$

The degree of scattering is determined from the atomic form factors, f_n, of the charge distributions of individual atoms (c_D). This scattering is considered in relation to the atomic positions, denoted by their fractional coordinates (x_n, y_n, z_n) and the Miller indices (h, k, l), which index the crystal lattice planes. In this way, the combination of peak position and intensity and can be seen to be dependent on the exact geometry and type of atoms within the sample. Each peak in an XRD pattern can be assigned, using the Miller indices, to a specific plane and hence the crystal phase from which the reflection originated.

Once the phases present have been determined, their structural and microstructural properties can be calculated from the different features of the diffractogram. To carry out a detailed analysis, a least squares refinement of the pattern is carried out, such as that embodied in the Rietveld method. Properties such as preferential orientation, site occupancy and isotropic displacement factors are realised by closely matching a calculated diffractogram to that measured. A full description of the method by which this is achieved is given in Ref.[80]. However, with the thin film nanocrystalline and multiphase samples investigated in this thesis, this method is only able to yield accurate information on the phases present, their lattice parameters and peak broadening which may also be obtained by the simpler methods given below.

The smallest unit of atomic periodicity within a crystal lattice is termed the unit cell, which has dimensions a, b and c, denoted the lattice parameters. From the 2θ position of the Bragg peaks (which using Bragg's law, Eq.5.1, gives d_{hkl}), a and c for a tetragonal crystal structure (where $a = b$) are determined using Eq.5.3.

$$\frac{1}{d^2{}_{\mathrm{hkl}}} = \frac{h^2 + k^2}{a^2} + \frac{l^2}{c^2} \tag{5.3}$$

By comparing the calculated lattice parameters to literature values, changes in the unit cell can be identified. This is particularly useful when considering alloying of phases, for example the inclusion of Ga within the $\mathrm{CuInSe_2}$ crystal structure, which results in a contraction of the unit cell parameters. A change in the unit cell can also denote alterations in the crystal structure and hence can be used to identify phase transitions, e.g. in Ref.[81].

The broadness of the peaks in a diffractogram is proportional to the size of coherently scattering domains within a crystal. The domain size, D, was shown by Scherrer to be related to the integral breadth of a peak, β_{sample} by Eq.5.4.

$$D = \frac{K\lambda}{\beta_{sample}\cos\theta} \tag{5.4}$$

K is the Scherrer constant, for which a value of 0.9 is most commonly used [82]. In order to obtain β_{sample}, the broadening which is intrinsic to the XRD instrument must be deconvoluted from the observed peak breadth β_{obs}. This broadening, β_{instr}, is obtained by fitting the peaks of a standard in which the crystallite domains are of large enough dimension ($> 10\mu$m [83]) to not contribute to the peak width. This gives an angular dependent instrumental broadening function which can be applied to the 2θ position of the peak under analysis. For peak broadening determined using a pseudo-Voigt line profile, β_{sample} is obtained from β_{obs}, using Eq.5.5.

$$\beta_{sample} \approx \beta_{obs} - \frac{\beta_{instr}^2}{\beta_{obs}} \tag{5.5}$$

It must be noted that peak broadening is not only a function of the domain size but also the strain within the crystal. To deconvolute the broadening due to strain from that caused by a limiting domain size, a method such as a Williamson-Hall plot can be used [84]. However, the Scherrer formula alone offers a valuable and useful method for determining the crystal coherence of samples and therefore is used in this work both as an indication of crystal growth and the removal of structural defects.

5.1.3 Depth profiling methods: X-ray Photoelectron Spectroscopy (XPS) and Auger Electron Spectroscopy (AES)

Whilst GIXRD gives an indication of how the phase composition changes through the depth of the absorber layer, an accurate picture of elemental positions is only achieved using an atomic depth profiling technique. This section will briefly discuss two of these methods; X-ray Photoelectron Spectroscopy (XPS) and Auger Electron Spectroscopy (AES). Both these techniques can be used to gather information on chemical bonding and can achieve high surface sensitivity. Each technique may be calibrated to give an accurate composition through the depth. XPS is commonly chosen to obtain highly detailed information on the chemical state of elements whereas AES is used for compositional analysis and gives a high spatial resolution. The information presented in this chapter is taken from Ref.[85].

In XPS the sample is irradiated with an X-ray beam (in these measurements from an Al $k\alpha$ source). These X-rays interact with the sample and if of high enough energy are able to excite electrons to an unoccupied electronic state. The cascade of ensuing transitions may result in the release of an electron which is collected in an electron energy analyser. The kinetic energy of these collected electrons gives binding energies which are characteristic not only to a specific element, but also its electronic configuration. The binding energy is plotted against counts to give a spectrum. This spectrum exhibits a characteristic set of peaks for the electron shells, i.e. 2s, 2p, 3s etc., of each element present at the analysed surface of the sample. From the accurate position of these peaks, the oxidation state of an element can be determined and therefore its chemical environment. Furthermore, the integral intensity of the peaks is proportional to the fractional presence of each element in the sample. In order to determine the composition, the XPS signal must be corrected by a relative sensitivity factor (RSF) for each element. In these measurements, a correction factor determined from a $CuInSe_2$ vacuum deposited sample of known composition, was applied to literature elemental RSF values to correct for aberrations originating from the instrument and crystal structure. A depth dependent composition is achieved by sputtering the sample with an Ar^+ gun between each analysis.

The underlying principle of AES is the Auger effect. When an electron beam of sufficient energy (3 - 30 keV) is focused onto a sample an electron may be removed from a core shell within an atom leaving a hole. An electron from an elevated energy state then occupies this empty state (illustrated in Fig.5.1b) as removal of a K electron leaving a hole which is filled by a L shell electron). Energy is emitted by this process either as a photon (which is measured in EDX) or transferred to another electron. If the energy given to this so-called 'Auger'electron is sufficient, then the electron is excited to the vacuum level. The kinetic energy of this electron is measured and relates to the energy difference between the involved atomic shells. This follows the relationship: $E_{kin} = (E_{upper} - E_{core}) - E_{bind}$ where E_{upper} and E_{core} are the energy levels of the core and elevated electrons respectively, and E_{bind} the binding energy of the Auger electron released. Scanning through a kinetic energy range produces a spectrum, and the constituent elements in the sample are determined from the observed peaks. As with XPS, the integral peak intensity relates to the sample composition and in order to obtain accurate quantification, experimentally determined RSF are used.

Both AES and XPS measurements were carried out in collaboration with CRP Gariel Lippmann on their Kratos Axis Ultra and Thermo VG Microlab 350 instruments respectively, by Jérôme Guillot. Both experiments require ultra-high vacuum conditions in order to minimise surface contamination.

5.1.4 UV-Visible-NIR Spectroscopy

In order to measure the reflectance and transmittance of samples, Ultraviolet-Visible-Near Infrared spectroscopy (UV-Vis-NIR) is used. The measurements shown in this thesis were carried out using a Perkin Elmer Lambda 950 UV/Vis/NIR spectrometer. Detailed information on this technique can be found in Ref.[86][87]. A schematic to explain the operating principle of such an instrument is given in Fig.5.3.

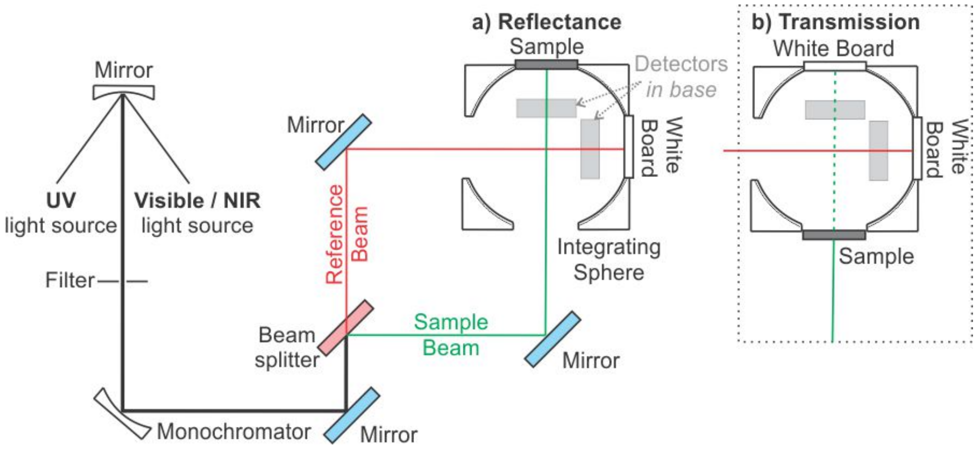

Figure 5.3: Schematic of typical UV-Vis-IR instrument showing the positions of the sample for a) Reflectance and b) Transmission measurements. Image based on Ref.[88]

In a UV-Vis-IR measurement the wavelength dependant transmission or reflection of a sample is measured. For both these spectroscopy techniques, the sample is irradiated with light with a typical wavelength range from 200 nm (UV) to 1400 nm (NIR). This radiation may be generated using a range of different light sources as represented in Fig.5.3. The measurements of this thesis were carried out under radiation from tungsten-halogen and deuterium lamps. A monochromator is used to select a narrow range of wavelengths from this emitted light [86]. The monochromatic light is split in order to give two beams of equal intensity. The reference beam goes to the detector and the second beam is focused onto the sample. For a reflection measurement the sample is placed within an integrating sphere, a hollow spherical cavity covered on the interior with diffuse white reflecting coating. This sphere ensures that any light reflected from the sample surface is scattered evenly within the cavity. This diffuse light is then detected using photomultiplier tube and InGaAs detectors in order to cover the full UV - NIR energy range, which are positioned within the sphere. In the case of transmission measurements, the sample is mounted at the front of the integrating sphere blocking the entrance point of the irradiating light. Any light that passes through the sample into the integrating sphere is detected.

In order to understand the results of these measurement, one must consider the interaction of the irradiating beam with the sample as given in Ref.[87]. Light impinging on a surface induces the atoms within the material to become polarised and oscillate causing each to emit a small secondary wave. The sum of these secondary waves determines the form of the propagating wave and gives specular reflection and refraction. The proportion of light which is reflected and refracted at the boundary is derived analytically using the Fresnel equations or computationally, by solving Maxwell's equations (see Section 7.4.1) [89][90][91]. Reflected light is either specular or diffuse depending on the nature of the interface. Specular or 'mirror-like' reflection occurs at a very smooth surface. In this reflection the angle of incidence equals the angle of reflection ($\theta_i = \theta_r$) and both rays lie in the same plane as the surface normal (see Fig.5.4). When light strikes a rough or polycrystalline material, it is scattered multi-directionally with the exact form of this diffuse light depending on the geometry of the interface. Using an integrating sphere allows for measurement of both diffuse and specular reflection, although these cannot be discerned from one another.

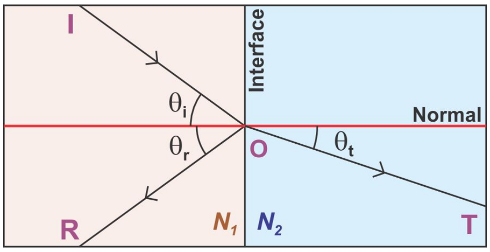

Figure 5.4: Interaction of Incident beam, IO, with the interface between two materials with refractive indices: N_1, N_2, to give a reflected beam, OR, and transmitted beam, OT.

Light that is not reflected at the interface is refracted. Each material (i.e. air/CISe) has a refractive index; n_1, n_2. The refractive index of an optical medium is determined from the ratio between the speeds of light in vacuum, c, and within the material, ν, i.e. $n = c/\nu$. The ratio between the angle of incidence and refraction is equivalent to the reciprocal of the ratio of the refractive indices as given in Snell's law, Eq.5.6 [89].

$$\frac{\sin\theta_i}{\sin\theta_t} = \frac{n_2}{n_1} \tag{5.6}$$

Therefore refraction results from a change of the phase velocity of the wave but its frequency remains constant. Within the medium some of the light is absorbed, and this is taken into account by defining a complex index of refraction, ñ, Eq.5.7 [91][92].

$$\tilde{n} = n + i\kappa \tag{5.7}$$

The imaginary part, κ is the extinction coefficient and indicates the absorption loss when an electromagnetic wave passes through a material. From κ, the wavelength dependant attenuation of the beam, the absorption coefficient α_λ, is calculated using Eq.5.8 [93].

$$\alpha_\lambda = \frac{4\pi\kappa}{\lambda} \tag{5.8}$$

If one considers a single material with surface and rear interface and thickness, x, then the transmission, T_λ, is calculated from α_λ and the reflection coefficient R_λ using Eq.5.9 (for derivation see Ref.[94]).

$$T_\lambda = \frac{(1 - R_\lambda)^2 \exp(-\alpha_\lambda x)}{1 - R_\lambda^2 \exp(-2\alpha_\lambda x)} \tag{5.9}$$

When αx is large, Eq.5.9 simplifies to Eq.5.10

$$T_\lambda = (1 - R_\lambda)^2 \exp(-\alpha_\lambda x) \tag{5.10}$$

Consequently the absorption coefficient can be calculated by combining the measured transmission and reflection using Eq.5.11.

$$\alpha_\lambda = -\frac{1}{x} ln \left[\frac{T_\lambda}{(1 - R_\lambda)^2} \right] \tag{5.11}$$

These relations makes UV-Vis-NIR measurements a valuable technique for characterising the optical properties of a thin film semiconductor. In practice, before carrying out a measurement, a zero value of transmission/reflection must be determined. This is achieved by making a measurement over the desired wavelength range without a sample in place and two white boards in place (similar to Fig.5.3b). Further information on the practical use of this technique is given in Ref.[95]. Another consideration when measuring the transmission of CISe samples is that the CISe film must first be ‘ripped off’ of the opaque Mo back contact. This prerequisite limits the usability of this technique on the fragile electrodeposited-laser annealed samples of this thesis.

5.1.5 Raman Spectroscopy

The advantages of Raman spectroscopy as a measurement technique lie in the fact that it is both non-destructive and can be carried out on small volumes of material. By analysis of its characteristic vibrational modes, the composition, bonding, alloying and the crystallinity of a sample surface (top 100 nm) may be determined. Further details of this technique, from which the information given here was taken, are found in Ref.[96][97].

In a Raman measurement, the sample is irradiated with laser light. For the measurements included in this thesis, excitation was performed using an Ar^+ (λ = 514 nm) laser. Whilst, transmission, absorption, reflection and refraction are the dominant photon-matter interactions, <1 % of the photons incident on the sample are scattered. If the scattered photon retains its energy the process is termed elastic scattering. In a scattering spectra as shown in Fig.5.5a), the elastic scattering is observed to give the highest intensity and is termed the Rayleigh signal. This appears at a frequency equal to that of the irradiating radiation, ω_1. This signal is due to the creation of a polarisation field within the sample by the incident electromagnetic wave. As this applied field oscillates, it causes the polarisation field of the material to be time dependant and therefore radiate energy at a frequency equal to the incident wave.

In the spectra in Fig.5.5a) there are also two lower intensity lines which are due to inelastic scattering and these are analysed in a Raman measurement. Within a crystalline material, at temperatures >0 K, the atoms are not static but undulate around their equilibrium positions with a certain frequency, Ω. This creates local polarisation fields at a different frequency to the incident electromagnetic wave. The magnitude of the shift in frequency between the atomic polarisation fields and the external electric field, Ω, is known as the Raman shift. The oscillation of these local fields results in the emission of radiation, shifted from the frequency of the incident beam by Ω (See Fig. 5.5). The shift of these two Raman contributions can be interpreted as the creation or annihilation a phonon with energy Ω. Creation of a phonon within in the crystal lattice results in the emission of lower energy photons (Stokes) than the incident photon and annihilation results in the emission of photons of higher energy (anti-Stokes).

These two contributions, along with the elastic (Rayleigh) scattering are indicated in Fig.5.5. The central, Rayleigh, line has the highest intensity as elastic interactions have a $10^6 - 10^9$ higher scattering intensity than the lines resulting from inelastic scattering [97]. Of the inelastic contributions, the Stokes component is used for Raman analysis due to its greater intensity compared to the anti-Stokes contribution. The intensity of a Raman signal is dependent on three factors: (1) the intensity of the source, (2) the polarisability of the atomic species and (3) the concentration of the Raman active species. The intensity of the source can be modulated, to some extent, to fit the experiment. For a bond in a crystal to be Raman active, a dipole moment must be created in the vibration which ensues the absorption of a photon. This follows a complex set of selection rules which are described by group theory. More information on this theory is given in Ref.[96][98].

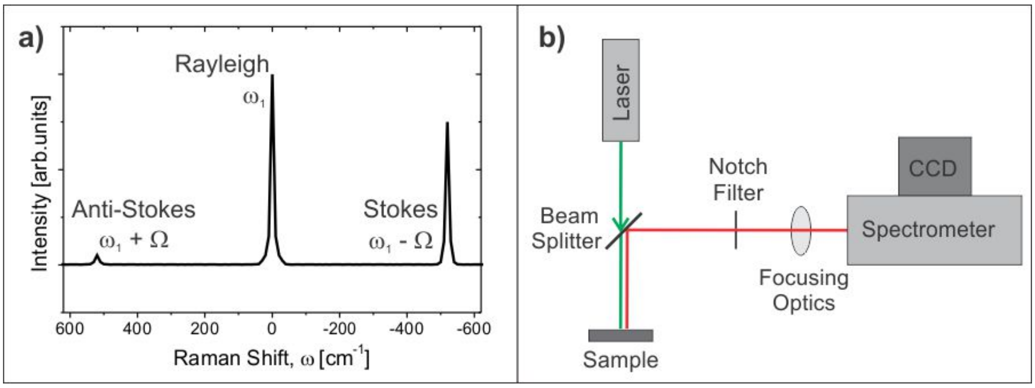

Figure 5.5: a) Scattering Spectrum of crystalline Si showing the Rayleigh (elastic), Stokes and Antistokes (inelastic) contributions. b) Sketch of a typical instrumental setup used for Raman and Photoluminescence.

CISe and the binary semiconductors ($Cu_{2-x}Se$ and In_2Se_3) have Raman active modes, and therefore produce characteristic lines in a spectra. By analysing the Raman shift, or frequency, at which these lines appear and their intensity and shape, it is possible to gain physical and chemical information about the sample. In this field of research, Raman spectroscopy is often used as complimentary to XRD. The value of Raman lies in identifying phases, e.g. $CuIn_3Se_5$, and lattice ordering, e.g. Cu(Au)-type ordering, that are difficult to elucidate with XRD. It is also possible to deduce the crystallinity and stresses present within a sample. However, Raman spectroscopy is a surface sensitive technique, with a λ = 514 nm Ar^+ laser only probing the surface $\approx$150 nm of a CISe sample.

In Fig.5.5b) a typical measurement set up is depicted. Excitation from a laser light source is focused on a sample. Radiation emitted from the sample is then refocused and measured, typically using a charge-coupled device (CCD) detector. For these measurements the beam diameter on the sample was observed to be $\approx 1.3\ \mu$m, although lateral resolutions below 1 μm can be achieved. The resolution is determined by the spectrometer focal length, diffractometer grating, the wavelength of the irradiation laser and the pixel size of the detector.

5.1.6 Photoluminescence (PL)

Detailed information on photoluminescence and its application to thin film solar cells can be found in Ref.[99].

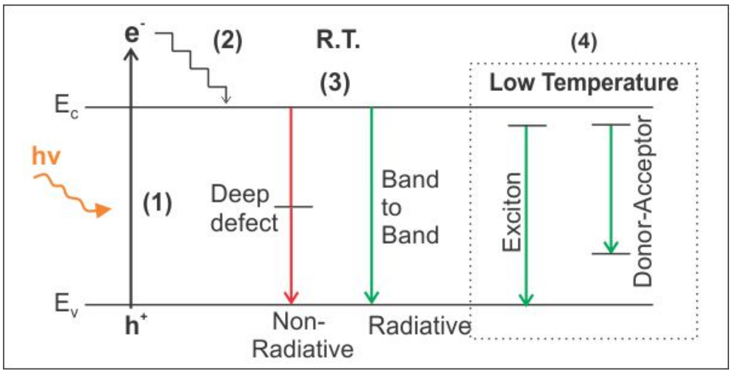

Figure 5.6: Diagram indicating common excitation and recombination pathways in a PL experiment. (1) Photon absorption creating an electron-hole pair. (2) Thermalisation to the band gap. (3) Recombination pathways at room temperature (R.T.). (4) Examples of low temperature recombination pathways.[99]

Irradiation of a semiconductor with a light source of sufficient energy can also result in the excitation of electrons from the valence band (VB) into the conduction band (CB) [99]. Electron-hole pairs formed deep within the band thermalise (emitting phonons) to the band edge and subsequently recombine with the emission of photons, a process termed luminescence. In photoluminescence (PL) photoexcitation stimulates the transitions which give rise to luminescence. Whilst the emitted photon should have an energy equal to $E_c - E_v$, a non-ideal material may also contain mid gap energy states or deep defects meaning that an indirect recombination route between the VB and CB becomes favourable (see Fig.5.6). These recombination processes are non-radiative and reduce both the PL yield, Y_{PL}, and the carrier lifetime, τ. τ is the average time between charge carrier generation and annihilation by recombination. Minority carriers (electrons in a p-type semiconductor) are generated up to a depth equalling the penetration depth of the incident photon beam defined as $1/\alpha_\lambda$. The detected photon flux $Y_{PL}(E)$ at room temperature is expressed using Eq.5.12 [100].

$$Y_{PL}(E) = \frac{1}{4\pi^2\hbar^3c^2}\frac{\alpha_b(E)E^2}{\exp(\frac{E-\Delta\mu}{k_BT} - 1)} \tag{5.12}$$

In this equation, the absorptivity at a specific energy (E), is given by $\alpha_b(E) = (1-R)(1-exp(-\alpha_\lambda d))$, where R is the reflectivity and d the film thickness. In Eq.5.12, $Y_{PL}(E)$ is linked to the quasi-Fermi level splitting, $\Delta\mu$. As $\Delta\mu$ is related to the maximum open circuit voltage, V_{oc}, of the photovoltaic device, PL is a valuable technique for quantitatively determining the quality of an absorber layer. To extract $\Delta\mu$ from a PL spectrum, the high energy wing of the PL signal is fitted. At energies above the band gap, $\alpha_b(E)$ is approximately constant and $\alpha_b(E) = 1$. Applying the Boltzmann approximation that $E - \Delta\mu \gg k_B T$ [101], Eq.5.12 can be expressed as [99]:

$$\ln\left(\frac{Y_{PL}(E)}{10^{23}E^2/cm^2eVs}\right) = \frac{E - \Delta\mu}{k_B T} \tag{5.13}$$

The linear fit of $\ln Y_{PL}$ against E(eV) can then be input into this equation, to calculate a value of T, the sample temperature, and subsequently $\Delta\mu$ [101]. This quantitative evaluation is carried out on spectra measured using room temperature PL, where the main transitions are band-to-band. Low temperature PL measurements can also be carried out using temperatures of around 10 K. This gives a higher luminescence efficiency and allows for the observations of defect transitions and excitons. These common transitions are given in Fig.5.6.

The PL measurements presented in this work were carried out at room temperature (RT-PL) on a home built set-up. An example of the typical equipment used for a PL measurement is given in Fig5.5. The excitation light source and the optical filters may closely resemble or match those used in a Raman experiment, and it is possible to use the two techniques in parallel to yield structural and optoelectronic information on a sample.

5.1.7 Photoelectrochemical Analysis of Absorbers (PEC)

PEC is a valuable characterisation technique in that it enables one to probe the optoelectronic properties of an absorber and to provide an approximate expectation of the solar cell efficiency [102] without fabrication of the complete device. A brief introduction to the measurement is given here and a detailed description of the theory behind photoelectrochemistry may be found in Ref.[103]. A typical photoelectrochemical cell is illustrated in Fig.5.7.

In PEC, the absorber layer forms the working electrode of a three-electrode electrochemical cell with counter and reference electrodes as described in Section 6.1.1. In the measurements described in this work, a platinum wire counter and Ag|AgCl reference electrodes and $Eu(NO_3)_3$ 0.1M electrolyte are used. A band diagram of the semiconductor and $Eu(NO_3)_3$ electrolyte, when there is no contact between the film and solution, is given in Fig.5.7b). When the CISe film is immersed in the electrolyte (Fig.5.7bii), the Fermi level of the semiconductor and the electrochemical potential of the redox couple in solution equalise, via the exchange of charge carriers. Due to the generally much higher concentration of species in solution compared to the doping density of the semiconductor, there is band bending and formation of a space charge region (SCR) on the semiconductor side of the junction.

The Eu electrolyte contains predominantly Eu^{3+} species. CISe is a p-type semiconductor and therefore, without illumination there should be no free electrons present in the film able to reduce the Eu^{3+} electrolyte to Eu^{2+}. If the film contains charged defects, short-circuiting conductive secondary phases or pin holes (holes in the film, which allow direct contact between electrolyte and Mo-back contact) then a simple faradaic reduction reaction can take place to produce Eu^{2+} ions. These re-oxidise at the CE and a current response is measured. Therefore the magnitude of the current measured in the dark, the dark current, can provide information on the relative film quality. When the semiconductor is illuminated (1) with light of energy greater than its band gap, E_g, electron-hole pairs are generated (2), as shown in Fig.5.7c). Under illumination two quasi Fermi levels are required to describe the charge carriers since the minority carrier population significantly increases. Free electrons formed within the SCR or that are therein

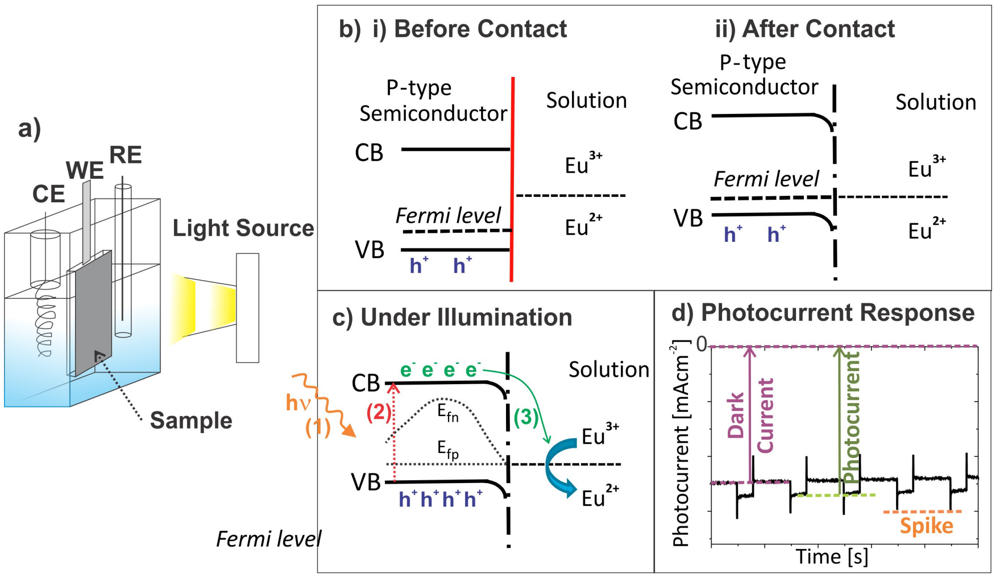

Figure 5.7: a) Diagram showing a typical electrochemical cell with working electrode, WE, counter electrode, CE and reference electrode, RE. A chopped white light with 30% duty cycle is used for photoexcitation. b) Band diagram of CISe semiconductor and Eu electrolyte, i) before and ii) after contact with the electrolyte. c) Band diagram illustrating electron-hole pair generation (2) in the semiconductor upon photoexcitation (1) and subsequent reduction of Eu^{3+} ions in the electrolyte (3). E_{fp} and E_{fn} correspond to the quasi-Fermi levels of holes and electrons respectively. d) Typical photocurrent response measurement of a film: the negative sign of photocurrent signifies photoreduction of the electrolyte and implies that the semiconductor has p-type doping.

transported, diffuse to the film surface due to a gradient of electrochemical potential where they can reduce the Eu^{3+} in the electrolyte and generate a current response, termed the photocurrent, in the external circuit. However, the photogenerated electron-hole pairs in the semiconductor are metastable and therefore may recombine before the electron reduces the Eu^{3+}. The lifetime of the electron-hole pair is reduced by defects in the film and at the interfaces. A shorter lifetime reduces the average diffusion length of charge carriers, decreasing the probability that they will reach the semiconductor surface and reduce the electrolyte. Therefore the measured photocurrent is a convolution of the charge carrier generation, transport and collection processes. The photocurrent and dark current are labelled on the current-time plot example given in Fig.5.7d).

The magnitude of the photocurrent is also dependent on the electrolyte, the wavelength of the irradiating light and the applied potential, therefore only results on absorber films measured under the same conditions provide meaningful qualitative assessments. During a PEC experiment a potential is applied to the WE. This shifts the position of the Fermi level in the CISe film and leads to an increase or decrease in band bending. With a more negative potential than the equilibrium condition, the SCR width becomes smaller and there is steeper band bending. This reduces the energy barrier for electron transfer to the electrolyte. However, at very negative or very positive potentials faradaic electrochemical processes can damage the film by reducing or oxidising it, respectively. In order to determine an optimum applied potential for a PEC experiment a cyclic voltammogram (CV) is measured. Both CVs and the usable potential range are described in section 6.1.2. Common potentials used are from -0.1 to -0.3 V and the film is held at this potential during which the current is measured over time, while the film is illuminated with chopped white light with 30 % duty cycle.

5.2 Completed device optoelectronic properties

Once a promising absorber layer is produced, it may be completed into a photovoltaic device. The final CIGSe device is constructed as shown in Fig.4.1. It is the characterisation of this device, by measuring its response to photoexcitation, that allows determination of power conversion efficiency and which forms the final goal of all research efforts. The information provided here on the analysis of photovoltaic devices may be found in Ref.[104], in which one can research these techniques in greater detail.

5.2.1 Current Voltage (IV)

The merit of a solar cell is judged principally by its efficiency, a value that accumulates and links all the device properties. Efficiency is calculated from a current voltage (IV) measurement, were the output current of a device is recorded as a function of the applied voltage. Initially the current response of the device is measured without illumination, under reverse and forward bias, to examine the semiconductor diode behaviour. This ‘dark IV curve’ is depicted in Fig.5.8. The measurement is then repeated under illumination with a known power (P_{in}) and spectral illumination, which, in the measurements presented in this thesis, was from a cold mirror halogen lamp. The halogen lamp illumination intensity is calibrated to 0.1 Wcm^{-2} using a silicon Solar Reference Cell (SRC-1000-RTD-QZ).

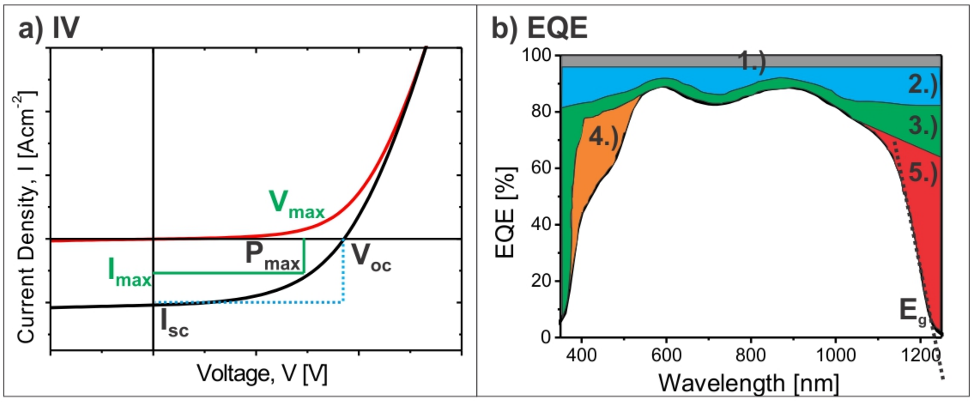

Figure 5.8: a) Typical IV curves of a CIGS-based device in the dark (red) and under illumination (black). The points corresponding to V$_{max}$, I$_{max}$, V$_{oc}$, I$_{sc}$ and P$_{max}$ are indicated. b) Representation of an external quantum efficiency measurement for this device showing optical and collection losses: 1) grid shading, 2) surface reflextion, 3) ZnO absorption, 4) CdS absorption, 5) insufficient absorption and collection. As given in Ref.[105]

To understand the appearance of the dark curve, the behaviour of the p-n junction at equilibrium and under reverse and forward biased is considered. This is presented in a simplified manner in Fig.5.9. The position of the Fermi level, E$_f$, of a material in relation to its conduction band, E$_c$, and valence band, E$_v$, is dependent on the doping of the material. It is seen in Fig.5.9 that in the p-type absorber layer E$_f$ is closest to E$_v$, whereas in the n-type buffer layer, E$_f$ is closer to E$_c$. To form the heterojunction device, such as illustrated in Fig.4.1, E$_f$ equilibrates to a constant energy with band bending at each interface created by the diffusion-driven recombination of excess charge carriers. This creates a charged, depleted region at the interface of the materials known as the space charge region (SCR) as indicated in Fig.5.9a). The difference between the conduction bands of the two materials is termed the built in potential, V_{bi}. To measure an IV curve, the potential is swept from reverse to forward bias. With an applied potential, the Fermi level is no longer constant through the system. Under reverse bias, the Fermi level in the n-type material is lowered beneath that in the p-type material, by a quantity dictated by the applied voltage. This leads to an increase in V_{bi} and there is very little electron transfer from the n- to p-type material. Hence $I \approx 0$ under reverse bias, as observed in Fig.5.8a). In contrast, at forward bias the Fermi level of the n-type material is lowered, facilitating electron transfer from the n- to p-type material and $I > 0$ is measured. The current density in the dark, I_d is given by the diode equation, Eq.5.14 [104].

$$I_d = I_{sat}\left[\exp\frac{qV}{k_BT} - 1\right] \tag{5.14}$$

Eq.5.14 relates the net current density flowing through the diode, I_d, to the saturation current density, I_{sat}. The thermal voltage, k_bT/q, gives the temperature dependence of the curve, and comprises, k_b, the Boltzmann constant and q the absolute value of electron charge. This equation assumes a single p-n junction with ideal behaviour and no losses.

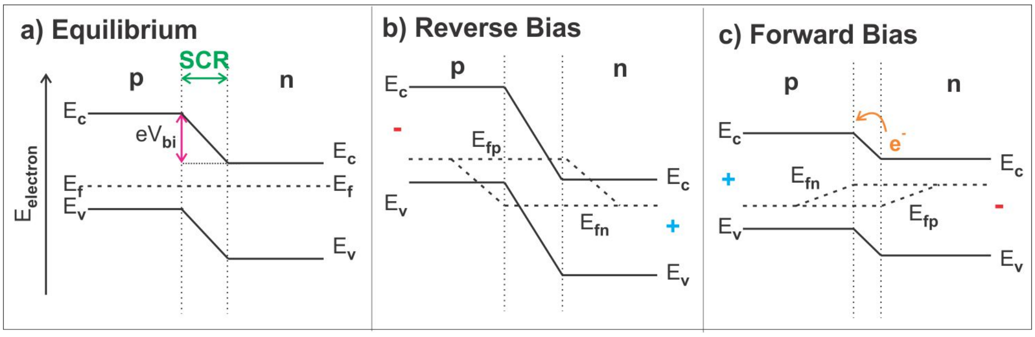

Figure 5.9: Band diagrams of a p-n junction showing a) an equilibrium situation, where p-type and n-type materials are in contact. The Fermi level, E$_f$, of the two materials has equalised leading to band bending, and a built-in potential, V_{bi} at the junction. Applying a b) reverse and c) forward bias across the p-n junction results in a splitting of the Fermi levels into quasi-Fermi levels of electrons, E$_{fn}$ and holes, E$_{fp}$. This changes the height of the energy barrier at the p-n junction [106].

When the IV curve is measured under illumination, it can be seen in Fig.5.8a) that this results in a negative shift of the curve by a near constant value. This value, is the short circuit current density, I_{sc}, the current flow at zero applied bias. I_{sc} can be approximated to the photocurrent density, I_{ill}, assuming the collection function is independent of bias (note that the IV curves of Fig.5.8 do not obey the superposition principle). Therefore, under illumination, an additional term is added to Eq.5.14 to give Eq.5.15. Where I is the current density measured under illumination.

$$I = I_{sat}\left[\exp\frac{qV}{k_BT} - 1\right] - I_{ill} \tag{5.15}$$

This equation assumes a diode quality factor, A = 1 [107]. The diode quality factor, A, is a measure of how closely the investigated diode obeys the ideal diode equation [108].

The voltage measured at zero current is the open circuit voltage, V_{oc}. For each point on the IV curve, the output power can be calculated from P_{out} = I.V. At one point, P_{out} will reach a maximum, P_{max}, where P_{max} = I_{max} . V_{max} (see Fig.5.8a). P_{out} can be compared to the incident illumination power, (P_{in}), from the halogen lamp in order to determine the power conversion efficiency of the device, η_{eff}, as given in Eq.5.16 [109].

$$\eta_{eff} = \frac{P_{out}}{P_{in}} = \frac{V_{max}I_{max}}{P_{in}} = \frac{I_{sc}V_{oc}FF}{I_0} \tag{5.16}$$

Where I_0 is the incident light intensity. Another factor which can be extracted from an IV curve, and is given in Eq.5.16, is the fill factor, FF. FF is defined as the squareness of the IV curve [109] and is calculated by finding the ratio between the area of the rectangle formed by P_{max} to that formed from I_{sc} and V_{oc} (as indicated on Fig.5.8a). Shockley and Queisser determined a theoretical limit for the efficiency of p-n junction solar cells [110] and showed that even in the ideal case, the curve is not described by this rectangular form but with the diode equation given in Eq.5.15. Using this equation, the maximum FF of CIGS with a band gap of 1.15 eV at 300 K is calculated as 87 % and η_{eff} = 32.8 % [105].

Other deviations from ideality are betrayed in the series, R_s, and parallel (shunt), R_{sh}, resistance values, as well as the diode ideality factor, A. These parasitic resistances reduce solar cell efficiency by dissipating power, and thus decrease the fill factor. The diode equation, Eq.5.15 can be extended to included these parameters as shown in Eq.5.17 [107].

$$I = I_{sat}\left[\exp\frac{q(V - R_sI)}{Ak_BT} - 1\right] + \frac{V - R_sI}{R_{sh}} - I_{ill} \tag{5.17}$$

From the dark IV curve the magnitude of R_s and R_{sh} can be measured. The shunt resistance is determined from the slope of the IV curve near the I_{sc} point and the series resistance at voltages more positive than the V_{oc}. In the ideal case, R_{sh} = ∞ and R_s = 0. This equation assumes that the recombination rate, R, is proportional to the product of electron and hole carrier concentrations ($R \propto np$) and that the carrier mobility is sufficiently high to extract charge carriers at all voltages under consideration [104]. If A is $>$1 then this indicates a change in the magnitude or type of recombination, e.g. to within the depletion region.

5.2.2 Quantum Efficiency (QE)

In an ideal scenario, each incident photon with energy greater than the band gap ($h\nu > E_g$) would generate an electron hole pair within the absorber layer, which is then transported and collected to contribute to I_{sc}. In reality there are a number of current loss mechanisms within a device. To identify these losses, the external quantum efficiency, EQE, is measured. An EQE measurement compares the wavelength dependant number of electrons collected, dI_{sc}/q with the incident photon flux, $d\Phi$, as given in equation 5.18 [104].

$$EQE = \frac{dI_{sc}(E)}{qd\Phi(E)} \tag{5.18}$$

An EQE measurement is carried out by irradiating a sample using a light source with monochromatic illumination, which varies over a given spectral range, and measuring the collection current as a function of wavelength. The photon flux is ascertained using a reference sample. Comparing this incident photon flux to the collection current (Eq.5.18) gives an EQE plot. Each layer in a device has a characteristic absorption spectrum which results in a loss in the EQE at a specific wavelength. Therefore, the EQE spectrum gives a fingerprint from which areas of major current loss in specific layers of the full device can be identified. Due to the wavelength dependence of the absorption coefficient it is also possible to determine the location of loss mechanisms within the absorber layer. When the energy of the incident radiation is below the band gap of the absorber layer the incident photons are of insufficient energy to be absorbed within the device. The EQE of a semiconductor can be described in terms of its absorption coefficient α_λ, the width of its space charge region, W, and the minority carrier diffusion length, L. using the equation derived by Gärtner, Eq.5.19 [111].

$$EQE = 1 - \frac{\exp(-\alpha_\lambda W)}{1 + \alpha_\lambda L} \tag{5.19}$$

High quality polycrystalline thin films have minority carrier diffusion lengths, L, of only 1 - 2 μm [112]. In this thesis fine grained absorbers are used which show low radiative recombination compared to high quality films, and therefore L for these absorbers is expected to be very small. In such a case Eq.5.19 is simplified to Eq.5.20 [113].

$$EQE = 1 - \exp(-\alpha_\lambda W) \tag{5.20}$$

When the incident photon energy is near the band gap of a direct band gap material such as CISe, the absorption coefficient can be expressed using Eq.5.21 [113].

$$\alpha_\lambda h\nu = A(h\nu - E_g)^{1/2} \tag{5.21}$$

Where A is a constant. Combining Eq.5.20 and Eq.5.21 leads to Eq.5.22.

$$-h\nu \ln(1 - EQE) = WA(h\nu - E_g)^{1/2} \tag{5.22}$$

Plotting $(h\nu \ln(1 - EQE))^2$ against the photon energy, $h\nu$, gives a straight line intercepting the x-axis at the band gap, E_g.

EQE measurements presented in this work were made on a home built set up where a Xe and W lamp were used for sample illumination and photocurrent was measured using a lock-in amplifier. Calibration measurements were made using Si and InGaAs photodiodes

6 Precursor Fabrication

The samples investigated in this thesis were formed using electrodeposition. This technique can produce a wide variety of precursor films and is favoured for its relatively simple and low cost methodology. The precursors investigated in the scope of this work were briefly introduced in the introduction (see Section 4.2.1 and Fig.4.2) and include layers of each metal (Cu/In/Se), the binary selenides (In_2Se_3/$Cu_{2\text{-}x}Se$) and finally codeposition of Cu, In and Se. This section will first give a general explanation of electrodeposition and then link it to electrochemical theory. In this context, the specific deposition method of each precursor type will be given and finally, their appearance, the phases they consist of and their microstructure will be analysed.

6.1 Electrodeposition and Electrochemistry

Electrochemical deposition (ED) involves the electrically induced reduction of ions in solution to form a solid plating on an electrode. A brief introduction to the theory of electrochemistry and electrodeposition is given here, further details can be found in ref. [114][115][116].

6.1.1 Electrochemical reactions at electrodes

All precursors used in this thesis were electrodeposited using a standard 3 electrode cell as shown in Fig.6.1a). In an ED process, a conductive substrate is submersed in a solution containing the elements to be deposited in ionic form (the electrolyte). The substrate forms the working electrode (WE) and oxidation or reduction reactions take place at its surface. These redox (reduction-oxidation) reactions are generalised in the form:

$$O^{+} + ne^{-} \longleftrightarrow R \tag{6.1}$$

O is the oxidised species, R the reduced species and n an integer number of electrons. To balance the reaction at the WE, a second electrode is required where an opposing oxidation or reduction reaction takes place. This is termed the counter electrode (CE). The CE lies parallel to the WE to ensure an even distribution of current density over the cell and has a surface area multiple times that of the WE (see Fig 6.1). In the depositions discussed here, the CE was a large area (16 cm^2) Pt foil.

When an electrode is first immersed in a solution, there is an equilibration between the electrochemical potential of the electrode and the solution. This process takes place by the transfer of electrons and creates a potential drop between the metal electrode and solution. When no current is passed then this potential difference reaches a steady value E_e. E_e is measured by adding a reference electrode (RE) to the electrochemical cell. The RE forms a separate electrochemical system, separated from the other two electrodes by a porous membrane. No current is passed by this electrode as this may affect its sensitive redox couple on which the deposition potential is set. The standard hydrogen electrode (SHE) is the RE against which all potential

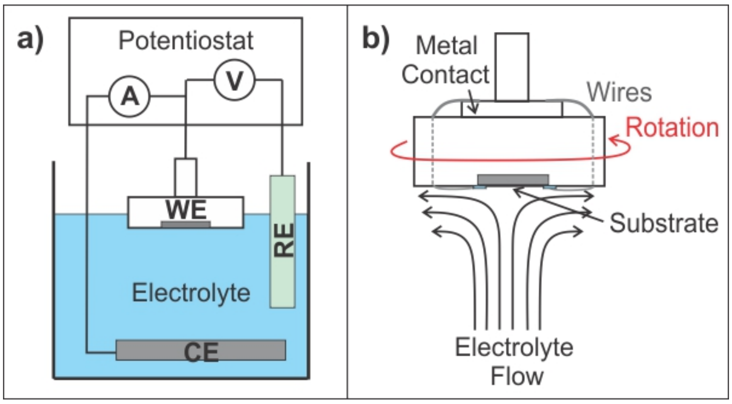

Figure 6.1: a) Three electrode cell used for electrodeposition. Working electrode, WE, reference electrode, RE and counter electrode CE. b) RDE head indicating the flow of the electrolyte over the surface of the substrate.

differences are set and has the following redox couple:

$$\tfrac{1}{2}H_2 \longleftrightarrow H^+ + e^-$$

The SHE is, by convention, defined as possessing E = 0. Measuring the potential difference between the SHE and a specific charge transfer redox couple, at 298.15 K and 1013 mbar gives the standard electrode potential, E^0. For example the redox reaction $Cu^{+2} + e^- \leftrightarrow Cu^+$ has $E^0 = 0.15$ V. Deviations from ideal conditions cause E^0 to be replaced by the equilibrium potential E_e as described using the Nernst equation.

$$E_e = E^0 + \frac{R_m T}{nF} ln \frac{[O]}{[R]} \tag{6.2}$$

$[O]$ and $[R]$ are the bulk concentrations of the oxidised and reduce species respectively. R_m is the molar gas constant, F is the Faraday constant. Unless stated, the depositions in this thesis were carried out using a Ag|AgCl RE which has a standard electrode potential of $E^0 = +0.23$ V (vs. SHE). The use of a RE ensures that all depositions are repeatable and consistent.

6.1.2 Measuring a CV

In a deposition set up (e.g. Fig.6.1a)) a specific value of E_e is reached (dependent on the electrodes, electrolyte, pressure and temperature) and at this potential no current flows. Under these conditions, E_e is referred to as the open circuit potential (OCP). In order to carry out an electrodeposition an overpotential (η) is applied between the RE and WE, which shifts the system away from E_e. η is the difference between the equilibrium reduction potential of the redox couple and the applied potential, $\eta = E - E_e$. Plotting the current flow with respect to E forms a cyclic voltammogram (CV) as shown in Fig.6.2 for an aqueous electrochemical redox couple. The starting point for the CV measurement is the OCP (E_e; i = 0 mAcm^{-2}) and E is swept back and forth between a minimum and maximum potential.

In order to interpret a CV, the electrochemical processes taking place at the WE must be understood. Applying an overpotential results in the flow of current. The magnitude of the current depends on the rate of oxidation/reduction. The redox reaction rate is dependent on two

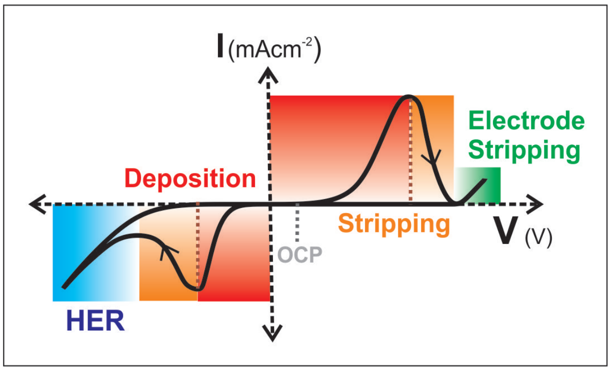

Figure 6.2: Schematic showing an exemplary CV showing the electrochemical system for a simple aqueous redox couple. The physical processes which take place are indicated in respect to the applied potential.

parameters: the mass transport of redox species to the electrode and the rate of electron transfer, k_e, to this species from the electrode. The slowest of these two processes governs the deposition rate. The deposition current, I_{dep} is summarised in Eq.6.3.

$$I_{dep} = FA(k_{e-ox}[R]_0 - k_{e-red}[O]_0) \tag{6.3}$$

In this equation $[R]_0$ and $[O]_0$ are the concentration of oxidised and reduced species at the electrode. A is the frequency factor which gives the rate of collision of the reactant with the electrode. k_{e-ox} and k_{e-red} are the rate constants for the oxidation and deposition processes respectively (see appendix 12.2).

Electron Transfer Kinetics

At the start of the CV measurement (where E is close to E_e, the red regions in Fig.6.2), the concentrations of the reactants at the electrode equal their concentration in bulk solution: $[R]_0$ = $[R]_{bulk}$, $[O]_0$ = $[O]_{bulk}$. Therefore, the current is limited by the kinetics of the redox reaction. In this situation the flow of current, I_{bv}, is determined using the Butler-Volmer equation, Eq.6.4.

$$I_{bv} = I_{ex}\left[\exp\left(\frac{(1-\alpha)F\eta}{RT}\right) - \exp\left(\frac{-\alpha F\eta}{RT}\right)\right] \tag{6.4}$$

I_{ex} is the exchange current density which describes the ‘reversibility’ of the reaction. For example, when I_{ex} is large, a low value of η is necessary to drive the reaction, with the direction (either anodic or cathodic) according to the sign of η. A small I_{ex} corresponds to a irreversible reaction and larger vales of η are required to induce current flow. α is the ‘transfer coefficient’, the sensitivity of the transition state to the drop in electrical potential between the metal and the solution. It can take a value $0<\alpha<1$ although commonly $\alpha = 0.5$, which indicates that the transition state has a structure and behaviour lying at a mid-point between the reactants and products. Details on transition state theory and rate constants k_{ox} and k_{red} are found in [115].

The CV in Fig.6.2 considers the case where an electrochemical species is deposited by applying a negative overpotential and then stripped when $\eta > 0$ is applied. A negative η raises in the Fermi level of the working electrode and allows electrons to be transferred to the species in solution. To form a deposit the ions are reduced to their 0 oxidation state. For example in the reduction of Cu, $Cu^{2+}_{(aq)}$ becomes $Cu^{0}_{(s)}$ when $E > E^0$ = 0.34 V. The $Cu^{0}_{(s)}$ forms a solid deposit on the surface of the electrode. When $\eta > 0$ electrons flow from the redox couple to the electrode and therefore the $Cu^{0}_{(s)}$ is oxidised, to form soluble $Cu^{+}_{(aq)}$/$Cu^{2+}_{(aq)}$ ions, and resulting in a stripping of the deposit.

Experimentally, the value of E giving the fastest rate of deposition and stripping is observed in the CV as the point where the electrolytic current reaches its maximum magnitude (see brown lines in Fig.6.2). Increasing η beyond these values results in a decrease in the electrolytic current (orange areas of Fig.6.2)) and therefore a slowing of the redox reaction rate. This is explained by a change in the limiting reaction kinetics (See Eq.6.3). In the case of deposition, this decrease is explained by a depletion of metal ions in the electrolyte in the vicinity of the electrode. Therefore the kinetics of the mass transport of redox species to the electrode must now be considered.

Mass Transport

Mass transport occurs via three main processes: diffusion, convection and migration.

Migration. Migration describes the movement of ionic species due to the presence of a electrostatic force. The potential difference at the electrodes exerts an electrostatic force upon the redox ions in solution. However, the electrolyte generally contains additional electrochemically inert, ionic species at significantly greater concentration ($>$100 x) than the redox ions. These shield the electrostatic field of the electrode and maintain charge neutrality in the electrolyte and thus neutralise the effects of migration.

Convection. Convection describes the movement of ions due to external agitation of the solution. The methods by which convection is applied to the deposition and the effects they have on current generation are described in Section 6.2.1.

Diffusion. In a static electrolyte, mass transport to the electrode occurs solely by diffusion. Diffusion is driven by concentration gradients, acting to maximise entropy, and moves species from regions where they are in higher concentrations to where they are in lower concentration. Under these conditions the reaction is said to be diffusion limited and the deposition current density, I_c can be described by the Cottrell equation, Eq.6.5.

$$I_c = \frac{nF[O]_0\sqrt{D}}{\sqrt{\pi t}} \tag{6.5}$$

D is the diffusion coefficient, t is the time passed and $[O]_0$ is the initial concentration of the species to be reduced. In the CV of Fig.6.2, the Cottrell equation corresponds the orange regions where large overpotentials are applied.

At the most negative applied potential the current decreases sharply (blue region) due to the breakdown of water in the electrolyte. This process is known as the hydrogen evolution reaction (HER) and the evolution of H_2 gas is via the following reactions:

$$\mathrm{H}^{+}_{(aq)} + e^{-} \rightarrow \tfrac{1}{2}\mathrm{H}_{2(g)}$$

$$\mathrm{H_2O} + e^{-} \rightarrow \tfrac{1}{2}\mathrm{H}_{2(g)} + \mathrm{OH}^{-}_{(aq)}$$

Due to the high concentrations of water in the electrolyte, a large volume of H_2 gas can be created which interferes with the deposition process and may change the pH of the solution.

When the current is swept towards positive potentials and $E > E_e$, the current increases, due to the stripping of the deposit. This process is controlled first by the electrode kinetics (red region) and then by mass transport (orange region) as with the deposition. At the extreme positive end of the CV the current further increases due to the oxidation of the metal composing the WE (green area). Both the electrode stripping and HER reactions are detrimental to the control of the deposition and quality of the deposit and therefore the CV illustrates an electrochemical deposition window.

6.2 Experimental

6.2.1 Electrodeposition Equipment

Substrate Preparation

All CISe precursors are deposited onto a substrate (lateral dimension 1” x 1”) which consists of either 2 or 3 mm thick glass sputtered with a thin film (400 nm) of Mo. Prior to deposition, the Mo surface is etched in NH_4OH solution to remove any oxides. Immediately after etching, the substrate is fixed into a rotating disc electrode, RDE (see below). Electrical contacts are made to the Mo surface by taping electrical wires onto it with chemically resistant polyimide tape. These wires are screwed into a metallic block on the backside of the RDE head which is connected to an external circuit. The quality of the contact between the front of the film and the back of the RDE head, is checked with a ohmmeter (resistance tolerance $\leq 1.5\ \Omega$). The RDE head containing the mounted substrate is then screwed into a holder which allows the substrate (WE) to be rotated and to be lowered face down into the electrolyte. Care must be taken to ensure no bubbles form on the WE at this point or during the deposition as this prevents the formation of a smooth film (this issue arises particularly when carrying out co-deposition of CISe, see Section 6.2.2).

Electrolytes

The electrolyte contains, in ionic form, the elements to be deposited. To form this solution, salts of these elements are dissolved in deionised water (resistivity of 18.2 MΩ cm). The concentration of these species is dependent on the reaction kinetics and desired composition although are generally in the 10 - 100’s mM range. For deposition baths containing multiple deposition ions, the relative diffusion rates and activities of each ionic species must be considered to achieve the correct film composition.

An inert salt is dissolved into the electrolyte, for example LiCl, KCl or NaOH. The concentration of this background species greatly exceeds that of the deposition species and is commonly > 1 M. The presence of these background ions gives a highly conductive deposition solution and furthermore may aid with pH control and facilitate the dissolution of the metal salts. The high concentration of ionic species evens out any gradient in electrical field through the deposition bath and therefore negates the effects of migration. In addition, the electrolyte may also contain complexing agents, which have the effect of stabilising the deposition ions and additives such as surfactants which improve film quality. Full details of composition of the electrolytes used in this thesis are given in Appendix 12.1.

RDE

In the deposition set up shown in Fig.6.1a), the WE takes the form of an RDE. This is a large, non-conductive disc into which the substrate is fixed. The RDE allows for the substrate to be suspended horizontally in the deposition bath and additionally enables rotation during deposition, both of which are shown to improve film homogeneity. Rotation of the RDE causes a flow of electrolyte within the electrochemical cell. This results in a constant supply of fresh electrolyte to the electrode, increasing mass transport, and therefore modifying the reaction rate. In this convection controlled system, the current flow is described by the Levich equation (Eq. 6.6).

$$I_L = 0.62nF[O^{n+}]_0 v^{-\frac{1}{6}} D^{\frac{2}{3}} \omega^{\frac{1}{2}} \tag{6.6}$$

Where I_L is the current density, v is the kinematic viscosity (viscosity divided by density) of the electrolyte (v = 10^{-6} $\mathrm{m}^2 s^{-1}$ for water at 20 ^{o}C) and ω is the angular velocity of the RDE (in rad/s). All depositions described in this thesis used external agitation of the electroylte either using a rotating RDE or with a stirrer bar.

6.2.2 Electrochemical approaches for $CuInSe_2$ formation

In the following section the important considerations for each deposition process are discussed with the references to where a more detailed description is given. Also presented are the visual appearance of each of the layers with reference to Fig. 6.3.

Electrodeposition is carried out either by applying a constant potential (potentiostatic deposition) or current (galvanostatic deposition). Application and measurement of a current and potential is carried out through a control unit. In most cases potentiostatic deposition is used, where a constant potential is applied and the deposition current measured. To control the thickness of the deposits (d) the total charge passed during each deposition was monitored. This value is determined by integrating the current density, I, over the deposition time as given in Eq.6.7.

$$d = \frac{M_w.I}{n.\rho.F} \tag{6.7}$$

Where M_w is the molecular mass of the deposited species, ρ its density and n is the number of electrons transferred. However, electrons can also be spent in parasitic reactions e.g. HER and therefore, without a value for the plating efficiency, this equation only gives an indication of deposit thickness.

Cu / In / Se

Deposition of the individual metallic elements presents the simplest electrochemical system, as only a single reduction reaction needs to be considered for each element. However, a drawback is in the multiple deposition steps, each requiring different electrolytes and techniques. The first layer of the stack is Cu. This is deposited in two separate steps, initially a thin layer (50 nm) is deposited from a strongly alkaline solution (pH $\approx$ 13) [117] which protects the Mo from the strongly acidic (pH $<$ 1), second deposition solution which is required to grow a thick, homogeneous layer [118]. The alkaline Cu deposition is in contrast to the other, acid-based depositions of this thesis, and due to its high pH requires a Hg|HgO (1 M KOH: +0.123 V) RE to be used. The acid-based Cu deposition is galvanostatically controlled as this deposition technique was

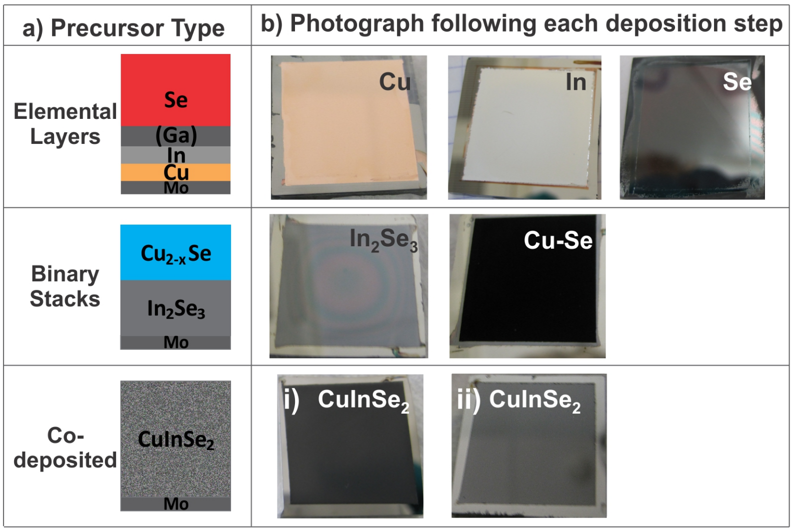

Figure 6.3: a) Illustrations of the layer-ordering of different electrodeposited $CuInSe_2$ precursors and b) images of the sample surface following deposition of each layer, i) and ii) denote codeposited CISe precursors fabricated using methods in Appendix 12.1.3 and 12.5 respectively.

designed for industrial purposes where it is more challenging to maintain a constant potential (potentiostatic deposition) over large area. Homogeneity of the deposit was achieved by rotation of the RDE (300 / 200 rpm). Total Cu layer thickness is 125 nm and homogeneity of this deposit has been proven by EDX to have a variation of $<$ 10 % over the 1" x 1" sample area.

The acidic Cu deposition gives a smooth, shiny surface onto which the In is immediately deposited to give a light grey deposit. The deposition bath was designed based on that supplied by the Indium Corporation [119], using 0.26 M In to give fast plating rates. RDE rotation was not used as it was found to result in increased thickness variation.

Finally Se must be supplied to this metallic precursor. A Se cap can be either electrodeposited [120][121] or evaporated onto the sample surface. The evaporation procedure used in this thesis was carried out using a RTP. An elemental Se source is placed in the graphite box of the RTP and is heated to 500 ^{o}C for 5 mins, vaporising the Se. Subsequent, rapid cooling results in condensation of Se onto a baseplate into which the precursor film is fixed. The sample temperature is kept constant during the process and there are no observable changes in sample crystallinity (XRD) or composition (EDX). The thickness of the Se cap was adjusted by altering the sample position, mass of Se and process temperature. The layers used in this thesis range from $\approx$100-500 nm thick. This evaporation results in a smooth metallic/red deposit of amorphous Se.

In_2Se_3 / $Cu_{2-x}Se$

When depositing binary species, the molar concentrations of the elements in the electrolyte are important in order to accurately control film composition. The phases present in a deposit are determined by comparing its elemental ratio to its binary phase diagram. The stoichiometry can also affect the morphology of a deposit. Full details of the In_2Se_3 and $Cu_{2-x}Se$ deposition baths are given in ref.[25]. As highlighted in the introduction, research into this precursor type is impeded by the difficulties of the In_2Se_3 deposition. An elevated temperature (T = 80^{o}C) is required to prevent the deposition of amorphous Se which increases the film resistivity and limits the plating thickness. The low deposition potential of In_2Se_3 (-0.6 V vs. Ag|AgCl [25]) coincides with the HER, resulting in loss of adhesion between the film and the Mo. To counter this effect, the deposition is carried out in an air tight chamber with N_2 atmosphere. This gives a shiny, grey film. The deposition of $Cu_{2\text{-}x}Se$ onto this film requires only the simple deposition equipment depicted in Fig.6.1. However, the $Cu_{2\text{-}x}Se$ forms a dark, rough film which is fragile and is easy damaged by contact. The RDE is rotated at 400 and 100 rpm for each deposition respectively. Charge passed for each layer is calculated to give a thickness of 800 nm, which after annealing in a furnace gives a final absorber layer thickness $\approx 1\ \mu$m.

Co-deposited $CuInSe_2$

Deposition of a ternary species presents the most challenging of these electrochemical systems, where the concentration of three separate ions must be considered. However, this process has been refined over years of experimentation and its properties are well established [47][122]. The method used in this thesis was based on that described in [34]. Variations to this method include the substrate being fixed within the RDE head, positioned face down in the deposition bath instead of hanging vertically, to improve homogeneity. A glass frit (semi-porous membrane) was positioned between the CE and RDE, as during the long deposition $>$70 mins, there was time for bubbles to form on the CE and float up onto the substrate. The RDE remained stationary, as drendritic growth is observed with increased convection [123]. The low concentration of the ionic redox species used in this electrolyte, mean its use is limited to 6 film depositions. Co-deposition of $CuInSe_2$ results in a smooth, grey film with 1 μm thickness.

Summary of Electrodeposition of precursors

By using a range of electrolytes, electrodes and deposition equipment it is possible to produce a wide variety of films. Comparing the images in Fig.6.3, the differences in the visual appearance of each precursor is identified; whilst metallic deposits form shiny layers, semiconductor materials such as $Cu_{2\text{-}x}Se$ and CISe are darker due to their absorption of light. Whilst by eye it is easy to discriminate differences in macroscopic homogeneity, the microscopic appearance and structure must also be considered. These are analysed in detail in the following section.

6.3 Precursor Characterisation

The objective of this work is to develop suitable precursors for laser annealing. In a laser process the selection of a singular wavelength and the very short annealing times, impose limitations on an appropriate precursor structure. Therefore, the precursors' structural and optical properties become of key importance. In this section first the structural properties of each precursor is presented after which their suitability for laser annealing is discussed.

Morphology

The surface and cross sectional appearance of the precursors is analysed using SEM. Thickness, density and grain size of each component precursor material can be determined from SEM micrographs all of which will influence the result of laser annealing. SEM micrographs of the

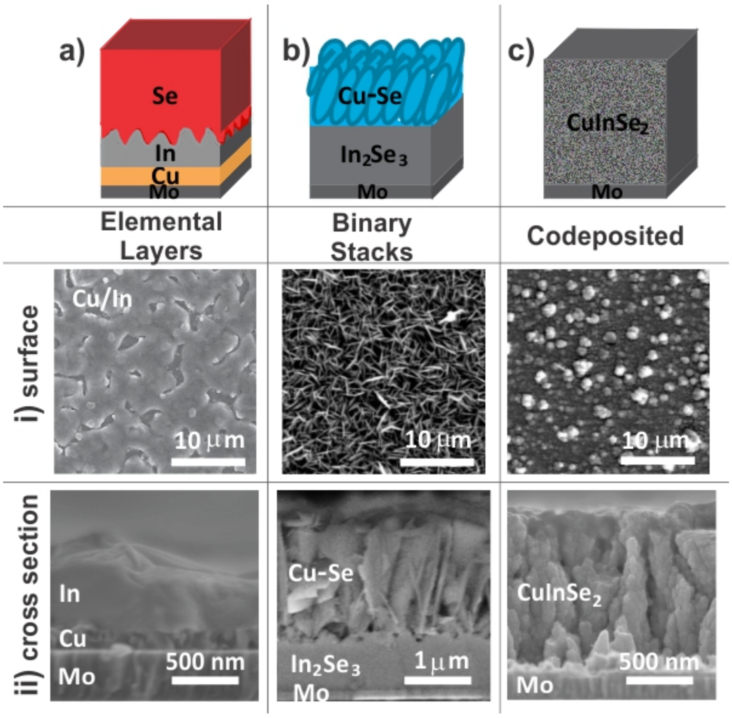

Figure 6.4: SEM micrographs of i) the surface (20 keV) and ii) the cross sectional (7 keV) appearance of a) Elemental layers, b) Binary stacks and c) Codeposited precursors. Note that ai) and aii) show the precursor appearance before Se capping

precursors are presented in Fig.6.4. From these micrographs it is observed that each compound has a very different structure. The key features of each precursor are subsequently discussed.

In metallic stacks of Cu/In/Se, Cu forms a compact, smooth layer. SEM surface analysis of this Cu deposit (not shown), indicates a nanocrystalline compact structure with grain sizes 20-50 nm. In deposition onto this surface results in a layer - island growth pattern: after a few monolayers of In have been deposited, a critical thickness is reached, after which islands form (see Fig 6.4ai-ii)). This growth is described by the Stranski-Krastanov mechanism and is common to all In depositions [124], even when a Cu-In alloy is deposited [125]. Se is evaporated onto this surface forming a smooth layer (not shown in SEM micrographs for clarity).

The surface of the In_2Se_3 / $Cu_{2-x}Se$ stacks appears needle-like (Fig.6.4bi)). This structure is elucidated in the cross sectional image (bii). Whereas In_2Se_3 forms a compact layer at the base of the stack, the $Cu_{2-x}Se$ layer is constituted of large platelets. This morphology is represented in the schematic, (b). Due to the low density of the $Cu_{2-x}Se$ layer, the actual layer thickness is approximately 1.8 μm, much greater than the expected 0.8 μm.

The co-deposited films (Fig. 6.4c)) consist of a 1 μm thick, compact, granular layer (grain size $\leq$ 10 nm). Small surface obtrusions are present as seen in the rough surface appearance.

Crystallographic Structure

Whilst SEM is able to elucidate the microstructure and density of a deposit XRD identifies the phases present within the film and can give an accurate measure of their crystallinity. XRD patterns of each of the precursor types are given in Figure 6.5.

Considering first the stacked elemental layers of Cu/In/Se (Fig.6.5a)) the diffractogram shows

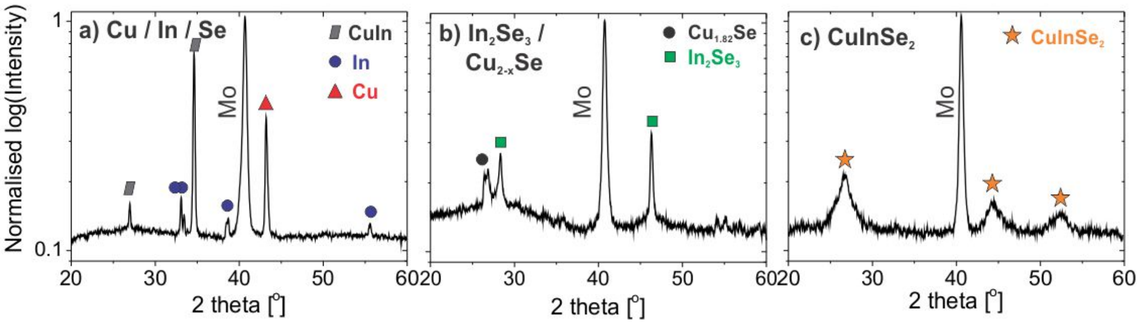

Figure 6.5: XRD patterns ($\theta 2\theta$ geometry) of a) Elemental layers of Cu/In/Se, b) binary stacks of In_2Se_3 / $Cu_{2\text{-}x}Se$, c) codeposited $CuInSe_2$. Peaks are labelled with the phases present.

that whilst the Cu and In layer were deposited separately, room temperature alloying has occurred to form CuIn. However, there is no apparent reaction between this phase and the Se to form binary selenides or CISe. There are no peaks relating to Se in the diffractogram due to its amorphous structure. Both elemental Cu and In phases remain present, showing the intermixing is incomplete: with longer times, or higher temperatures the thermodynamically most stable phase $Cu_{11}In_9$ is expected to form [126]. The binary stack precursor also shows peaks relating to only the two deposited phases In_2Se_3 and $Cu_{2\text{-}x}Se$ present, with no indication of interdiffusion of the Cu and In. In the codeposited sample phase analysis is difficult due to the broad, asymmetric $CuInSe_2$ peaks. These indicate its nanocrystalline nature and may hint at the presence of additional phases (i.e. binary selenides).

6.4 Summary

In this section the theory and methodology of the electrodeposition technique has been presented for a range of Cu-In-Se precursor types. The differences between each precursor in terms of their visual appearance, morphology and crystallographic phases present has been analysed. By using furnace annealing, all of these precursor types may be successfully fabricated into photovoltaic devices (see Section 4.3). The conditions used in furnace annealing (for example long annealing times and Se atmosphere) ensure that the necessary changes are satisfied to transform a Cu-In-Se precursor into an absorber layer. Each precursor differs slightly in its annealing requirements, for example whilst a layered structure necessitates diffusion and chemical reaction to form CISe, grain growth and defect removal are the key objectives when annealing co-deposited samples. A laser process differs significantly from furnace annealing, for example in the time-scales used, irradiating wavelength and that it is a directional heat source. As a result, the structural and the optical properties of the precursor must be considered. The phases present, stacking order and density of the precursor component materials will all affect the annealing and the precursor's optical properties i.e. reflection and absorption determine the power density through the sample depth. The following chapter presents the laser process in detail and how the precursor properties can be matched to those of the laser.

7 Laser Annealing of $CuInSe_2$ Precursors

Having discussed the formation methods and characteristics of each precursor type in Chapter 6, the laser annealing process is now investigated. The advantages of using a laser, compared to a furnace, lie in its precision, selective penetration depth and high fluxes, which result in rapid heating of the material and significantly reduced annealing times. Firstly the theory behind laser annealing is introduced and how, by choosing a suitable wavelength and mode (e.g. pulsed / continuous) this processing technique is applied to electrodeposited $CuInSe_2$ precursors. Subsequently, the optical properties of a range of precursor types are discussed. Having identified the key parameters, these are then applied in a finite element model to predict the dissipation of the laser power through the precursor stack during annealing, with the aim of identifying the most suitable distribution profile. Finally, the results of these simulations are compared to experimentally achieved results.

7.1 Laser Annealing: Theory

Lasers are optical oscillators capable of producing an intense, highly collimated beam of coherent radiation [89]. Lasers operate via a process known as stimulated emission. If an incident electromagnetic wave interacts with an atom in an excited state, the atom drops a lower energy resulting in the emission of a photon corresponding to a wave with the same phase, frequency and direction as the incident electromagnetic wave [89][90]. This is in contrast to spontaneous emission where the principle of energy minimisation causes atoms in higher energy levels to relax to lower energy levels irrespective of an electromagnetic field. Diagrams to indicate the processes of spontaneous and simulated emission are given in Fig.7.1a).

The rate of stimulated emission is proportional to the number of atoms in the excited state [89]. In order to force atoms into higher energy states (a population inversion) the gain medium within a laser is pumped using atomic collisions, chemical reactions, electrical or optical excitation [91] (see Fig.7.1ai). The gain medium is a material with properties that amplify the photons generated by stimulated emission and must also be capable of sustaining a population inversion. The gain medium (e.g. a Nd:YAG crystal) determines the laser wavelength, λ. It is contained in an optical cavity of specific length to match the photon wavelength (λ) (cavity length, $L_c = m.\lambda/2$ where m is an integer value). At each end are mirrors causing the photons to resonate within the cavity, passing through the gain medium (see Fig.7.1b) [89]. The gain medium is continually pumped, to create atoms in higher energy states. These excited atoms spontaneously decay to lower energy states emitting photons. Emitted photons can then interact with atoms, either in the lower energy level, leading to stimulated absorption, or in higher energy states resulting in stimulated emission [90]. Assuming a population inversion is present then the second process is more likely. These photons resonate within the cavity, interacting with atoms in excited states and leading to stimulated emission and a gain in the number of res-

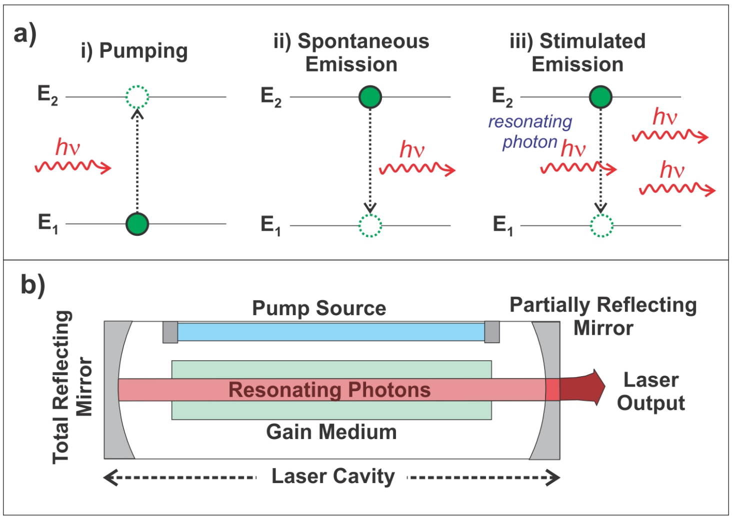

Figure 7.1: a) electron excitation and relaxation processes i) pumping of electrons into excited states, ii) spontaneous emission, iii) stimulated emission by the interaction between the resonating photons and pumped gain medium. b) Diagram of the laser cavity showing the beam bath (in red) and the mirrors, one of which is partially reflecting to allow for the laser beam output. [89]

onating photons in the cavity with matching wavelength. A partially transmitting mirror at one end of the cavity releases photons to give the laser beam output [89]. This situation describes a laser operating in continuous wave (CW) mode, where the emission intensity of photons is constant with time. It is also possible to operate a laser in pulsed mode by using an optical shutter known as a Q-switch [91]. When the Q-switch is closed, the photons remain resonating within the cavity, there is no lasing and the population inversion reaches a maximum value. Opening the Q-switch releases the large amount of stored energy in a short (ps-ns) burst. Therefore pulsed mode gives a high peak power, but low average power, and CW lasing has a higher average power, but low peak power.

7.2 Wavelength

The wavelength (λ) of the emission is determined by the gain medium, and is reinforced by the optical cavity length. λ is important as it determines the absorption mechanism of the incident radiation by a material. There are two main mechanisms of photon absorption in a semiconductor [127]:

a) If the incident photon has a lower energy than E$_g$ of the material $h\nu < E_g$ then the dominant method of photon absorption is by electrons already in the conduction band or holes in the valence band (‘free carrier absorption’).
b) When $h\nu > E_g$ it is possible to excite an electron from the valence band to the conduction band (band to band transition), forming an electron-hole pair.

For the most effective laser annealing, the photon energy is chosen to lie within the semiconductor absorption band ($h\nu > E_g$) resulting in band to band transitions. If $h\nu >> E_g$ then the electron-hole pairs must thermalise to the band edge where they diffuse and eventually recombine. Energy is released in both the thermalisation and non-radiative recombination processes and is converted to heat in the lattice. In the scope of this work, three different lasers were available with $h\nu > E_{g(CISe)}$, as summarised in the table of Fig.7.2a).

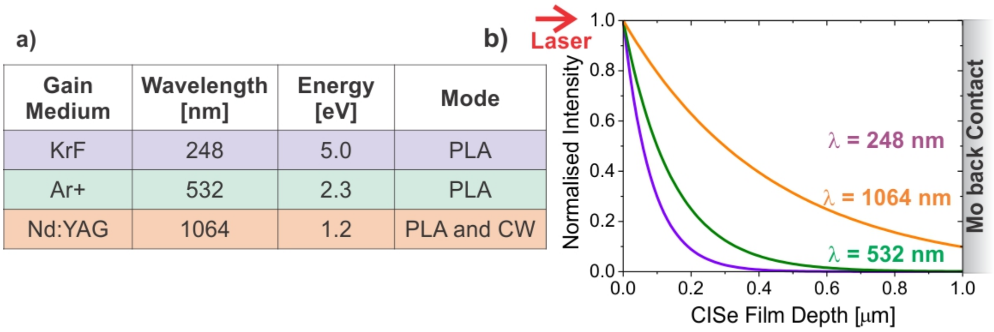
a)

Gain Medium	Wavelength [nm]	Energy [eV]	Mode
KrF	248	5.0	PLA
Ar+	532	2.3	PLA
Nd:YAG	1064	1.2	PLA and CW

Figure 7.2: a) Table of available lasers types with their emission wavelength and whether they operate in pulsed (PLA) or continuous wave (CW) mode. b) Calculated (normalised) decay of an incident laser beam with each of the wavelengths given in a) within a 1 μm CuInSe$_2$ film using α_λ values as given in ref.[128].

As a beam passes through a medium, its intensity, I, decays as photons are absorbed, in accordance with the Beer-Lambert law (Eq.7.1).

$$\frac{dI}{dx} = -\alpha_\lambda I \tag{7.1}$$

x is the depth within the material (x = 0 at the surface). α_λ is the absorption coefficient which gives the energy dependent absorption properties of the material. α_λ and its relationship to the complex refractive index of a material via the extinction coefficient, κ was introduced in section 5.1.4. Using α_λ or κ the attenuation of a beam within a material can be calculated, with the intensity of the incident beam as a function of x, given in Eq.7.2.

$$I = I_0 e^{-\alpha_\lambda x} \tag{7.2}$$

I_0 is the incident laser intensity. Using Eq.7.2 and values of κ taken from ref.[128], the energy intensity through the depth of the CISe film is calculated for each of the lasers of Fig.7.2a) and the results presented in Fig.7.2b).

Comparing the penetration depth through the CISe film of each of the lasers it is observed in Fig.7.2b) that increasing λ results in the incident energy being distributed through a greater depth of the film. When the incident energy, $h\nu >>$ E$_{gCISe}$ there is strong absorption and the incident radiation is completely absorbed within a narrow region at the film surface. For example, with a laser of λ = 248 nm ($h\nu$ = 5.0 eV), the incident beam intensity decays to 1/e within 100 nm. In contrast, when $E_{laser} \approx E_{gCISe}$ (e.g. Nd:YAG, with E_{laser} = 1.2 eV), the energy is only weakly absorbed and therefore penetrates the full 1 μm film depth with $\approx$10 % of the incident beam intensity reaching the Mo back contact.

In this thesis, the objective of the laser annealing process is to induce chemical reactions and atomic diffusion through the full CISe film depth in order to improve its structural and optoelectronic properties. Fig.7.2b) indicates that the 248 nm and 532 nm lasers are both strongly absorbed at the CISe surface. This absorption profile results in heat generation being localised within a narrow domain, relying on the thermal transport properties of the CISe film to provide energy for reactions and diffusion within its bulk. Furthermore, past work with these lasers has shown that, at the high fluences required to bring about structural changes, the CISe film melts [129]. Liquid phase CISe de-wets the Mo substrate leaving an interface incompatible with device fabrication (see Appendix 12.3). Lower fluxes induced no measurable change in peak widths in the XRD pattern indicating minimal atomic diffusion and gain growth in the films. However, increasing the flux above a threshold value leads to surface melting and dewetting. It should be noted that both the λ = 248 / 532 nm lasers detailed in Fig.7.2b) only operate in pulsed mode. In PLA a high peak power is concentrated within a short pulse time exacerbating the negative effects observed. On this basis, the Nd:YAG laser (λ = 1064 nm) in CW mode was chosen for pursuing further investigation.

7.3 Simplified consideration of laser-precursor interaction

To determine the interaction between the laser beam and precursor the optical properties of its component materials are examined. A fundamental difference between the commonly used tube furnace and a laser is in their emission (ϵ_λ). A furnace is an incoherent source of radiation meaning it emits over a wide spectral range. In contrast, the emission profile of a laser is coherent (i.e. confined to a single wavelength). Consequently, only $\alpha_{\lambda=1064nm}$ of the precursor material need be considered. As the electromagnetic radiation passes between media with different refractive indexes, a portion of the incident beam is reflected (with a wavelength dependence given by R_λ). This section examines $\alpha_{\lambda=1064nm}$ and $R_{\lambda=1064nm}$ for each CISe precursor. By comparing the relative magnitude of each coefficient, a preliminary prediction of the interaction between the laser beam and each precursor is made.

7.3.1 Reflectance

When the 1064 nm Nd:YAG laser impinges on a semiconductor, a portion of the beam energy is deflected away and is unavailable for absorption. The reflected energy is made up of specular and diffuse components (see Section 5.1.4). The axis of propagation of the laser beam is at a normal to the surface plane of the sample, therefore the incident angle, θ_i, should equal 0. However, the rough surfaces of each precursor and the presence of internal grain boundaries mean that both specular and diffuse reflection is possible. To determine the reflectivity of each precursor, reflection spectra were measured using a UV-Vis spectrometer the results of which are presented in Fig.7.3.

It is observed in Fig.7.3 that the elemental layer precursor reflects the most radiation, with R_{1064nm} = 32 % compared to 2 % for binary stacks and 7 % for codeposited CISe. This correlates with Cu/In/Se having a shiny metallic appearance (see Fig.6.3) and means that the portion of incident energy available for absorption is lowest in this sample. In contrast, binary stack and codeposited precursors visually appear dark, indicating they absorb strongly in the visual spectra, and the micrographs of Fig.6.4 showed they have a rough surface and therefore will only reflect diffusely. Also presented in Fig.7.3 (red lines) are the reflection spectra of each sample after laser annealing. All samples show a shift in R_{1064nm}, indicating possible changes in morphology and composition with annealing. This shift puts each precursor within the reflectivity range measured for CISe with R_{1064nm} 10-25 % (coevaporation [130] - single crystal

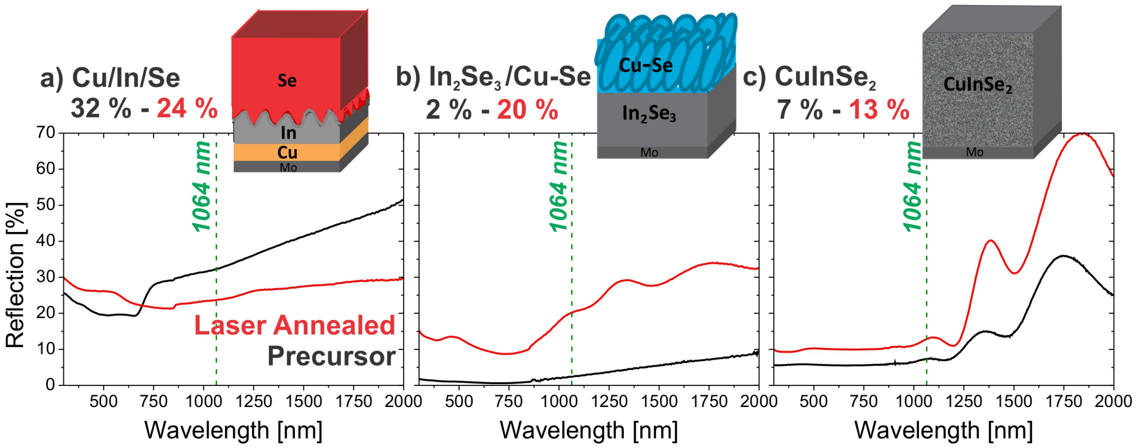

Figure 7.3: Figures showing the percentage of light reflected over an energy spectrum for a) elemental layers, b) binary stacks, c) codeposited precursors (black) and after laser annealing each of these precursors at 150 Wcm^{-2}, with a 1 s dwell time (red). Values of reflectivity are given for the precursor and laser annealed sample at ($\lambda = 1064$ nm)

[128]). However, using reflection alone, it is impossible to draw conclusions on any chemical or morphological changes. These are analysed in detail in Section 7.5.

7.3.2 Absorption Coefficient

In Section 5.1.4 the complex refractive index and its relationship to the absorption coefficient was described. The complex refractive index is used to describe the propagation of an electromagnetic wave through a medium. The real part of the refractive index, n, indicates the phase velocity, whereas the imaginary part, κ, is termed the extinction coefficient and describes the attenuation of a wave by the material. At the irradiating beam wavelength, λ = 1064 nm, CISe has κ = 0.3 [128] and therefore using Eq.5.8, α_{1064nm} = 3.5 $\times$ 10^4 cm^{-1}. The reciprocal of α_λ, gives the distance within a material by which the incident radiation (I_0) is attenuated to $I = I_0/e$, known as the ‘penetration depth’. Therefore the laser irradiation penetrates to a depth, 1/$\alpha_{1064nm} \approx$ 400 nm in a CISe film, corresponding to nearly half its thickness.

The value of ref.[128] corresponds to measurement of a stoichiometric CISe single crystal. To test the applicability of this value to the co-electrodeposited Cu-poor thin films investigated in this work, transmission and reflection spectra were measured using UV-Vis spectroscopy. The results of this analysis are presented in Appendix 12.4. This method yielded a value of α_{1064nm} = 3.3 $\times$ 10^4 cm^{-1} for a laser annealed absorber layer therefore validating the use of κ = 0.3 in the subsequent modelling. It can be seen in Table 7.1 that an alternative measurement of $\alpha_{CISe1064nm}$ gave a value slightly lower than this of 2.0 $\times$ 10^4 cm^{-1}. In order to compare the optical coefficients of each of the CISe precursor stacks, values of n, κ and α at 1064 nm are listed for each of the key component materials in Table 7.1.

Considering first Cu/In/Se stacks, Se has α_{1064nm} = 0 and therefore the beam passes, unabsorbed, through the Se cap. However, In metal has the largest α_{1064nm} of the listed materials and therefore the incident beam is attenuated by only ~8 nm of In resulting in negligible incident energy reaching the Cu layer. In the case of In_2Se_3/$Cu_{2-x}Se$, α_{1064nm} of $Cu_{2-x}Se$ is an order of magnitude less than for In, and thus 1/α_{1064nm} = 70 nm. However, the $\approx$ 2 μm thickness and

Optical Property	Mo [131]	Se [132]	In [133]	In_2Se_3 [134]	$Cu_{2-x}Se$ [135]	$CuInSe_2$ [128]
n	2.4	2.8	2.0	3.2	3.4	3.0
k	4.4	0	10	0.3	10.2	0.3
α_{1064nm} [cm^{-1}]	5.2 x 10^5	0	1.2 x 10^6	3.5 x 10^4	1.4 x 10^5	2.0 x 10^4 [136]

Table 7.1: Table listing the optical constants of the key component materials of each precursor stack. Ref.[136] corresponds to a Cu-poor, electrodeposited $CuInSe_2$ precusor.

low density of the $Cu_{2-x}Se$ layer will restrict incident radiation from reaching the In_2Se_3 layer. To form CISe absorber layers, each of the component atoms: Cu, In and Se, requires energy for diffusion and reaction. This is only achieved in the codeposited precursor and is facilitated by it comprising only a single layer and having a relatively low absorption coefficient. However, Fig.7.2 evidences a complication caused by this weak absorption, as the beam intensity at the CISe/Mo interface $\gg 0$. Consequently, there will also be reflection and refraction at the CISe/Mo interface. In order to take these interactions into account, an analytical approach is chosen.

7.4 Modelling power dissipation during annealing

In this section the method is presented by which to build a model capable of simulating the power dissipation using the properties of the incident radiation and the precursor material. Firstly, the principles of an analytical modelling technique are described. Subsequently, the key points of the experiment are considered in order to generate an accurate model. Finally the results of these simulations are presented and interpreted in terms of how these energy distributions may be reflected experimentally.

7.4.1 Finite Element Modelling

A laser beam is an electromagnetic wave and therefore its propagation is governed by electric and magnetic fields. The interdependency of these fields is described by Maxwell's equations [91][90]. The complex differentials encompassed in these equations are both time and space dependent and therefore are best solved via computer modelling. In this work Finite Element Modelling (FEM), encapsulated in the COMSOL Multiphysics software, is used. This chapter will give only simple details on the key formula and its application in the model and does not aim to give a background to optical modelling. The model was written by Ashish Bhatia of the University of Utah. In FEM, a material is split into sub-domains, named finite elements, and differential equations are solved for each point in this domain matrix. In order to set up an accurate simulation, a number of input parameters must be considered.

7.4.2 Setting up a model

The goal of the simulations detailed in this section was to map the power dissipation density (Wm^{-2}) through the depth of the precursor stack. This model considers only a single, symmetrical annealing spot and therefore uses a 2D representation of the precursor. Each component material of the precursor (including Mo/glass substrate) is input as adjacent rectangular blocks with their stacking order and x-dimension determined from the SEM micrographs of Fig.6.4.

The y-dimension was limited to 2 mm to reduce computation time, but infinite boundary conditions were specified to extend the material beyond these borders. The element size is defined in terms of maximum and minimum values. The distribution and formation of these elements within the modelled object is termed 'meshing'. The mesh shape and dispersion is adapted to the experiment for example to increase calculation points at interfaces compared to the bulk. A simple linear mesh (perpendicular to beam direction) was used for these simulations, with an element size ranging from 5 nm to 80 μm. There is a layer of air at the surface of the precursor from which the electromagnetic radiation enters. The beam is at a normal to the sample surface and its width is 2 mm. The lateral energy distribution of this beam is assumed as constant and equal to the average flux measured experimentally (i.e. 150 Wcm^{-2}). It should be noted that this flux value takes the average from a Gaussian power distribution. Therefore, the model underestimates the incident flux at the beam centre and gives an overestimation at the beam edge. Hence the power dissipation values within the CISe film calculated in this model are considered as those averaged over the full width of the beam. The limitations of this simplified approach become important when heat generation is taken into account and is discussed in greater detail in Section 9.2.2.

The electric field wave equation in matter, consistent with Maxwell's equations, is given by Eq.7.3 [137].

$$\bigtriangledown \times (\bigtriangledown \times E) - k_0^2 \left(\varepsilon_r - \frac{j\sigma}{\omega \varepsilon_0} \right) E = 0 \tag{7.3}$$

Where E is the electric field vector and j is the current density. k_0 and ω are the wavenumber and angular frequency of the wave. ε_0 and ε_r are the relative permittivities of the wave in free space and within the material respectively, with ε_r calculated using $\varepsilon_r = (n - i\kappa)^2$. σ is the electrical conductivity of the material and in this model it is assumed that σ = 0. Therefore, this formula enables calculation of E by inputting the optical properties of the material; n and κ (given in Table 7.1) and the properties of the wave; k_0 and ω. The laser pulse time was 1 s, which was input as a temporal square function, and calculation points were made at time steps of 0.02 s.

7.4.3 Results of modelled interaction

The simulation results are presented in Fig.7.4. The shape of the power density distribution is in agreement with the predictions made in the previous section from the absorption coefficient. The model yields two additional pieces of information: (1) the time dependent propagation of the beam and (2) the case of incomplete absorption. (1) Whilst, only a single distribution profile is shown in Fig.7.4, corresponding to the time at which the power dissipation density reached a maximum, it is possible to plot the development of the energy distribution against the pulse time. (2) When α is large, the penetration depth of the beam is described by 1/α and its decay by the Beer-Lambert law. However, when α is small, 1/α is of a similar magnitude to the film thickness and thus a portion of the incident radiation reaches the back of the CISe film. At the CISe/Mo interface there is reflection and refraction of the beam, causing a proportion of the energy to be reflected back into the CISe film where it creates interference patterns, known as Fabry-Perot oscillations (as observed for the codeposited precursor in Fig.7.4c). This interference pattern is difficult to predict using only 1/α. Both the time dependence and the interference pattern of the dissipated power become important when considering heat generation and transport within the layer as discussed in Section 9.2.

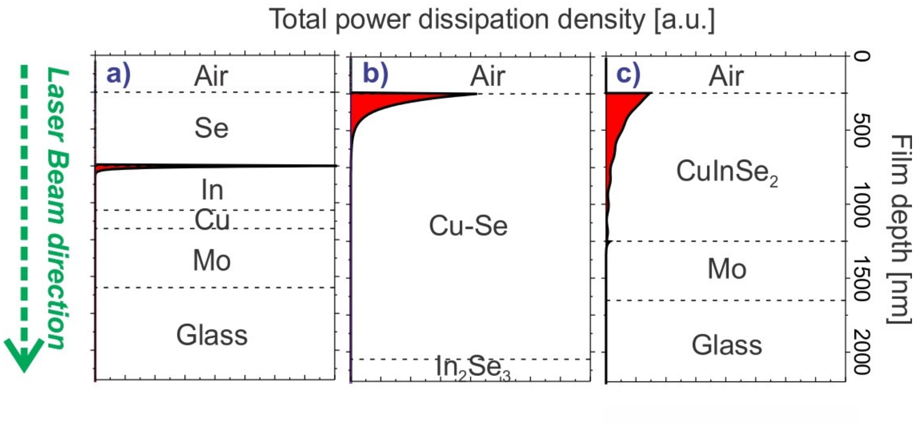

Figure 7.4: Modelled power dissipation density within precursor films after irradiation with Nd:YAG laser (=1064 nm) 150 Wcm-2 for 1 s, for a) elemental layers, b) binary stacks, c) co-electrodeposited. Graphs plot only the result corresponding to the time at which the maximum total integrated power density is achieved.

On the basis of these simulations a number of experimental hypotheses are made. For a successful annealing, the incident laser beam must supply energy to drive chemical reactions, bring about structural changes i.e. atomic diffusion and grain growth, and consequently to augment the optoelectronic performance of the absorber layer. In order to homogenise the composition through the depth of the absorber, the laser energy must be sufficiently distributed to all elemental constituents of the precursor film. Considering the power dissipation densities shown in Fig.7.4, this is only achieved within the co-deposited CISe precursor. The strong absorption of In and Cu$_{2\text{-x}}$Se, combined with the layered structure of Cu/In/Se and In$_2$Se$_3$/Cu$_{2\text{-x}}$Se, limits the distribution of the incident power to the materials at the rear interface of each stack. This limits heat generation into narrow bands and relies on effective thermal transport through the stack to supply energy to all component materials. On the basis of purely the power distribution, it is hypothesised that laser annealing Cu/In/Se and In$_2$Se$_3$/Cu$_{2\text{-x}}$Se precursors will result in minimal CISe formation, whereas there will be evidence of structural improvements in the codeposited precursor.

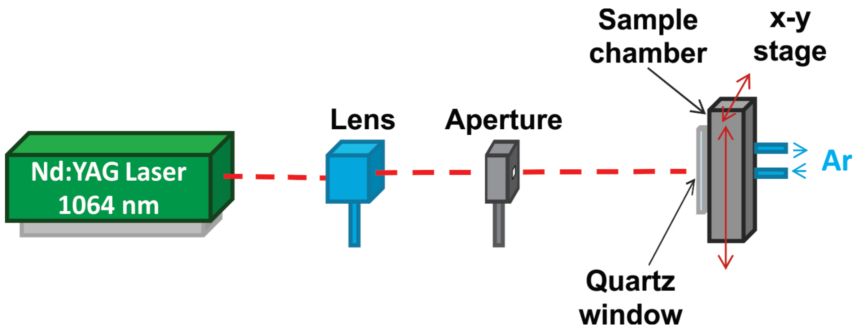

Figure 7.5: Schematic respresentation of the laser annealing set up.

7.5 Experimental and Results

Each of the Cu/In/Se, $In_2Se_3/Cu_{2-x}Se$ and codeposited CISe precursors were laser annealed using a CW, 1064 nm Nd:YAG laser with a flux of 150 Wcm^{-2} (matching the conditions used in the model). The experimental set up is shown in Fig.7.5. The laser beam is collimated and passed through an aperture to give an approximate 2 mm x 2 mm spot size on the sample. The precursor was affixed into an airtight, minimal volume annealing chamber which was continually purged with Ar during annealing. The sample is scanned through the beam, using a remotely controlled x-y stage, at 2 mms^{-1} giving a 1 s dwell time per sample area. The change in surface morphology, phases present and grain size, induced in the precursors by laser annealing, are subsequently presented and placed in the context of the predictions made in the past two sections.

7.5.1 Cu/In/Se

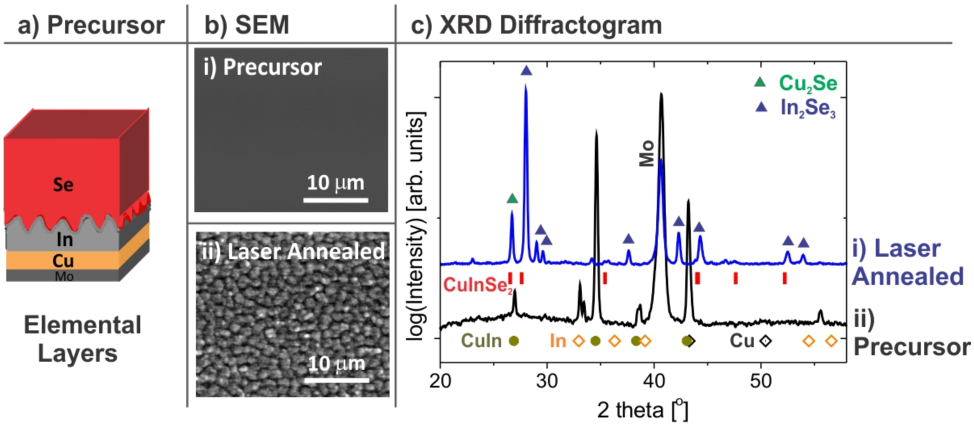

Figure 7.6: a) Schematic, bi) surface view SEM micrograph and cii) XRD pattern of elemental layer Cu/In/Se precursor. After laser annealing this precursor at 150Wcm^{-2}, 2 mms^{-1} bii) surface view SEM micrograph and ci) XRD pattern. XRD measurements were made in $\theta 2\theta$ configuration.

Modelling Cu/In/Se precursors indicated that the incident laser energy is absorbed predominantly at the In/Se interface, resulting in strong, localised heat generation. The consequence of such an absorption profile can be seen in the SEM micrographs presented in Fig.7.6b) where the flat, smooth layer of Se (i) is transformed to a rough, granular surface (ii) after laser annealing. The change in surface morphology may relate to vaporisation of the Se cap layer and melting of the In and/or the formation of In_2Se_3. In_2Se_3 is observed to be the dominant phase present within the annealed film from the XRD pattern given in Fig.7.6ci). However, there is an additional reflection at $26.6^o 2\theta$ which may correspond to the 112 Bragg peak of $CuInSe_2$ (JCPDS card file: 01-075-2916) or the 222 peak of Cu_2Se (JCPDS card file: 053-0523). The presence of either of these phases indicates diffusion and reaction of Cu atoms from the bottom layer of the stack. Whilst modelling shows a negligible portion of the incident beam energy to reach the Cu layer, the high thermal conductivity of In (82 $Wm^{-1}K^{-1}$ [138]) will lead to the Cu and In layers being isothermal. Furthermore, the XRD pattern of the precursor (cii) shows that significant room temperature interdiffusion of Cu and In has occurred to form the CuIn alloy. This alloy (not included in the model due a lack of optical data on this metastable phase) would facilitate the formation of $CuInSe_2$. However, the low intensity of the peak at $26.6^o 2\theta$ (in Fig.7.6ci) and the absence of further characteristic peaks for the $CuInSe_2$ or Cu_2Se phases indicate that their presence in the absorber layer remains minimal. The most likely factor prohibiting CISe formation, is the unavailability of Se to react with the metallic elements during annealing. Se is highly volatile (see vapour pressure curve in Fig.8.3b) and reaches a vapour pressure equal to atmospheric pressure (1×10^5 Pa) at 685 ^{o}C [139]. Therefore, at the high temperatures reached during laser annealing (see Section 9.2) Se is expected to be rapidly vaporised. Without a mechanism to keep this $Se_{(g)}$ directly available to the sample (see Chapter 11.1.3), it will be lost to the surroundings. As a consequence of this Se loss, it is difficult to form single phase CISe from this precursor type.

7.5.2 $In_2Se_3/Cu_{2\text{-}x}Se$

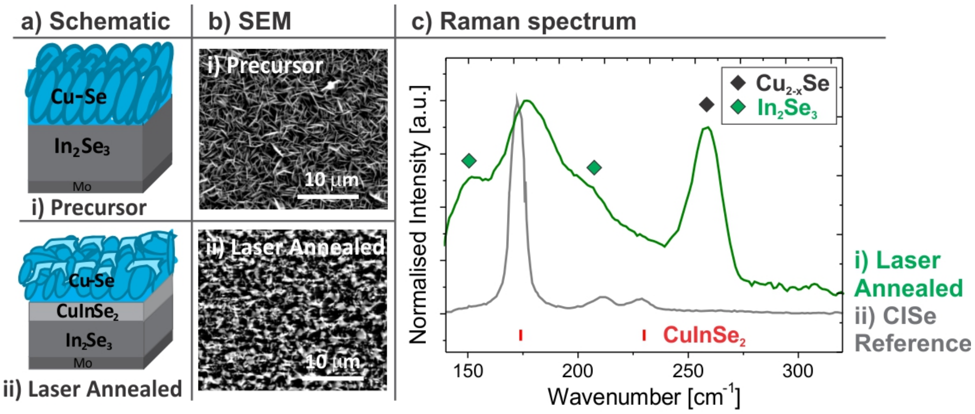

Figure 7.7: ai) Schematic and bi) surface view SEM micrograph SEM of a $In_2Se_3/Cu_{2\text{-}x}Se$ precursor. After laser annealing this precursor at 150Wcm^{-2}, 2 mms^{-1} aii) schematic representation, bii) surface view SEM micrograph SEM and ci) Raman spectrum. Positions of modes relating to $Cu_{2\text{-}x}Se$ and In_2Se_3 are taken from Ref.[140] and Ref.[141] respectively. Also shown for comparison is a cii) Raman spectrum of pure $CuInSe_2$ taken from Ref.[140].

Modelling confirmed that in $In_2Se_3/Cu_{2\text{-}x}Se$ precursors the laser power is dissipated within a narrow region at the surface of the $Cu_{2\text{-}x}Se$ layer. A key problem identified in $In_2Se_3/Cu_{2\text{-}x}Se$ precursors is that the $Cu_{2\text{-}x}Se$ layer is electrodeposited as low-density, platelets (this morphology was not included in the model). As a result, the $Cu_{2\text{-}x}Se$ thickness greatly exceeds the penetration depth of the incident radiation which may only reach the In_2Se_3 layer by passing between the $Cu_{2\text{-}x}Se$ platelets. With sufficient incident power, the focused heat generation in the surface region of the $Cu_{2\text{-}x}Se$ platelets and poor thermal transport due to the voids in this layer are expected to result in melting as visualised in the schematic representations (Fig.7.7a). This hypothesis can be applied to explain the appearance of the SEM micrographs (Fig.7.7b). The needle like appearance of the precursor (i) becomes blurred after laser annealing (ii) relating to the tops of the $Cu_{2\text{-}x}Se$ platelets melting. The phases within this absorber layer are identified by comparing its Raman spectrum to that of a $CuInSe_2$ reference (Fig.7.7c). Raman spectroscopy is utilised due to the main modes of CISe and $Cu_{2\text{-}x}Se$ having different wavenumbers, whereas their XRD peaks occur at similar 2θ positions. In addition to peaks identified as relating to $Cu_{2-x}Se$ and In_2Se_3 there is a broad peak at similar wavenumbers to the $CuInSe_2$ A_1 vibrational mode although this is shifted from that of the reference sample. It would therefore appear that laser annealing results in some $CuInSe_2$ formation and that sufficient energy is transmitted to the In_2Se_3 for diffusion and reactions to occur. However, it is impossible to assess the relative quantities of phases within this sample using this measurement technique, considering the limited information depth of Raman spectroscopy ($\sim$ 150 nm) and without knowledge of how the beam penetrates the micro-structured $Cu_{2\text{-}x}Se$ layer.

7.5.3 Codeposited $CuInSe_2$

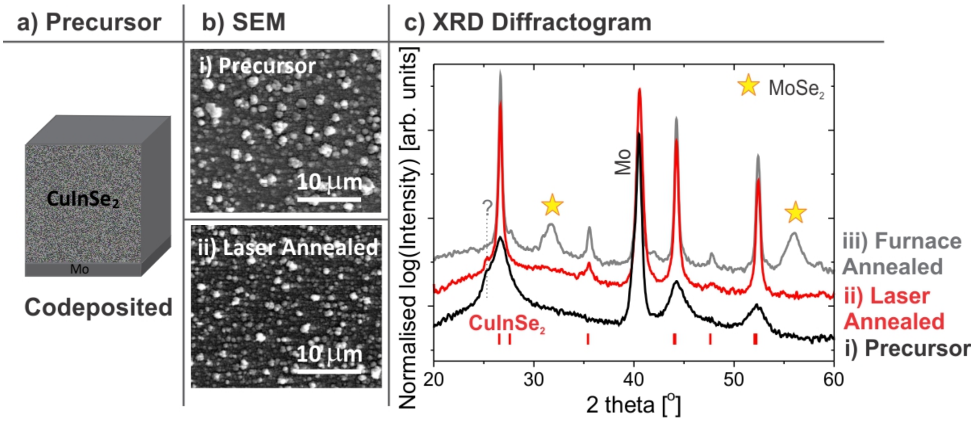

Figure 7.8: a) Schematic, bi) surface view SEM micrographs and c) XRD pattern of co-electrodeposited $CuInSe_2$ precursor. After laser annealing this precursor at 150 Wcm^{-2}, 2 mms^{-2} bii) SEM micrograph and cii) XRD pattern, compared to ciii) XRD pattern of a furnace annealed co-electrodeposited sample. The origin of the peak labelled “?”is discussed in Ref.[142].

Due to the low α_{1064nm} of $CuInSe_2$ (believed to be the dominant phase in this precursor), modelling indicated that the incident laser power is dissipated through its full depth. Comparing the SEM micrographs of the precursor and laser annealed absorbers in Fig.7.8b) evidences little difference in their surface appearance. However, when the depth of the film is probed using XRD, changes in the phases present and grain size, induced by annealing, are elucidated (Fig.7.8c). The broad, asymmetric peaks of the $CuInSe_2$ phase in the diffractogram of the precursor (i), portray its multiphase and nanocrystalline nature. The narrowing of these peaks after laser annealing (ii) indicates an improvement in crystal coherence length. A mean size of the crystallite domains (D parameter), calculated from the CISe 112 peak using the Scherrer formula (Eq.5.4), gives a value of 10 ±2 nm for the precursor and 118 ±2 nm after laser annealing. This value compares favourably with a furnace annealed electrodeposited sample, with D = 160 ±2 nm. Furthermore, only peaks relating to the CISe phase and Mo substrate are visible in the diffractogram indicating the minimal quantity of secondary phases. Therefore, even within the 1 s laser annealing time significant grain growth is achieved.

To summarise the experimental results, only with the co-electrodeposited precursor does laser annealing lead to a crystalline CISe absorber layer containing minimal secondary phases, as would be required for solar cell fabrication. The combination of the material properties and the irregular distribution of the incident laser energy (predicted via modelling) through both the binary stacks and elemental layer precursors restricts CISe formation and results in the final absorber consisting predominantly of the binary selenide phases. Consequently, it is not valuable to fabricate final devices from these layers.

7.6 Summary

This section has shown how the properties of a precursor can be matched to the laser wavelength. Annealing with a suitably chosen laser and Cu-In-Se-based precursor leads to the formation of a CuInSe$_2$ absorber layer. On the basis of its penetration depth, the Nd:YAG laser with λ = 1064 nm was chosen and tested with each of the precursor types. Initially the optical properties of each precursor was considered and then these were incorporated into an analytical model. The modelled power dissipation of the incident laser beam through each precursor film allowed for an interpretation of the experimental results. Thus, using this approach, the codeposited precursor was shown to give a crystalline, single phase CuInSe$_2$ absorber layer after laser annealing for 1 s and hence is the focus of further investigation. In the next section we will examine in greater detail the structural changes that result from laser annealing and importantly the opto-electronic properties of these absorber layers.

8 Laser Annealing with a Se atmosphere

In Section 7 the co-deposited CISe precursor was found to be the most suitable precursor type for laser annealing. The even distribution of the incident laser energy through its full layer thickness brought about a solid state recrystallisation. In this section an in-depth analysis is carried out on the absorber layers produced by this method to visualise both the structural and optoelectronic changes achieved by laser annealing. This analysis clearly shows the fundamental importance of considering thermodynamic chemical equilibria when operating at non-ambient conditions. From the reduction reactions of $CuInSe_2$ the importance of a sufficient background partial pressure of Se (P_{Se}) during the annealing is established. This chapter demonstrates how an elevated P_{Se} is achieved during annealing and investigates the effect that laser annealing under different background P_{Se} has on the properties of the resulting absorber layer as well as final devices.

8.1 Laser annealing of codeposited $CuInSe_2$

The purpose of thermal annealing is to form photo-active semiconductor material from a precursor. Therefore the input energy is required to drive the following processes:

1. Grain growth (improvement in crystal coherence length)
2. Atomic rearrangement
3. Chemical reactions
4. Removal of impurities and optoelectronic defects

The XRD pattern presented in Fig.7.8 gave evidence of an increased crystal coherence length in the laser annealed absorber layer when compared to the co-deposited precursor. To test whether requirements (2)–(4) have also been achieved, further analysis is required. The level of atomic rearrangement and the chemical reactions which have taken place are determined from elemental depth profiles. Firstly the phase composition and elemental distribution of the precursor is elucidated from the XPS elemental depth profile shown in Fig.8.1a).

It is revealed in Fig.8.1a) that the composition of the co-electrodeposited precursor varies greatly through its depth. The top quarter of the film is very Cu-poor, with the Cu/In ratio dropping below 0.2, although slightly increasing at the film surface. The Cu/In ratio increases through the film depth, reaching Cu/In $>$ 1 at the Mo interface. Importantly, whilst the concentration of Se near the surface is above stoichiometry, it decreases through the material depth, dropping to Se/(Cu+In) $<$ 1. These compositions lie far from the Cu:In:Se = 1:1:2 ratio of stoichiometric $CuInSe_2$ and lead to the assumption that binary selenide secondary phases are present at certain depths within the precursor film (as labelled on Fig.8.1a). The multiphase nature of the codeposited precursor is also observed in literature and has been assigned to In_2Se_3 and $Cu_{2\text{-}x}Se$ [122][143][144] along with elemental Se [145] with the exact phase composition dependent on the deposition potential.

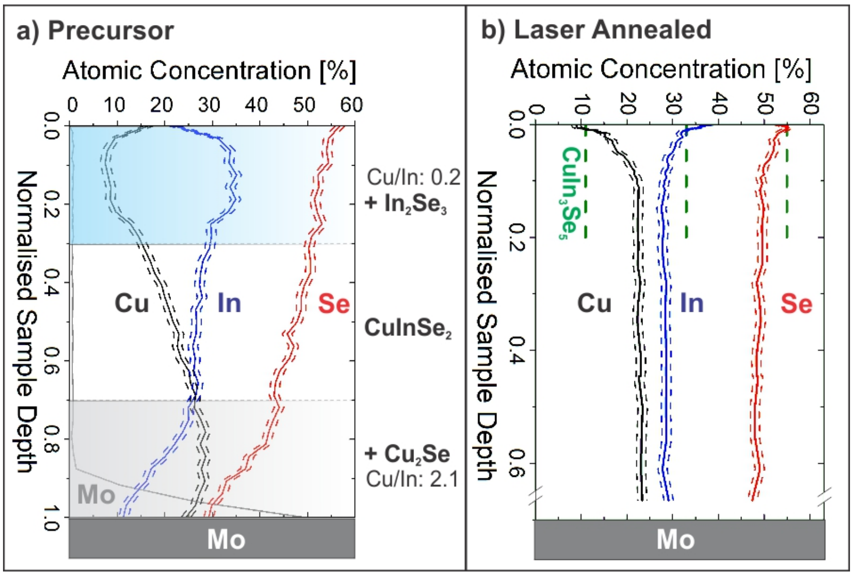

Figure 8.1: XPS elemental depth profiles of a) co-electrodeposited precursor, indicating expected secondary phases and b) after laser annealing at 150 Wcm^{-2} for 1 s. Short dashed lines give the measurement uncertainty and long dashed lines (green) indicate the stoichiometric composition of CuIn$_3$Se$_5$

This inhomogeneous and multiphase composition betrays a significant weakness in the modelling results of Chapter 7. This is partially ameliorated by using in the modelling an $\alpha_{1064nmCISe}$ (as given in Table 7.1) which relates to an electrodeposited precursor film [136]. However, the precursor film was considered to be a single block of CISe, due to the difficulty in pin pointing the exact phase mixture and the spatial position of each phase and how these would change during the pulse time. The nanocrystalline nature of the film makes the phase composition difficult to identify by XRD. To improve the model it is clear that better characterisation of the precursor and its behaviour during laser annealing would be required. The data shown is therefore to serve as a first approximation and representation of the dissipation of the laser beam energy and later, in Chapter 9, the temperature reached in such films.

In order to form a single phase semiconductor absorber layer the laser annealing process must result in chemical reaction between the binary selenides and drive atomic diffusion to homogenise the composition through the depth. The success of laser annealing is judged by comparing the depth profile of the precursor to that of the absorber layer in Fig.8.1b).

In Fig.8.1b) the bulk of the absorber layer has a depth constant, Cu-poor composition as desired for high efficiency devices [146]. However, there is a gradient in the elemental profiles at the film surface. The stoichiometry of this region reaches values consistent with that of the ordered vacancy compound (OVC) CuIn$_3$Se$_5$ phase. This compound is commonly found as a thin layer at the surface of CuInSe$_2$ films and is proposed to be favourable for the formation of a low-recombination interface with the CdS buffer layer in solar cells [147]. However, the 150 nm thickness of this surface layer in the laser annealed absorber, is much greater than the normal 50 nm or so observed in films produced using physical vapour deposition (PVD) [148].

Whilst the surface of the absorber layer is Se rich, the bulk is Se-poor at 48.5 ± 1.0 at%. Integrating the elemental profiles shown in Fig.8.1 gives Se/(Cu+In) = 0.97, close to stoichiometry for the precursor whereas this drops to Se/(Cu+In) = 0.94 for the absorber layer. Coupling these values with the condensed Se residues observed inside the laser annealing chamber, it is evident that even within a 1 s annealing time Se is lost from the precursor.

8.2 Importance of Se Partial Pressure

In order to determine the origin of this Se loss, this section presents proposed reduction reactions of CISe. Henceforth, the key requirement of considering the thermodynamic equilibria of materials when operating at elevated temperatures is emphasised.

8.2.1 Thermodynamic equilibria reaction of $CuInSe_2$

All compounds lie in equilibrium with their constituent elements. The difference in energy between a reactant and its products is determined by the change in Gibbs Free Energy of the reaction (ΔG_R). The Gibbs free energy, G describes the amount of energy stored in an orderly way in a material that is therefore free to do work [149]. It is related to the enthalpy, H, and entropy, S, of a system by Eq.8.1 [149].

$$G = H - TS \tag{8.1}$$

Absolute values for H, S and G are difficult to determine and therefore it is more common to use the change in these values when considering a chemical reaction. ΔG_R values for selected thermodynamic equilibria reactions associated with $CuInSe_2$ are given in Table 8.1.

	Reaction	ΔG_R [$kJmol^{-1}$] *at 550 °C*	p [Pa]
1	$CuInSe_2 \leftrightarrow \frac{1}{2} Cu_2Se + \frac{1}{2} In_2Se_3$	3 - 50 [150][51]	
2	$2 Cu_2Se \leftrightarrow 4 Cu + Se_{2(g)}$	201	5×10^{-10}
3	$2 In_2Se_3 \leftrightarrow 4 InSe + Se_{2(g)}$	189	3×10^{-9}
4	$In_2Se_3 \leftrightarrow In_2Se_{(g)} + Se_{2(g)}$	270	4×10^{-5}

Table 8.1: Reduction reactions of $CuInSe_2$ and their corresponding Gibbs Free Energy changes (ΔG_R) and equilibrium vapour pressures (p) [51]. Note that p was calculated from the sum of ΔG_R (1) + (2)-(4) taking an intermediate value of 25 $kJmol^{-1}$ for ΔG_R (1).

The most thermodynamically favourable decomposition reaction of CISe is into the binary selenides $Cu_{2\text{-}x}Se$ and In_2Se_3 (Table 8.1, reaction (1)). When $\Delta G_R < 0$ a reaction is said to be spontaneous i.e. there is a tendency for the reaction to occur [149]. Whilst in reaction (1) $\Delta G_{R(CISe)} > 0$, its magnitude of 3 - 50 $kJmol^{-1}$ [51][150] indicates the small difference in energy between the reactants and products at this elevated temperature and therefore the minimal energy expenditure associated with their interconversion.

Also shown in Table 8.1 are the equilibrium vapour pressures. The pressure of a system is related to the Gibbs free energy by considering that $H = U + Pv$, where U the internal energy, P the pressure and v the volume. Assuming a closed system and the absence of non-expansion work, Eq.8.2 can be deduced from Eq.8.1 (for full derivation see Ref.[151]).

$$\Delta G = v\Delta P - S\Delta T \tag{8.2}$$

From this equation, it is observed that the size of ΔG is dependent on the pressure, which is much greater for a gas than a condensed phase. To find ΔG for a reaction, the terms of Eq.8.2 can be split into the Gibbs free energy of the reactants, G_r and products G_p and their respective pressures; P_r and P_p, giving Eq.8.3 (assuming constant temperature) [151].

$$G_p = G_r + v(P_p - P_r) \tag{8.3}$$

In a perfect gas, $v = R_m T/P$. Integrating the term $v\Delta P$ over the pressure change gives leads to Eq.8.4 (see Ref.[151]).

$$G_p = G_r + R_m T \ln \frac{P_p}{P_r} \tag{8.4}$$

Where R_m is the molar gas constant (R_m = 8.314 JK^{-1}mol^{-1}). The pressures P_r and P_p are representative of the activity of the chemical species [152]. In the case of reactions (2)-(4) where the reactant is a solid, then P_r = 1. Therefore Eq.8.4 can be adapted to give the equilibrium vapour pressure p; Eq.8.5 [51].

$$p = p^{\varnothing} \exp\left(\frac{-\Delta G_R}{R_m T}\right) \tag{8.5}$$

Where p is the pressure exerted by a vapour in thermodynamic equilibrium with its condensed phase in a closed system and $p^{\varnothing}$ is the pressure of an ideal gas in its standard state. In order to determine the p values given in Table 8.1, ΔG of Eq.8.5 must comprise two terms. First CISe must break down into its binary selenides (ΔG_R (1)) and then added to this term, is the ΔG_R corresponding to the decomposition into gaseous species (i.e. ΔG_R (2), (3) or (4)). Hence Eq.8.6 uses the term $\Sigma\Delta G_R(T)$. Furthermore, for reactions involving two gaseous species i.e. A and B, p is divided into their separate partial pressures, p_A and p_B respectively giving Eq.8.6 [51].

$$p_A^m p_B^n = p^{\varnothing} \exp\left[\frac{-\Sigma\Delta G_R(T)}{R_m T}\right] \tag{8.6}$$

The partial pressure is defined as the pressure that a gas would exert if it occupied a given volume alone [152]. p_A and p_B are dependent on the mole fraction of each species and therefore Eq.8.6 includes the molar coefficients, m and n, which are taken from the balanced chemical reactions (Table 8.1).

The breakdown of CISe during laser annealing is thermodynamically favourable until the equilibrium vapour pressures (p) given in Table 8.1 are reached. Comparing the magnitude of p gives an idea of the relative measure of decomposition of each compound. Therefore the release of Se is most facile via In_2Se_3, as given in reaction (4). It should be noted that even though reactions (2)-(4) have positive ΔG_R, annealing at 550^{o}C leads to an appreciable partial pressure of gaseous products to form as a result of the decomposition of CISe. Moreover, p gives the vapour pressure of the gaseous products which develops above the material in a closed system. In an open system, such as represents the laser annealing condition thus far presented, the gaseous Se is continually removed. Therefore, reactions evolving Se will not reach steady state and the Se loss via the breakdown of CISe is continuous. Loss of Se may leave the absorber layer with Se/(Cu+In) $<$ 1, increasing the likelihood of defect formation [53]. Furthermore, CISe breakdown not only reduces the volume of CISe semiconductor material but forms binary selenide secondary phases. Each of these effect are linked to a loss in optoelectronic performance

[153][154].

In order to make the reduction of CISe thermodynamically unfavourable, the background vapour pressure of Se (P_{Se}) must exceed p of its corresponding formation reactions. To achieve an elevated background P_{Se} during annealing there are two possible approaches:

(1) Increasing the Se content of the precursor. For example by capping it with Se or depositing an Se-rich precursor. This partly counteracts the effect of Se loss and the Se vaporised during annealing may temporarily elevate the P_{Se} to reduce breakdown of the CISe.

(2) A continual supply of Se during the annealing process e.g. in the form of H_2Se gas.

Whilst option (2) is envisaged if the process was used industrially (see Section 11.2), the toxicity of H_2Se makes its use impractical in a laboratory setting. Subsequently, the addition of excess Se to the precursor is investigated.

8.2.2 Supplying Se to the Precursor

One method of adding Se to the co-electrodeposited CISe precursors is to deposit a capping layer of Se (*e.g.* via the method of Section 6.2.2). In Fig.8.2ai) a schematic of the Se capped precursor and its cross sectional appearance (ii) is given. Visually, the Se cap appears as a smooth grey layer possibly due to the surface roughness of codeposited precursors and in contrast to the metallic/red layer which is observed on the surface of Cu/In stacks in Section 6.2.2. Microscopically, the Se is seen in Fig.8.2aii) to partially infiltrate the rough surface morphology of the codeposited precursor. Excess Se, provided by the cap, is hypothesised to be vaporised during laser annealing, elevating the P_{Se} at the film surface. Increasing the background P_{Se} lowers the driving force for CISe breakdown and defect formation and therefore absorber layers resulting from Se capped precursors are expected to show improved optoelectronic properties over those from uncapped precursors. In order to test this hypothesis, a Photoelectric Current measurement (PEC) is used to measure the photocurrent response of each absorber layer, and the results of these measurements are compared in Fig.8.2.

Fig.8.1 indicated a $\approx$ 100 nm thick layer of n-type $CuIn_3Se_5$ at the sample surface which can reach up to 200 nm thickness on Se capped samples (see Ref.[155]). However, all the measured samples show a negative photocurrent (decrease in the current when illuminated) which is indicative of bulk p-type character [156]. Both laser annealed absorber layers, (i) and (ii), show a similar photocurrent response of $\approx 3\ \mu\text{Acm}^{-2}$ which is only marginally higher than that of (iii) the precursor ($\leq 2.5\ \mu\text{Acm}^{-2}$). The magnitude of the measured photocurrent in PEC experiments indicates how well charge carriers are generated, transported and collected. Therefore, the laser annealing process may slightly improve the generation or reduce the recombination of charge carriers within the film. The Se capped sample (Fig.8.2i) also shows negative and positive spikes in the photocurrent, corresponding to the times when the light is switched on and off. The presence of these spikes may indicate that there is potential for improved photocurrent but that this is currently restricted by trapping and detrapping defects at the surface of the semiconductor [156][157]. Whilst similar photocurrents are measured for all samples, there is a significant difference in the magnitude of the dark current, with the dark current of the precursor exceeding that of the annealed samples by an order of magnitude.

A higher dark current shows either that there are shunts caused by pinholes in the semiconductor film, or that a greater number of minority charge carriers are present in the semiconductor film without illumination (i.e. a highly compensated semiconductor) and that these are transported to the film surface, where they reduce the electrolyte species. The electrochemical dark

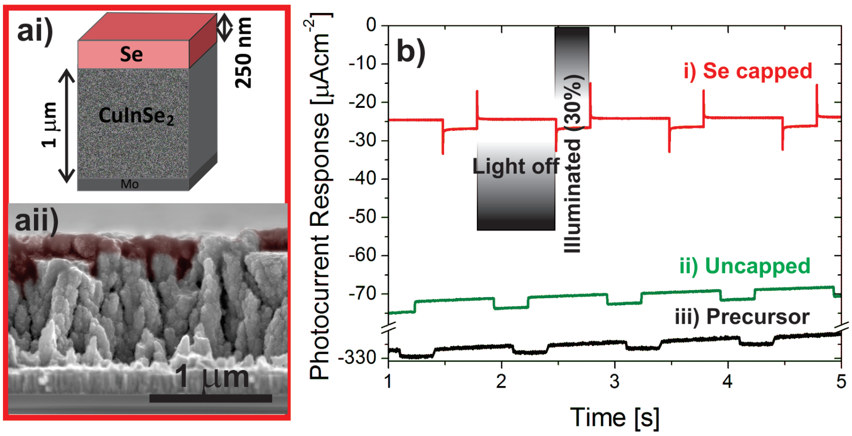

Figure 8.2: a) i) Schematic and ii) SEM cross sectional micrograph of a coelectrodeposited CISe precursor capped with 250 nm Se. b) Measurement of the PEC photocurrent response over time of absorber layers formed from laser annealing at 945 Wcm^{-2} for 1 s (i) Se capped (red) and (ii) uncapped (green) co-electrodeposited precursors (iii). Prior to measurement samples are etched for 60 s in 5 % KCN. A -0.3 V vs Ag|AgCl potential is applied and chopped white light is used to illuminate the sample with a 30 % duty cycle.

current can be considered as a convolution of reverse saturation current, I_{sat}, and shunt conductance of the absorber film when used in an electrolyte junction. Thus, all other things being equal, absorber films with lower electrochemical dark currents are expected to provide solid state devices with better quality. The ideal diode equation and its extended form was given in Section 5.2.1 (Eq.5.17). Assuming the series resistance, R_s = 0 one reaches Eq.8.7 [158][107].

$$I = I_{sat}\left[\exp\frac{qV}{Ak_bT} - 1\right] + \frac{V}{R_{sh}} - I_{ill} \tag{8.7}$$

Where q is the absolute value of electron charge, V is the applied voltage and A is the diode ideality factor. In the dark I_{ill} = 0, and therefore, to have minimal current flow in the dark, as should be found in an ideal absorber, $R_{sh} \to \infty$ (i.e. a low shunt conductance) and I_{sat} should tend to a minimum value limited by the rate of recombination [110]. Consequently, a more negative electrochemical dark current often corresponds to an absorber layer which would have a lower efficiency if completed into a solid state device. The large dark current measured for the precursor sample is in accordance with the observations that it contains highly conductive secondary phases such as $Cu_{2-x}Se$ [144]. After laser annealing the dark current is notably reduced from that of its precursor, and the dark current is lowest in the Se capped sample indicating a higher quality material in terms of lower saturation current and/or shunting.

Whilst PEC indicated that Se capping is effective at improving the optoelectronic properties of an absorber layer, these improvements were not sufficient at solid state level, because devices fabricated from these samples did not show diode behaviour in current voltage measurements. An explanation for this poor performance is whilst vaporisation of the excess Se provided by the Se cap momentarily raises the P_{Se}, the gaseous Se instantaneously condenses on the cool quartz window of the annealing chamber. Once the excess Se of the precursor is consumed $CuInSe_2$ breakdown becomes favourable.

8.2.3 Forming a Partial Pressure of Se during Laser Annealing

To prevent the loss of $Se_{(g)}$ and ensure that the excess Se provided to the precursor serves to elevate the P_{Se}, the annealing chamber is adapted to form a closed system. In addition to the chamber being gas-tight, the condensation of Se must be prevented. This is achieved using a specially designed annealing chamber shown in Fig.8.3a). The glass window of this annealing chamber is sputtered with a thin film of fluorine doped tin oxide (FTO). The FTO/Glass is transparent to the laser beam (at 1064 nm, FTO/Glass gives 71 % transmission, compared to 91 % for plain glass) but is conductive, and so, by applying a current to the FTO film, the glass is resistively heated. Current is supplied using a variable power supply and the glass temperature monitored using an IR camera. In addition to reducing Se condensation, heating the window affects the P_{Se} formed from the vaporisation of the excess Se of the precursor. The temperature dependence of P_{Se} is given in Fig.8.3b).

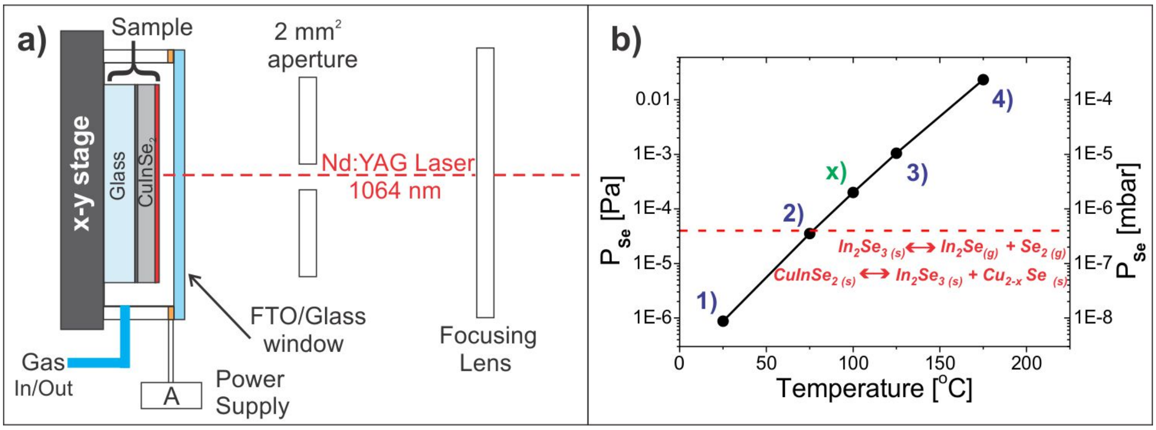

Figure 8.3: a) Diagram of the annealing chamber used to form a controlled atmosphere. b) P_{Se} as a function of temperature (CRC Handbook [159]). The values of P_{Se} and T used experimentally (1)-(4) and for the device (x) are indicated and the red dotted line relates to the highest value of p given in Table 8.1.

Fig.8.3b) shows the exponential relationship between P_{Se} and temperature. Whilst at room temperature (25 ^oC), Se has $P_{Se} = 9 \times 10^{-7}$ Pa, at 100 ^oC, P_{Se} increases by nearly 3 orders of magnitude to 2×10^{-4} Pa. From the binary selenide decomposition reactions listed in Table 8.1, Reaction (4) has the highest equilibrium vapour pressure with $p = 4 \times 10^{-5}$ Pa (at 550^oC). To render the reduction reactions of CISe thermodynamically unfavourable at this temperature, a background P_{Se} must be present which exceeds this value. This is achieved when the temperature of elemental Se exceeds 75 ^oC as indicated by the red dotted line in Fig.8.3b).

In order to investigate the effect of P_{Se} on the properties of CISe absorber layers, laser annealing was carried out under elevated P_{Se}. To achieve different P_{Se} values, the FTO window of the chamber in Fig.8.3a) is heated to a specified temperature. During an annealing process it is assumed that the FTO window is the coolest surface and that there is gas phase Se in equilibrium with this window. Therefore the minimum P_{Se} is dictated by the FTO temperature. This gives the following P_{Se} values (FTO temperature in brackets): **1)** 9×10^{-7} Pa (25 ^oC), **2)** 4×10^{-5} Pa (75 ^oC), **3)** 1×10^{-3} Pa (125 ^oC), and **4)** 2×10^{-2} Pa (175 ^oC) (as indicated on Fig.8.3b). Precursors are annealed using the irradiation of Nd:YAG laser (λ = 1064 nm), at 150 Wcm^{-2}, and 1 s dwell time (scan rate = 2 mms^{-1}). In order to provide the excess elemental Se to form this elevated P_{Se}, two different precursor types were investigated. The first had a stoichiometric CISe film (as analysed in Section 8.1) capped with ≈100 nm Se. For the second, the deposition was modified to give CISe precursors with Se/(Cu+In) = 1.3-1.4 (determined using EDX, the deposition method is detailed in appendix 12.5). The results of annealing these two sample types are subsequently presented. The effectiveness of the new annealing chamber is judged in terms of both the structural and optoelectronic parameters of the resulting CISe absorber layers and final device performance.

In order to test that the observed results were directly caused by the changing P_{Se} and not solely radiative heating due to the CISe film being in close proximity to the heated FTO, a sample was mounted in the annealing chamber and the FTO window heated to 175 ^{o}C and held at this temperature for 30 mins. XRD patterns measured before and after this test showed no shift in peak position or FWHM. The composition of the CISe film, determined using EDX and averaging the values measuring on three different positions on the sample, showed no change in either Cu/In or Se/(Cu+In) ratios. From these analyses it was concluded that heating of the CISe film by the FTO window has negligible effect on atomic diffusion and grain growth and that the significant structural changes subsequently presented result from the differences in P_{Se}.

8.3 Laser annealing with a controlled P_{Se}

This Section analyses the results from absorber layers produced by annealing both sets of CISe precursors with an elevated Se content under the P_{Se} conditions (1) - (4). Firstly the phases present and grain size of these absorbers are examined, secondly their composition and lastly their optoelectronic properties. By sufficient augmentation of each of these factors a first device is fabricated using this process.

8.3.1 Composition and Microstructure

It has been shown that furnace annealing codeposited precursors under increasing P_{Se} gives rise to a larger grain size in the absorber layer [49]. The effect of P_{Se} on the crystal coherence length measured in the absorber layer is determined using XRD and the grain size by examining the film microstructure with SEM. These results are presented in Fig.8.4.

Comparing the diffractogram of the precursor to those of the laser annealed samples presented in Fig.8.4a) it is observed that the annealing process results in a significant narrowing of the peaks relating to CISe. Using the Scherrer formula (Eq.5.4), an average size of crystallite domains is calculated from the FHWM of the CISe 112 Bragg peak and the values are plotted in Fig.8.4b). Whereas the precursor has crystallite dimensions in the range of 10 nm, both absorber layer types exhibit D parameters of 100–200 nm. Comparing the D parameters to the background P_{Se} during annealing, a positive correlation is observed for both series with the exception of the anomalously high grain size observed in the Se capped sample annealed under the lowest P_{Se} (1). Generally, increasing the P_{Se} leads to a larger crystal coherence length and is in agreement with the trend observed for furnace annealing [49]. To corroborate the D parameter values, the crystal size of the absorber layers is visualised in the SEM cross section micrographs presented in Fig.8.4c). Laser annealing results in the small grains of the precursor becoming larger and more angular. The grain sizes within both the presented absorber layers (i) and (ii) are of a comparable magnitude to the 100–200 nm coherence length range indicated by the Scherrer formula. Comparing the D parameters for the two series given in Fig.8.4b),

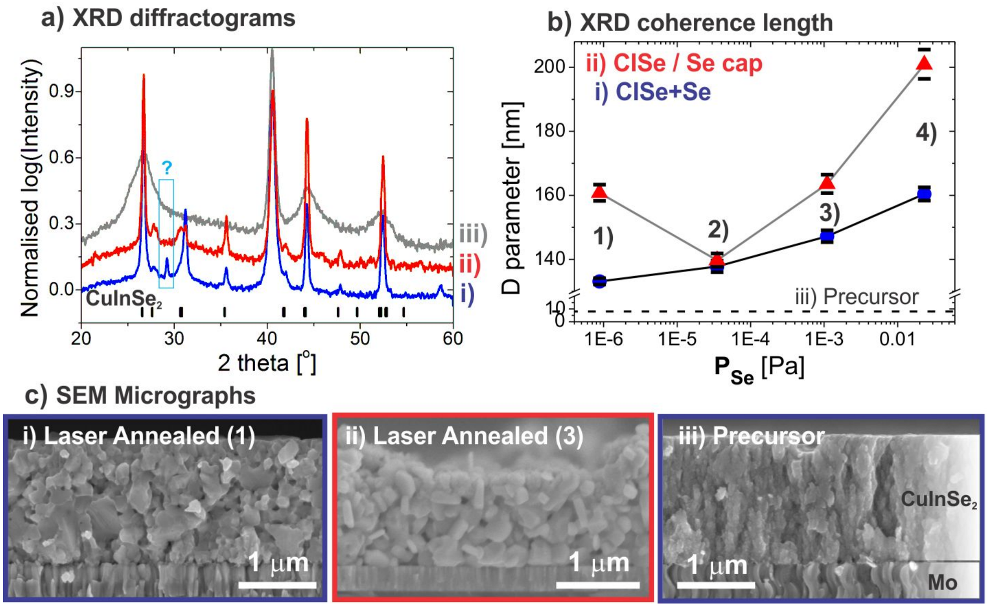

Figure 8.4: a) XRD patterns of absorber layers produced by laser annealing at 150 Wcm^{-2}, 2 mms^{-1} under P_{Se} (4): 2×10^{-2} Pa, a precursor with (i) additional Se in deposition (blue) or (ii) Se capped (red). These are compared to (iii) precursor with additional Se. b) Coherence lengths (D parameters) calculated from Scherrer formula of the absorber layers annealed at 150 Wcm^{-2}, 2 mms^{-1} with P_{Se} (1)-(4). Lines between the sample points are to guide the eye. c) SEM cross section micrographs of absorbers laser annealed with energy given in a) from i) a precursor with elevated Se with P_{Se} (1): 9×10^{-7} Pa, ii) Se capped precursor with P_{Se} (3): 1×10^{-3} Pa and iii) a precursor with elevated Se.

the Se capped precursor appears to result in slightly larger coherence lengths after annealing. Furthermore, the diffractogram of the absorber layer formed from a high Se content precursor (Fig.8.4ai) has an additional, unknown peak at 29.2 $^{o}2\theta$. A possible identity of this reflex is that it relates to an In_2Se_3 secondary phase (201 Bragg-peak at 29.3 $^{o}2\theta$: JCPDS card file: 00-040-1407), resulting from the precursor composition lying far from stoichiometry (Cu/In: 0.92, Se/(Cu+In): 1.36). In order to measure the effect of the background P_{Se} on the Se content of the absorber layer and furthermore, to see whether the elevated Se content of the precursor remains after annealing, the composition of absorber layers were measured using EDX as given in Fig.8.5.

The composition of the absorber layers resulting from the Se capped precursor (Fig.8.5ii) is observed to be, within error, constant and close to the value of the precursor before the capping step (with 100 nm Se cap, Se/(Cu+In) $\approx$ 1.7). The Se/(Cu+In) $>$ 1 (between 1.05$-$1.1) of these absorber layers indicates the likely presence of a surface OVC layer [142][155]. In contrast, the absorber layers resulting from the elevated Se content precursor (Fig.8.5i) show a general trend of increasing Se/(Cu+In) with higher background P_{Se}. It should be noted that repeating this experiment with precursors where no additional, elemental Se was added, resulted in absorbers with Se/(Cu+In) $<$ 1 for all but P_{Se} = (3) (data shown in Appendix 12.3). In this precursor type a partial pressure of Se will still be created, corresponding to the film temperature, but the Se is released directly from the CISe lattice. The increased Se content of absorbers where additional

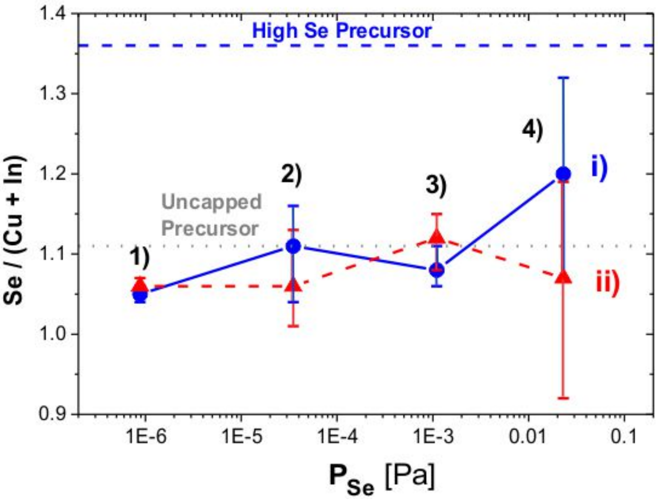

Figure 8.5: Se/(Cu+In) composition, determined from EDX measurements of absorber layers produced by laser annealing at 150 Wcm^{-2}, 2 mms^{-1} under P_{Se} (1)-(4) from electrodeposited CISe precursors with elevated Se (i) and with an Se cap (ii). The composition of each precursor is also shown for comparison (the composition before the Se capping step for the capped precursor). Each composition is an average of three different measurement points on the same sample and error bars indicate the maximum and minimum measured values. Lines connecting the sample points are to guide the eye.

or excess Se had been supplied to the precursor indicates the P_{Se} requirement was fulfilled by vaporisation of excess Se and not decomposition of the CISe. Reducing the breakdown of CISe is expected to result in an absorber layer with improved optoelectronic properties. Furthermore, a higher Se content reduces the driving force for the formation of V_{Se} defects. However, as the Se/(Cu+In) remains significantly above stoichiometry (particularly at the highest P_{Se}) this may also lead to secondary phase formation, as hinted in the XRD patterns (Fig.8.4). It can also be considered that the increase in grain size with higher P_{Se}, detected by SEM, will reduce the surface area of grain boundaries where recombination is possible, and therefore is also expected to enhance the photovoltaic properties of a final device.

8.3.2 Optoelectronic Properties

To measure the interplay between each of the effects of background P_{Se}, room-temperature photoluminescence, RT-PL, measurements were performed and the results are presented in Fig.8.6. These measurements and the subsequent Fermi-level splitting analysis were carried out by David Regesch, University of Luxembourg.

Considering the spectra of Fig.8.6a) corresponding to samples containing additional Se in the precursor, the precursor itself is seen to give a no PL signal within the measured range. The lack of PL yield at an energy matching the band gap of CISe ($E_g \approx 1$ eV), indicates the absence of high quality CISe semiconductor material. After laser annealing, the PL yield increases in correlation to the P_{Se} during annealing. An increased PL yield corresponds to a higher level of radiative recombination, and thus indicates an enhancement in the semiconductor material quality. Only the absorber layer annealed under the highest P_{Se} (4): $P_{Se} = 2 \times 10^{-2}$ Pa) gives a

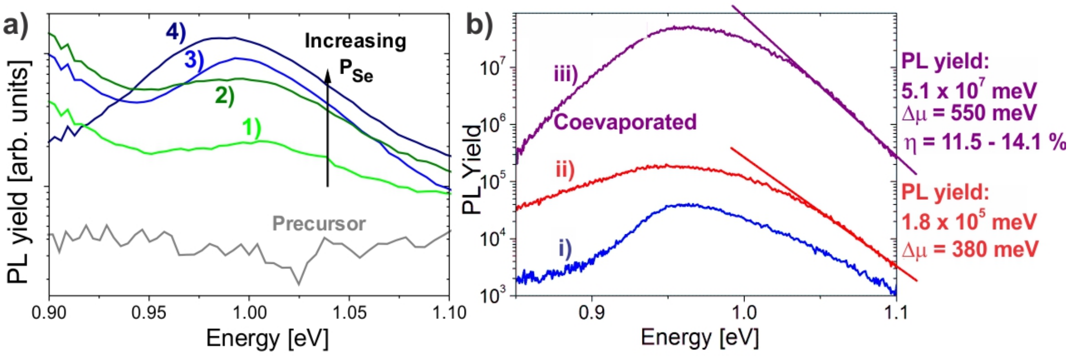

Figure 8.6: a) RT-PL spectra of the electrodeposited CISe precursor with increased Se and after laser annealing at 150 Wcm^{-2}, 2 mms^{-1} with P$_{Se}$: (1)-(4). b) Calibrated RT-PL measurement of absorber layers formed by laser annealing under P$_{Se}$ (3) = 1×10^{-3} Pa: precursors with (i) increased Se and (ii) an Se cap. Compared to (iii) an absorber fabricated in a single stage co-evaporation process.

single peak in PL intensity at $\sim$1 eV, assumed to relate to band to band transitions. The absorber layers which had been annealed under lower P$_{Se}$ show a further increase in the PL yield at lower energies, indicating transitions via defect states or secondary phases. This gives evidence that the breakdown of CISe may be favourable at P$_{Se}$ (2) and (3) even though they exceed the highest value of p given in Table 8.1 of 4×10^{-5} Pa for the breakdown of In$_2$Se$_3$. At these intermediate P$_{Se}$ values, it is proposed that the Se loss could be directly from the CISe lattice resulting in V$_{Se}$ defects. The observed trend towards a higher PL yield with increasing P$_{Se}$ and the reduction in intensity of the second, low energy peak supports the hypothesis that a background P$_{Se}$ reduces CISe decomposition and Se loss during annealing, leading to higher quality absorber layers.

However, XRD and EDX of these absorber layers (where the precursor was deposited with an elevated Se-content) indicated that their off stoichiometric composition may also be problematic. Fig.8.6b) compares the RT-PL spectra of absorber layers produced from (i) elevated Se and (ii) Se capped precursors. The near doubling in the PL yield from (i) to (ii), indicates that Se capping is more effective in producing higher quality absorber layers. To contextualise these values, the relative magnitude of their PL yield is compared to that of an absorber layer fabricated using a single stage co-evaporation process. The PL yield of this vacuum evaporated absorber layer (iii) exceeds that of the best laser processed absorber layer by two orders of magnitude. In order to determine the quasi-Fermi level splitting ($\Delta\mu$) within these two samples the method described in section 5.1.6 is used. The high energy wing of the peak at 1 eV is fitted for both samples and input into Eq.5.13 to determine T and subsequently $\Delta\mu$. This analysis gave $\Delta\mu$ of 550 meV and 380 meV for the co-evaporated and electrodeposited-laser annealed absorbers respectively. $\Delta\mu$ is related to the maximum achievable V$_{oc}$ of a final device. Solid state devices fabricated from an equivalent co-evaporated absorber layer to that shown in Fig.8.6biii) gave a maximum of 14.1 % power conversion efficiency (all cells $\eta > 11.5$) and a V$_{oc}$ = 476 mV. Based on the values of $\Delta\mu$, and assuming that α_λ of the co-evaporated and electrodeposited samples are comparable, it is estimated that the laser annealed absorber could give a potential V$_{oc}$ $\approx$ 300 mV. This result is promising, particularly considering the non-vacuum deposition and 1 s annealing time. However, the quasi-Fermi level splitting does not take into account the current generation within the absorber layer and other loses that may be encountered on completion into a final device.

8.3.3 Final Device Characteristics

In order to understand the properties of the device realised from a laser annealed absorber layer, a brief introduction to chalcopyrite devices is given. This information was taken from Ref.[104] and is in addition to that given on IV measurements in Section 5.2.1.

Chalcopyrite devices

A schematic of a typical chalcopyrite device is given in Fig.4.1. Separation of charge carriers occurs at the p-n heterojunction interface of the p-type CISe absorber layer and n-type CdS buffer and ZnO window layers. In order to construct the band diagram for this device the band offsets of each of the materials must be defined in relation to the vacuum level (the energy of a free stationary electron outside of a material, in a perfect vacuum). In Fig.8.7 the p-type absorber layer has E_f closer to E_v, whereas in the n-type buffer layer, E_f is closer to E_c. As discussed in Section 5.2.1, E_f equilibrates to a constant energy, with band bending at each interface created by the recombination of excess charge carriers. Focusing on the p-n junction between the CISe and CdS, it is seen that the SCR is located largely within the CISe layer which is due to the much lower doping in CISe compared to CdS [147].

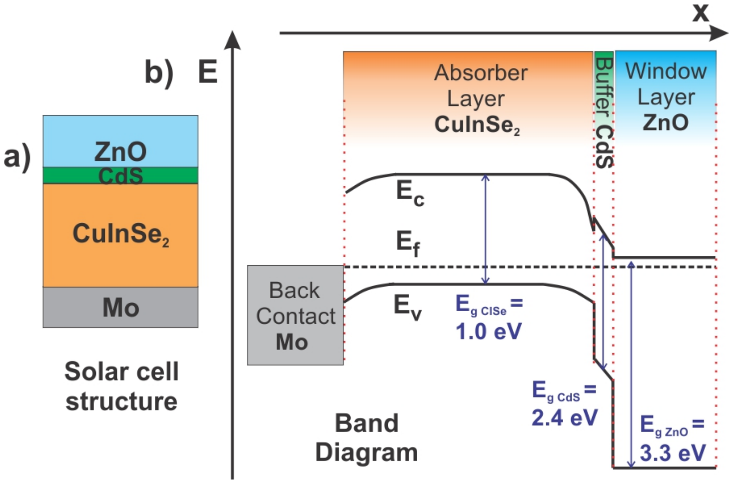

Figure 8.7: a) Simplified diagram of CISe solar cell structure. b) Schematic illustrating the typical band alignment within such a device, showing back contact/absorber/window/buffer heterojunction at equilibrium (as ref [15]). Typical band gap energies are given in [160]

When the device is illuminated, incident photons with an energy $>E_g$ are absorbed in the CISe semiconductor absorber layer generating electron-hole pairs with an energy distribution identical to that of the absorbed photons [100]. Electrons excited deep within the conduction band will then thermalise to the band edge. The photogenerated charge carriers are meta-stable and will exist on an average time-scale equal to the minority charge carrier lifetime, τ, after which they recombine [100]. Band-to-band recombination, where an electron in the conduction band recombines directly with a hole in the valence band, results in photon emission and is termed ‘radiative recombination’. However, electron-hole pairs may also recombine non-radiatively via defect states or Auger recombination. In order to generate a current, electrons and holes must be extracted before they recombine [104]. Any charge carriers generated within the SCR are separated by the p-n junction preventing recombination. Electron hole pairs generated in the semiconductor bulk diffuse due to the chemical potential created as a results of the concentration gradient [100]. A parameter termed the diffusion length describes the mean distance that a charge carrier will diffuse within its lifetime. Minority charge carriers that reach the SCR before recombining are transported across the p-n junction due to its electric field. If the solar cell is short circuited *i.e.* there is a connection between front and back contacts, then the charge carrier can be transported into the external circuit where it dissipates its energy producing a current and a voltage.

The probability of collecting the minority carriers is highly dependent on the properties of the absorber layer as well as parameters of the device, which determine the layout of the band diagram of Fig.8.7. Hence all regions of the device must be optimised to improve efficiency, although this thesis focuses only on the absorber layer. The quality of the absorber layer affects the level of non-radiative recombination and therefore the minority carrier lifetime, τ. A lower τ reduces the diffusion length, L, and therefore the collection probability. The diffusion length and consequently the maximum photocurrent of the semiconductor, is decreased by a number of parameters, for example, the presence of grain boundaries and the defect density.

Laser Annealed Device

To assess the suitability of this processing route for solar cells, devices were fabricated from absorber layers annealed under increasing P_{Se} by the project collaborators IRDEP. However, it should be noted that cells fabricated from both absorber layer series shown above could not be completed into functioning devices, as problems in the electrodeposition lead to pinholes in the CISe films. However, a second set of Se capped precursors were laser annealed under P_{Se} **1)** = 9 × 10^{-7} Pa and P_{Se} **x)** = 2 × 10^{-4} Pa (see Fig.8.3). These laser annealed absorber layers were etched with 5 wt% KCN for 30 s and a 50 nm layer of CdS followed by the ZnO window layer were deposited on this etched surface to complete the device. The sample was scribed to have cells of 0.1 cm^2 area and measurements were made by contacting directly to the ZnO. The current-voltage (IV) characteristics of the two devices are presented in Fig.8.8.

Comparing the IV curves of Fig.8.8a) for samples annealed under different background P_{Se} shows how influential the P_{Se} is on device performance. With P_{Se} = 9 × 10^{-7} Pa during laser annealing (Fig.8.8ai) the resulting absorber layer shows diode behaviour but with negligible efficiency. However, when the P_{Se} was increased to 2 × 10^{-4} Pa (Fig.8.8aii), the resulting device gave 1.64 % power conversion efficiency with a V_{oc} of 194 mV and a J_{sc} of 23.0 $mAcm^{-2}$. The external quantum efficiency (EQE) measurements of the device from the absorber annealed under P_{Se} = 2 × 10^{-4} Pa shows an overall improvement over the full wavelength range when compared to the device formed from an absorber annealed at a lower P_{Se} (Fig.8.8b). The increase is more pronounced for wavelengths $>$ 600 nm suggesting a significant improvement in carrier collection. An increase in the SCR width can be responsible for such an improvement. Still, since the shape of the EQE is not rectangular above 800 nm, there is still a deficiency in carrier collection. The drop in EQE at wavelengths $<$ 500 nm is due to absorption by the CdS layer. By fitting the low energy wing of this EQE spectrum, using the method given in Section 5.2.2, it is possible to determine the band gap of the absorber layer. It is observed in Fig.8.8c) that this absorber has a band gap of 1.0 eV corresponding to that of CISe [161]. The slow decay

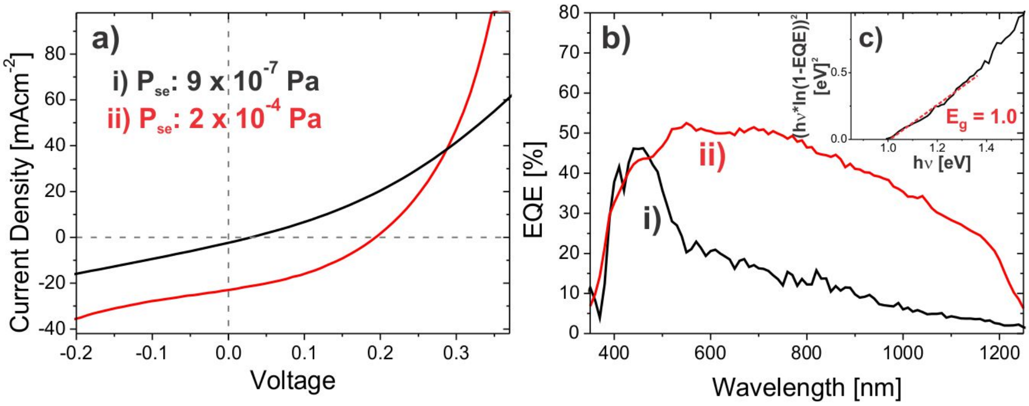

Figure 8.8: a) Current-Voltage (IV) curves under illumination and b) External Quantum Efficiency (EQE) measurements of solid state devices fabricated from Se capped CISe precursors laser annealed at 150 Wcm^{-2}, 2 mms^{-1}, under a P$_{Se}$ of (i) 9 $\times$ 10^{-7} Pa (black) and (ii) 2 $\times$ 10^{-4} Pa (red).

rate of the EQE signal, seen in the inset plot of Fig.8.8c), suggests the absorber layer is defective, with a high density of states with energy close to the band gap of CISe. Additionally, the presence of secondary phases within the film, resulting from the breakdown of the CISe, cannot be excluded. Whilst the 1.6 % efficiency is low, these results present the first published CISe device formed from electrodeposition-laser annealing [162].

8.4 Summary of the importance of Se partial pressure during annealing

In this section, further investigation has been carried out on the precursor chosen as suitable for laser annealing in the previous section. It has been shown that, whilst laser annealing this precursor under an inert atmosphere improves its structural and optoelectronic properties, these conditions were inadequate for forming a final device with diode behaviour. This demonstrates the key importance of considering thermodynamic equilibria reactions when operating at elevated temperatures. To minimise CISe decomposition a raised background P$_{Se}$ was created during annealing. Laser annealing under higher background P$_{Se}$ improved both the absorber layer's structural properties, demonstrated by an increased grain size, and its optoelectronic performance, shown in its higher PL yield. With sufficient background P$_{Se}$, an absorber layer is produced of sufficient quality to give the first solid state device produced by the electrodeposition-laser annealing technique with 1.64 % power conversion efficiency. The EQE spectra betrayed significant electrical losses within the device. However, the PL results indicated that absorbers annealed under higher P$_{Se}$ will have increased radiative recombination and therefore charge carrier lifetime and consequently have the potential for higher efficiency devices. The following section investigates the properties of this device, with the aim that, by understanding its deficits, the electrodeposition and the laser annealing processes can be adapted in order to lead to higher device efficiencies in the future.

9 Understanding and Optimising the Laser Annealing Process

Chapter 7 established a suitable laser-precursor combination and Chapter 8 identified the absolute necessity for an elevated partial pressure of Se during annealing. In this section, the absorbers produced using this process are analysed in detail. Initially, the effect of beam flux on the absorber properties is examined. In order to explain the observed variations, the film temperature during annealing is modelled. The effect that the modelled thermal fluctuations have on the rates of elemental diffusion and grain growth are examined. Furthermore, it is observed that the rate of these processes is altered by the composition of the precursor film in terms of the Cu/In ratio and the presence of dopant atoms. Studying the relationship between each of these parameters will form the basis by which to optimise the laser annealing process.

9.1 Effect of Power Distribution of the laser beam

In Section 8.3.3 the first device from laser annealing electrodeposited CISe was presented. However, its low efficiency of 1.6 % confirms the need for improvement. Since the laser annealed absorbers visually appear non-uniform, light beam induced current (LBIC) was used to analyse the homogeneity of the photocurrent over the device area. An LBIC measurement gives a spatial mapping of the EQE of the sample (see Section 5.2.2 for information on EQE measurements). A single excitation wavelength is used, in this case 540 nm. The beam size was 1.0 mm and 0.2 mm steps were made in x-y directions over the device area. Patterns of variation in this signal can hint to its origin: circular or random spots would be related to the deposition, whereas striped patterns would be caused by the laser.

The output radiation from a laser has a Gaussian shape relating to the fundamental mode of the cavity. This beam, with a $1/e$ diameter of approximately 15 mm, is passed through optics to modify its size and shape, including, finally a 2 x 2 mm aperture. Whilst the aperture reduces the dispersion in flux reaching the sample, some power variation remains which was approximated at the sample surface to have a Gaussian power distribution with FWHM $\sim$1.8 mm. The laser beam was rastered horizontally across the sample surface (by moving the sample using an x-y stage), with vertical translations of 1.8 mm. This forms a distinctive pattern on the sample as observed in Fig.9.1a).

The pale and dark lines visible on the absorber surface in Fig.9.1a) indicate the path over which the laser beam has rastered (as represented by the red line). To complete into a device, the absorber was etched with KCN, layers of CdS and ZnO deposited onto its surface, and scribed with cells of dimension 3 mm x 3 mm. Even after this process, the inhomogeneity remains visually distinguishable (Fig.9.1b). Measuring the LBIC over the device area relates its optoelectronic performance to the visual patterns on the absorber. On Cell 1, which gave η = 1.6 %, there is a single, $>$ 1 mm^2 area where an EQE $>$ 60 % was measured (Fig.9.1c). However, on cell 2 (η = 1.4 %) there are two areas where the EQE is $>$ 60 % but these are separated by

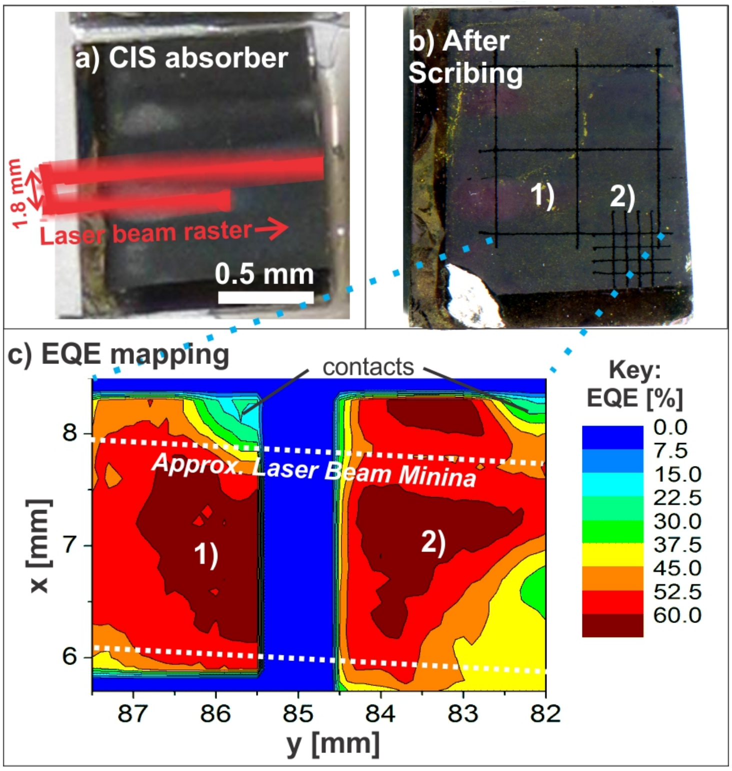

Figure 9.1: a) Appearance of absorber layer formed by rastering a laser beam (indicated by red line) at 150 Wcm^{-2}, 2 mms^{-1} with P_{Se} = 2 × 10^{-4} Pa over an a Se capped CISe precursor. b) after KCN etching, CdS/ZnO deposition and scribing this absorber (cell area: 3 x 3 mm). c) EQE map of cells 1) and 2) as indicated on (b).

a line where the EQE drops to 52.5 - 60 %. Such linear parallel features (as indicated by the white dotted lines on Fig.9.1c), indicate that the device inhomogeneity is caused by the laser raster. These results indicate the effect of a spatially inhomogeneous laser flux on final device performance.

In order to determine the effect that the laser beam flux has on the properties of the absorber and therefore begin to understand the patterns observed in the LBIC, a second sample was laser annealed, using the same raster speed and beam energy as used for the device, but with only a single pass of the laser beam across the centre of the sample as shown in Fig.9.2a). The microstructure and photoluminescence are analysed at specific points along this annealed line as indicated in Fig.9.2(i-iii). (i) is an area far from where the beam has passed, assumed to correspond to precursor material, (ii) is the visual edge of the beam line and (iii) its centre. A representation of the variation in laser beam flux on the sample area is shown in Fig.9.2b).

Grain Size and Atomic Composition

Firstly, the grain growth is determined from SEM cross sections shown in Fig.9.2c). Comparing these micrographs, the nanocrystalline grains of the precursor (i) have grown and become more angular, within the areas (ii) and (iii), over which the laser beam has passed. Comparing the edge (ii) to the centre (iii) of the beam line, corresponding to the areas receiving approximately the highest and lowest laser flux, the dimensions of the grains nearly double, reaching the range

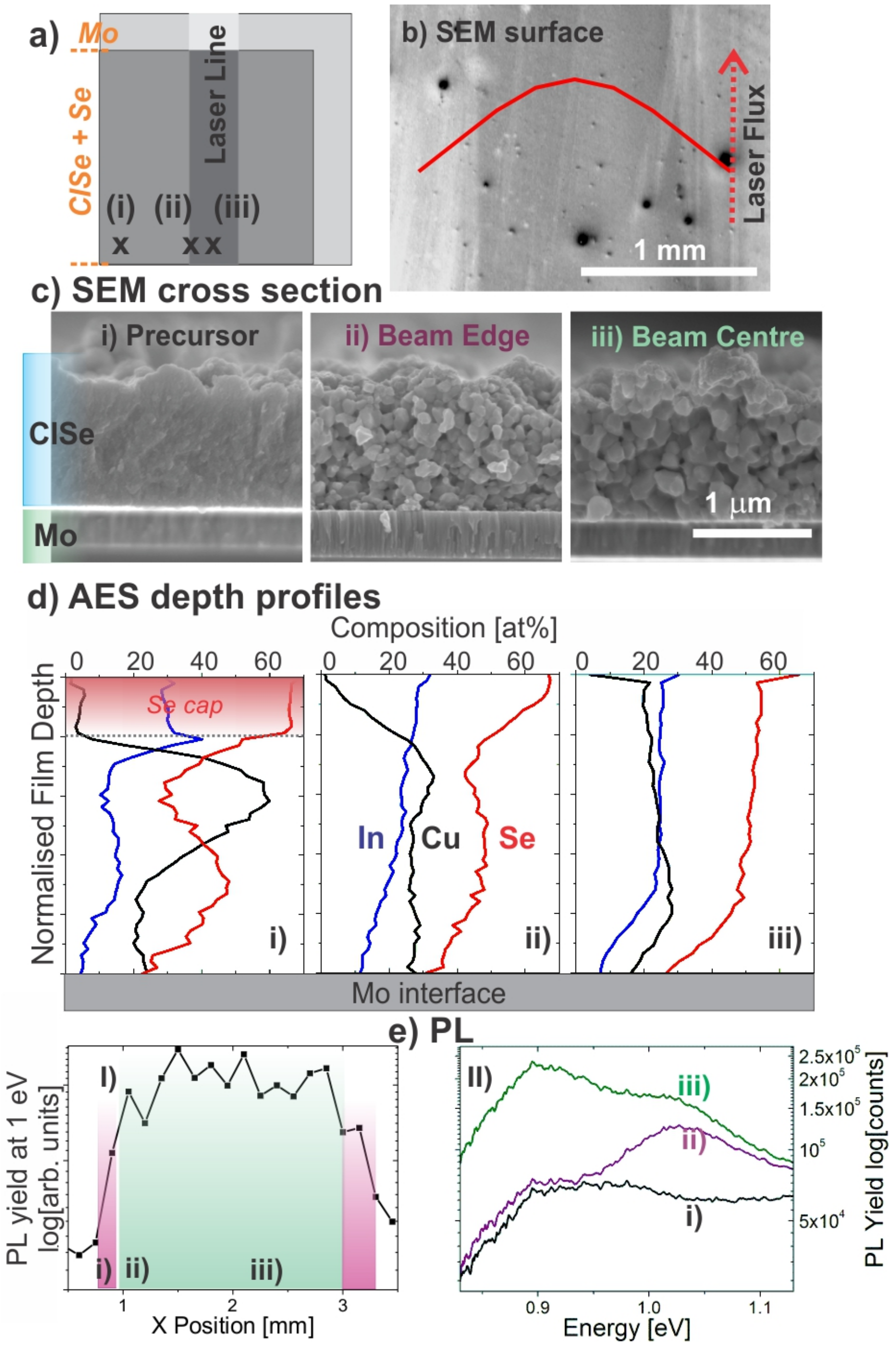

Figure 9.2: a) Diagram and b) SEM surface micrograph of a CISe film after a single pass of laser beam (150 Wcm^{-2}, 2 mms^{-1}, $P_{Se} = 4 \times 10^{-5}$ Pa) across its centre. The flux distribution of the laser beam over the annealed area is represented by the colour bar on (b). Points (i) precursor, (ii) beam edge and (iii) beam centre indicate the areas where the following analyses were made: c) SEM cross sections, d) Auger elemental depth profiles e) RT-PL measurements: (I) PL yield at 1 eV taken from spectra measured at points across the beam line and (II) individual spectra corresponding to points (i)-(iii).

of tenths of microns. The elemental composition through the film depth is analysed using the Auger depth profiles of Fig.9.2d). The precursor area (i) has high elemental disorder through its depth, as seen in the fluctuating profiles of each of its component elements. The surface is Se-rich as a consequence of the Se cap but its level fluctuates and drops significantly below 50 % in the film bulk. This compositional profile is further evidence of the multiphase nature of the precursor (as observed in Section 8.1). The profiles suggest, in addition to CISe, the presence of In_2Se_3 at the film surface and below this $Cu_{2-x}Se$ towards the Mo rear contact. Comparing the depth profile of (i) to those measured at points (ii) and (iii), within the beam line, the profiles of each element have flattened to give a more homogeneous composition through the depth. Whilst at the beam edge (ii) the surface of the sample remains Cu-poor, reminiscent of the precursor, at the centre of the beam line (iii), the composition is constant and close to stoichiometry through a large part of the film depth. This homogenisation of the composition reinforces the findings of Section 8.1, that laser annealing stimulates atomic diffusion and promotes chemical reactions. Furthermore, from Fig.9.2c) and d) it appears that the rates of grain growth and atomic diffusion depend on the applied laser flux and hence film temperature.

Photoluminescence

The larger grain size found in the film areas receiving a higher laser flux reduces the surface area of grain boundaries at which recombination occurs. Therefore assuming the same bulk and interface defect levels in both areas, area (iii) has the potential for improved optoelectronic properties compared to point (ii). To have the same defect levels also assumes that the background P_{Se} still exceeds the equilibrium vapour pressures, p, of the thermal decomposition reactions of the CISe at the temperature reached by the centre of the film. Furthermore, an increased rate of chemical reactions and atomic diffusion is expected to lead to fewer secondary phases and defects within the film, reducing the number of non-radiative recombination pathways. These hypotheses are tested by measuring RT-PL spectra (analysis area $\approx 100\ \mu$m) across the beam line, and the PL yield at 1 eV determined from each spectra is plotted in Fig.9.2e). The measured PL yield is observed to broadly follow the squared Gaussian profile of the beam flux. Outside of the beam area (i), a broad spectra with the lowest PL yield is measured. There is a tripling in the PL yield at 1 eV between (i) and the beam centre (iii). A higher PL yield at this energy would indicate an increase in radiative band-to-band recombination of the CISe. From this analysis it is deduced that there is an improvement in the quantity and/or quality of CISe within this area of film. However, comparing the individual PL spectra, one observes three distinct regions with similar spectra (as illustrated by the white, purple and green regions in Fig.9.2eI) with examples given in Fig.9.2eII). At the beam edges (purple) there is a single maximum in the PL yield at 1.03 eV correlating to the CISe band gap determined in Fig.8.8c). However, within the central 1.5 mm of the beam line (green) where the highest PL yield is measured, there is an additional peak in the spectra at 0.9 eV. This low energy peak indicates that the dominant transitions are within the band gap, possibly corresponding to the presence of secondary phases or defects states. The formation of these could be indicative that the P_{Se} above this central region of film was insufficient to prevent Se loss. The background $P_{Se} = 4 \times 10^{-5}$ Pa supplied during this annealing only exceeds p of the CISe breakdown reactions at 550 ^{o}C using Eq.8.6. This P_{Se} is lower than that supplied to the absorber which was fabricated into the device which showed improved properties at the beam centre (Fig.9.1). Consequently, it is hypothesised that the peak temperature at the beam centre exceeds 550 ^{o}C.

In this section, the importance of the applied laser flux on absorber layer properties and thus final device performance has been established. It has been observed that the applied laser flux dictates the level of atomic diffusion, grain growth, chemical reactions and improvement of PL yield in a CISe film during annealing. Each of these parameters is affected by the film temperature and furthermore this dictates the minimum background P_{Se} which must be supplied during the annealing process in order to prevent CISe decomposition. Therefore, the next section investigates the modelling of the film temperature during annealing.

9.2 Modelling the film temperature during annealing

Calculating the film temperature during laser annealing presents a challenging problem both in its conception and verification. Firstly, the absorption of the laser energy by the precursor stack must be accurately determined, as considered in Section 7.4, and secondly the heat generation and thermal transport properties of the material must be taken into account. This section begins by presenting the basic thermodynamic theory and subsequently applies it specifically to the laser heating process in order to generate equations which are used in a finite element model (FEM). The modelled temperature profiles are presented and used to understand the relationships between the absorber properties and annealing flux presented in Section 9.1. A method is demonstrated which aims to verify these calculated temperatures experimentally. Finally, the model is extended to account for the Gaussian power distribution and the rastering of the beam and suggestions are given by which the accuracy of the model may be further improved.

9.2.1 The theory of Heating

The flow process used to solve the laser heating problem is illustrated in Fig.9.3. The first step given in this flowchart is calculating the absorption of the laser energy by the CISe, which gives a depth dependent power distribution (1.). Thermal conduction transports this heat energy through the film (2.). Combining these parameters gives the heating equation (3.). By considering convection and radiation at the sample boundaries (4.), one may determine the film temperature. The subsequent sections explain each of these steps in greater detail. For a complete explanation of heat transport, the reader is referred to [163].

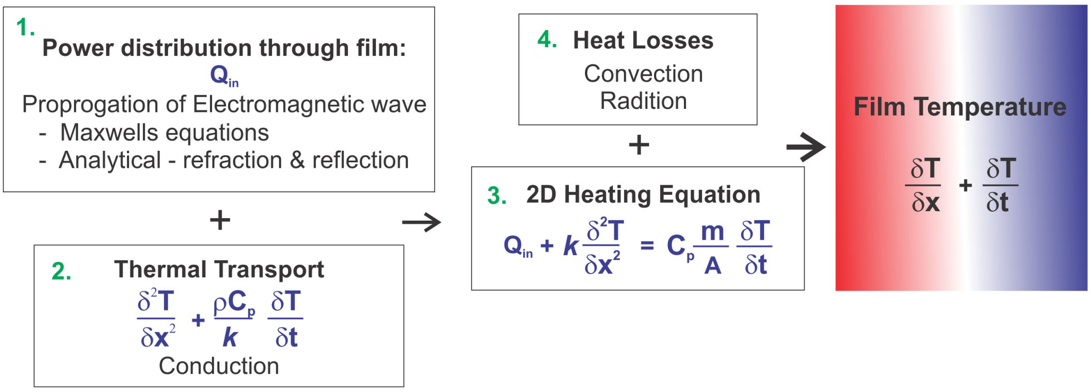

Figure 9.3: Flowchart indicating the key calculation steps required to determine the film temperature in a 1D model during a laser annealing experiment.

Laser Heating of Semiconductors

1. Deriving Q_{in}.

In a semiconductor, lattice heating is via phonons which are generated by a number of mechanisms. The incident laser energy may either be absorbed by 'free carriers'; electrons in the conduction band and holes in the valence band respectively (see Fig.9.4a) or by (b) an electron in the valance band, generating electron hole pairs. Free carriers quickly release their energy as phonons into the lattice thus generating heat. Alternatively, photon absorption can lead to electron hole pair generation. The energetic density of states of the generated charge carriers matches that of the incident radiation [100]. These 'hot carriers' will rapidly ($< 10^{-12}$ s) thermalise to the band edge by collisions with the lattice releasing phonons (see Fig.9.4c). As the laser supplies photons of $h\nu$ = 1.17 eV, and $E_g(CISe) \approx$ 1.0 eV, this thermalisation supplies only a limited quantity of phonons to heat the lattice. Therefore, a significant mechanism of lattice heating stems from the non-radiative recombination of electron hole pairs. In an ideal, direct band gap semiconductor the main recombination mechanism should be radiative as shown in Fig.9.4d). An unavoidable subsequent recombination process is the re-absorption of the emitted photon by a free carrier, a process known as Auger recombination. The hot carrier then thermalises, with the release of phonons to the band edge (similar to Fig.9.4a). Finally, electron hole pairs can combine non-radiatively via defect states within the band, releasing phonons to the lattice (Fig.9.4e), a process known as Shockley-Read-Hall recombination [147].

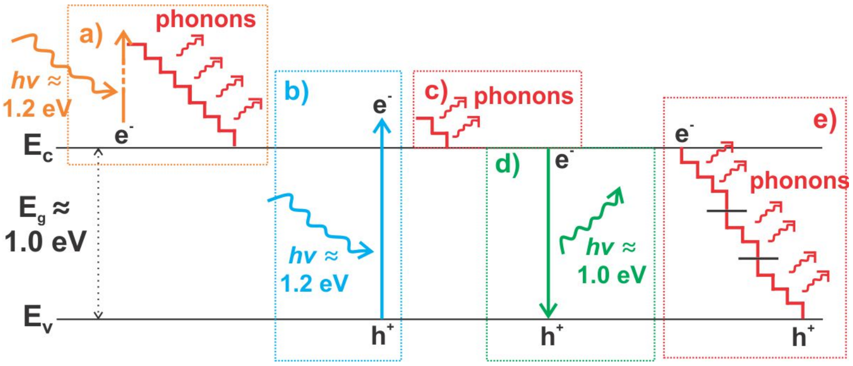

Figure 9.4: Summary of photon and phonon absorption and emission processes. a) Free carrier absorption by an electron in the conduction band. b) Photon absorption generates an electron hole pair. c) Thermalise of hot carriers to the band edge emitting phonons. d) Radiative recombination of the electron-hole pair releasing a photon. e) Non-radiative recombination of electron-hole pair via defect states (Shockley-Read-Hall recombination).

The absorption of the laser energy by the semiconductor, as a function of its depth, was considered in Section 7.5. This model used the optical coefficients n and κ, to calculate a power dissipation density through the film. This dissipated power, in Wcm^{-2}, gives the energy supplied by the laser (considering a 2D model) which is available to the semiconductor for lattice heating and is subsequently termed Q_{in} (step **1.** of Fig.9.3). It is also possible to derive Q_{in} analytically, by considering the reflection and refraction at each interface, a method which is used in the 3D modelling of Section 9.2.2. In order to calculate the generation and transport of heat within the film from the input power distribution, the laws of thermodynamics are thus considered.

Thermodynamics

The information presented in this explanatory section can be found in Ref.[163], where a more detailed description of the terms used and the derivation of equations is given.

The First Law of Thermodynamics, Eq.9.1, defines the rate of change of internal thermal energy over time (dU/dt) with respect to the energy input and outflow of the system.

$$Q = W_k + \frac{dU}{dt} \tag{9.1}$$

Where the heat transfer rate, Q, and work transfer rate, W_k, describe the flow of energy per unit time into and away from the system respectively and are expressed in Js^{-1} or W. To calculate the temperature change in place of the free energy derivative, and assuming that no work is done by the system and its pressure remains constant Eq.9.2 is used.

$$Q = mC_p\frac{dT}{dt} \tag{9.2}$$

Where C_p is the specific heat capacity at constant pressure and m is the mass of material. For CISe, C_p = 0.3 Jg^{-1}K^{-1} [164]. Eq.9.2 can be used to calculate the instantaneous heat generation from the laser energy distribution function, using Q_{in} = Q.

Thermal Transport

Having determined the energy input into the system, this section considers thermal transport. There are three methods of heat transfer: conduction, convection and radiation.

2. Conduction

The main thermal transport method within the CISe film is conduction; the transfer of energy by the elastic vibrations of the lattice. This mechanism transports heat from where it is generated, to cooler areas of the film. One dimensional heat transfer by thermal conduction is described by the Fourier law given in Eq.9.3, which states that the heat transfer rate, q (Wcm^{-2}), is proportional to the magnitude of the temperature gradient.

$$q = -k\frac{dT}{dx} \tag{9.3}$$

Where k is its thermal conductivity (k_{CISe} = 0.037 Wcm^{-1}K^{-1} [164]). In order to solve for T, the heat transport through a one dimension differential element (δx), with area, A_{sys}, is considered. The net heat conduction out of this element, Q_{out} is given by Eq.9.4.

$$Q_{out} = qA_{sys} = -kA_{sys}\left\{\frac{\frac{\partial T}{\partial x}(x+\delta x) - \frac{\partial T}{\partial x}(x)}{\delta x}\right\}\partial x = -kA_{sys}\frac{\partial^2 T}{\partial x^2}\delta x \tag{9.4}$$

Q_{out} is then calculated using Eq.9.2, as shown in Eq.9.5.

$$-Q_{out} = \frac{dU}{dt} = \rho C_p A_{sys}\frac{dT}{dt}\delta x \tag{9.5}$$

Where ρ is the density of the CISe (ρ = 5.77 gcm^{-3} [164]). By combining Eq.9.5 and Eq.9.4, the generalised heat diffusion equation in its one dimensional form, Eq.9.6, is derived [163].

$$\frac{\partial^2 T}{\partial x^2} = \frac{\rho C_p}{k}\frac{\partial T}{\partial t} \tag{9.6}$$

3. Heating Equation

Applying the principle of energy conservation given in the first law of thermodynamics (Eq.9.1), the work done by the system and change in its internal energy, as given in Eq.9.6 is combined the energy input to the system Q_{in} to give Eq.9.7 [137].

$$Q_{in} + k\frac{\partial^2 T}{\partial x^2} = C_p\frac{m}{A_{sys}}\frac{\partial T}{\partial t} \tag{9.7}$$

As this model considers only two dimensions, note that ρ is replaced by m/A_{sys}. From this equation the temperature generation and transport as a function of the annealing time, t, and through the sample stack depth, x, can be calculated.

4. Heat Losses

In addition to heat transport within the material there will also thermal loses at the external interfaces of the sample. These loses are convection and radiation.

Convection

When energy is transferred from the system to molecules within a liquid or gas, it promotes the diffusion or advection of these molecules which carries heat away from the system. Newton proposed that the rate of convectional cooling is proportional to the temperature difference between the system (T_{sys}) and the cooling fluid (T_f), as given in Eq.9.8.

$$\frac{dT_{sys}}{dt} \propto T_{sys} - T_f \tag{9.8}$$

If the system is constantly heated then its temperature remains approximately constant and Eq.9.8 becomes Eq.9.9.

$$Q_{conv} = \bar{h}A(T_{sys} - T_f) \tag{9.9}$$

Where Q_{conv} is the steady state energy change per unit area and $\bar{h}$ is the area averaged heat transfer coefficient. $\bar{h}$ is dependent on both the material and its temperature and in the FEM model $\bar{h}$ is approximated as $\bar{h} = h_{air}(A_{sys}.p_{ext}.T_{ext}.v_{ext})$ where h_{air} is the heat transfer coefficient of air at the calculated temperature and p_{ext}, T_{ext} and v_{ext} are its pressure, temperature and velocity. A_{sys} is the area of the exposed interface of the heated body. The internal thermal energy change in the cooling fluid is determined using Eq.9.2, to give Eq.9.10.

$$\frac{dU}{dt} = \frac{d}{dt}[\rho C_p V_f (T_{sys} - T_f)] \tag{9.10}$$

Where V_f is the volume of the cooling fluid. Applying the first law of thermodynamics, Eq.9.1, Eq.9.10 and Eq.9.9 are combined to give the rate of convectional cooling Eq.9.11.

$$\frac{d(T_{sys} - T_f)}{dt} = \frac{\bar{h}A_{sys}}{\rho C_p V_f}(T_{sys} - T_f) \tag{9.11}$$

Considering convectional cooling in the context of the laser heating problem, its main application is at the CISe surface / air interface and therefore A_{sys} is the surface area of the sample. To gain an idea of the relative magnitude of heat dissipation by convection, dT/dt is approximated. Assuming h_{air} = 10 Wm^{-2}K^{-1}, T_{air} = 125 ^{o}C, v_{ext} = 0 ms^{-1} and p_{ext} = 1 bar and a sample surface area of 1.6 cm^{2} at constant T$_{CISe}$ = 500 ^{o}C, the CISe film would be cooled by 8 Ks^{-1} by convection.

The effects of convectional heating are accounted for in the FEM model by extending Eq.9.7 to give the COMSOL input formula, Eq.9.12 [137].

$$Q_{in} + k\frac{\partial^2 T}{\partial x^2} = C_p\frac{m}{A_{sys}}\frac{\partial T}{\partial t} + C_p u\frac{m}{A_{sys}}\frac{\partial T}{\partial x} \tag{9.12}$$

Where u is the velocity of the convection fluid.

Thermal Radiation

All bodies with a temperature greater than absolute zero emit energy in the form of electromagnetic radiation. The intensity of the radiation is dependent on the temperature of the body. This relationship varies as a fourth power of absolute temperature and therefore whilst radiation can be neglected at lower temperatures, at elevated temperatures, such as with laser annealing, it becomes increasingly significant. The flux of energy radiating from a body ($e(T)$) is given by the Stefan-Boltzmann Law Eq.9.13

$$e(T) = \sigma_B T^4 \tag{9.13}$$

Where σ_B is the Stefan-Boltzmann constant (5.67 × 10^{-8} Wm^{-2}K^{-4}). The most significant loss of heat from the modelled structure will be at the CISe/air interface.

In the simulation, the energy lost at the CISe film surface due to thermal radiation is calculated from Eq.9.14.

$$Q_{rad} = A_{sys}\epsilon\sigma_B(T_{air}^4 - T_{sys}^4) \tag{9.14}$$

Where ϵ is the surface emissivity of the CISe film. This is a dimensionless quantity, the magnitude of which can be gauged from a material's absorption properties with ϵ = 1 for blackbodies (perfect absorbers). For Cu(In,Ga)Se$_2$ values between 0.18 - 0.34 have been measured [165][166]. As CISe has similar absorption properties to Cu(In,Ga)Se$_2$ [128] a value of 0.2 was chosen for the simulations.

9.2.2 Finite Element Modelling of Film Temperature

Having considered each of the processes detailed in Fig.9.3, the derived expressions are built into a finite element model. In this chapter two models are considered. Firstly, the 2D model of Section 7.4 is extended using the data of Fig.7.4 to give Q_{in}. Whilst this model gives a first approximation of the average film temperature it is unable to explain the observations of Section 9.1 and ignores the scanning motion of the laser. Hence a subsequent 3D FEM was created. This section will describe each method, present their results and compare these to those achieved experimentally. Finally efforts are made to prove the models' validity.

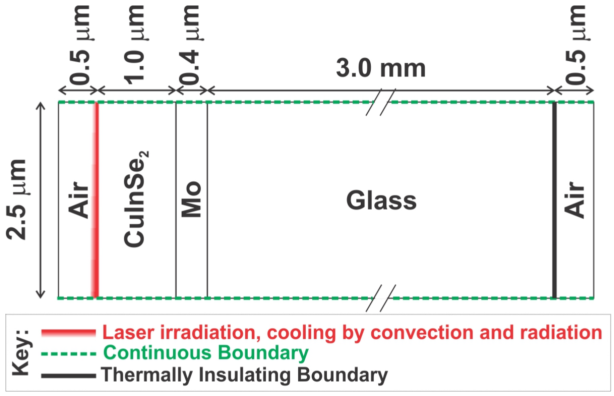

Figure 9.5: Diagram showing the material geometries and boundary types used in simulating the CISe stack using a 2D model.

Method: 2D

The 2D FEM was written by Ashish Bhatia, University of Utah. The film construction was kept as a simple 2D stack, built of adjacent rectangular blocks of each of the component materials as detailed in Section 7.4.2 and shown diagrammatically in Fig.9.5. The following adaptations were made to the model to calculate of the film temperature during annealing. For reduced computation time, the y dimension was limited to 2.5 μm. It can also be assumed that the beam is homogeneous over such a small dimension and therefore the generated temperature corresponds only to the area of CISe film irradiated by the part of the laser beam with power equal to the average measured flux. However, a continuous boundary condition is imposed on the x-axes boundaries (parallel to the irradiating laser) to give y dimension periodicity of the film. This area is meshed with rectangular elements, the x-dimensions of which are chosen as a fraction of the layer thickness: CISe = 10 nm, Mo = 8 nm, Glass = 600 nm, with y-dimensions 500 nm. C_p, k and ρ were input for each material, as summarised in Table 9.1 .

	Thickness [μ m]	Density [gcm^{-3}]	C_p [Jg^{-1}K^{-1}]	k [Wcm^{-1}K^{-1}]
CuInSe$_2$	1.0	5.77	0.30	3.7
Mo	0.4	10.28	0.25	138
Glass	3000	2.20	0.70	1.4

Table 9.1: Table of parameters used in the FEM models. Values of ρ, C_p and k for CISe taken from ref.[164] and for Mo and glass from the COMSOL library

Q_{in} is taken from the power dissipation density (given in Wcm^{-2}), the solution of the generalised Maxwell equation (Eq.7.3). The model uses this value of Q_{in} to calculate the time and spatially dependent film temperature using Eq.9.7. The time of the laser pulse is modelled as a square function. The laser is assumed to heat equally the full 2.5 μm y-dimension surface of the stack for the full duration of the pulse. 500 nm layers of air were modelled at the front and rear surfaces of the sample. Cooling via convection and radiation is assumed only at the CISe/air interface. At the Glass/air interface there is a thermally insulating boundary condition, due to the uncertainty in the exact nature of this interface and giving, in the worse case an overestimation of the temperature at this boundary.

Results

Using the FEM detailed above, the film temperature is calculated for experimental conditions of 150 Wcm^{-2}, 1 s laser pulse (no scanning). The result of this simulation is shown in Fig.9.6.

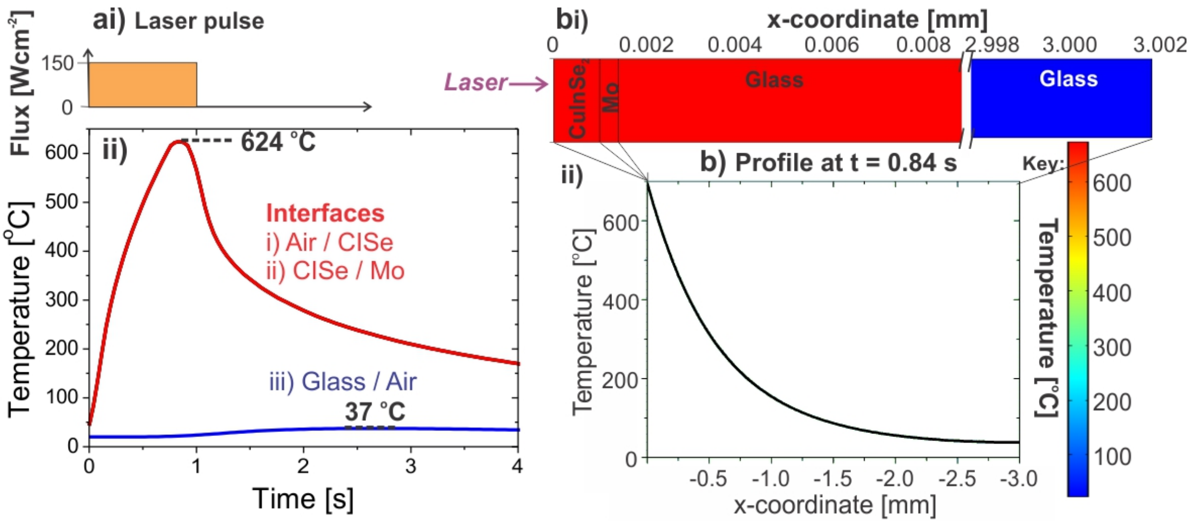

Figure 9.6: ai) Diagram of laser pulse and b) Graph of FEM modelled temperature at the interfaces of the stack i) Air/CISe, CISe/Mo, Mo/Glass, ii) Glass/Air. bi) colour plot indicating the temperature (see key) of each of the labelled materials and ii) the temperature plotted against the stack depth (x-coordinate) at t = 0.84 s.

In Fig.9.6a) the temperature of each of the interfaces of the sample stack is plotted as a function of time. The temperature profiles of the Air/CISe, CISe/Mo and Mo/Glass interfaces overlap meaning that the CISe layer and Mo reach the same peak temperature of 624 ^{o}C and that there is a negligible temperature gradient within the CISe and Mo films. This is seen more clearly in the temperature colour map of the surface and rear of the stack as shown in Fig.9.6bi). The front 8 μm of the stack, comprised of CISe, Mo and glass are a constant red colour indicating that this entire area is heated to the same temperature. This result is unsurprising considering the even dissipation of the laser energy within the CISe (see Fig.7.4c) and that the Mo substrate also absorbs energy and is a good conductor of heat. The temperature at the rear surface of the glass remains $<$ 100 ^{o}C at all times. The lower thermal conductivity and large mass of the glass, compared to the CISe and Mo, mean that the heat is slowly dispersed within the substrate. This gives a temperature gradient over the 3 mm thick glass, observable in the graph of Fig.9.6bii), and demonstrates that even when the CISe film reaches its peak temperature, the rear surface of glass has only heated 2 ^{o}C above its ambient temperature of 20 ^{o}C. There is delayed heating of the air/glass interface which reaches a maximum temperature of 41 ^{o}C, 2.5 s after the start of the experiment, as indicated on Fig.9.6a). This small temperature increase offers a mechanism by which the model may be validated experimentally.

Validation

An ideal validation of this model would be direct measurement of the film surface temperature via a thermocouple, IR or thermal imaging camera but practically the experimental set up makes this difficult [167][168].

A key observation of Fig.9.6a) is that there is a measurable temperature change at the rear surface of the glass. The temperature at this interface was measured using a “stick on” thermocouple (TC) of 2 mm x 2 mm area (x 0.8 mm thickness), equivalent to laser beam area on the sample. The TC is affixed to the sample chamber using its self-adhesive backing and double sided tape is used to firmly attach it to the rear of the glass substrate of the sample (as shown in Fig.9.7a). The active area of the TC is positioned to exactly correspond with the beam path. The laser beam irradiates the CISe film at the sample surface for a specified pulse time, during which the temperature at the reverse of the sample is measured. To test the model, CISe / Mo films on both 2 and 3 mm glass substrates were irradiated. The experimental results are compared to the simulations in Fig.9.7.

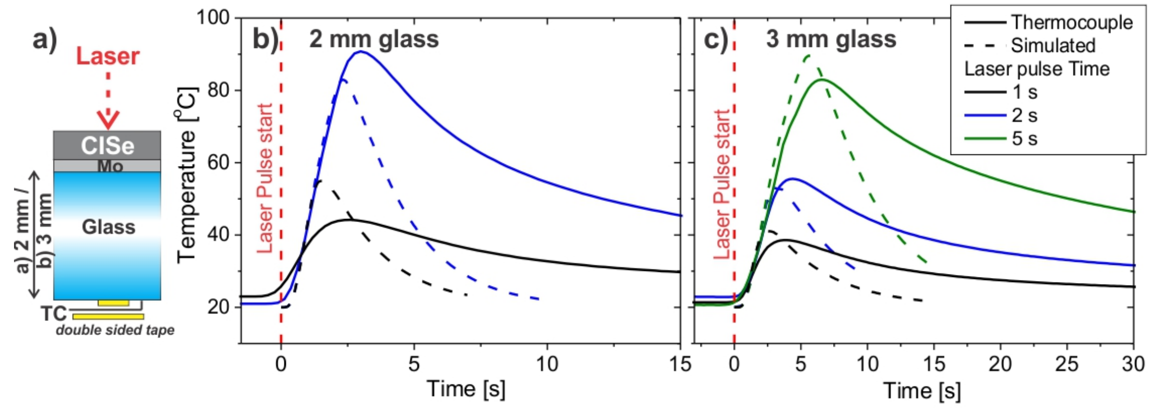

Figure 9.7: Temperature at the rear of the glass substrate of a CISe film. The CISe is irradiated by a laser at 150 Wcm^{-2}, for 1 s (black), 2 s (blue) and 5 s (green). Solid lines show the temperature measured by a thermocouple stuck to the back of the CISe / Mo / glass stack: a) 2 mm, b) 3 mm thick glass compared to the simulated temperature at this interface (dotted lines)

In Fig.9.7b) and c) it is observed that the simulated temperature profile shows a similar heating rate to that measured. There is also reasonable agreement in the maximum temperature with $<$ 10 % deviation in all but the 1 s pulse on a 2 mm substrate. In order to test the response time of the TC, the active area of the TC was put into contact with a screw of 3 mm diameter positioned on a hot plate and was found to reach within 10% of the set temperature in $<$ 1 s accounting for the observed discrepancy. The main divergence between the two results is in the speed of the cooling, which is more rapid in the simulation than the experiment. Fitting the difference between the cooling slopes of the modelled and experimental data gave a polynomial function of the type T = a + 11$\pm$1 t - 0.65$\pm$0.05 t^2, where -12$\leq$ a $\geq$ -36. As the difference functions of the cooling slopes for all pulse times are approximately equal, the cooling in the model appears to be incorrect by a second order function. A major discrepancy between the real situation and the model is that, in the later case, this rear interface is left undefined, with the thermocouple being omitted from the simulation due to the uncertainty of its thermal properties and those of the double sided sellotape by which it was attached to the rear of the glass. Heat is conducted into and out of these materials at a different rate to thermal transport within the glass (which is what is simulated in the model) due to their different C_p, k and ρ. This is expected to cause a significant divergence from the measured cooling rate.

Sensitivity of the model

The sensitivity of this model was tested by varying the input parameters, within a reasonable range, and evaluating their effect on the output temperatures. The number of calculation points, determined by the mesh size, has the most dramatic effect on the calculated temperatures. Larger elements (either triangular or rectangular) lead to peak film temperature predictions over a wide range: 450-890 ^{o}C. However, narrower meshes than that used gave similar values, for example, reducing the element size within the film and Mo to 5 nm, gave a temperature within 4 % of the previous. Due to the increased calculation time with smaller element sizes, the largest mesh size is chosen which gives a converging temperature.

Parameters were also tested in accordance with the known variations in the film. For example, as the deposition bath ages the plating efficiency decreases. This leads to deviations in the film thickness of ± 100 nm. Inputting this variance into the model gave less than 3 % shift in peak temperature.

The absorption coefficient is of key importance when considering heat generation and thus the maximum temperature of the CISe film. In Appendix 12.4 it was shown that the absorption coefficient varied according to CISe fabrication method, composition, and deposition / annealing procedure. Values of the measured absorption coefficient ranged from 2.5×10^4 cm^{-1} for a Cu-poor precursor to 3.3×10^4 cm^{-1} after laser annealing. This leads to a calculated range in maximum temperature of 40 ^{o}C. The absorption coefficient of a film is also changed by film composition, importantly the Cu/In ratio. The affect of the Cu/In ratio on the absorption coefficient and thus the peak temperature is analysed in Section 9.5.1.

One important deficit of using a 2D model is that the raster movement of the beam and its lateral deviation in flux cannot be considered.

3D modelling

Accordingly, this section explains how a 3D model was built, capable of accounting for the power distribution of the laser beam and its scanning motion over the film surface. This 3D model was created by Brian Simmonds, University of Utah.

The sample is modelled as a stack of blocks (See Fig.9.8a) with dimensions x = y = 12.7 mm and z = 1 μm (CISe), 400 nm (Mo) and 3 mm (glass). This volume is meshed using triangular elements of sizes 12 –1250 μm with a higher density of calculation points within the irradiated beam line and at the film surface.

Figure 9.3 presented the steps taken to solve a heating problem using FEM and this process remains unchanged in the 3D model. The first step is calculating Q_{in}, the energy dissipation within the film. In the previous model, Q_{in} was calculated within COMSOL by solving Maxwell's equations. However, this is computationally expensive. For simplification, Q_{in} is determined analytically from n and k using Matlab as shown in Fig.9.8b), and the solution imported into COMSOL. This analytical solution closely resembles that of the FEM, as given in Fig.7.4. The Matlab programme was written by James Nagel, University of Utah.

Secondly, the Gaussian nature of the laser beam is considered. It is assumed that the laser outputs radiation with perfectly Gaussian distribution, which is circularly symmetrical. To ascertain the parameters of the beam when it reaches the sample, the power density is measured before and after the 2 x 2 mm aperture. From their ratio, the spreading function of the Gaussian beam (w) is calculated from which the intensity of the beam at the centre of the Gaussian (I_0).

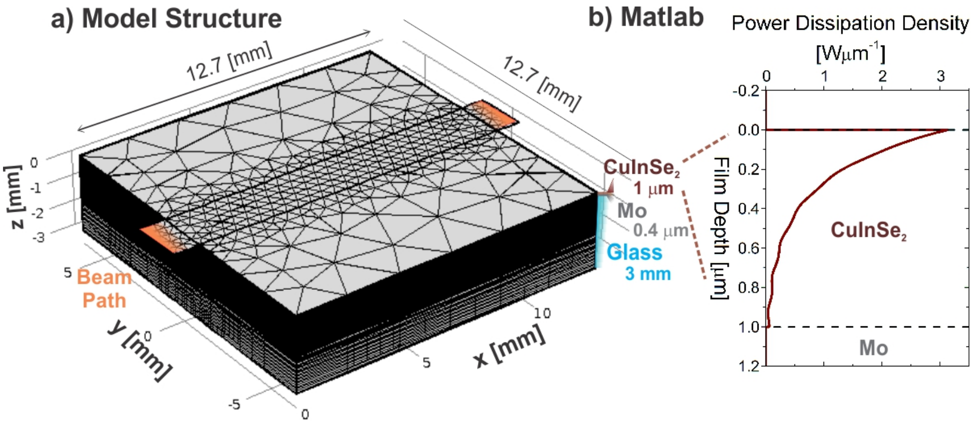

Figure 9.8: a) Model construction used for 3D simulations showing the material dimensions and how this volume is meshed. b) Matlab solution of electromagnetic wave propagation through 2D stack of CISe/Mo

The intensity, I, at any x, y location is then given by the function 9.15.

$$I(x,y) = I_0 \exp \frac{-2(x^2+y^2)}{w} \tag{9.15}$$

w and I_0 were calculated in Mathematica, giving w = 1.9 mm and I_0 = 211 Wcm^{-2}, for a measured average flux of 150 Wcm^{-2}.

To calculate the film temperature over 3D space, Eq.9.12 is extended to give Eq.9.16.

$$\rho C_p \frac{dT}{dt} + \rho C_p u \nabla T = \nabla(k\nabla T) + Q_{in} \tag{9.16}$$

Thermal transfer via convection and radiation is accounted for at the film surface and sample edges. The rear interface of the glass is considered to be thermally insulating.

Figure 9.9 presents the results of simulating a laser beam making a single pass across the sample at 2 mms^{-1} and with Gaussian profile parameters corresponding to an average flux of 150 Wcm^{-2}.

Considering the temperature profiles over the sample volume shown in Fig.9.9a), as the beam moves onto the sample surface it is rapidly heated (i), reaching a peak temperature of 755 ^{o}C at the centre of the Gaussian beam. As the beam scans across the sample this peak film temperature increases slightly (ii). This can be correlated to the accumulative energy of the higher substrate temperature combined with the supplied heat from the laser. The highest temperature of 907 ^{o}C is reached as the centre of the laser beam hits this edge of the sample (iii). This is clearly observed in the temperature profiles of Fig.9.9bi), where the profile 6.8 s after the start of the annealing (exactly corresponding to when the beam centre reaches the edge of the sample) is anomalously higher than the temperature profiles at other times. These results show that the scanning direction and sample geometry will have an effect on the film properties due to the 150 ^{o}C temperature difference between the peak temperature at each extreme edge of the film. Taking the average of the maximum temperatures of the heating profiles shown in the Fig.9.9bi) gives an average peak film temperature of 780 ^{o}C, slightly higher than the value of 748 ^{o}C calculated in the 2D model.

These peak values correlate to the temperatures reached in areas of the film irradiated by the

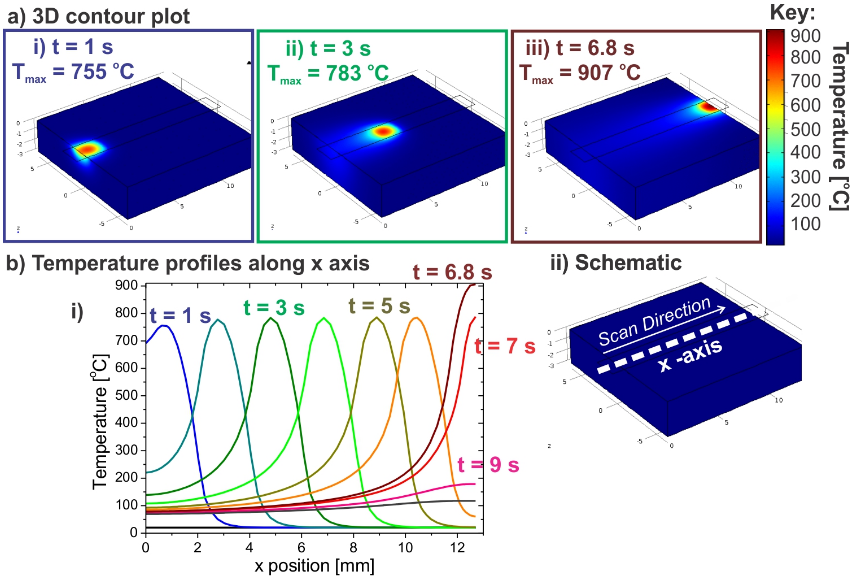

Figure 9.9: a) 3D contour map showing the temperature distribution over the sample volume at specified times. T$_{max}$ is the peak film temperature (correlating with the sample area at the laser beam centre). b) Surface temperature plotted against the x-axis (along the scan line, as indicated in the schematic) at the times given.

centre of the laser beam. However, the key finding of this 3D model is the substantial temperature gradient which arises as a consequence of the Gaussian laser beam power distribution incident on the sample. Fig.9.10a) shows an expanded view of the sample area being irradiated by the laser beam. Where the centre of the laser beam (with an intensity I_0 = 211 Wcm^{-2}) hits the CISe film, this peak temperature is reached. However, the film temperature rapidly decreases to $<$ 50 ^{o}C, 3 mm from the beam centre. The Gaussian power distribution of the laser beam is reflected in the near-Gaussian temperature distribution observed in Fig.9.10b) where the film temperature is plotted at a normal to the laser raster direction. The implication of such a temperature profile on the properties of the CISe film was apparent when analysing the single beam line of Section 9.1. In Fig.9.2, the microstructure and PL yield of a sample laser annealed under conditions matching the model were analysed at points along the indicated 'y-axis'. Analysis was made at film areas (as indicated on Fig.9.10) corresponding to (1) the centre of the beam, y = 0 mm, (2) the visual beam edge, y = ± 1.1 mm and (3) the edge of the sample, y = 6 mm. The temperature at each of these points is determined from Fig.9.10b) and compared to the sample properties (repeated for clarity in Fig.9.10c). At y = 6 mm (3) the modelled film temperature remains at the 20 ^{o}C ambient temperature, and consequently the material at this location remains as precursor, correlating with its measured nanocrystalline structure and low PL yield at 1 eV. At the visual edge of the beam line (2), the film temperature reaches 350 ^{o}C and it was observed that some grain growth had occurred and the PL yield at 1 eV had increased. Finally, at the beam centre (1), the peak temperature of 784 ^{o}C was calculated, and the CISe film shows the largest grain size along with the CISe film composition becoming homogeneous through its depth (See Fig.9.2diii). However, the PL yield at 1 eV remains nearly constant over the central 1.5 mm of the irradiated area even though it is calculated to have a temperature difference of 230 ^{o}C (see Fig.9.10b). This correlates to the observations of Section 9.1 where at the highest laser power the material appeared to degrade, evidenced by a second peak in the PL spectra. The

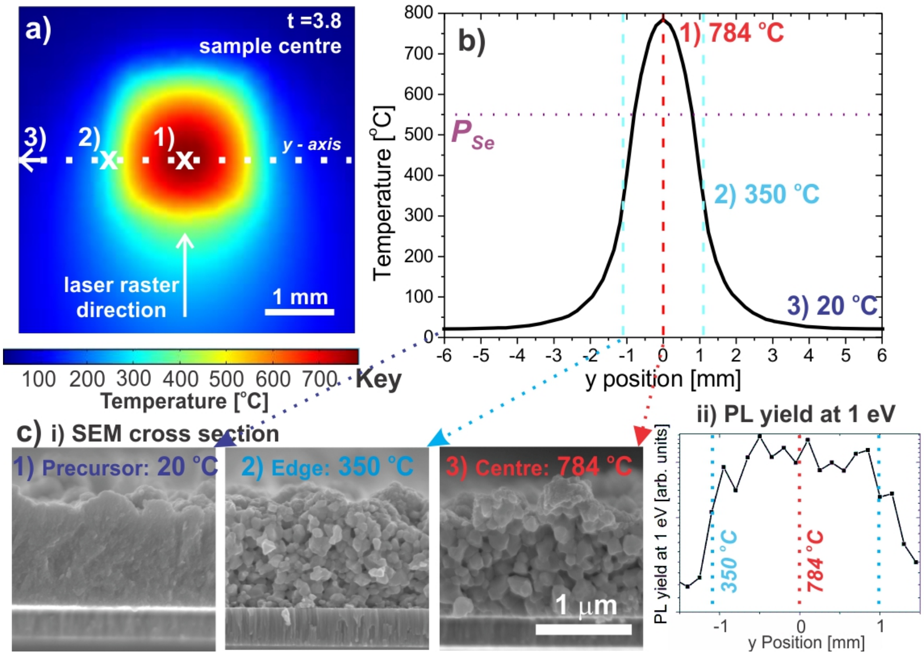

Figure 9.10: a) Enlargement of the temperature colour map of the area surrounding the beam, when it reaches the centre of the sample (at t = 3.8 s). b) Plotted temperature distribution along the y-axis (as indicated in a). ci) SEM cross sectional micrographs at the points labelled 1)-3) in (a) and ii) PL spectra along this y-axis (repeated from Fig.9.2).

relatively poor optoelectronic properties in this region may be explained by considering that the background P_{Se} supplied during the annealing was sufficient to prevent CISe breakdown only for temperatures $< 550\ ^{o}$C. The temperature exceeds $550\ ^{o}$C (as indicated on Fig.9.10b) over the central 1.5 mm area of film and therefore CISe decomposition would be favourable within this region.

The lateral fluctuations in peak temperature over the CISe film during laser rastering can also be applied to explain the variation in EQE observed in the device of Fig.9.1. By calculating the maximum temperature that the film reaches over two raster lines one achieves the temperature profile of Fig.9.11a). This profile was created by Brian Simmonds, University of Utah.

In the photograph of the CISe absorber (Fig.9.11b) which has been laser annealed using a rastering process, pale and dark horizontal lines are observed corresponding to the movement of the laser beam over the sample. The position and shape of these features reflect the simulated peak temperatures over the film as shown in Fig.9.11a). The highest temperatures are reached as the laser beam hits the sample edges and can be correlated to the palest areas on the absorber surface. This temperature profile can also be compared to the EQE of the final device, the results of the two best cells are given in Fig.9.11c). Section 9.1 noted the two regions of high EQE on cell 1). This pattern appeared to indicate that this cell lies over two raster lines which is in agreement with the two pale areas seen on the absorber surface in the area of the cell (see Fig.9.11b). It can now also be related to the simulated temperature profile and an example of how this cell could be positioned on this profile is indicated on Fig.9.11a). Forming a device over this indicated location would mean that the CISe film reaches peak annealing temperatures

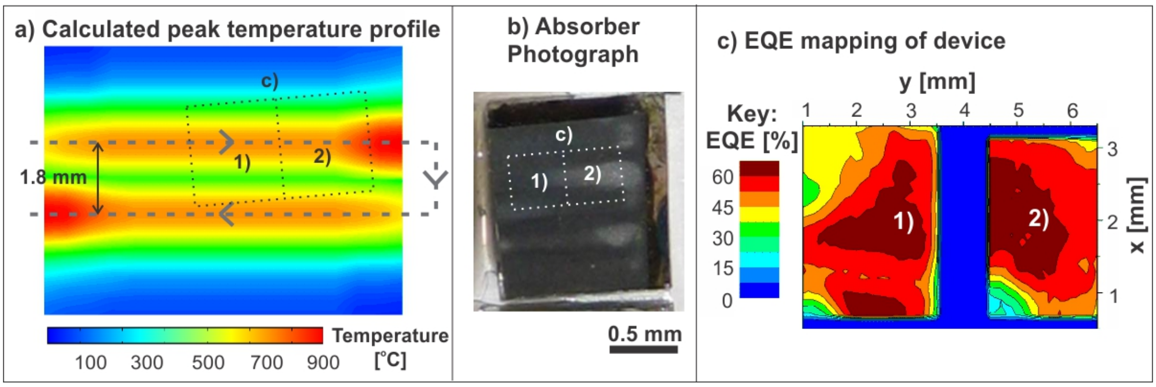

Figure 9.11: a) Peak temperature of a CISe film calculated using the 3D model over two raster lines with laser flux, 150 Wcm^{-2}, scan rate 2 mms^{-1}. b) photograph of CISe absorber which had been laser annealed under these conditions and fabricated into a device, c) the EQE mapping over two cells of this device. An approximate positioning of these cells is indicated by the dotted lines on (a) and (b).

which vary by $\approx$ 400 ^{o}C and Fig.9.10 showed the effect that this has on the sample properties for example the grain size and PL yield.

These results emphasise that to ensure a CISe absorber with uniform lateral properties and therefore optimal device performance, a homogeneous temperature profile is required. One method to achieve this is demonstrated in Section 11.1.2. Section 9.3 examines the temperature dependence of grain growth and atomic diffusion. This analysis aims to find the rate limiting step in the annealing transformation process and therefore to calculate the minimum film temperature required. Having demonstrated a viable method to calculate the film temperature from the applied flux, it is hoped that future work can optimise the processing parameters to form more homogeneous films, and achieve higher device efficiencies.

Conclusions and Extensions

In this section, the conception and operation of a model capable of estimating film temperature during annealing has been demonstrated. The initial approach used a 2D model, the results of which were compared to thermocouple measurements of the rear surface of the sample. Subsequently a 3D approach was implemented to explain the variations in sample properties on a perpendicular axis to the beam raster. The peak film temperature calculated using both approaches showed a reasonable agreement. However, even with the 3D model, there are still three major dissimilarities from the experiment, the incorporation of which are foreseen to improve the model's accuracy.

Firstly, in order to create a P_{Se}, the sample is sealed into a specialised chamber. This chamber comprises an FTO window positioned $<$ 2 mm from the sample surface which is heated to temperatures from 75 ^{o}C to 175 ^{o}C. This may change slightly the initial film temperature and importantly will affect the convectional and radiative cooling of the film surface during annealing.

Secondly, the rear of the glass substrate is fixed to the chamber using double sided tape, allowing for conduction of heat via this interface. To model this situation the thermal properties of the adhesive tape and the Macor sample chamber would need to be determined.

Finally, the composition and roughness of the CISe film itself are known to affect the energy absorption. Mooney et al. [136], measured different α_λ for Cu-poor and Cu-rich precursors which affects the power density distribution within the film, as modelled in ref.[62]. Consequently, the film temperature is expected to vary according to precursor composition, a parameter which is discussed in Section 9.5.1. Additionally, α_λ was observed to change between precursor and annealed sample [136]. A possible reason for this is that the film composition changes from a multiphase precursor to single phase CISe during annealing (see Section 7). Both the $Cu_{2\text{-}x}Se$ and In_2Se_3 secondary phases present in the precursor will have their own absorption and thermal properties, affecting the heating of the film. However, without detailed measurements of the microstructure, composition, thermal and optical properties of the precursor, it is difficult to correct for this inaccuracy. It can also be considered that these properties, e.g. C_p and k, are temperature dependent, although the change in their values upon heating is not expected to have a significant effect on the calculated temperatures.

9.3 The Effect of Laser Fluence

In the previous section, the 3D model evidenced how the film temperature depends on the applied laser flux, assuming a constant dwell time. However, the annealing time or beam raster rate, is also hypothesised to affect the film temperature and therefore its properties. The product of flux and time is termed the fluence and relates to the impinging laser energy per unit area (Jcm^{-2}). In this investigation, a single codeposited CISe precursor was diced into 4 mm^2 pieces. Each piece was annealed with a different laser flux and raster speed combination. XRD patterns were measured on each sample in order to determine the effect that the laser fluence, and consequently the film temperature, has on the absorber's properties. The peak width in x-ray diffractograms is proportional to the size of coherently scattering domains within a film, which are affected by the temperature dependent parameters of atomic diffusion and grain growth. Accordingly, the crystal coherence length was calculated from the FWHM of the CISe 112 peak in XRD patterns of the absorbers, using the Scherrer formula (Eq.5.4). These values are plotted against the dwell time (calculated from the scan speed) in Fig.9.12a).

Considering the samples annealed with the same dwell time in Fig.9.12a), there is an increase in the coherence length with higher beam fluxes, in agreement with the observations of Section 9.1. For example, with 1 s annealing time, coherences lengths between 108 $\pm$3 nm - 167 $\pm$5 nm are measured with applied laser fluxes of 125 - 175 Wcm^{-2}. Similarly, at a constant flux, longer annealing times lead to a increased coherence length as seen for samples annealed at 300 Wcm^{-2} for 0.3 - 0.5 s, where the average coherence length rises from 114 $\pm$3 nm to 177 $\pm$5 nm. Consequently, it may be expected that there will be a correlation between the product of flux and time, the fluence, and the crystal coherence length, as is plotted in Fig.9.12b). However, this graph evidences no clear relationship between these parameters. For example, an annealing fluence of 150 Jcm^{-2} results in a range of coherence lengths from 128 $\pm$3 nm to 188 $\pm$6 nm. Notably, a fluence of only 16 Jcm^{-2} results in a absorber layer with coherence length of 170 $\pm$8 nm. This fluence relates to a scan rate of 50 mms^{-1} with a dwell time per area of just 0.04 s. The impressive level of crystallinity achieved within this time-scale indicates the potential of this process to industrial up-scaling, which is considered further in Chapter 11.

An interesting observation of Fig.9.12a) and b) is that higher powers applied over shorter annealing times appear to lead to larger coherence lengths than a lower power but much longer

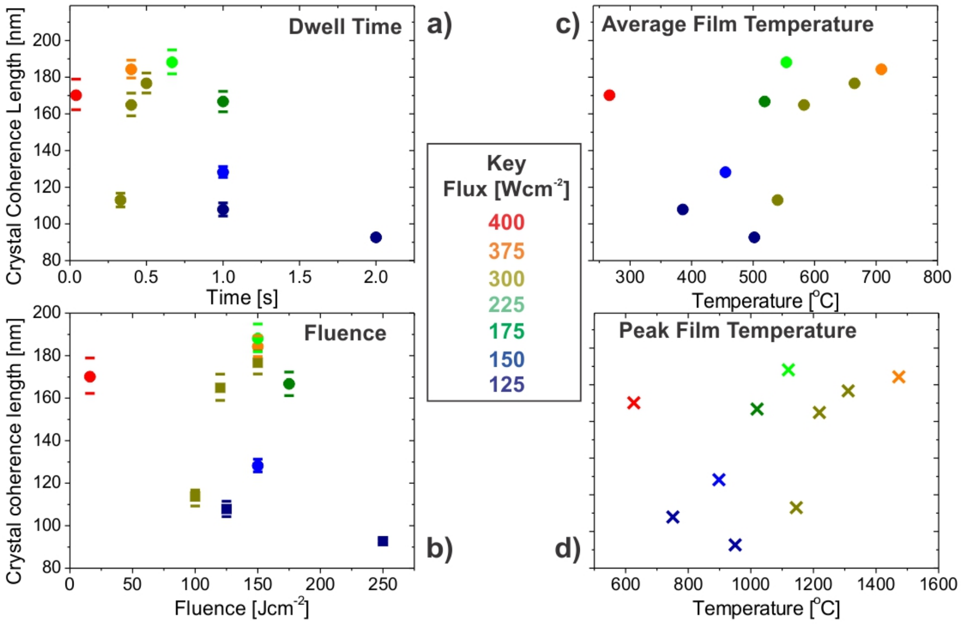

Figure 9.12: a) Average crystal coherence length calculated using the Scherrer formula, from the FWHM of the CISe 112 peak in XRD patterns of absorber layers formed by laser annealing codeposited CISe precursors at the stated fluxes and dwell times (calculated from the scan speed). b) D parameter of (a) plotted against the annealing fluence. D parameter against c) average and d) peak film temperatures calculated using 3D model where the sample area = 2 x 2 mm and I_0 was scaled in relation to the applied flux. Points are colour coded as to the annealing flux used.

time scale. A possible explanation for this trend is that these samples were annealed with very low background P_{Se} = 9 × 10^{-7} Pa. Eq.8.6 indicates that, at this partial pressure, the decomposition reactions of CISe are favourable at film temperatures $>$ 425 ^{o}C, as reached during the annealing process. Using longer annealing times, increases the duration at which the film temperature exceeds 425 ^{o}C and so is hypothesised to increase Se loss [155]. The Se loss results in V_{Se} defect formation and potentially secondary phases within the CISe film, and thus to a lower crystal coherence length. In order to test whether the film is hot enough to promote Se loss and to furthermore test if the crystal coherence length is linked to the film temperature, the film temperature was calculated using the 3D model and the results are shown in Fig.9.12c) and d). In this model, the 2 mm x 2 mm sample area is rastered by a beam with peak flux, I_0, determined from the average flux. In Fig.9.12c) the crystal coherence length is plotted against an 'average' temperature and in (d) a 'peak' temperature. The peak temperature represents the highest value calculated during the full experiment time and over the whole 2 mm x 2 mm sample area. The average film temperature is the mean of these values. Both the peak and average film temperatures show a general trend of higher annealing temperatures leading to increased coherence length in the absorber. However, the CISe film annealed at 400 Wcm^{-2} for 0.04 s remains anomalous. It may be noted that some of the peak temperature values of Fig.9.12d) lie above the T_m = 990 ^{o}C melting temperature of CISe [169]. The viability of these values is corroborated in Appendix 12.7. SEM micrographs measured on the sample annealed at 375 Wcm^{-2} for 0.4 s (that with the highest calculated peak temperature), show localised melting and small areas where the film has been vaporised. Furthermore the sample has cracked due to the differing rates of thermal expansion between the front and the rear of the glass substrate.

This analysis evidences the link between crystal coherence length and the annealing temperature. To explain this result, the two components of the x-ray coherence length are considered: the grain size and the presence of structural defects. Accordingly, the subsequent sections investigate the temperature dependence of atomic diffusion (as a higher atomic mobility would be expected to lead to a reduction in structural defects) and grain growth.

9.4 Atomic Diffusion

In Section 9.2.2 it was observed that the Gaussian flux distribution of the laser beam was reflected in the temperature profile of the CISe film, perpendicular to the scanning direction (see Fig.9.10) and that this affected both grain size and peaks observed in the PL spectra. In this section, the impact of temperature on atomic diffusion is analysed. Firstly a brief introduction into the theory of atomic diffusion is given. Using the method detailed in ref.[170] diffusion coefficients, D, are calculated for each element across the beam line. These values of D are then compared to those derived by estimating a mean diffusion distance from measured depth profiles. This process explains the relationship between a lateral temperature gradient across the CISe film and a changing composition profile through its depth. Comparing the D values calculated using each technique to those measured in literature, gives an indication of their validity. This analysis aims to identify the limiting mechanism in atomic diffusion and therefore the minimum film temperature / annealing time required to homogenise elemental composition through the CISe depth.

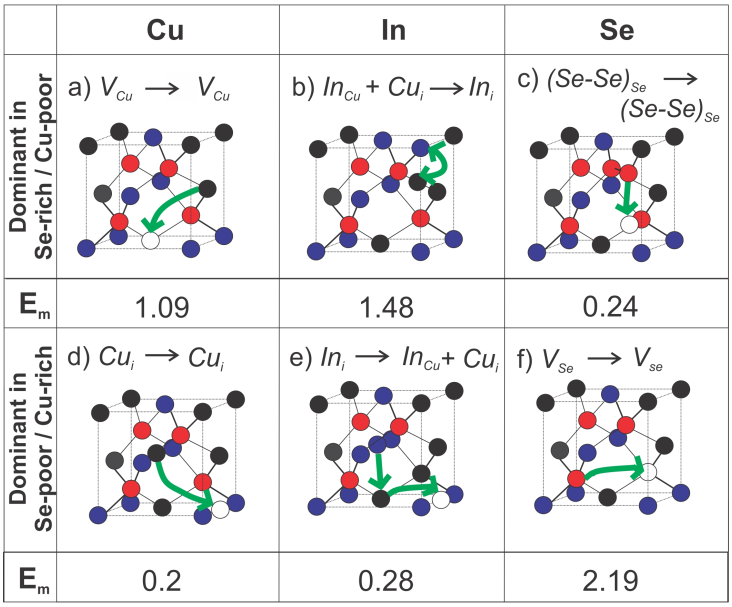

Figure 9.13: Illustrations representing the most favourable diffusion pathways of each element and its associated energy migration barrier E_m within a single unit cell where Cu is represented in black, In in blue and Se in red (similar to ref.[170]). The mechanisms are arranged to indicate those which dominate in Cu-rich and Cu-poor CISe.

9.4.1 Diffusion Theory

Atomic diffusion describes the net transport of atoms that results from their random, thermally activated movement. The rate of diffusion is expressed by the diffusion coefficient, D, which is determined using an Arrhenius equation as given in Eq.9.17.

$$D = A_D \exp\left(\frac{-E_a}{k_b T}\right) \tag{9.17}$$

Where A_D is a constant, relating to the maximum rate of diffusion in a specific material and k_b is the Boltzmann constant (8.62×10^{-5} eVK^{-1}). E_a is the activation barrier and its magnitude depends on the diffusion pathway. Mass transport in a solid takes place by means of a number of mechanisms including via point defects e.g. an atom exchanging with a vacancy, or hopping through interstitial space as shown in Fig.9.13a) and d) respectively.

In order to calculate the diffusion coefficient, Eq.9.17 can be broken into its component parts using the method of Oikkonen et al. [170]. Each possible diffusion mechanism has an individual energy barrier, E_m. Therefore the diffusivity of vacancies, D_v, and interstitials, D_i, is calculated in Eq.9.18.

$$D_{i/v} = \exp\left(\frac{-E_m}{k_b T}\right) \tag{9.18}$$

Examples of the dominant diffusion mechanisms for each element in CISe in two different material stoichiometries and their corresponding energetic barrier are given in Fig.9.13.

The dominant diffusion mechanism of each element is that which has the lowest barrier, E_m i.e. the highest diffusivity. From Fig.9.13 it is observed that both Cu and In favour an interstitial diffusion mechanism (d) and (e), which is particularly advantageous in Cu-rich CISe, whereas the diffusivity of Se is highest in Se rich material (c) where Se can diffuse via 'dumbells'. The probability of an element diffusing via each of these mechanisms therefore also depends on the defect concentration, C_i or C_v for vacancies and interstitials respectively [170]. The defect concentration at thermodynamic equilibrium is described by an Arrhenius relationship as given in Eq.9.19.

$$C_{i/v} \propto \exp\left(\frac{-E_f}{k_b T}\right) \tag{9.19}$$

Where E_f is the formation energy of each respective defect. The self diffusion coefficient, D_{self}, for each element is the total of the product of the diffusivity and defect concentration for each defect diffusion mechanism, as summarised in Eq.9.20.

$$D_{self} = \Sigma_i C_i D_i + \Sigma_v C_v D_v \tag{9.20}$$

Where Σ_i and Σ_v are the sum of all the interstitial and vacancy-mediated diffusion mechanisms respectively. D_{self} gives the diffusion coefficient of an element in the absence of a chemical gradient and at thermodynamic equilibrium. In Section 9.1 it was seen that irradiating a sample with a laser beam of spatially fluctuating power density lead to differences in atomic diffusion and Section 9.2.2 showed that this correlated with the spatial temperature variation over the CISe film. The modelled temperature over an area of CISe film under laser irradiated is shown in Fig.9.14a).

In order to calculate values for D$_{self}$, the temperature at each of the points at which atomic depth profiles were measured is determined in Fig.9.14. Thus the following temperatures are

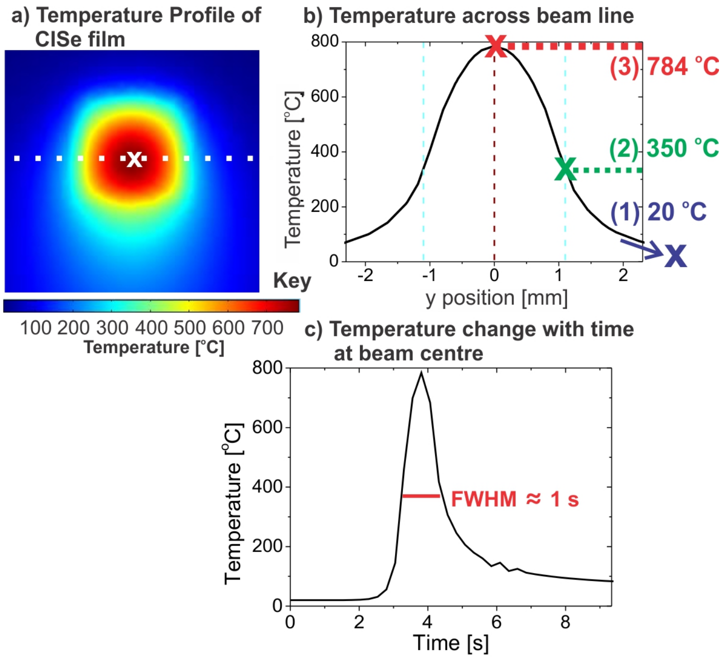

Figure 9.14: a) Simulated temperature profile of a CISe film irradiated by laser beam with 150 $\mathrm{Wcm^{-2}}$, 2 $\mathrm{mms^{-1}}$ (as given in Fig.9.10). b) Graph showing the temperature profile across the white dotted line of (a). c) Temperature plotted against time for the point of the CISe film reaching the highest temperature as indicated on by the white cross on (a).

used in subsequent calculations: (1) 20 ^{o}C far from the beam line (precursor), (2) 350 ^{o}C at the visual beam edge and (3) 784 ^{o}C at its centre. An approximate diffusion time of 1 s was calculated from the FWHM of the transient temperature plot shown in Fig.9.14b). Using Eq.9.20, values of D were calculated for each element in different compositions of CISe for point (2), the visual beam edge and the results are given in Table 9.2.

		D_{self} [$\mathrm{cm^2s^{-1}}$] 350 ^{o}C	<x> [nm] 350 ^{o}C
Cu	Cu-rich	9.1×10^{-5}	67330
	Cu-poor	3.7×10^{-11}	43
In	In-rich	7.6×10^{-27}	1.2×10^{-6}
	In-poor	1.4×10^{-13}	5.3
Se	Se-rich	4.7×10^{-20}	3.1×10^{-3}
	Se-poor	7.7×10^{-27}	1.2×10^{-6}

Table 9.2: Values of D_{self} and root mean squared diffusion distance <x> calculated using the method of ref.[170] for different CISe stoichiometries at 350 ^{o}C

The values of Table 9.2 indicate that the material composition is strongly influential on the rate of diffusion, with the D values of each element changing by more than six orders of magnitude depending upon the material stoichiometry. Whilst Cu is the most mobile element in CISe, the low D values of In or Se indicate that their diffusion may limit the homogenisation of the precursor composition during the rapid annealing of CISe. However, concentration gradients within a material (such as those found in the CISe precursor, Fig.9.2) drive atomic diffusion and therefore D_{self} is an inadequate description of the rate of diffusion in this material. Fick's First Law in one dimension, Eq.9.21, describes the affect of a concentration gradient.

$$J = -D\frac{\partial \Phi}{\partial x} \tag{9.21}$$

Φ is the concentration of the diffusing species and J is the diffusional flux. In order to measure the diffusional flux and therefore establish D values which can be compared to the values of D_{self} in Table 9.2, depth profiles were measured at each of the analysis points across the beam line and are plotted with respect to the atoms Cu, In and Se in Fig.9.15a). Section 9.2.2 calculated the peak temperature reached at each of these points. Therefore, each point effectively represents the atomic composition through the depth after annealing for 1 s at the calculated temperature. From the difference in elemental depth profile between the precursor (blue) and beam edge (green), an approximate diffusion length or root mean squared distance, <x>, is ascertained. For example, there is a high concentration of Cu in the central 200 nm depth of the precursor film (Fig.9.15ai): blue line) which has equalised at the beam edge (green) to give a nearly constant Cu-composition in the bulk with a Cu-poor surface. Therefore the average diffusion distance is estimated to be in the range of 500 nm (as indicated by the orange dotted line in Fig.9.15ai), equal to half the film thickness. From <x>, the diffusion coefficient, D, is calculated using Eq.9.22.

$$D = \frac{\text{<x>}^2}{2t} \tag{9.22}$$

The values of <x> and D_{350oC} determined using this analysis are given in Table 9.15b).

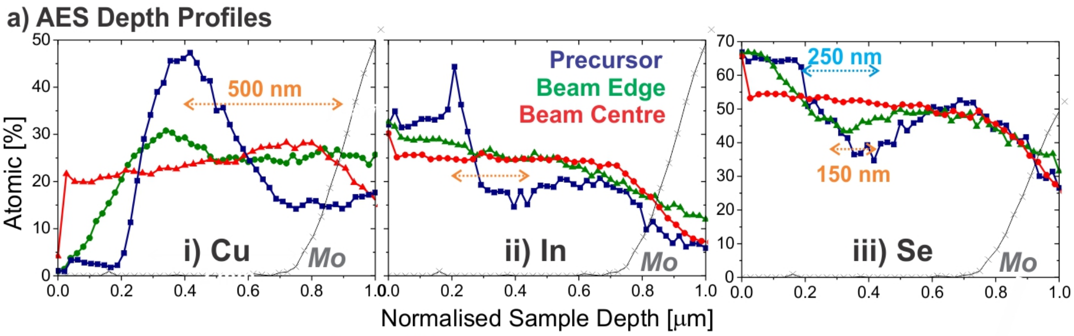

a) AES Depth Profiles

b) Diffusion: Precursor -> Beam Edge

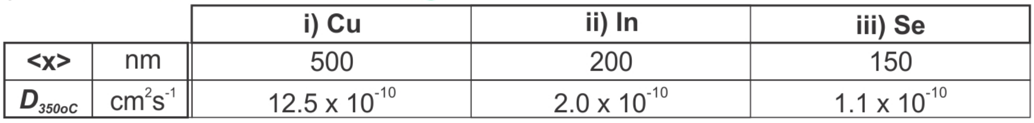

		i) Cu	ii) In	iii) Se
<x>	nm	500	200	150
D_{350oC}	cm^2s^{-1}	12.5×10^{-10}	2.0×10^{-10}	1.1×10^{-10}

Figure 9.15: a) Auger elemental depth profiles (as in Fig.9.2) for i) Cu, ii) In and iii) Se at positions on the sample corresponding to the 20 ^{o}C precursor (blue), 350 ^{o} C visual beam edge (green) and the 784 ^{o} C beam centre (red). b) Table with the estimated root mean squared diffusion distance, <x>, of each element (i)-(iii) which is required to bring about differences observed in (a - indicated by yellow arrow) between the precursor area and beam edge, and the diffusion coefficient, D, required to give this value of <x>, assuming an annealing time of 1 s.

9.4.2 The Diffusion of Cu, In and Se in CuInSe$_2$

Comparing the values of D_{350oC} calculated from <x> in Fig.9.15b) to the theoretical D_{self} values of Table 9.2, it is observed that only in the case of Cu, is the rate of self-diffusion sufficient to satisfy the experimentally observed level of atomic rearrangement. For In and Se it can be deduced that their diffusion is predominantly driven by the diffusion gradients present in the codeposited CISe precursor. In order to validate the empirically derived D_{350oC} values, a brief literature review of the diffusion of each element is carried out.

Cu

Cu is the most mobile element in CISe [171]. In Cu poor CISe, this high mobility is attributed to the low formation energy (0.64 eV) and thus high density of V_{Cu} defects whereas in Cu-rich CISe there is a low barrier (0.2 eV) for Cu$_i$ defects to diffuse via interstitial hopping [170]. The contribution of each of these mechanisms is dependent both on material composition and the position of the Fermi level leading to a wide range of measured self diffusion values from D_{Cu} = 3.0 × 10^{-14} cm^{2}s^{-1} [172] (at 350 ^{o}C) up to 3.3 × 10^{-7} cm^{2}s^{-1} (at 20 ^{o}C) [173]. Fig.9.15a) evidences the strong variation in elemental composition through the depth of the precursor film and therefore it could be expected that D will also be influenced by concentration gradients, as given in Eq.9.21. The D_{350oC} = 1.25 × 10^{-9} cm^{2}s^{-1} determined experimentally (i.e. affected by the diffusional flux) is close to the to average of the values given in Table 9.2, D_{self} = 5 × 10^{-8} cm^{2}s^{-1}, in accordance with the precursor comprising regions of Cu-rich and Cu-poor material. These values can be compared to those calculated by Gartsman et al. [171] of diffusion of Cu into a single crystal of CISe. At 400^{o}C and with Cu concentrations of 10^{18} - 10^{21} cm^{-3} values of D_{Cu} = 10^{-8} - 10^{-9} cm^{2}s^{-1} were observed. As the Cu concentration at the precursor centre is $\approx$ 10^{20} cm^{-3} this range of D values appears applicable and D_{Cu} = 10^{-8} - 10^{-9} cm^{2}s^{-1} gives <x> = 0.4 - 1.4 μm. However, as there is incomplete homogenisation of the Cu profile after 1 s annealing at 350 ^{o}C, it can be reasoned that <x> lies below the 1 μm film thickness, and thus that D_{Cu} is $<$ 5 × 10^{-9} cm^{2}s^{-1}, and that this element slightly restricts elemental homogenisation at 350 ^{o}C.

Se

Fig.9.13 details two diffusion mechanisms for Se: via ‘Se dumbbells’ (c) or vacancies (f). The facile formation of V$_{Se}$ under Se-poor conditions has already been noted in Section 8 and is a consequence of their low formation energy, E_f = 1.04 eV [170]. Consequently, D_{Se}, is also dependent on the atmospheric Se activity [174]. However, the migration of V$_{Se}$ is impeded by a high energy barrier of E_m = 2.19 eV. Under Se rich conditions, the additional Se is accommodated within the CISe lattice by the formation of Se ‘dumbbells’, a process which is energetically costly. Therefore, even though the exchange of these dumbbells has a low energy barrier of 0.24 eV [170], both Se-rich and Se-poor conditions have very low D_{Self} values. The low mobility of Se within the crystal lattice is confirmed in literature with $D_{Se} < 1 \times 10^{-12}$ cm^{2}s^{-1} even at 700 ^{o}C, for single crystal CISe [174]. These values would imply that Se diffusion is negligible during laser annealing. In polycrystalline samples, however, there is also diffusion via grain boundaries, where the higher defect concentration facilitates mass transport. Kumar et al. found a change in activation energy from 1.98 eV for lattice diffusion to 0.26 eV via grain boundaries [175]. Their studies on a polycrystalline sample gave E_a = 0.29 eV indicating that grain boundary diffusion dominates in polycrystalline CISe. The nanocrystalline nature of the electrodeposited samples in this study results in a high density of grain boundaries. Using Eq.9.17 to calculate D_{Se} with this lower, grain boundary assisted, E_a = 0.29 eV gives 7 $\times$ 10^{-9} cm^{2}s^{-1} at 350 ^{o}C giving a diffusion length of 1.2 μm. Such a diffusion length implies that the Se profile should flatten even with 1 s at 350 ^{o}C. As there remains some fluctuation in Se composition through the depth, it appears that the grain boundary contribution is less in these samples. For complete homogenisation of the profile, a diffusion distance of 250 nm is required (blue dotted line in Fig.9.15aiii), equivalent to D_{Se} = 3.1 x 10^{-10} cm^{2}s^{-1}. Assuming the activation energy determined by Kumar et al. but using the value of D_{350oC} determined in Fig.9.15 to shift the line in a plot of $1/T$ vs. $\log D$, the temperature required to give a diffusion length of 250 nm is calculated as 485 ^{o}C.

In

The formation of In vacancies and interstitials is thermodynamically unfavourable due to their high oxidation state (V$_{In}^{-3}$, In$_i^{+3}$) and thus In defects have high formation energies at all compositions [170]. Any In$_i$ formed will favourably displace a Cu atom to form In$_{Cu}$ + Cu$_i$ as shown in Fig.9.13e). The low defect concentration impedes the mobility of In within the CISe film, as demonstrated by the low values of Table 9.2. The low diffusivity of In is also observed by Marudchalam [176] and Djessas et al [177] who consider a In-rich phase on a $CuGaSe_2$ film. For example, Djessas finds D_{In} = 1.7 $\times$ 10^{-13} cm^{2}s^{-1} at 350 ^{o}C [177]. Considering the composition of the electrodeposited precursor through its depth (Fig.8.1), with adjacent regions of predominantly $Cu_{2-x}Se$ and In_2Se_3, a D_{In} of 1 $\times$ 10^{-13} cm^{2}s^{-1} seems reasonable. However, such a low D gives a diffusion length of only <x> $\approx$ 5 nm, significantly less than that observed in Fig.9.15. Using A_D and E_a values from Djessus in Eq.9.17, it is calculated that 550 ^{o}C must be reached to give the <x> $\approx$ 200 nm distance estimated to homogenise the In profiles as observed experimentally in Fig.9.15aii). Whilst the temperature at the beam centre is $>$ 550 ^{o}C, this assumption does not explain the profile at the beam edge. However, there are two situations where the diffusion of In may be increased. (1) In diffusion is higher in Na-free films, a property of the laser annealed samples presented here (see Section 9.5.2). (2) In diffusion is facilitated by the $Cu_{2-x}Se$ phase commonly found in Cu-rich films [178]. Characteristic flakes were observed on the surface of this CISe film (not shown) indicating that whilst its composition was close to stoichiometric there is some $Cu_{2-x}Se$ present.

To summarise, even at 350 ^{o}C, Cu diffuses relatively easily through the CISe film, via both vacancy and interstitial mechanisms and aided by the highly Cu-rich and Cu-poor regions of the CISe precursor. However, the highly fluctuating composition of Cu through the precursor film requires long diffusion lengths, which are not fully reached after 1 s at 350 ^oC. Se diffusion within crystals is impeded by a high energetic barrier leading to negligible values of $D_{self-Se}$. However, in the nanocrystalline samples investigated in this work, the more facile grain boundary diffusion is expected to occur. Whilst the contribution of this more rapid diffusion method to the diffusion coefficient cannot be accurately determined in this analysis, a preliminary calculation implies that temperatures $>$ 485 ^{o}C would give sufficient diffusion lengths to homogenise the composition of Se. Finally, In dominantly diffuses via interstitials and the low concentration of these defects lead to its very low mobility. As its concentration is seen to partially homogenise through the film depth, it is possible that the absence of Na and presence of Cu-Se may lead to higher D_{In} values. In conclusion, annealing at 350 ^{o}C for 1 s provides insufficient energy for atomic diffusion to completely homogenise all the elements, as would be expected. Extrapolating D_{In} indicated that temperatures > 550 ^oC were sufficient to homogenise all elements within 1 s. Indeed, at the beam centre, where the FEM model calculated a temperature of 784 ^oC, the profiles of Fig.9.15a) (red lines) are reasonably depth constant. However, without depth profiles measured in the range 350 - 784 ^oC it is not possible to verify that a lower temperature would indeed be sufficient.

9.4.3 Summary and Discussion

D values at 350 ^oC have been determined and evaluated for each of the elements, Cu, In and Se. The theoretical method of Oikkenen [170] placed upper and lower bounds on the values for D_{self} for each element. These values were combined with D derived experimentally which takes into account the diffusion flux resulting from the inhomogeneous precursor composition. This analysis indicates that whilst, even at relatively low temperatures, Cu may diffuse through the full film depth within the 1 s annealing time, In and Se are much less mobile. Comparing the experimentally derived D values to those of literature enabled approximate minimum temperatures to be calculated for the homogenisation of Se and In. From this analysis it is hypothesised that at temperatures > 550 ^oC sufficient energy is provided to the film for the composition to homogenise. On this basis, a depth independent composition is expected within the central 1.5 cm of the annealed area where T > 550 ^oC, a hypothesis which could be tested in future work. Outside this area, insufficient energy is supplied to the CISe for a complete atomic rearrangement within the 1 s time period. These results further emphasise that in order to achieve rapid annealing times the laser beam flux, and thus the film temperature, must be homogenised.

The literature examined in this section showed that elemental diffusion is strongly affected by parameters including Cu/In and Se/(Cu+In) ratios, gaseous Se activity and also the presence of dopant atoms like Na. In Chapter 8 the Se activity above an absorber and its Se/(Cu+In) composition was investigated, Section 9.5.1 will consider the chemical composition of the precursor.

9.5 Chemical Properties

Section 9.4 introduced how the film composition effects the rate of atomic diffusion. This section extends this approach to investigate the properties of absorbers created by laser annealing precursor films of various compositions. Firstly the effect of the Cu/In ratio is analysed and subsequently, the influence of Na and K dopants.

9.5.1 Effect of Cu/In ratio

A key milestone in the research history of CISe was the recognition that absorbers with a Cu-poor composition (Cu/In = 0.8-0.95, see green area of Fig.9.16), led to the highest efficiency devices [147][146]. This result is explained by considering the pseudo-binary Cu_2Se-In_2Se_3 phase diagram of Fig.9.16. $CuInSe_2$ exhibits a single-phase region from Cu/In: 0.95–1.0. The stability of Cu-poor CISe may be explained by the low formation energy of the V_{Cu} defect [170] noted in Section 9.4.2. Furthermore, when Cu/In < 0.95, the $CuIn_3Se_5$ secondary phase forms. This ordered vacancy compound (OVC) is derived from the CISe unit cell by the periodic introduction of In_{Cu} and V_{Cu} defects [180]. $CuIn_3Se_5$ has wider band gap (1.17 eV [181]) than

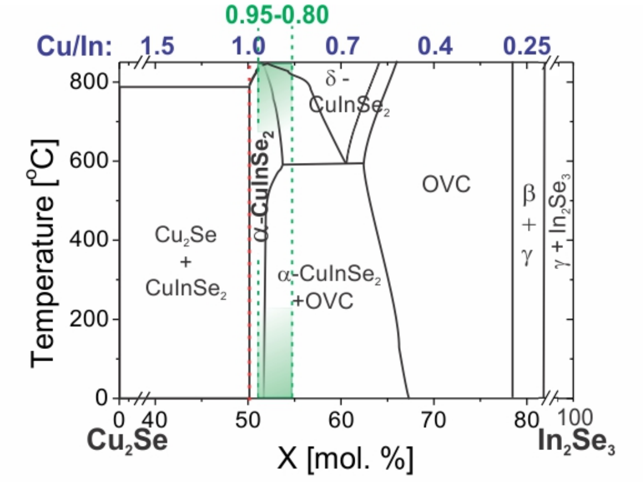

Figure 9.16: Pseudo-binary phase diagram indicating the compounds present in the Cu_2Se-In_2Se_3 system as a function of temperature [179]. α-$CuInSe_2$ relates to the chalcopyrite phase, β to the OVC, $CuIn_3Se_5$, phase, γ to the $CuIn_5Se_8$ phase and δ to the sphalerite phase. The red dotted line indicates stoichiometric $CuInSe_2$ and the green area, the composition range recognised to give the highest efficiency devices.

CISe and, present as a thin layer on the CISe surface, influences the p-n heterojunction leading to lower interface combination [147][182]. In contrast, Cu/In > 1 result in the formation of the Cu_2Se secondary phase. Cu_2Se shows metallic conductivity [183] and leads to a deterioration in device performance [182]. However, the absorber layers found in many of the record efficiency devices were fabricated using a process which comprised a Cu-rich growth step, such as that employed in the '3-stage' co-evaporation process [184]. Cu-rich films are frequently demonstrated to exhibit larger grain sizes and enhanced electronic properties, e.g. better defect densities, transport properties and bulk recombination [185], than their Cu-poor counterparts [147][186][187].

The device of Section 8.3.3 had a Cu/In = 0.93, within the range of stoichiometries shown to lead to high efficiencies (see Fig.9.16). However, Bhatia et al. (within the framework of the LASER project) observed double the reduction in FHWM after laser annealing Cu-rich precursors when compared to their Cu-poor equivalents [62]. This section investigates the laser annealing of precursors with a range of Cu/In compositions. In order to gain a better understanding of the kinetics of diffusion and grain growth during laser annealing, the effect of annealing time on the crystal coherence length is also studied as shown in Fig.9.17.

The increase in crystal coherence length with annealing time is observed in Fig.9.17 to depend on the composition of the precursor. A longer crystal coherence length is measured in absorbers from precursors with higher Cu/In ratios, matching previous literature observations [62][188]. A gain in x-ray coherence length is due to an increase in the average size of coherently scattering domains within the sample and the observed difference between absorbers from Cu-rich and Cu-poor precursors can be explained by a number of factors. Atomic rearrangement is facilitated by the high mobility of the Cu atom in CISe. With higher Cu-contents, the dominant diffusion mechanism changes from vacancy assisted to interstitial hopping [170] which has a lower activation energy and this, accompanied by a greater concentration of Cu_i defects, increases D_{Cu}. Furthermore, the $Cu_{2-x}Se$ secondary phase in Cu-rich CISe is pro-

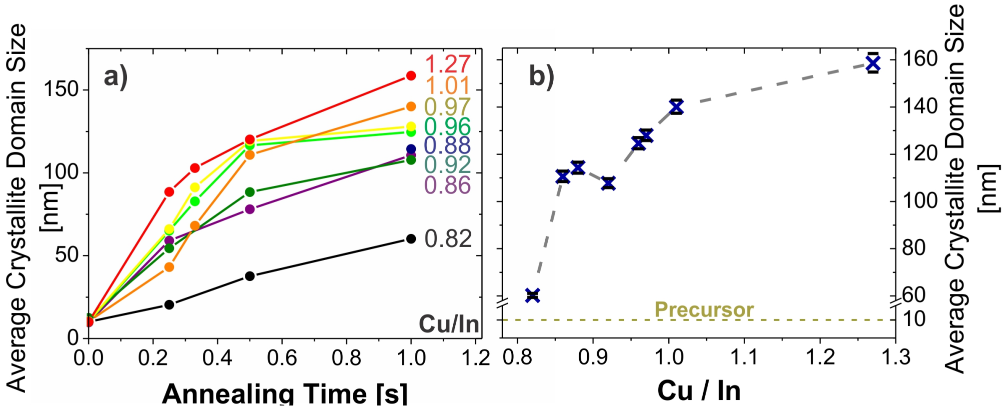

Figure 9.17: a) The crystal coherence length determined using the Scherrer formula from the FWHM of the CISe 112 Bragg peak of XRD patterns for absorber layers laser annealed at 150 Wcm^{-2} for the given annealing time (= laser spot size (mm) / scan rate (mms^{-1})) from precursors with the stated composition and with $\mathrm{P}_{Se} = 4 \times 10^{-5}$ Pa. b) Coherence lengths of absorbers in (a) corresponding to 1 s annealing time.

posed to act as a flux agent or to have a favourable crystal structure which promotes growth of the ternary CISe [189]. $\mathrm{Cu}_{2\text{-x}}\mathrm{Se}$ is liquid / pseudo liquid under the high annealing temperatures used (melting temperature, T_m(CuSe) = 550 ^{o}C, T_m($\mathrm{Cu_2Se}$) = 1113 ^{o}C [190]).

The optoelectronic properties of CISe are affected by its composition, with more Cu-rich stoichiometries having a wider band gap [191] and an increased absorption coefficient [136]. The change in absorbance of CISe electrodeposited precursors with their stoichiometry is observed in reflectance spectra, which show R_{1064nm} = 7 % and 10 % in Cu-rich and Cu-poor films respectively (see Fig.9.18). This results in an increased power density dissipated within Cu-rich than Cu-poor films and therefore the film is expected to reach higher temperatures [62]. This hypothesis is tested using literature values of α_{1064nm} for Cu-poor and Cu-rich electrodeposited precursors of 1.8×10^4 cm^{-1} and 3.5×10^4 cm^{-1} respectively [136]. Peak film temperatures of 700 ^{o}C and 750 ^{o}C were estimated using the 2D FEM model (assuming an average flux = 150 Wcm^{-2}, dwell time = 1 s) for Cu-poor and Cu-rich films respectively. The higher temperatures lead to increased atomic mobility in Cu-rich samples, and therefore the potential for less chemical gradients and lattice defects when compared to Cu-poor films. However, Section 9.4.2 indicated that even 1 s at these temperatures is sufficient to remove gradients in elemental concentration through the film depth. A final consideration is that at these peak temperatures the background P_{Se} is no longer sufficient to prevent Se decomposition. The potential loss of Se and breakdown of the CISe crystal lattice in the samples annealed for 1 s is expected to increase lattice disorder and thus may act against the gain in crystal coherence length brought about by atomic diffusion. This defect creation effect and that at temperatures $>$ 700 ^{o}C elemental diffusion lengths are on a similar magnitude to the film thickness, is eventually expected to lead to a plateauing of the crystal coherence length with longer annealing times. As Fig.9.17a) shows a near linear gain in crystal coherence length with increasing annealing time for all precursor compositions, either this situation is not reached within 1 s or there is a second thermally activated / time dependent process which limits the coherence length.

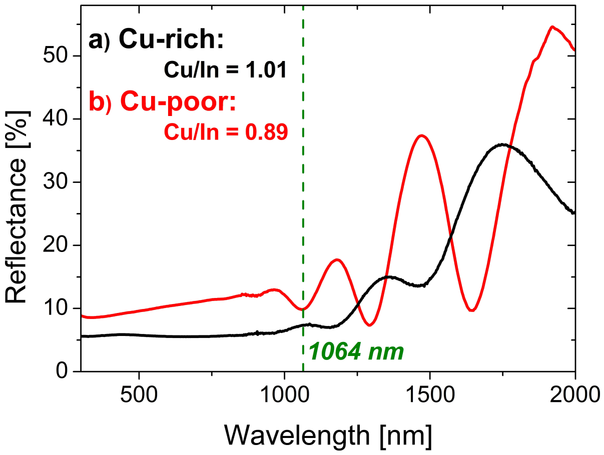

Figure 9.18: Reflectance Spectra measured using UV-Vis-IR of a) Cu-rich (Cu/In = 1.01) and b) Cu-poor (Cu/In = 0.89) electrodeposited CISe precursors.

Grain Growth

An increase in crystal coherence length is a product of two effects: the removal of structural defects e.g. dislocations and stacking faults, and/or an increase in grain size. Chapter 8 showed that an increased crystal coherence length measured by XRD corresponded to a larger grain size observed in SEM micrographs. Therefore, to explain the observations of Fig.9.17a) grain growth must be considered in addition to atomic diffusion. Grain growth results from the coalescence of grains [192] and is driven by the minimisation of surface energy as grains with low energy orientations consume grains with higher energy orientations [193]. This process occurs via a flattening of the grain boundaries [194] along with movement of triple boundaries [195]. The main factors influencing the rate of grain growth are [196]:

1. The movement of grain boundaries. This is a temperature dependent process with an Arrhenius-type relationship of the form: $M = M_0 exp(-E_a/(k_b T)$, where M is the rate of grain boundary movement, E_a, its activation energy and M_0 a constant.

2. Grain size. The average crystallite size is inversely proportional to the total grain boundary area and therefore the total excess surface energy of grains. In nanocrystalline material where the grain size, $L < 100$ nm (lower than a critical grain size, L_{crit}) it has been proposed that the rate limiting step is not grain boundary migration, but the movement and rearrangement of features such as triple boundaries [197] or the release of excess free volume when grain boundaries are removed [198]. However, if the grain dimensions equal the film thickness there is a ‘thin film effect’ where the lower grain boundary area and curvature inhibit the rate of grain growth.

3. The presence of solute and particles (e.g. impurities) in the film, pin the grain boundaries and eventually cause a stagnation of the grain growth [199].

4. Texture: if highly textured, the film contains a larger number of low angle boundaries which lessens the driving force for grain growth.

The simplest grain growth model considers isothermal ‘normal’ grain growth in a high purity, single phase, coarse grained polycrystalline material. Under these circumstances, the rate of grain growth has a linear relationship to the inverse grain size ($dL/dt = k_L/L$). Integrating this function gives Eq.9.23 [194].

$$L_t = (k_L t + L_o^2)^{\frac{1}{2}} \tag{9.23}$$

Where L_o and L_t are the grain sizes at the start of the experiment and at time, t, respectively. k_L is a material dependent rate constant related to the mobility of grain boundaries (M) and their curvature [196]. k_L shows an Arrhenius relationship to temperature ($k_L \propto exp(-E_L/k_bT)$) where k_b is the Boltzmann constant (k_b = 8.62 × 10^{-5} eVK^{-1}) and E_L is the activation energy of the growth process.

The thin films investigated in this work were nanocrystalline and are known to contain impurities. The rate slowing effect of these properties introduces a second term to the rate equation, the limiting grain size, L_{max}, giving $dL/dt = k_L(1/L - 1/L_{max})$ which is integrated to give equation 9.24.

$$\frac{k}{L_{max}^2}t = \frac{L_0 - L_t}{L_{max}} + \ln\left(\frac{L_{max} - L_0}{L_{max} - L_t}\right) \tag{9.24}$$

However, these equations only relate to an isothermal situation, where the sample is held at constant temperature for a time, t. In the case of laser annealing, the temperature changes as a function of time. To test the inapplicability of these equations to the transient temperature situation of laser heating, a value for k_L was determined for each point in Fig.9.17. k_L values were derived from plots of either L_t^2 against t for ‘normal’ grain growth or $(L_0 - L_t)$ against t for ‘size limited’ grain growth. Each singular absorber, along with its corresponding precursor was plotted to determine k_L. An Arrhenius plot of $\ln k_L$ against 1/T (where T is the average film temperature determined using the 2D FEM) is then plotted for each grain growth mechanism as shown in Fig.9.19.

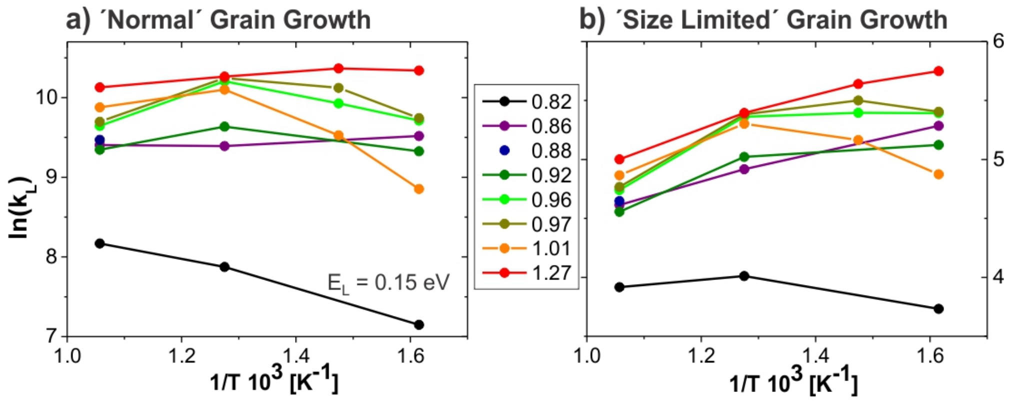

Figure 9.19: Arrhenius plot of showing $\ln k$ values determined for each absorber of Fig.9.17 using the equation for a) ‘normal’ grain growth and b) ‘size limited’ grain growth.

The unsuitability of both grain growth theories to the laser annealed samples is clearly apparent from these plots. In an Arrhenius plot, $\ln k_L$ against 1/T should give a linear plot with a gradient equal to $-E_L/k_b$. Only the absorber with Cu/In = 0.82 and using the theory of ‘normal’ grain growth (Fig.9.19a), gives a reasonable activation energy of E_L = 0.15 eV. The other composition absorbers give non-linear plots or a flat or positive gradient. Such a gradient implies $E_L \leq 0$ and whilst negative activation energies are physically possible [200], it implies a barrier-less and spontaneous process which is unreasonable in this case.

There has been very little investigation into modelling the grain growth during transient heating although Krause et al. [201] did propose a simpler relationship to fit these circumstances which is given in Eq.9.25.

$$L \propto \sqrt{\frac{D_{CISe}t^*}{T}} \tag{9.25}$$

Where t^* is an effective time, based on the time-temperature profile (e.g. Fig.9.14) and D_{CISe} is a diffusion coefficient based on the mobility of the constituent elements of the sample and thus has an Arrhenius-type temperature dependence. Due to the uncertainties involved in calculating t^* and D_{CISe}, derivation of an activation energy was not attempted using this approach.

Whilst this analysis of grain growth has not been able to derive an adequate relationship which fits to the laser annealing process, a number of conclusions can be drawn. Transient heating does not fit a 'normal' grain growth model as evidenced by the zero gradient Arrhenius plots. A 'size limited' grain growth is determined inapplicable due to the negative activation energies calculated from Fig.9.19b), and the near linear increase of grain size with time / temperature observed in Fig.9.17a). This observation suggests that the grain size would increase with longer annealing times. Therefore, within a 1 s annealing time neither a maximum grain size, where solute drag slows the grain growth rate [199], or a critical grain size, where a change in growth rate is observed due a lessening of the effects of triple boundaries [197], is reached. It is probable that the grain size is limited by a thermally activated process such as the mobility of the grain boundaries. Heating the film to higher temperatures, either using a longer dwell time or increasing the laser flux is expected to lead to a larger crystallite size assuming a sufficient background P_{Se}. Furthermore, the SEM micrographs of Section 8.3.1 showed the grain size to increase with P_{Se} evidencing that in this rapid, transient process it is the P_{Se} that is the decisive factor determining grain growth.

This analysis has shown that the crystal coherence length of laser annealed CISe absorbers increases in accordance with the precursor Cu/In ratio. A larger grain size results in a decrease in grain boundary area where recombination is possible, and therefore samples with bigger grains may exhibit improved optoelectronic properties. However, it has been noted that the presence of the $Cu_{2-x}Se$ phase is highly detrimental to cell performance. To see the impact of each of these factors the optoelectronic properties of absorbers of different composition are subsequently examined.

Optoelectronic Properties

Cu-rich films are recognised to have better electronic properties than their Cu-poor counterparts [186]. For example, Cu-poor films have a high density of donor and acceptor defects (highly compensated) which causes a spatially fluctuating electrostatic potential, and a broad range of possible recombination energies [202]. Consequently the effect of Cu/In composition should be clearly visible in the photocurrent of the absorber layers which is measured using PEC as given in Fig.9.20.

In Fig.9.20a) the photocurrent of Cu-rich and Cu-poor samples is compared. The magnitude of the dark current (current flowing without illumination) is highest in the Cu-rich sample (iii), most likely due to a high shunt conductivity arising from the presence of the $Cu_{2-x}Se$ secondary phase, which, even after KCN etching, may remain along grain boundaries. The lowest dark current is measured for the Cu-poor absorber layer (Cu/In = 0.91). The magnitude of the dark current has been suggested to correlate inversely to the final device efficiency, and Cu/In = 0.91 lies within the compositional range known to give the highest device efficiencies [146]. In con-

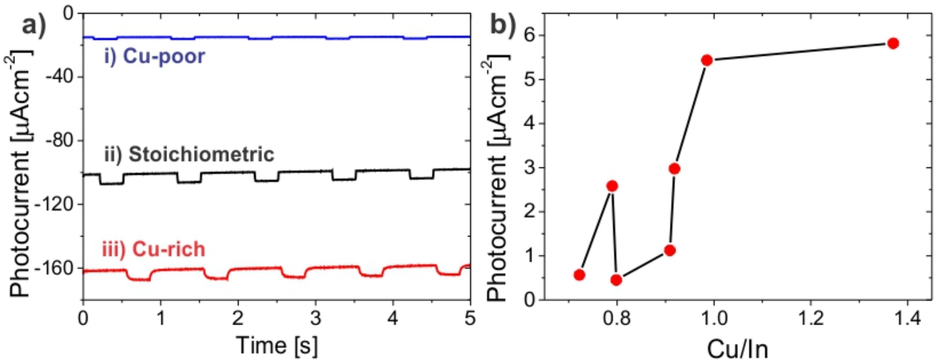

Figure 9.20: a) Photocurrent response over time of laser annealed absorber layers (150 Wcm^{-2}, 2 mms^{-1}, P_{Se} = 9 × 10^{-7} Pa) from i) Cu-poor (Cu/In = 0.91), ii) Stoichiometric (Cu/In = 0.99), iii) Cu-rich (Cu/In = 1.37) CISe codeposited precursors. Absorbers are etched for 60 s in KCN prior to measurement. b) Photocurrent response of absorber layers against the Cu/In composition of their precursor.

trast, comparing the Cu/In ratio of precursors to the photocurrent measured on their resulting absorber layers (Fig.9.20b) has the opposite trend. The two absorbers from Cu-rich precursors have at least double the photocurrent response of their Cu-poor counterparts and therefore improved generation, transportation or collection of charge carriers.

Summary

In this section the effect of a precursor's Cu/In ratio on the properties of its laser annealed absorber has been analysed. All absorber compositions showed an increasing grain size with longer annealing times / higher film temperatures. Grain growth theories were tested and found to be invalid for this transient heating situation and therefore it was not possible to derive an activation energy for each composition. In agreement with literature, more Cu-rich precursors led to absorbers with larger grain size and improved generation and transport of charge carriers when compared to those with a lower Cu-content. However, there are a number of issues that need to be addressed before Cu-rich CISe films can compete with Cu-poor films for record efficiencies. For example, the highly conductive $Cu_{2-x}Se$ secondary phase, present in all Cu-rich films, would lead to a reduction in the fill factor and efficiency of a final device if still present in the absorber layer bulk after etching.

9.5.2 The influence of Dopants

The most recent record power conversion efficiencies $> 20\ \%$ were achieved by the introduction of additional, dopant atoms into the CISe film [184][203]. This section considers the mechanisms by which Na and K may enhance the properties of CISe films and investigates what effect they have on laser annealed absorbers.

It has been suggested that Na has three effects on a CISe absorber [204]:

1. Na can replace Cu forming the stable $NaInSe_2$ compound. This has a larger band gap (1.92 eV [204]), leading to a higher achievable V_{oc}.

2. Na forms the anti-site point defect Na_{Cu}. Na_{Cu} is electrically inactive and replaces some of the V_{Cu} defects present under equilibrium conditions. Alternatively, Na_{Cu} may also replace the In_{Cu} antisite defect which can raise the hole density of the film. It has been shown experimentally that adding Na to more Cu-poor films, which contain a higher density of V_{Cu} and In_{Cu} defects, leads to a larger increase in power conversion efficiency than the addition of Na to higher Cu-content films. The passivation of these defects reduces the formation of the OVC phase, which results from clusters of ($2V^{-}_{Cu}$ In^{+2}_{Cu}).

3. Na plays a role in the quenching of the parasitic V_{Se} defects [153], which have been shown to lower cell efficiency [205][206]. In the presence of atomic oxygen the V_{Se} defect can be substituted by O_{VSe}. Na catalyses the dissociation of O_2 making atomic oxygen available at the absorber surface.

Furthermore, Na inclusion has been linked to a larger grain size and a reduction in lattice defects [207].

In the two-stage fabrication method, Na is usually incorporated into the CISe film via in-diffusion from the soda lime glass during annealing. However, measuring the surface composition of a laser annealed absorber using XPS, showed no characteristic Na peak, although this peak was clearly observed in a furnace annealed equivalent. The absence of Na in the laser absorber is possibly as a result of the lower average glass temperature during annealing and the shorter time-scales, being insufficient to promote Na in-diffusion. To gain the beneficial effects of Na inclusion in laser annealing, two different methods were tested: (1) the substitution of the LiCl electrolyte in the deposition bath with NaCl and (2) pipetting 0.1 M NaCl solution onto the sample surface. In Fig.9.21 the effect of dopant atoms on the grain size and optoelectronic properties of films is analysed.

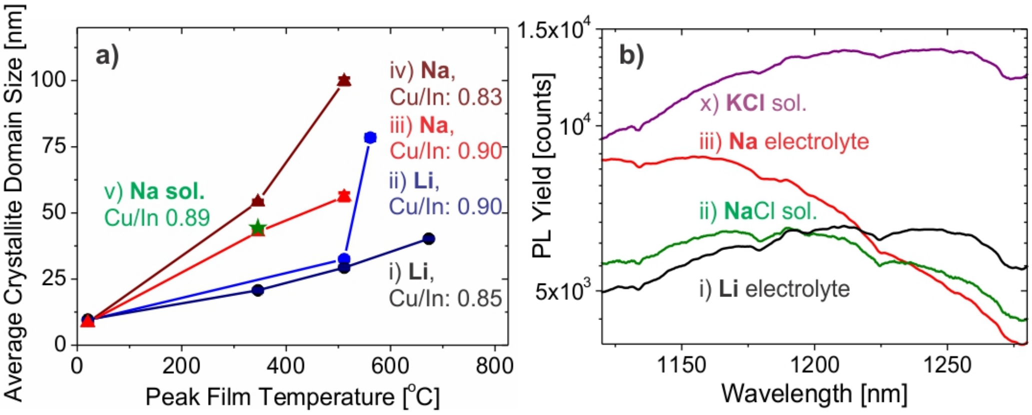

Figure 9.21: a) Crystal coherence length determined from the FWHM of the CISe 112 peak of XRD patterns of laser annealed absorber layers (150 Wcm^{-2}, 2 mms^{-1}, P_{Se} = 9 $\times$ 10^{-7} Pa) from precursors deposited in i),ii) LiCl electrolyte, iii),iv) NaCl electrolyte and v) LiCl electrolyte with 0.1 M NaCl solution added to the surface after deposition and evaporated off. Peak Film temperature was calculated using the 2D FEM. b) PL spectra of absorber layers annealed at 150 Wcm^{-2}, 2 mms^{-1}, P_{Se} = 1 $\times$ 10^{-3} Pa, from precursors with Cu/In = 0.9 deposited in (i) LiCl electrolyte and with (ii) 0.1 M NaCl and (x) 0.1 M KCl solution pipetted on and (iii) deposited in NaCl electrolyte.

Considering Fig.9.21a), the increase in the crystal coherence length with annealing time is affected by the change from LiCl to NaCl electrolyte. At both Cu/In ratios, the samples deposited in NaCl electrolyte show a larger average apparent crystallite dimension than their LiCl deposited replicates. Pipetting NaCl solution onto the surface of a LiCl deposited precursor also led an absorber with an equivalent coherence length to that deposited in NaCl electrolyte (Fig.9.21a) (star)). Furthermore, the NaCl deposited sample with the lower Cu/In ratio shows the greatest increase in crystal coherence length (from 9 - 100 nm) with 0.5 s laser annealing. This result is particularly significant considering that a sample of equivalent Cu/In ratio but deposited in LiCl electrolyte shows the least crystal growth (from 9 - 100 nm). A possible reason for a greater increase in crystal coherence length in Na deposited samples of low Cu/In composition may stem from the Na passivation of V_{Cu} and In_{Cu} defects. The formation of Na_{Cu} to replace these defects could induce less distortion and stress in the crystal lattice and furthermore restrict the presence of the $CuIn_3Se_5$ secondary phase in increasingly Cu poor samples. A second reason may be related to the higher Se content (Se/(Cu+In) = 1.12 - 1.18 in films with Cu/In = 0.85, compared to 1.05 - 1.09, when Cu/In = 0.90) which occurs as a consequence of the deposition. Na is known to form $Na_2(Se)_n$ (n = 1-6) complexes [208][207]. The bound Se is more readily available to the film during the annealing process, which may lead to larger crystals, as analysed in Section 8.3.1. Additionally, complexation of Se may reduce its vaporisation from the CISe lattice during annealing with low background P_{Se} as used in this experiment. This theory is supported by the XRD patterns of absorbers from a similar set of Li/Na-containing precursors annealed under a elevated background $P_{Se} = 1 \times 10^{-3}$ Pa between which there was no discernible difference in crystal coherence length.

To analyse how Na affects the optoelectronic performance of CISe absorber layers, a second set of samples were annealed under elevated P_{Se} (a Se atmosphere is required for measurable optoelectronic properties). Comparing the PL spectra of these samples in Fig.9.21b), there is only minimal gain in radiative recombination when Na is added during (iii) or after (ii) the precursor deposition over the Na-free absorber (i). This matches the observations detailed above where the elevated background P_{Se} ensures Se is available during the annealing of all samples, and not only those where Na is present to 'lock' the Se into $Na_2(Se)_n$ complexes. All PL spectra display a broad, ill-defined signal and it should be noted that these results relate to poor quality absorber layers (highly pinholed). One interesting result however arises from the addition of KCl solution to the surface of a LiCl deposited precursor before laser annealing. The resulting absorber is seen in Fig.9.21bx) to give a similar shape spectrum to its LiCl equivalent, but has the highest PL yield of all absorbers measured. The effect of K on CISe films is less well studied than Na, but is believed to alter the Cu depletion layer at the absorber surface, beneficially changing the p-n junction with CdS [203].

In this section the role of the precursor composition on both the crystal coherence length and PL yield of the absorber layer has been analysed. Changing the Cu/In ratio and adding Na or K to electrodeposited CISe precursors has the potential to enhance the structural and optoelectronic properties of the resulting absorbers. These studies indicate the wide parameter space available for optimising the absorber layer and thus mechanisms by which device performance may be improved.

9.6 Summary

This chapter demonstrates an increase in the understanding of the processes which take place during laser annealing. Analysis of the 1.6 % efficient device has proved the importance of annealing flux on the absorber properties. A method has been established by which to model the sample temperature during annealing, and therefore link the laser flux to the film temperature. The modelled temperatures have been related to the absorber properties including grain size, elemental composition through depth and PL yield. By analysing the temperature dependence of atomic diffusion and grain growth these results have been explained. This process showed that at temperatures exceeding 550 ^{o}C even for only 1 s, it is the rate of grain growth and not atomic diffusion which limits the structural transformation of a CISe precursor into an absorber. Finally the composition of the precursor on these processes has been analysed. This indicates that absorber properties can be enhanced by either changing the stoichiometry of the film or with the addition of dopant atoms. Combining the increased understanding of the laser annealing process demonstrated in this section should allow future work to optimise this method and lead to higher device efficiencies. With absorber, and thus device improvement, this processing method will become one stage closer to the dream of an industrial reality, as discussed in Chapter 11.

10 Conclusions

The aim of this thesis was to demonstrate a method capable of transforming electrodeposited CISe precursors into absorber layers suitable for device fabrication using a rapid laser annealing process.

The following route has been taken to achieve this aim.

- Chapter 6 fabricated the precursors and investigated their composition and crystallinity.
- Chapter 7 then considered the laser interaction with each precursor both theoretically and experimentally.
- Chapter 8 was able to turn this absorber into a device by minimising the loss of volatile Se during annealing.
- Finally Chapter 9 looked to understand and optimise this process.

The final device efficiency achieved using this process was 1.6 %. This represents the first reported efficiency using this fabrication route and was achieved using only a 1 s dwell time on CISe thin films deposited using a low energy expenditure method. However, it is recognised that this value needs to be significantly improved in order to validate this as a new CISe absorber fabrication route. The value of this work is in the knowledge that has been gained, which would provide a strong basis for future research as well as being applicable to the wider field of rapid annealing of volatile materials. These learning points are subsequently detailed.

Process Development

The first step in developing an electrodeposition-laser annealing process was to establish a suitable CISe precursor. The phases present, morphology and optical properties of elemental layers, binary selenides and co-deposited precursors were analysed. Comparing the absorption profile of the laser energy within each of these precursor types to the experimental results showed that the co-deposited precursor was best fitted to this method due to the even distribution of energy through the full depth of the CISe film. The low density $Cu_{2-x}Se$ layer of the binary selenide precursors leads to poor thermal conductivity through the film. Elemental stacks show strong absorption by the In metal, and while heat is easily transported to the Cu and Se layers, there is no mechanism to prevent the loss of volatile Se (a point which is reconsidered in Section 11.1.3). The volatility of Se is an important consideration for all CISe annealing routes and this work demonstrates its importance even with annealing times of $<$ 1 s. The thermodynamic equilibrium reactions which govern the breakdown of the CISe lattice to release Se are made energetically unfavourable with a sufficient background partial pressure of Se, P_{Se}. An elevated P_{Se} during the laser annealing of co-deposited CISe precursors led to enhanced grain size, Se content and PL yield in absorbers. The importance of sufficient Se activity is proven by producing the first device from electrodeposition-laser annealing which gave 1.6 % conversion efficiency only when there was an elevated background P_{Se}.

Therefore the key findings of the process development are:

1. The laser wavelength must be matched to the precursor and the annealing objective. For example, 248 - 532 nm lasers penetrate only the surface 50 - 100 nm of CISe films.

Consequently, it is difficult to stimulate long range diffusion in layers exceeding this thickness without a liquid-phase intermediate stage.

2. Laser annealing with short pulse times or using a raster process induces rapid heating and cooling of the CISe film and means that thermodynamic equilibrium is not reached. Therefore, energy absorption profiles, which indicate the instantaneous heat generation by a sample stack, are useful predictive tools for predicting the effectiveness of an annealing method.
3. The thermodynamic equilibrium reactions of materials containing volatile elements are an important consideration when operating under elevated temperature. Even on the timescale of seconds, the loss of such elements can be significant enough to impact on the properties and thus performance of a compound semiconductor. The requirement of supplying a background atmosphere constituted of the gaseous products of a material's equilibria reactions is applicable to any field aiming to incorporate a rapid annealing process in the production of a compound containing a volatile element.
4. Further to **3.**, the properties of a CISe absorber, including grain size and optoelectronic performance correlate to partial pressure of gaseous chalcogen. This work indicates that higher partial pressures of volatile chalcogenide species during annealing may augment the properties of future absorbers from this process.

Process Understanding

In order to explain the low device efficiency, this work looks to gain an understanding of the laser annealing process and the material changes which occur. The temperature of the CISe film during laser processing was modelled. The Gaussian nature and scanning motion of the laser beam result in variations in the incident flux across the CISe sample and lead to fluctuations in peak film temperature. The spatially inhomogeneous performance of the device from a laser annealed absorber is linked to this changing peak film temperature which leads to different rates of grain growth and atomic diffusion and thus affects the PL yield per unit area. The thermal dependence of atomic diffusion and grain growth is investigated, reinforcing these findings. Both Se and In have low mobilities and are deduced to restrict the homogenisation of the CISe film composition through its depth, within 1 s and below 550 ^{o}C. Above this temperature, grain growth is assumed to be the process constraining the increase in crystal coherence length. However, as laser annealing is a transient technique, with interdependent temperature and time, it does not fit to standard grain growth models. Finally, the effect of precursor composition is analysed. Higher Cu/In ratios lead to increased crystal coherence lengths in laser annealed absorbers due to the high mobility of the Cu ion and the increased absorption of the laser energy in Cu-rich films. However, the structural and optoelectronic improvements must be balanced against the negative effects of a Cu-rich composition. There is also preliminary indication that the addition of the dopants Na and K enhance the coherence length and PL yield measured in an absorber.

Therefore the key findings of the process optimisation are:

5. Finite Element Modelling gives verifiable predictions of the film temperature during laser annealing. For example, annealing CISe films with a Gaussian laser beam of average flux 150 Wcm^{-2} and a dwell time of 1 s gives a peak film temperature of $\approx$ 900 ^{o}C in the area of film irradiated by the Gaussian beam centre.
6. There is a direct correlation between the laser flux and sample temperature. Variations in lateral flux on the sample, for example caused by the Gaussian power distribution of the

laser beam, lead to deviations in peak temperature across the film. Over the approximate 2 mm width of the beam, the peak film temperature was modelled to vary by $\approx 400\ ^{o}$C.

7. Variations in the film temperature lead to different rates of atomic diffusion and grain growth across the film. Hence an absorber annealed by a laser beam with inhomogeneous flux shows variations in optoelectronic properties. These fluctuations are translated into a loss of performance in a final device.
8. Higher film temperatures drive thermodynamic equilibria reactions towards the evolution of volatile species. The background activity of the volatile element must be adjusted in accordance with the peak film temperature in order to make decomposition unfavourable.
9. The rates of grain growth and atomic diffusion are affected by the film composition, including the addition of alkali metals. The enhancement of structural properties must be balanced against the optoelectronic performance of an absorber.

To summarise, a method has been developed which enables an electrodeposited precursor to be transformed into an absorber layer suitable to be completed into a working device. Clear objectives for future research are identified as:

i.) Homogenisation of laser flux and film temperature.
ii.) Improvement to the CISe precursor.

These recommendations are examined in Chapter 11.

11 A future for the laser annealing of $CuInSe_2$?

Whilst the objective of this project was to increase the fundamental understanding of laser annealing, there was a final dream that one day this knowledge could be used to guide improvements in photovoltaic manufacturing by providing a rapid, lower cost and readily up-scalable process. The previous sections considered the development and optimisation of a method to laser anneal CISe films, both in terms of material synthesis and laser processing, which was able to produce a preliminary device. In order to create a viable new fabrication technique, clearly device efficiency must be enhanced. This chapter firstly considers promising research routes by which to achieve this goal. Subsequently the industrial up-scaling of this process is envisaged, considering the method, infrastructure and costs involved.

11.1 Future Recommendations

In order to develop a new process a wide variety of experiments were carried out in the course of the research presented here. Due to time constraints, a number of promising preliminary results were not able to be pursued sufficiently. Chapter 9 highlighted that device efficiency was constrained by both the material quality and aberrations in the laser beam power. This section explores the route by which both these parameters may be ameliorated. Firstly, the introduction of Ga is investigated, followed by the homogenisation of the laser beam, and finally how laser annealing of the Cu/In/Se precursor can be successfully achieved.

11.1.1 Alloying with Ga: $Cu(In,Ga)Se_2$

One possible route to higher efficiencies is by replacing a portion of the In atoms in the CISe lattice with Ga, forming the solid state alloy $CuIn_yGa_{1-y}Se_2$ (CIGSe). Adjusting y between $0 \leq y \leq 1$ tunes the band gap energy from $\sim$ 1.68 - 1.00 eV [169][191][209], as shown in Fig.11.1a). An increased band gap permits a higher maximum V_{oc}. However, a material with a larger band gap absorbs a lower proportion of the incident spectral irradiation. The balance of these effects gives the graph of limiting efficiency of a p/n junction as shown in Fig.11.1b). A maximum efficiency value is reached at two band gap energies; 33 % at 1.35 eV and 32.8 % at 1.15 eV, linking to compositions of $CuIn_{0.48}Ga_{0.52}Se_2$ and $CuIn_{0.7}Ga_{0.3}Se_2$. As absorber layers with composition $CuIn_{0.7}Ga_{0.3}Se_2$ have been fabricated into devices giving the highest power conversion efficiencies [184], this is the target stoichiometry of much research. A second important research focus is on grading the Ga/In composition through the film, known as ‘band gap engineering’. By careful positioning of the regions of low and high Ga-content, the device may benefit from the dual advantages of improved spectral absorption (from a low band gap material) and voltage (from a high band gap material). Furthermore, by having a high band gap material at the film surface and a bulk composition closer to CISe, it is possible to build in electrostatic fields to improve carrier collection [210]. This section briefly examines the potential of using CIGSe in the electrodeposition-laser annealing technique and the band gap grading within these films.

1 μm thick CIGSe precursors were formed using the co-electrodeposition method given in appendix 12.8 to give films with Cu/(In+Ga) = 0.85 - 0.92 and Ga/(Ga+In) = 0.25 - 0.34 (EDX). The XRD patterns measured on laser annealed CIGSe absorbers are given in Fig.11.1c).

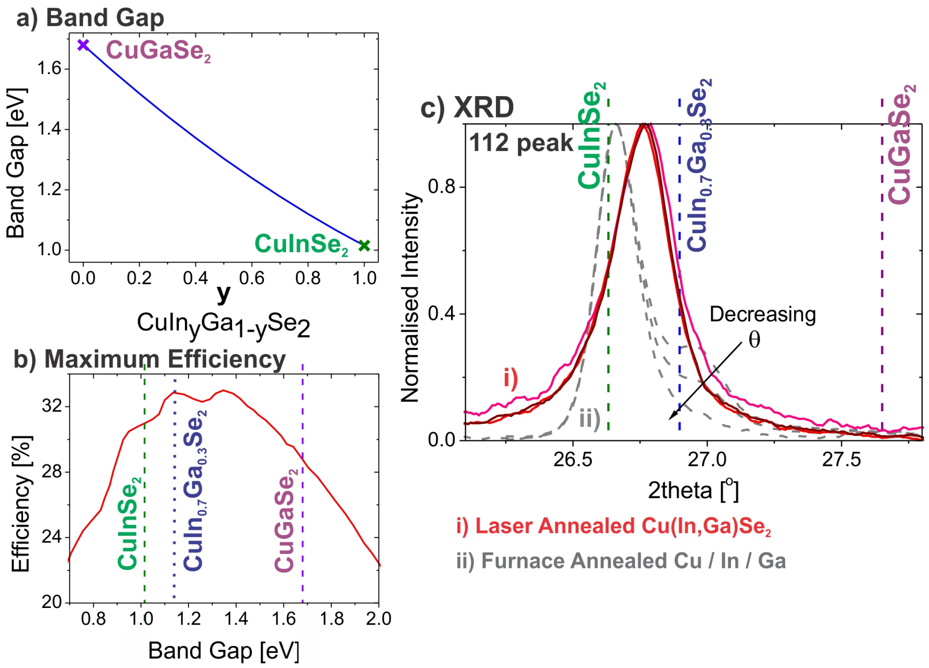

Figure 11.1: a) Band gap of Cu(In,Ga)Se$_2$ as a function of Group III metal composition [210]. b) Maximum efficiency (Schockley-Quiesser limit) for a p/n junction, illuminated by AM1.5 spectrum, as a function of semiconductor band gap [105]. c) GIXRD patterns focusing on the 2θ range around the CISe 112 peak, of i) a coelectrodeposited Cu(In,Ga)Se$_2$ precursor laser annealed at 150 Wcm^{-2}, 2 mms^{-1}, P$_{Se}$ = 9 x 10^{-7} Pa and ii) electrodeposited Cu/Ga/In layered precursor [211] RTP annealed at 250 ^{o}C, 2 min, 550 ^{o}C, 3 min with 100 mg Se at 100 mbar N$_2$H$_2$ atm. Diffractograms with θ = 1 - 3 ^{o} are presented and 2θ angles for the 112 peak of the main chalcopyrite phases are labelled.

Whilst in Cu-poor CISe, the excess In occupies In$_{Cu}$ anti-sites, in Cu-poor CIGSe, In$_i$ and Ga$_i$ interstitial defects are formed [212][213][214]. The unit cell parameters of CIGSe, and thus d-spacing, are smaller than for CISe, consequently shifting the XRD peaks of the chalcopyrite phase to higher 2θ values. This shift is observed in Fig.11.1ci); diffractograms of laser annealed CIGSe display a 112 peak at 27.8 ^{o}2θ, shifted from the position of CISe (26.7 ^{o}2θ). From the peak position, the film composition is determined to be CuIn$_{0.85}$Ga$_{0.15}$Se$_2$ (JCPDS card file: 00-061-0076). This composition lies below the Ga/(Ga+In) = 0.3 measured on the precursor and indicates the difficulties in determining the composition of the depth-inhomogeneous co-electrodeposited precursor. Furthermore, measuring GIXRD patterns at incident angles: θ = 1 - 3 ^{o}, gives a compositional depth profile of the film (see Section 5.1.2). For the laser annealed sample (Fig.11.1ci) the peak shape and position is independent of the incident angle and therefore the film is single phase through its depth. This is compared to diffractograms measured on an absorber formed from stacked layers of Cu/Ga/In and RTP annealed (Fig.11.1cii). The main peak observed in the diffractogram of this absorber layer corresponds to the position of CISe, but there is a shoulder to this peak at higher 2θ angles, the relative intensity of which varies with the incident angle, θ. At $\theta = 1^o$ the x-rays have the lowest penetration depth and therefore the measurement is surface sensitive and this leads to a single peak at 26.7^o 2θ, whereas when $\theta = 3^o$ there is a contribution from the full film depth and the shoulder is most pronounced. From this measurement, it is determined that there is segregation of a Ga-rich phase to the back of the film. While neither the laser or furnace annealed sample show an ideal Ga grading, the laser absorber will have a slightly larger band gap in the SCR and therefore introduction of Ga has the potential of raising the V_{oc} in this absorber layer.

Future investigations are recommended to test the optoelectronic properties of CIGSe, forming devices in order to quantify the benefit of Ga inclusion on V_{oc}. For an optimal gain in V_{oc} the Ga distribution through the film depth must be controlled. Ideas to achieve this include: (1) A multi-stage electrodeposition, either by using stacked elemental layers (Cu/In/Ga or Cu/Ga/In) or modifying the co-deposition bath. (2) Adapting the annealing process to promote favourable Ga diffusion.

11.1.2 Linearisation of the Laser Beam

To reduce the variation in beam flux reaching the sample, a linearising lens was used to elongate the beam along a single axis. After this beam is passed through a 7 mm x 1 mm aperture, it has a profile as pictured in Figure 11.2a).

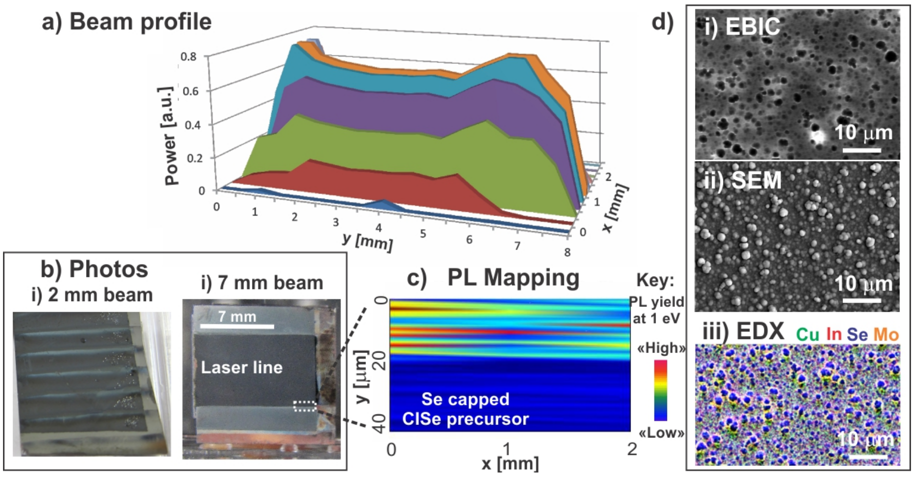

Figure 11.2: a) Measured power profile of the beam at the sample surface. b) Photos of Se capped CISe precursors after laser annealing with i) the 2 mm beam, rastered over the whole sample (150 Wcm^{-2}, 2 mms^{-1}, P_{Se} = 1 x 10^{-3}), ii) a single pass of the 7 mm laser beam (140 Wcm^{-2}, 2 mms^{-1}, P_{Se} = 1 x 10^{-3}). c) PL mapping of the edge of the beam line of bii). Colours indicate the relative PL yield at 1 eV. di) EBIC image, ii) SEM micrograph and iii) EDX mapping of laser annealed absorber.

The peak power of the beam is seen in Fig.11.2a) to deviate by < 20 % over its ≈ 7 mm length. The higher power measured at $y \approx 1$ mm and $y \approx 7$ mm results from an edge effect of the aperture. The beam has a Gaussian shape in the x (scanning) direction. Laser annealing

CISe precursors with this beam, compared to the 2 mm beam with Gaussian distribution, results in samples with a surface appearance as shown in Fig.11.2b). The absorber annealed with the 2 mm beam (bi) has a striped appearance with pale lines relating to remnants of the Se capped precursor. These indicate that in some areas the laser irradiation is insufficient even to evaporate the Se cap. Annealing with such a power distribution leads to inhomogeneous material properties within each line, as demonstrated Section 9.1, making it difficult to fabricate a working device. In contrast, after annealing with the 7 mm beam (bii), a dark line of constant 7 mm width and homogeneous colouration is observed. Mapping the PL signal over the border between precursor and absorber areas (shown in Fig.11.2c) demonstrates the effect annealing with this beam has on the sample's optoelectronic properties. The PL yield at 1 eV over the Se capped precursor area is reasonably constant and lower than in the laser annealed part. However, the PL yield within the annealed area, even over the mapped 0.02 x 2 mm region, is inhomogeneous, with variations in the PL yield from 6500 counts down to 1700 counts (close to the maximum of 1300 counts measured in the precursor area). As the spatial fluctuations in PL yield appear to be random, they are assumed to relate to variations in the precursor properties. This is supported by Electron Beam-Induced Current (EBIC) measurements (made by Laurent Lombez, IRDEP) of the annealed area (Fig.11.2di) where the photo-generated current has photo-inactive areas (black) which correspond to the granular surface appearance of codeposited samples (ii). The differences in current generation between grains is explained by EDX mapping (iii) which indicates spatial variation in the film composition. In particular, the pale surface grains observed in the SEM micrograph (ii) do not relate to CISe, due to their low Cu and In content, which explains their photo-inactivity. All co-deposited CISe films have a similar appearance, and thus this analysis gives evidence of the intrinsic inhomogeneity of these precursors and emphasises the necessity to consider alternative sample types in future studies.

11.1.3 Cu/In/Se

Having identified these issues a more suitable precursor type must be identified. Chapter 6 explained the choice of the codeposited precursor from the three different precursor types due it having the most favourable energy distribution through the full film thickness. Whilst the instantaneous heat generation in Cu/In/Se layered precursors was focused in the In layer the high conductivity of the metals will to lead to an isothermal temperature profile through the stack. The constraining factor was identified as the loss of volatile Se at the elevated annealing temperatures. There are two main advantages in this precursor type over the co-deposited. Firstly, it is easier to uniformly deposit Cu and In layers over large areas than the Cu-In-Se alloy. Secondly, formation of CISe from its elemental constituents gives a larger gain in free energy of CISe formation: $\Delta G^0_{f,298K}$ = - 201 kJmol^{-1} [150], than if the semiconductor is, at least partially, formed during the deposition. This gain in energy is expected to result in larger grained absorber layers and the potential for higher efficiencies.

In order to successfully transform Cu/In/Se precursors into CISe absorber layers by laser annealing, two important parameters must be considered. Firstly, their layered structure demands atomic diffusion through the whole film depth. Section 9.4, highlighted that the rate of atomic arrangement is limited by the low mobility of In and Se, with temperatures > 550 ^{o}C required for In to diffuse a length of 200 nm in 1 s. To evenly disperse these elements over the full 1 μm film thickness, requires diffusion lengths of $\approx$ 500 nm. This may be achieved using higher temperatures (> 650 ^{o}C, for 1 s), or annealing times > 1 s. Secondly, Se forms the top layer of the stack and has T_{vap}(Se) = 685 ^{o}C [139]. Thus care must be taken to ensure Se remains available to the sample during annealing. Consequently, for laser processing Cu/In/Se precursors, the FTO window was heated to 125 ^{o}C, ensuring vaporised Se forms a Se atmosphere above the sample, with $P_{Se} \approx 1 \text{ x } 10^{-3}$ Pa. The laser flux was lowered to 125 Wcm^{-2} and the beam rastered across the sample twice at 1 mms^{-1}, increasing the annealing time whilst keeping the FEM calculated $T_{CISe} \leq 600$ ^{o}C, thus below T_{vap}(Se). XRD patterns of the precursor and double annealed absorber are presented, along with the SEM cross sectional appearance, in Fig.11.3.

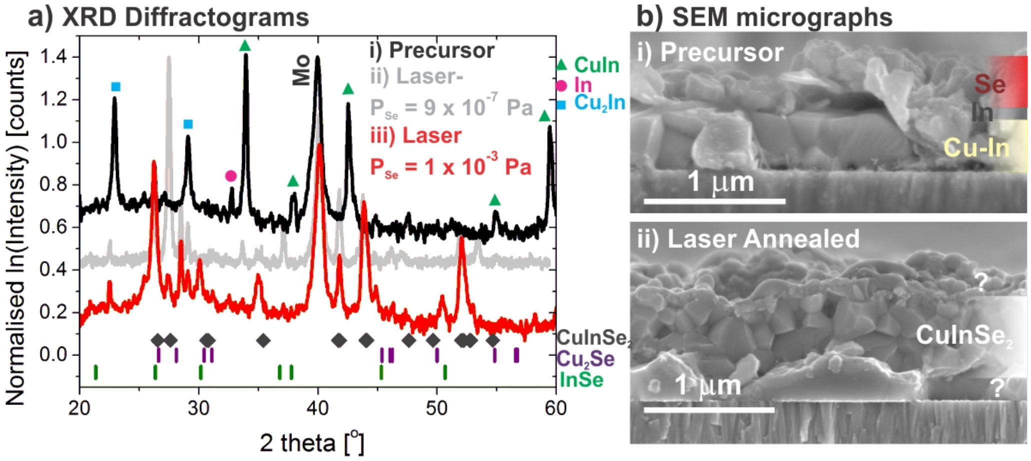

Figure 11.3: a) XRD patterns of i) Cu/In/Se stacked precursor and after annealing at ii) 150 Wcm^{-2}, 2 mms^{-1} (2 x 2 mm beam area), P_{Se} = 9 x 10^{-7} Pa and iii) 125 Wcm^{-2}, 1 mms^{-1} (7 x 1 mm beam area), P_{Se} = 1 x 10^{-3} Pa, twice. The Bragg-peaks corresponding to the main phases present in each sample are indicated. b) SEM cross sectional micrograph of i) Cu/In/Se precursor, and after KCN etching (5 wt %, 60 s) sample aiii).

In the diffractograms of Fig.11.3ai) the precursor is seen to consist of Cu-In alloy phases, as well as a small quantity of elemental In. These phases, along with the known stacking order, is used to assign the layers observed in the SEM micrograph of bi). After laser annealing with an elevated P_{Se}, the XRD pattern (Fig.11.3aiii) exhibits the low intensity Bragg-peaks characteristic to the chalcopyrite phase i.e. 103 (2θ = 27.6^{o}) and 221 (2θ = 35.4^{o}: JCPDS card file: 04-013-0152). Whilst peaks relating to CISe show the highest intensity in this diffractogram, there are a number of additional peaks relating to the binary selenides, Cu_2Se and InSe, indicating that the reaction has not fully reached completion. Additionally there are minimal quantities of the Cu_2In alloy phase remaining from the precursor. However, comparing Fig.11.3aiii) to the diffractogram of the absorber annealed under a lower P_{Se} (Fig.11.3aii), where the binary phases dominate the spectrum, the importance of an elevated P_{Se} during annealing these precursors is apparent. The potential of this precursor type is determined from the SEM cross sectional micrograph presented in Fig.11.3bii). The body of the film is composed of crystallites with dimensions 100-500 nm, larger than those observed after annealing co-deposited samples (see Fig.8.4cii). However, the secondary phases are observed as a thin, nanocrystalline surface layer and the > 1 μm diameter amorphous globules at the Mo interface, which future work would need to address.

11.1.4 Further ideas

Section 9.5.2 indicated the potential to improve the properties of a CISe film with the introduction of Na and K. Doping of CIGSe has become particularly of interest after Tiwari *et al.* achieved a record device efficiency after utilising Na and K treatment steps [203]. Consequently it is hypothesised that steps to incorporate Na and K will be integrated into future production lines. In ref.[203], K and Na form a post deposition treatment to the co-evaporated, crystalline CIGSe. To achieve a similar result in a non-vacuum or roll-to-roll production process would require two annealing steps: absorber layer formation and selenisation with dopant atoms. A representation of the inclusion of this step into a roll-to-roll production line is illustrated in Fig.11.4. To test the viability of this idea, further research must optimise the laser processing conditions of each step and the dopant inclusion to the film. Both carrying out a deposition with NaCl electrolyte and pipetting KCl and NaCl solution onto the CISe precursor gave interesting preliminary results, however, the solution based surface treatment may be more facile for controlling dopant concentrations.

For a roll-to-roll production line as shown in Fig.11.4 and novel applications in portable electronics and building design [203], the thin film solar cells are fabricated onto a flexible substrate such as polyimide or stainless steel. To test the feasibility of the electrodeposition-laser annealing process on flexible substrates, CISe was co-electrodeposited on stainless steel (500 μm)/Mo (400 nm) substrates and laser annealed at 150 Wcm^{-2}, 2 mms^{-1}, P$_{Se}$ = 9 x 10^{-7} Pa. Whilst the electrodeposited precursor had the same composition and morphology as those deposited on Mo/glass substrates, the laser annealing resulted in diffusion of Fe from the steel into the CISe film, a phenomena known to deteriorate device performance [215]. Furthermore, XRD indicated that the same laser annealing conditions gave a much lower crystallinity on steel than on glass substrates. This is proposed to be due to the high thermal conductivity of the steel, which quickly conducts heat away from the CISe film, compared to the insulating, and thicker, glass substrate.

To summarise this section, there are a number of promising routes which future research could take in order to improve absorber quality. With a mechanism to minimise Se loss, the potential of Cu/In/Se layers is realised, forming highly crystalline absorber layers. The properties of these layers can be further enhanced by addition of Ga and the dopant atoms Na and K, although their concentration and location within the film must be controlled. Finally annealing precursors with an elongated beam with marginal flux variation along its length is expected to minimise temperature gradients and thus spatial variations in absorber properties, as well as reducing processing times, making this method more appealing industrially. In Section 11.2 this industrial scale-up is envisaged.

11.2 Scaling up the Laser Annealing Process

If one is to dream of a future fabrication method of CIGSe solar cells it could take the form of Fig.11.4. The first step (a) is a rapid electroplating of the precursor film onto an Mo-coated flexible substrate. For example ref.[216] demonstrates a < 4 s electrodeposition method. The manufacturer Solopower authenticates the applicability of a large-scale, robust and repeatable electrodeposition process by plating CIGSe films on 13.5” wide, 400 ft long, foil substrates with < 10 % variation in composition and thickness [217]. Following precursor deposition, the film

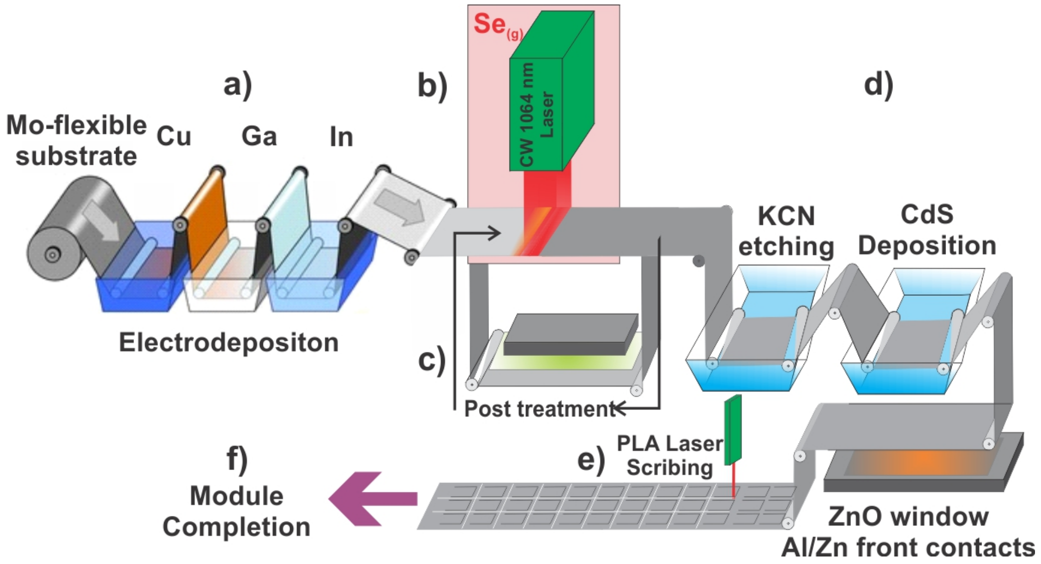

Figure 11.4: Illustration of how a CW laser annealing step could be incorporated into a roll-to-roll production line for solar cell fabrication. Electrodeposition image courtesy of J. Scragg.

passes under a CW 1064 nm laser beam (b) where a Se-rich atmosphere is created using H_2Se gas. This laser processing step allows for a continuation of the roll-to-roll production line, more facilely than current furnace techniques. The laser beam diameter would be elongated to equal the width of the substrate (e.g. 13.5”) to impart a homogeneous power density. The samples of this work were achieved using a 6 W laser, which, when operating at maximum power could give a homogeneous beam width of up to 10 mm x 1 mm (with 150 $\mathrm{Wcm^{-2}}$ flux). Therefore to achieve a beam the width of the 13.5” substrate, the power of the laser would need to be quadrupled; a requirement far below that of, for example, $>$ 100 W industrial lasers [218]. With the additional power, the beam area on the sample could be increased. For example, a beam area of 40 x 4 mm is possible with a 100 W laser. Section 9.3 substantiated a 0.05 $\mathrm{ms^{-1}}$ scan rate with a 1 s dwell time and therefore, with the larger beam, 0.2 $\mathrm{ms^{-1}}$ is feasible. For K/Na incorporation (c), a second laser process would follow post-treatment steps [203]. This optimal absorber layer is then immediately passed through chemical baths (d) containing the etchants and buffer layer, and potentially chemical-based depositions of the window layer, anti-reflective coating and even ink-jet printed front contacts [219]. Finally, the scribing of the completed stack (e) is achieved using a rapid pulse laser. Laser scribing is already favoured for thin film solar cell manufacturing [220] due to its high precision and minimal material loss, *e.g.* laser ablation of a 20 - 50 μm wide path at 2 - 16 $\mathrm{ms^{-1}}$ [221][222]. Finally (f) the cells are strung and encapsulated into modules ready for sale. Hence a fully roll-to-roll process is maintained from end-to-end of the production line, greatly improving productivity.

11.2.1 Costing on the Lab Scale

In order to realise this dream of incorporating laser annealing into the high speed production line of the future, its benefits, compared to currently used industrial processes need to be clearly identified. For its adoption a financial advantage must be demonstrated. In order to quantify the value of replacing furnace with laser annealing, a costing exercise is carried out considering the

(1) infrastructure, (2) time and (3) energy costs associated with the laboratory-scale equipment used in this thesis. Whilst this situation clearly lies far from how such processes are carried out industrially, it gives a simple and reliable basis from which to discuss an commercial scale-up.

1. Hardware Even on a laboratory scale, neither furnace or laser systems can be easily purchased 'off the shelf'. Quotes of $\approx$ €20 000 were given for both a brand new laboratory furnace (Carbolite) and laser (Coherent). Industrially, a uncustomised 1 kW CO_2 laser, such as that used in ref.[220], cost €150 000 - €200 000. Industrial furnaces, are slightly cheaper at €70 000 - €110 000 [223] with power ratings from 15 - 85 kW. An advantage of industrial lasers is that, whilst similar lifetimes of $\approx$ 100 000 hrs [224][225] are quoted for both systems, the maintenance of a furnace more difficult, requiring full process shut down in order to replace the internal cladding. This causes a significant loss in productivity, compared to a relatively quick and easy tube replacement for a laser.

2. Speed The previous sections have demonstrated the rapid annealing times achievable using a laser. To give a quantitative comparison to a furnace process the heating profile of ref.[29] is considered. Whilst 300 mins represents an upper bound on annealing process times, the slow ramping and cooling will be common to all indirect heating techniques. The graphite box sample chamber has a capacity limited to two samples. To laser anneal one sample, using a w = 1.8 mm beam scanning at 2 mms^{-1} with a 1.8 mm vertical step requires 240 s. In order to create a P_{Se} the FTO window is heated prior to annealing, adding 180 s to the annealing time. The 14 min total process time for two samples represents just 5 % of that required for furnace processing. Furthermore, repeating these calculations for the 7 mm width laser beam reduces the annealing time/sample to 60 s and total, 2 sample process time to 8 mins (including FTO heating). This represents $<$ 3 % of the furnace annealing time and is approbative even when compared to RTP processes, which typically require $\approx$ 30 mins including rapid heating and cooling. These numbers give quantitative evidence of this process' potential in industry where it would represent a significant increase of throughput in a roll-to-roll production line.

3. Energy The annealing times of (2) are used to calculate the energy usage of each process. The furnace has a power rating of 3 kW. The power supplied to the elements is modulated meaning that the furnace only draws the maximum power during the fastest heating ramps and a feedback system reduces the power once the specified temperature is reached. Considering the heating profile of ref.[29], it is assumed the maximum power is drawn only during the 20.7 $^oCs^{-1}$ ramp, with both maintaining 550 ^{o}C and the slow heat to 100 ^{o}C requiring only 1/3 of the rated power. There is no assisted cooling mechanism signifying that no energy is expended during the cool-down. Using these assumptions, the annealing of two samples uses 8.3 MJ. The laser unit, including its integrated cooling system, has a power rating of 6 kW which is unmodulated. Therefore, the 14 mins taken to anneal two samples consumes 5.0 MJ, 2/3 of the energy required by the furnace. Considering an industrial energy price of 0.1 €/kWh [226], annealing two samples with a furnace costs €0.23, compared to €0.14 with the laser: a saving of nearly 5 cents/sample.

This analysis has detailed the financial benefit in switching from a furnace to a laser annealing system. Whilst initial set up costs of a laser may be slightly greater, significant savings are possible due to their easy maintenance and higher productivity in accordance with reduced annealing times.

11.3 Summary

In this section a potential future for the laser annealing process has been presented, both in research and in an industrial scale-up. In order to achieve the efficiencies required to make this process viable, future work is recommended to investigate the absorber layer fabrication, by using stacked elemental layers, improving the Ga, K and Na incorporation and also to expand the laser beam area. By presenting a future roll-to-roll production line and discussing the feasibilities of each step using real-life examples, this analysis hopes to purport the benefit of this technique to industry.

Bibliography

[1] Eurobarometer. Special Barometer 365 - EB75.2 Attitudes of European citizens towards the environment. *available online at http://ec.europa.eu/environment/pdf/EB_PresentationEB752.pdf*, May 2011. 13

[2] Worldometers. Real time world statistics. World population clock: 7 billion people. *available online at http://www.worldometers.info/world-population/*, 2013. 13

[3] Energy Information Administration (US). *International Energy Outlook 2013 With Projections to 2040*. Government Printing Office, 2013. 13

[4] bp.com/statisticalreview. BP statistical review of world energy 2013. *available online at bp.com/statisticalreview*, June 2013. 13

[5] ipcc Intergovernmental Panel on Climate Change. Climate change 2013. the physical science basis, summary for policy makers. Technical report, IPCC Intergovernmental Panel on Climate Change, October 2013. 13

[6] J. Tsao, N. Lewis, and G. Crabtree. Solar FAQs. *US department of Energy*, 2006. 13

[7] M. J. de Wild-Scholten. Energy payback time and carbon footprint of commercial photovoltaic systems. *Solar Energy Materials and Solar Cells*, 119:296–305, 2013. 13

[8] EPIA European Photovoltaic Industry Association. Global market outlook for photovoltaics 2013 - 2017. Technical report, EPIA, 2013. 13

[9] solarbuzz. PV equipment quarterly. a guide to solar cell manufacturing and equipment trends. *available online at: http://www.solarbuzz.com/reports/pv-equipment-quarterly*, 2013. 14

[10] O. Madelung. *Numerical data and functional relationships in science and technology Group III: Crystal and solid state physics*, volume III/41. Springer, Berlin-Heidelberg, 2000. 14

[11] ZSW. ZSW sets 21.7 % CIGS cell record. *available online at http://www.pv-tech.org/news/zsw_sets_21.7_cigs_cell_record*, 2014. 14, 15

[12] M. A. Green, K. Emery, Y. Hishikawa, W. Warta, and E. D. Dunlop. Solar cell efficiency tables (version 41): Solar cell efficiency tables. *Progress in Photovoltaics: Research and Applications*, 21(1):1–11, January 2013. 14

[13] S. Wiedeman, J. Kessler, L. Russell, J. Fogleboch, S. Skibo, and R. Arya. Progress in thin film CIGS modules. *AIP Conference Proceedings*, 394:133–142, 1997. 14

[14] U. Rau, K. Taretto, and S. Siebentritt. Grain boundaries in Cu(In,Ga)(Se,S)$_2$ thin-film solar cells. *Applied Physics A*, 96(1):221–234, 2008. 14

[15] H.-W. Scheer, R.; Schock. *Chalcogenide Photovoltaics*. Wiley-VCH Verlag GmbH & Co., 2011. 14, 74

[16] E. Wallin, U. Malm, T. Jarmar, O. Lundberg M. Edoff, and L. Stolt. World-record Cu(In,Ga)Se$_2$-based thin-film sub-module with 17.4% efficiency. *Progress in Photovoltaics: Research and Applications*, 20(7):851–854, 2012. 15

[17] Solar Frontier Press Release. Solar frontier sets new efficiency world record. *Available online at http://www.solar-frontier.com/eng/news/2012/C002980.html*, 2012. 15

[18] V. K. Kapur, A. Bansal, P. Le, and O. I. Asensio. Non-vacuum processing of CuIn$_{1-x}$Ga$_x$Se$_2$ solar cells on rigid and flexible substrates using nanoparticle precursor inks. *Thin Solid Films*, 431-432:53–57, 2003. 15

[19] Solopower. SoloPower sets 13.4% flex CIGS aperture efficiency record backed by NREL - PV-Tech. *available online at http://www.pv-tech.org/news/solopower_sets_13.4_flex_cigs_aperture_efficiency_record_backed_by_nrel*, 2013. 15

[20] Solar Frontier. Solar frontier sets thin-film PV world record with 20.9% cis cell. *available online at http://www.solar-frontier.com/eng/news/2014/C031367.html*, 2014. 15

[21] NREL. CIGS-based solar cells prepared from electrodeposited precursor films. *NREL highlights. Available online at: http://www.nrel.gov/docs/fy11osti/51752.pdf*, 2011. 15

[22] R. N. Bhattacharya, M.-K. Oh, and Y. Kim. CIGS-based solar cells prepared from electrodeposited precursor films. *Solar Energy Materials and Solar Cells*, 98:198–202, 2012. 15

[23] B. M. Basol, M. Pinarbasi, S. Aksu, J. Freitag, P. Gonzalez, T. Johnson, Y. Matus, B. Metin, M. Narasimhan, D. Nayak, G. Norsworthy, D. Soltz, J. Wang, T. Wang, and H. Zolla. Status of electroplating based CIGS technology development. In *Photovoltaic Specialists Conference (PVSC), 2009 34th IEEE*, pages 002310–002315, 2009. 15

[24] V Bermudez. NEXCIS CIGS technology: from R&D to industry. *4th International Workshop on CIGS Solar Cell Technology*, 2013. Conference talk, unpublished. 16

[25] J. Fischer. *CuInSe$_2$ Thin Film Solar Cells Synthesised From Electrodeposited Binary Selenide Precursors*. PhD thesis, Université du Luxembourg, Luxembourg, 2013. 16, 47, 48, 146

[26] J. Fischer, J. K. Larsen, J. Guillot, Y. Aida, T. Eisenbarth, D. Regesch, V. Depredurand, N. Fevre, S. Siebentritt, and P. J. Dale. Composition dependent characterization of copper indium diselenide thin film solar cells synthesized from electrodeposited binary selenide precursor stacks. *Solar Energy Materials and Solar Cells*, 126:88–95, 2014. 16

[27] E. Chassaing, N. Naghavi, G. Rocha, V. Bockelee, E. Leite, M. Bouttemy, J. Vigneron, A. Etcheberry, and D. Lincot. Recent advances in electrodeposition of interfacial buffer layers in chalcopyrite-based solar cells. *ECS Transactions*, 35:127–134, 2011. 16

[28] T. Voss, J. Schulze, A. Kirbs, J. Palm, V. Probst, S. Jost, R. Hock, and M. Perwins. CIS solar cells by high rate electrodeposition technology. *22nd European Photovoltaic Solar Energy Conference*, 1940 - 1945, 2007. 16

[29] D. Berg. *Kesterite Equilibrium Reaction and the Discrimination of Secondary Phases from Cu_2ZnSnS_4*. PhD thesis, Université du Luxembourg, 2013. 16, 124

[30] P. J. Sebastian, M. E. Calixto, Rommel Noufi Bhattacharya, and Rommel Noufi. CIS and CIGS based photovoltaic structures developed from electrodeposited precursors. *Solar energy materials and solar cells*, 59(1):125–135, 1999. 16

[31] C. Sene, M. E. Calixto, K. D. Dobson, and R. W. Birkmire. Electrodeposition of $CuInSe_2$ absorber layers from pH buffered and non-buffered sulfate-based solutions. *Thin Solid Films*, 516(8):2188–2194, 2008. 16

[32] D. Guimard, P. P. Grand, N. Bodereau, P. Cowache, J. F. Guillemoles, D. Lincot, S. Taunier, M. Ben Farah, and P. Mogensen. Copper indium diselenide solar cells prepared by electrodeposition. In *Photovoltaic Specialists Conference, 2002. Conference Record of the Twenty-Ninth IEEE*, pages 692–695. IEEE, 2002. 16

[33] B. Ndiaye, C. Mbow, M. S. Mane, and C. Sne. One-step electrodeposited CuInSe2 absorber layers for efficient PV cells. *Revue des Energies Renouvelables*, 15(4):609–620, 2012. 16

[34] P. J. Dale, A. P. Samantilleke, G. Zoppi, I. Forbes, and L. M. Peter. Characterization of $CuInSe_2$ material and devices: comparison of thermal and electrochemically prepared absorber layers. *Journal of Physics D: Applied Physics*, 41(8):085105, 2008. 16, 48

[35] K. T. L. De Silva, W. A. A. Priyantha, J. K. D. S. Jayanetti, B. D. Chithrani, W. Siripala, K. Blake, and I. M. Dharmadasa. Electrodeposition and characterisation of $CuInSe_2$ for applications in thin film solar cells. *Thin Solid Films*, 382(12):158–163, 2001. 16

[36] X. Donglin, X. Man, L. Jianzhuang, and Z. Xiujian. Co-electrodeposition and characterization of $Cu(In,Ga)Se_2$ thin films. *Journal of Materials Science*, 41(7):1875–1878, 2006. 16

[37] K. Bouabid, A. Ihlal, A. Manar, A. Outzourhit, and E.L. Ameziane. Effect of deposition and annealing parameters on the properties of electrodeposited $CuIn_{1-x}Ga_xSe_2$ thin films. *Thin Solid Films*, 488(1-2):62–67, 2005. 16

[38] S. Merdes, R. Kaigawa, J. Klaer, R. Klenk, R. Mainz, A. Meeder, N. Papathanasiou, D. Abou-Ras, and S. Schmidt. Increased open circuit voltage in $Cu(In,Ga)S_2$ based solar cells prepared by rapid thermal processing of metal precursors. In *Proceedings of the 23rd European Photovoltaic Solar Energy Conference*, volume 1, 2008. 16

[39] B. M. Basol, M. Pinarbasi, S. Aksu, J. Wang, Y. Matus, T. Johnson, Y. Han, M. Narasimhan, and B. Metin. Electroplating based CIGS technology for roll-to-roll manufacturing. *Twenty third European PVSEC*, pages 2137–2141, 2008. 16

[40] C. M. Ruiz, X. Fontane, A. Fairbrother, V. Izquierdo-Roca, C. Broussillou, S. Bodnar, A. Perez-Rodriguez, and V. Bermudez. Impact of electronic defects on the raman spectra from electrodeposited Cu(In,Ga)Se_2 solar cells: Application for non-destructive defect assessment. *Applied Physics Letters*, 102(9):091106, 2013. 16

[41] C. C. Landry and A. R. Barron. Synthesis of polycrystalline chalcopyrite semiconductors by microwave irradiation. *Science*, 260(5114):1653, 1993. 16

[42] J. C. Bernède and L. Assmann. Polycrystalline $CuInSe_2$ thin films synthesized by microwave irradiation. *Vacuum*, 59(4):885 – 893, 2000. 16

[43] R. Kaigawa, N. Nakayama, and R. Klenk. Instantaneous preparation of $CuIn(S_{1-x}, Se_x)_2$ films by means of sparks using microwave irradiation. *Thin Solid Films*, 520(15):4996–4999, 2012. 16

[44] R. Kaigawa, K. Ban, S. Merdes, T. Dittrich, and R. Klenk. In and Ga diffusion in Cu(In,Ga)Se_2 and Cu(In,Ga)S_2 films instantaneously prepared in a non-vacuum process. *Energy Procedia*, 10:297–302, 2011. 16

[45] L Zhang, F.D Jiang, and J.Y Feng. Formation of $CuInSe_2$ and Cu(In,Ga)Se_2 films by electrodeposition and vacuum annealing treatment. *Solar Energy Materials and Solar Cells*, 80(4):483–490, 2003. 16

[46] M. Kaelin, D. Rudmann, and A.N. Tiwari. Low cost processing of CIGS thin film solar cells. *Solar Energy*, 77(6):749–756, 2004. 16

[47] R. N. Bhattacharya. Solution growth and electrodeposited $CuInSe_2$ thin films. *J. Electrochem. Soc.: Electrochemical Science and Technology*, 130(10):2040–2042, 1983. 16, 48

[48] R. P. Singh and S. L. Singh. Electrodeposited semiconducting $CuInSe_2$ films. II. photoelectrochemical solar cells. *Journal of Physics D: Applied Physics*, 19(9):1759, 1986. 16

[49] J. F. Guillemoles, A. Lusson, P. Cowache, S. Massaccesi, J. Vedel, and D. Lincot. Recrystallization of electrodeposited copper indium diselenide thin films in an atmosphere of elemental selenium. *Advanced Materials*, 6(5):376 – 379, 1994. 16, 17, 70

[50] J. Hedstrom, H. Ohlsen, M. Bodegard, A. Kylner, Lars Stolt, D. Hariskos, M. Ruckh, and H. Schock. ZnO/CdS/Cu(In,Ga)Se_2 thin film solar cells with improved performance. In *Conference Record of the Twenty Third IEEE Photovoltaic Specialists Conference, 1993*, pages 364–371, 1993. 17

[51] J. J. Scragg, P. J. Dale, D. Colombara, and L. M. Peter. Thermodynamic aspects of the synthesis of thin-film materials for solar cells. *ChemPhysChem*, 13(12):3035–3046, 2012. 17, 65, 66

[52] R. S. Srinivasa and J. G. Edwards. Phase equilibria, chemistry, and thermodynamics during vaporization of indium selenide. *Journal of The Electrochemical Society*, 134(7):1811–1817, 1987. 17

[53] Q. Cao, O. Gunawan, M. Copel, K. B. Reuter, S. J. Chey, V. R. Deline, and D. B. Mitzi. Defects in Cu(In,Ga)Se_2 chalcopyrite semiconductors: A comparative study of material properties, defect states and photvoltaic performance. *Advanced Energy Materials*, 1:845 – 853, 2011. 17, 66

[54] W. N. Shafarman, S. Siebentritt, and L. Stolt. *Handbook of Photovoltaic Science and Engineering: Chapter 13: Cu(InGa)Se_2 Solar Cells*. Wiley, second edition, 2010. 17

[55] M. Igalson and P. Zabierowski. Electron traps in Cu(In,Ga)Se_2 absorbers of thin film solar cells studied by junction capacitance techniques. *OPTOELECTRONICS REVIEW*, 11(4):261–268, 2003. 17

[56] A. Einstein. On the quantum theory of radiation. *Physikalische Zeitschrift*, 18:121–128, 1917. 17

[57] T. H. Maiman. Stimulated optical radiation in ruby. *Nature*, 187(4736):493–494, August 1960. 17

[58] J. Hecht. Short history of laser development. *Optical Engineering*, 49(9):091002, 2010. 17

[59] B. S. Yilbas. *Laser Heating Applications: Analytical Modelling*. Elsevier, 2012. 17

[60] W. Guo and B. Liu. Liquid-phase pulsed laser ablation and electrophoretic deposition for chalcopyrite thin-film solar cell application. *ACS Applied Materials & Interfaces*, 4(12):7036–7042, 2012. 17

[61] S. Jost, R. Schurr, F. Hergert, R. Hock, J. Schulze, A. Kirbs, T. Vo, M. Purwins, J. Palm, and I. Mys. The formation of $CuInSe_2$ thin-film solar cell absorbers by laser annealing of electrodeposited precursors. *Solar Energy Materials and Solar Cells*, 92(4):410–417, 2008. 18

[62] A. Bhatia, H. Meadows, A. Crossay, P. J. Dale, and M. A. Scarpulla. Continuous wave solid phase laser annealing of single-pot electrodeposited $CuInSe_2$ thin films: Effects of Cu/In stoichiometry. *Journal of Applied Physics*, 114(4):044904, 2013. 18, 94, 103, 104

[63] I. W. Boyd and J. I. B. Wilson. Laser annealing for semiconductor devices. *Nature*, 287(5780):278–278, 1980. 18

[64] R. T. Young and R. F. Wood. Laser processing of semiconductor materials. *Ann. Rev. Mater. Sci.*, 12:323 – 350, 1982. 18

[65] M. C. Joliet L. D. Laude. Laser-induced synthesis of thin $CuInSe_2$ films. *Solar Cells*, pages 199–209, 1985. 18

[66] M. C. Joliet, R. Antoniadis, R. Andrew, and L. D. Laude. Laser-induced synthesis of thin $CuInSe_2$ films. *Applied Physics Letters*, 46(3):266–267, 1985. 18

[67] G. D. Mooney and A. M. Hermann. Novel thin-film $CuInSe_2$ fabrication. Technical report AC02-83CH10093, Solar Energy Research Inst., Golden, CO., Technical Information Center Oak Ridge Tennessee, September 1990. 18

[68] D. Bhattacharyya, S. Bocking, and M. J. Carter. Detection of binary phases in $CuInSe_2$ films formed by laser annealing of stacked elemental layers of In, Cu and Se. *Journal of Materials Science*, 31(20):5451–5456, 1996. 18

[69] E. Ahmed, M. Amar, W. Ahmed, R.D. Pilkington, A.E. Hill, and M.J. Jackson. Laser annealing of flash-evaporated $CuInS_2$ thin films. *Journal of Materials Engineering and Performance*, 15(2):213–217, 2006. 18

[70] W. Xuege, S.S. Li, C. H. Huang, L.L. Kerr, S. Rawal, J.M. Howard, V. Cracium, T.J. Anderson, and O.D. Crisalle. Investigation of pulsed non-melt laser annealing (NLA) of CIGS-based solar cells. *Proceedings of 3rd World Conference on Photovoltaic Energy Conversion, 2003*, 1:396–399, 2003. 18

[71] A. Bhatia, H. Meadows, W.M. Hlaing Oo, P.J. Dale, and M.A. Scarpulla. Effects of pulsed laser annealing on deep level defects in electrochemically-deposited and furnace annealed $CuInSe_2$ thin films. *Thin Solid Films*, 531:566–571, 2013. 18

[72] A. Bhatia, H. Meadows, A. Crossay, P. J. Dale, and M. A. Scarpulla. Pulsed and continuous wave solid phase laser annealing of electrodeposited $CuInSe\ _2$ thin films. *Proc. of SPIE*, 8473:84730F, 2012. 18

[73] A.R. Jeong, W. Jo, C. Ko, M. Han, S.J. Kang, M. Kim, D.Y. Park, H. Cheong, and H.J. Yun. Growth and structural properties of pulsed laser-ablated $CuInSe_2$ nanoparticles by pulsed-laser ablation and selenization process. *Journal of Alloys and Compounds*, 509(31):8073–8076, 2011. 18

[74] J. Hermann, M. Benfarah, G. Coustillier, S. Bruneau, E. Axente, J.-F. Guillemoles, M. Sentis, P. Alloncle, and T. Itina. Selective ablation of thin films with short and ultrashort laser pulses. *Applied Surface Science*, 252(13):4814–4818, 2006. 18

[75] D. Ruthe, K. Zimmer, and T. Hche. Etching of $CuInSe_2$ thin filmscomparison of femtosecond and picosecond laser ablation. *Applied Surface Science*, 247(1-4):447–452, 2005. 18

[76] U. Rau, D. Abou-Ras, and T. Kirchartz. Electron microscopy on thin films for solar cells. In *Advanced Characterization Techniques for Thin Film Solar Cells*. Wiley-VCH Verlag GmbH & Co. KGaA, 2011. 23, 25

[77] J. Goldstein, D. E. Newbury, D. C. Joy, C. E. Lyman, P. Echlin, E. Lifshin, L. Sawyer, and J. R. Michael. *Scanning Electron Microscopy and X-ray Microanalysis - Third Edition*. Springer, 2003. 23, 25

[78] S. Schorr, C. Stephan, T. Törndahl, R. Mainz, D. Abou-Ras, T. Kirchatz, and U. Rau. X-ray and neutron diffraction on materials for thin film solar cells. In *Advanced Characterization Techniques for Thin Film Solar Cells*. Wiley-VCH Verlag GmbH & Co. KGaA, 2011. 25

[79] M. Birkholz. *Thin Film Analysis by X-Ray Scattering*. John Wiley & Sons, 2006. 25

[80] R. A. Young. *The Rietveld Method*. Oxford University Press, 1995. 27

[81] S. Schorr and G. Geandier. In-situ investigation of the temperature dependent structural phase transition in $CuInSe_2$ by synchrotron radiation. *Crystal Research and Technology*, 41(5):450–457, 2006. 27

[82] D.-M. Smilgies. Scherrer grain-size analysis adapted to grazing-incidence scattering with area detectors. *Journal of Applied Crystallography*, 42(6):1030–1034, 2009. 27

[83] J. G. M. van Berkum, G. J. M. Sprong, Th. H. de Keijser, R. Delhez, and E. J. Sonneveld. The optimum standard specimen for x-ray diffraction line-profile analysis. *Powder Diffraction*, 10(02):129–139, 1995. 27

[84] G. K Williamson and W. H Hall. X-ray line broadening from filed aluminium and wolfram. *Acta Metallurgica*, 1(1):22–31, 1953. 28

[85] V. Hoffmann, D. Klemm, V. Efimova, C. Venzago, A. A. Rockett, T. Wirth, T. Nunney, C. A. Kaufmann, and R. Caballero. Elemental distribution profiling of thin films for solar cells. In D. Abou-Ras, T. Kirchartz, and U. Rau, editors, *Advanced Characterization Techniques for Thin Film Solar Cells*, pages 411–448. Wiley-VCH Verlag GmbH & Co. KGaA, 2011. 28

[86] J. W. Robinson, E . M. Skelly Frame, and G. M. Frame. *Undergraduate Instrumental Analysis, Sixth Edition*. CRC Press, 2004. 29

[87] C. F. Bohren and D. R. Huffman. *Absorption and Scattering of Light by Small Particles*. John Wiley & Sons, 2008. 29, 30

[88] SHIMADZU. Diffuse reflectance measurement. *Available online at: https://www.ssi.shimadzu.com/products/product.cfm?product=uv_accy_solid_guide1*, Assessed Oct. 2014. 29

[89] F. L. Pedrotti and S.J. Leno S. Pedrotti. *Introduction to Optics*. Preston Hall, New Jersey, U.S., 2 edition edition, 1993. 30, 51, 52

[90] E. Hecht. *Optics*. Addison-Wesley, 4th edition, 2001. 30, 51, 56

[91] G. R. Fowles. *Introduction to Modern Optics*. Courier Dover Publications, 1975. 30, 51, 52, 56

[92] K.-E. Peiponen, E. M. Vartianen, and T. Asakura. *Dispersion, Complex Analysis and Optical Spectroscopy: Classical Theory*. Springer Science & Business Media, 1999. 30

[93] G. P. Smestad. *Optoelectronics of Solar Cells*. SPIE Press, Washington, U.S., 2002. 31

[94] J. I. Pankove. *Optical Processes in Semiconductors*. Courier Dover Publications, 2012. 31

[95] T. Owen. *Fundamentals of UV-visible spectroscopy*. Agilient Technologies, 2000. 31

[96] G. Bauer and W. Richter. *Optical Characterization of Epitaxial Semiconductor Layers*. Springer, first edition, 1996. 31, 32

[97] J. Álvarez Garca, V. Izquierdo-Roca, and A. Prez-Rodrguez. Raman spectroscopy on thin films for solar cells. In D. Abou-Ras, T. Kirchartz, and U. Rau, editors, *Advanced Characterization Techniques for Thin Film Solar Cells*, page 365–386. Wiley-VCH Verlag GmbH & Co. KGaA, 2011. 31, 32

[98] E. Silberman and H. W. Morgan. Use of group theory in the interpretation of infrared and raman spectra. *Oak Ridge National Laboratory*, 1977. 32

[99] T. Unold and L. Gtay. Photoluminescence analysis of thin-film solar cells. In D. Abou-Ras, Thomas K., and U. Rau, editors, *Advanced Characterization Techniques for Thin Film Solar Cells*, page 151175. Wiley-VCH Verlag GmbH & Co. KGaA, 2011. 33, 34

[100] P. Würfel. *Physics of Solar Cells: From Basic Principles to Advanced Concepts*. John Wiley & Sons, Weinheim, Germany, second edition, 2009. 33, 74, 75, 82

[101] J. K. Larsen. *Inhomogeneities in Epitaxial Chalcopyrites Studied by Photoluminescence*. PhD thesis, Universit du Luxembourg, Luxembourg, 2011. 34

[102] D. Colombara, A. Crossay, D. Regesch, C. Broussillou, T. Goislard de Monsabert, P.-P. Grand, and P. J. Dale. Prediction of photovoltaic pn device short circuit current by photoelectrochemical analysis of p-type CIGSe films. *Electrochemistry Communications*, 48:99–102, 2014. 34

[103] A. J. Bard and L. R. Faulkner. *Electrochemical Methods: Fundamentals and Applications*. Wiley, New York, second edition, 2000. 34

[104] T. Kirchartz, K. Ding, and U. Rau. Fundamental electrical characterization of thin-film solar cells. In D. Abou-Ras, T. Kirchartz, and U. Rau, editors, *Advanced Characterization Techniques for Thin Film Solar Cells*. Wiley-VCH Verlag GmbH & Co. KGaA, 2011. 36, 37, 38, 74, 75

[105] S. Siebentritt. What limits the efficiency of chalcopyrite solar cells? *Solar Energy Materials and Solar Cells*, 95(6):1471–1476, 2011. 36, 38, 118

[106] S. M. Sze and K. K. Ng. *Physics of Semiconductor Devices*. Wiley-Interscience, Hoboken, N.J, 3^{rd} edition, 2006. 37

[107] A. L. Fahrenbruch and R. H. Bube. *Fundamentals of Solar Cells: Photovoltaic Solar Energy Conversion*. Academic Press, 1983. 38, 68

[108] J. Nelson. *The Physics of Solar Cells*. Imperial College Press, London, UK, first edition, 2003. 38

[109] C. H. Solanki. *Solar Photovoltaics: Fundamentals Technologies And Applications*. PHI Learning Private Limited, New Delphi, 2009. 38

[110] W. Shockley and H. J. Queisser. Detailed balance limit of efficiency of p–n junction solar cells. *Journal of Applied Physics*, 32(3):510–519, 1961. 38, 68

[111] W. W. Gärtner. Depletion-layer photoeffects in semiconductors. *Physical Review*, 116(1):84–87, 1959. 39

[112] J. Poortmans and V. Arkhipov. *Thin Film Solar Cells: Fabrication, Characterization and Applications*. John Wiley & Sons, October 2006. 39

[113] J. J. Scragg, P. J. Dale, Laurence M. Peter, Guillaume Zoppi, and Ian Forbes. New routes to sustainable photovoltaics: evaluation of cu2znsns4 as an alternative absorber material. *physica status solidi (b)*, 245(9):1772–1778, 2008. 39

[114] A.J. Bard and L.R. Faulkner. *Electrochemical Methods. Fundamentals and Applications*. Wiley, second edition, 2001. 41

[115] A. C Fisher. *Modern electrode dynamics*. Oxford University Press, 1995. 41, 43

[116] C. M. A Brett and A. M. O. Brett. *Electrochemistry principles, methods, and applications*. Oxford University Press, Oxford; New York, 1993. 41

[117] J. J. Scragg. *Studies of Cu_2ZnSnS_4 films prepared by sulfurisation of electrodeposited precursors*. PhD thesis, University of Bath, May 2010. 46, 145

[118] E. Rusli, F. Xue, T. O. Drews, P. M. Vereecken, P. Andricacos, H. Deligianni, R. D. Braatz, and R. C. Alkire. Effect of additives on shape evolution during electrodeposition II. parameter estimation from roughness evolution experiments. *Journal of The Electrochemical Society*, 154(11):D584–D597, 2007. 46, 145

[119] The Indium Corporation. Indium sulfamate plating bath. available online at http://www.indium.com/thin-film/plating/. 47, 145

[120] S. Zein El Abedin, A.Y. Saad, H.K. Farag, N. Borisenko, Q.X. Liu, and F. Endres. Electrodeposition of selenium, indium and copper in an air- and water-stable ionic liquid at variable temperatures. *Electrochimica Acta*, 52(8):2746–2754, 2007. 47

[121] H. P. Fritz and P. Chatziagorastou. A new electrochemical method for selenization of stacked CuIn layers and preparation of $CuInSe_2$ by thermal annealing. *Thin Solid Films*, 247(1):129–133, 1994. 47

[122] L. Thouin and J. Vedel. Electrodeposition and characterization of $CulnSe_2$ thin films. *Journal of The Electrochemical Society*, 142(9):2996–3001, 1995. 48, 63

[123] M. G. Pavlović, Š. Kindlov, and I. Roušar. The initiation of dendritic growth of electrodeposited copper on a rotating disc electrode with changing copper concentration and diffusion layer thickness. *Electrochimica Acta*, 37(1):23–27, 1992. 48

[124] Q. Huang, K. Reuter, S. Amhed, L. Deligianni, L. T. Romankiw, S. Jaime, P.-P. Grand, and V. Charrier. Electrodeposition of indium on copper for CIS and CIGS solar cell applications. *Journal of The Electrochemical Society*, 158(2):D57–D61, 2011. 49

[125] J. C. Malaquias, M. Steichen, M. Thomassey, and P. J. Dale. Electrodeposition of CuIn alloys from a choline chloride based deep eutectic solvent for photovoltaic applications. *Electrochimica Acta*, 103:15–22, 2013. 49

[126] D. Bhattacharyya, I. Forbes, F. O. Adurodija, and M. J. Carter. Formation of $CuInSe_2$ by the selenization of sputtered Cu/In layers. *Journal of materials science*, 32(7):1889–1894, 1997. 50

[127] M. Bertolotti. Laser annealing of semiconductors. *Journal of Soviet Laser Research*, 6(4):395–404, 1985. 52

[128] M. Alonso, K. Wakita, J. Pascual, M. Garriga, and N. Yamamoto. Optical functions and electronic structure of $CuInSe_2$, $CuGaSe_2$, $CuInS_2$, and $CuGaS_2$. *Physical Review B*, 63(7), 2001. 53, 55, 56, 85

[129] A. Bhatia. *Laser annealing and defect study of chalcogenide photovoltaic materials*. PhD thesis, The University of Utah, 2013. 54, 149

[130] M. A. S. Bhuiyan, A. S. Bhuiyan, A. Hossain, and Z. H. Mahmood. Studies on optical characteristics of $CuInSe_2$ thin films. *Central European Journal of Engineering*, 3(2):170–173, 2013. 54

[131] M. A. Ordal, R. J. Bell, R. W. Alexander, L. A. Newquist, and M. R. Querry. Optical properties of al, fe, ti, ta, w, and mo at submillimeter wavelengths. *Applied Optics*, 27(6):1203–1209, 1988. 56

[132] L. Gample and F. M. Johnson. Index of refraction of single-crystal selenium. *Journal of the Optical Society of America*, 59(1):72–73, January 1969. 56

[133] A. I. Golovashkin, I. S. Levchenko, G. P. Motulevich, and A. A. Shubin. Optical properties of indium. *SOVIET PHYSICS JETP*, 24(6), 1967. 56

[134] H. T. El-Shair and A. E. Bekheet. Effect of heat treatment on the optical properties of In_2Se_3 thin films. *Journal of Physics D: Applied Physics*, 25(7):1122, July 1992. 56

[135] J. Schöldström, U. Zimmermann, and M. Edoff. Determination of the optical constants for $Cu(In,Ga)Se_2$ and Cu_xSe in the IR region. *Journal of Physics D: Applied Physics*, 45(11):115101, 2012. 56

[136] G. D. Mooney and A. M. Hermann. Novel thin-film $CuInSe_2$ fabrication. Technical report, NREL, 1991. 56, 64, 94, 104, 151

[137] COMSOL. Comsol multiphysics modelling software, version 4.0, 2010. 57, 84, 85

[138] V. Le Sant and G. Failleau. Thermal modelling of devices realizing temperature fixed-points. In *Proceedings of the COMSOL Users Conference*, 2007. 59

[139] M. Wakaki, T. Shibuya, and K. Kudo. *Physical Properties and Data of Optical Materials*. CRC Press, 2010. 60, 121

[140] X. Fontane, V. Izquierdo-Roca, L. Calvo-Barrio, J. Alvarez-Garcia, A. Perez-Rodriguez, J.R. Morante, and W. Witte. In-depth resolved raman scattering analysis of secondary phases in Cu-poor $CuInSe_2$ based thin films. *Applied Physics Letters*, 95(12):121907–121907–3, 2009. 60

[141] K. Kambas, C. Julien, M. Jouanne, A. Likforman, and M. Guittard. Raman spectra of α- and γ-In_2Se_3. *physica status solidi (b)*, 124(2):K105–K108, 1984. 60

[142] H. J. Meadows, A. Bhatia, C. Stephan, S. Schorr, M. A. Scarpulla, and P. J. Dale. Crystallographic study of phases present in $CuInSe_2$ absorber layers produced by laser annealing co-electrodeposited precursors. *Proc. of SPIE*, 8823:882302, 2013. 61, 71

[143] O. Ramdani, J.F. Guillemoles, D. Lincot, P.P. Grand, E. Chassaing, O. Kerrec, and E. Rzepka. One-step electrodeposited $CuInSe_2$ thin films studied by raman spectroscopy. *Thin Solid Films*, 515(15):5909–5912, 2007. 63

[144] F. J. Pern, R. Noufi, A. Mason, and A. Franz. Characterizations of electrodeposited $CuInSe_2$ thin films: Structure, deposition and formation mechanisms. *Thin Solid Films*, 202(2):299314, 1991. 63, 68

[145] A. Gobeaut, L. Laffont, J.-M. Tarascon, L. Parissi, and O. Kerrec. Influence of secondary phases during annealing on re-crystallization of $CuInSe_2$ electrodeposited films. *Thin Solid Films*, 517(15):4436–4442, 2009. 63

[146] P. Jackson, D. Hariskos, E. Lotter, S. Paetel, R. Wuerz, R. Menner, W. Wischmann, and M. Powalla. New world record efficiency for Cu(In,Ga)Se_2 thin-film solar cells beyond 20%. *Progress in Photovoltaics: Research and Applications*, 19(7):894–897, 2011. 64, 102, 107

[147] R. Scheer and H.-W. Schock. *Chalcogenide Photovoltaics: Physics, Technologies, and Thin Film Devices*. John Wiley & Sons, 2011. 64, 74, 82, 102, 103

[148] I.M. Kötschau and H.W. Schock. Depth profile of the lattice constant of the cu-poor surface layer in $(Cu_2Se)_{1-x}$ $(In_2Se_3)_x$ evidenced by grazing incidence x-ray diffraction. *Journal of Physics and Chemistry of Solids*, 64(9-10):1559–1563, 2003. 64

[149] P. Atkins. *The Laws of Thermodynamics: A Very Short Introduction*. Very Short Introductions, 2010. 65

[150] D. Cahen and R. Noufi. Free energies and enthalpies of possible gas phase and surface reactions for preparation of $CuInSe_2$. *Journal of Physics and Chemistry of Solids*, 52(8):947–961, 1991. 65, 120

[151] P. Atkins and J. D. Paula. *Elements of Physical Chemistry*. Oxford University Press, New York, 4th revised edition edition edition, 2005. 65, 66

[152] P. W. Atkins. *Physical Chemistry*. Oxford University Press, Oxford; New York, 5th revised edition edition edition, 1994. 66

[153] H. Y. Park, D. G. Moon, J. H. Yun, S. K. Ahn, K. H. Yoon, and S. Ahn. Efficiency limiting factors in Cu(In,Ga)Se_2 thin film solar cells prepared by Se-free rapid thermal annealing of sputter-deposited Cu-In-Ga-Se precursors. *Applied Physics Letters*, 103(26):263903, 2013. 67, 109

[154] J. R. Tuttle, D. S. Albin, and R. Noufi. Thoughts on the microstructure of polycrystalline thin film $CuInSe_2$ and its impact on material and device performance. *Solar Cells*, 30(14):21–38, 1991. 67

[155] H. J. Meadows, A. Bhatia, V. Depredurand, J. Guillot, D. Regesch, A. Malyeyev, D. Colombara, M. A. Scarpulla, S. Siebentritt, and P. J. Dale. Single second laser annealed $CuInSe_2$ semiconductors from electrodeposited precursors as absorber layers for solar cells. *The Journal of Physical Chemistry C*, 118(3):1451–1460, 2014. 67, 71, 95

[156] P. Dale, A. Samantilleke, G. Zoppi, I. Forbes, S. Roncallo, and L. Peter. Deposition and characterization of copper chalcopyrite based solar cells using electrochemical techniques. *ECS Transactions*, 6:535–546, 2007. 67

[157] L. M. Peter, J. Li, and R. Peat. Surface recombination at semiconductor electrodes: Part i. transient and steady-state photocurrents. *Journal of electroanalytical chemistry and interfacial electrochemistry*, 165(1):29–40, 1984. 67

[158] W. Shockley. The theory of p-n junctions in semiconductors and p-n junction transitors. *Bell System Technical Journal*, 28(3):435 – 489, 1949. 68

[159] D. R Lide. *CRC Handbook of Chemistry and Physics*. CRC Press LLC, 85 th edition, 2005. 69

[160] D. Schmid, M. Ruckh, and H. W. Schock. A comprehensive characterization of the interfaces in Mo/CIS/CdS/ZnO solar cell structures. *Solar Energy Materials and Solar Cells*, 41:281294, 1996. 74

[161] J. L. Shay and J. H. Wernick. *Ternary chalcopyrite semiconductors: growth, electronic properties, and applications*. Pergamon Press, New York, 1975. 75

[162] H. J. Meadows, A. Bhatia, S. Misra, V. Reis-Adonis, M.A. Scarpulla, and P.J. Dale. Photovoltaic semiconductor from $CuInSe_2$ precursor using 1 s laser annealing. *Manuscript in Preparation*, 2014. 76

[163] J. H. Lienhard and J. H. V. Lienhard. *A heat transfer textbook*. Prentice-Hall, New Jersey, 1987. 81, 83, 84

[164] A. D. Compaan, I. Matulionis, and S. Nakade. Laser scribing of polycrystalline thin films. *Optics and Lasers in Engineering*, 34(1):1545, 2000. 83, 86

[165] K. Shimazaki, M. Imaizumi, and K. Kibe. SiO_2 and Al_2O_3/SiO_2 coatings for increasing emissivity of $Cu(In,Ga)Se_2$ thin-film solar cells for space applications. *Thin Solid Films*, 516(8):2218–2224, February 2008. 85

[166] M. Günthner, M. Pscherer, C. Kaufmann, and G. Motz. High emissivity coatings based on polysilazanes for flexible $Cu(In,Ga)Se_2$ thin-film solar cells. *Solar Energy Materials and Solar Cells*, 123:97–103, 2014. 85

[167] Y. Ren, Y. Zhang, J. K. Chen, and Z. C. Feng. Inverse estimation of the front surface temperature of a 3-D finite slab based on the back surface temperature measured at coarse grids. *Numerical Heat Transfer, Part B: Fundamentals*, 63:1–17, 2013. 87

[168] J. Zhou, Y. Zhang, J. K. Chen, and Z. C. Feng. Inverse heat conduction using measured back surface temperature and heat flux. *Journal of Thermophysics and Heat Transfer*, 24(1):95–103, 2010. 87

[169] T. Tinoco, C. Rincn, M. Quintero, and G. Snchez Prez. Phase diagram and optical energy gaps for $\mathrm{CuIn}_y\mathrm{Ga}_{1-y}\mathrm{Se}_2$ alloys. *physica status solidi (a)*, 124(2):427–434, 1991. 95, 117, 154

[170] L. E. Oikkonen, M. G. Ganchenkova, A. P. Seitsonen, and R. M. Nieminen. Mass transport in CuInSe_2 from first principles. *Journal of Applied Physics*, 113(13):133510, 2013. 96, 97, 98, 100, 101, 102, 103

[171] K. Gartsman, L. Chernyak, V. Lyahovitskaya, D. Cahen, V. Didik, V. Kozlovsky, R. Malkovich, E. Skoryatina, and V. Usacheva. Direct evidence for diffusion and electromigration of Cu in CuInSe_2. *Journal of applied physics*, 82(9):4282–4285, 1997. 100

[172] J. Pohl and K. Albe. Thermodynamics and kinetics of the copper vacancy in CuInSe_2, CuGaSe_2, CuInS_2, and CuGaS_2 from screened-exchange hybrid density functional theory. *Journal of Applied Physics*, 108(2):023509, 2010. 100

[173] M. Kleinfeld and H. D. Wiemhfer. Chemical diffusion coefficients and stability of CuInS_2 and CuInSe_2 from polarization measurements with point electrodes. *Solid State Ionics*, 28-30:1111–1115, 1988. 100

[174] H. J. von Bardeleben. Selenium self-diffusion study in the 1-3-6_2 semiconductor: CuInSe_2. *Journal of Applied Physics*, 56(2):321–326, 1984. 100

[175] A. Praveen Kumar and K. V. Reddy. Lateral self-diffusion of selenium in CuInSe_2 thin films. *Thin Solid Films*, 304(12):365–370, 1997. 100

[176] M. Marudachalam, R. W. Birkmire, H. Hichri, J. M. Schultz, A. Swartzlander, and M. M. Al-Jassim. Phases, morphology, and diffusion in $\mathrm{CuIn}_x\mathrm{Ga}_{1-x}$ Se_2 thin films. *Journal of Applied Physics*, 82(6):2896–2905, 1997. 101

[177] K. Djessas. Diffusion of Cu, In, and Ga in $\mathrm{In}_2\mathrm{Se}_3$ / CuGaSe_2/SnO_2 thin film photovoltaic structures. *Journal of Applied Physics*, 95(8):4111, 2004. 101

[178] O. Lundberg, J. Lu, A. Rockett, M. Edoff, and L. Stolt. Diffusion of indium and gallium in Cu(In,Ga)Se_2 thin film solar cells. *Journal of Physics and Chemistry of Solids*, 64:1499–1504, 2003. 101

[179] B. J. Stanbery. Copper indium selenides and related materials for photovoltaic devices. *Critical Reviews in Solid State and Materials Sciences*, 27(2):73 – 117, 2002. 103

[180] R. Jacob, R. Geethu, T. Shripathi, G. S. Okram, V. Ganesan, B. Pradeep, K. S. Urmila, and R. R. Philip. Optoelectronic and low temperature thermoelectric effects in the OVC n-$\mathrm{CuIn}_3\mathrm{Se}_5$ thin films. *physica status solidi (a)*, 209(11):2195–2200, 2012. 102

[181] T. B. Elliot. *Trends in Semiconductor Research*. Nova Publishers, 2005. 102

[182] D. Schmid, M. Ruckh, F. Grunwald, and H.-W. Schock. Chalcopyrite/defect chalcopyrite heterojunctions on the basis of $CuInSe_2$. *Journal of Applied Physics*, 73(6):2902–2909, 1993. 103

[183] H. Hiramatsu, I. Koizumi, K.-B. Kim, H. Yanagi, T. Kamiya, M. Hirano, N. Matsunami, and H. Hosono. Characterization of copper selenide thin film hole-injection layers deposited at room temperature for use with p-type organic semiconductors. *Journal of Applied Physics*, 104(11):113723, 2008. 103

[184] P. Jackson, D. Hariskos, R. Wuerz, W. Wischmann, and M. Powalla. Compositional investigation of potassium doped $Cu(In,Ga)Se_2$ solar cells with efficiencies up to 20.8%. *Physica Status Solidi RRL*, 8(3):219–222, 2014. 103, 108, 117

[185] V. Deprdurand, D. Tanaka, Y. Aida, M. Carlberg, N. Fvre, and S. Siebentritt. Current loss due to recombination in Cu-rich $CuInSe_2$ solar cells. *Journal of Applied Physics*, 115(4):044503, 2014. 103

[186] V. Depredurand, Y. Aida, J. Larsen, T. Eisenbarth, A. Majerus, and S. Siebentritt. Surface treatment of CIS solar cells grown under Cu-excess. In *37th IEEE Photovoltaic Specialists Conference (PVSC)*, pages 000337–000342, 2011. 103, 107

[187] L. Gutay, D. Regesch, J. K. Larsen, Y. Aida, V. Depredurand, and S. Siebentritt. Influence of copper excess on the absorber quality of $CuInSe_2$. *Applied Physics Letters*, 99(15):151912, 2011. 103

[188] T. B. Elliot. *New Research on Semiconductors*. Nova Publishers, 2006. 103

[189] R. Klenk, T.s Walter, H.-W. Schock, and D. Cahen. A model for the successful growth of polycrystalline films of $CuInSe_2$ by multisource physical vacuum evaporation. *Advanced Materials*, 5(2):114–119, 1993. 104

[190] D. L. Perry. *Handbook of Inorganic Compounds, Second Edition*. CRC Press, May 2011. 104

[191] L. Gütay, D. Regesch, J. K. Larsen, Y. Aida, V. Depredurand, A. Redinger, S. Caneva, S. Schorr, C. Stephan, J. Vidal, S. Botti, and S. Siebentritt. Feedback mechanism for the stability of the band gap of $CuInSe_2$. *Physical Review B*, 86(4), 2012. 104, 117

[192] E. A. Holm and S. M. Foiles. How grain growth stops: A mechanism for grain-growth stagnation in pure materials. *Science*, 328(5982):1138–1141, May 2010. 105

[193] C. C. Wong, H. I. Smith, and C. V. Thompson. Surfaceenergydriven secondary grain growth in thin au films. *Applied Physics Letters*, 48(5):335–337, 1986. 105

[194] H. Gleiter. Nanostructured materials: basic concepts and microstructure. *Acta materialia*, 48:129, 2000. 105

[195] S. V. Bobylev and I. A. Ovid'ko. Mobility of triple junctions of grain boundaries during their migration in deformed nanocrystalline materials. *Rev.Adv.Mater.Sci.*, 22:39 – 51, 2009. 105

[196] F. J. Humphreys and M. Hatherly. Chapter 9 - recrystallization of two-phase alloys. In F. J. Humphreys and M. Hatherly, editors, *Recrystallization and Related Annealing Phenomena (Second Edition)*, pages 285–319. Elsevier, Oxford, 2004. 105, 106

[197] C. Krill, L. Helfen, D. Michels, H. Natter, A. Fitch, O. Masson, and R. Birringer. Size-dependent grain-growth kinetics observed in nanocrystalline Fe. *Physical Review Letters*, 86(5):842–845, 2001. 105, 107

[198] Y. Estrin, G. Gottstein, and L. S. Shvindlerman. Intermittent self-lockingof grain growth in fine-grained materials. *Scripta materialia*, 41(4):385–390, 1999. 105

[199] A. Michels, C. E. Krill, H. Ehrhardt, R. Birringer, and D. T. Wu. Modelling the influence of grain-size-dependent solute drag on the kinetics of grain growth in nanocrystalline materials. *Acta materialia*, 47(7):2143–2152, 1999. 105, 107

[200] M. Mozurkewich and S. W. Benson. Negative activation energies and curved Arrhenius plots. 1. Theory of reactions over potential wells. *The Journal of Physical Chemistry*, 88(25):6429–6435, 1984. 106

[201] S. J. Krause, S. R. Wilson, W. M. Paulson, and R. B. Gregory. Grain growth during transient annealing of as-implanted polycrystalline silicon films. *Applied Physics Letters*, 45(7):778780, 1984. 106

[202] S. Siebentritt and U. Rau. *Wide-Gap Chalcopyrites*. Springer, 2006. 107

[203] A. Chirilă, P. Reinhard, F. Pianezzi, P. Bloesch, A. R. Uhl, C. Fella, L. Kranz, D. Keller, C. Gretener, H. Hagendorfer, D. Jaeger, R. Erni, S. Nishiwaki, S. Buecheler, and A. N. Tiwari. Potassium-induced surface modification of Cu(In,Ga)Se_2 thin films for high-efficiency solar cells. *Nature Materials*, 12(12):1107–1111, 2013. 108, 110, 122, 123

[204] S.-H. Wei, S. B. Zhang, and A. Zunger. Effects of Na on the electrical and structural properties of $CuInSe_2$. *Journal of Applied Physics*, 85(10):7214, 1999. 108

[205] V. Alberts, J. Bekker, M. J. Witcomb, J. H. Schn, and E. Bucher. Control of V_{Se} - defect levels in $CuInSe_2$ prepared by rapid thermal processing of metallic alloys. *Thin Solid Films*, 361 - 362:432 – 436, 2000. 109

[206] S. Niki, R. Suzuki, S. Ishibashi, T. Ohdaira, P. J. Fons, A. Yamada, H. Oyanagi, T. Wada, R. Kimura, and T. Nakada. Anion vacancies in $CuInSe_2$. *Thin solid films*, 387:129–134, 2001. 109

[207] D. Braunger, D. Hariskos, G. Bilger, U. Rau, and H.W. Schock. Influence of Na on the growth of polycrystalline Cu(In,Ga)Se_2 thin films. *Thin Solid Films*, 361-362:161–166, 2000. 109, 110

[208] F. Hergert, S. Jost, R. Hock, M. Purwins, and J. Palm. A thermodynamical approach to the formation reactions of sodium-doped Cu(In,Ga)Se_2. *Thin Solid Films*, 511-512:147–152, 2006. 110

[209] B. Dimmler, H. Dittrich, R. Menner, and H. W. Schock. Performance and optimization of heterojunctions based on Cu(Ga,In)Se_2. In *19th IEEE Photovoltaic Specialists Conference*, volume 1, pages 1454–1460, 1987. 117

[210] T. Dullweber, G. Hanna, W. Shams-Kolahi, A. Schwartzlander, M. A. Contreras, R. Noufi, and H. W. Schock. Study of the effect of gallium grading in Cu(In,Ga)Se_2. *Thin Solid Films*, 361362:478–481, 2000. 118

[211] H. J. Meadows, J. C. Malaquias, M. Steichen, R. Djemour, D. Regesch, A. Malyeyev, M. Kurihara, A. A. Taylor, B. G. Mendis, and P. J. Dale. Influence of lateral elemental distribution on Cu(In,Ga)Se_2 absorber layers: from precursor to solar cell. *Physical Chemistry Chemical Physics*, Submitted, 2014. 118

[212] Christiane Stephan. *Structural trends in off stoichiometric chalcopyrite type compound semiconductors*. PhD thesis, Helmholtz Zentrum Berlin, 2011. 118

[213] C. Stephan, T. Scherb, C. A. Kaufmann, S. Schorr, and H. W. Schock. Cationic point defects in $CuGaSe_2$ from a structural perspective. *Applied Physics Letters*, 101:101907, 2012. 118

[214] C. Stephan, S. Schorr, and H. W. Tovar, M. Schock. Comprehensive insights into point defect and defect cluster formation in $CuInSe_2$. *Applied Physics Letters*, 98:091906, 2011. 118

[215] N. A. Stolwijk, Sh. Obeidi, J. Bastek, R. Wuerz, and A. Eicke. Fe diffusion in polycrystalline Cu(In,Ga)Se_2 layers for thin-film solar cells. *Applied Physics Letters*, 96(24):244101, 2010. 122

[216] M. Steichen, J. C. Malaquias, M. Arasimowicz, R. Djemour, N. R. Brooks, L. Van Meervelt, J. Fransaer, K. Binnemans, and P. J. Dale. High-speed electrodeposition from liquid metal salts for $Cu_2ZnSnSe_4$ solar cells. *Submitted to J. Phys. Chem. C.*, 2014. 122

[217] B. Basol. Commercialization of high efficiency low cost CIGS technology based on electroplating. Technical report, NREL, 2010. 122

[218] Coherent. Coherent inc. diode laser FAP systems with powers up to 350W QCW. *available online at https://www.coherent.com/products/?863/HighLight-FAP-System-Family*, 2014. 123

[219] Y. E. Romanyuk, H. Hagendorfer, P. Stcheli, P. Fuchs, A. R. Uhl, C. M. Sutter-Fella, M. Werner, S. Haass, J. Stckelberger, C. Broussillou, P.-P. Grand, V. Bermudez, and A. N. Tiwari. All solution-processed chalcogenide solar cells from single functional layers towards a 13.8% efficient CIGS device. *Advanced Functional Materials*, page early view, 2014. 123

[220] 3D MICROMAC. Applications in the photovoltaics industry - Laser Micromachining for Industrial Applications and R&D. *available online at http://3d-micromac.com/applications-in-the-photovoltaics-industry.html*, 2014. 123, 124

[221] rofin. Laser structuring of solar cells. *available online at http://www.rofin.com/en/markets/photovoltaic_industry/laser_structuring/*, 2014. 123

[222] TEL Solar. LSS innovative laser scribing solutions for the industrial production of large-area thin film silicon solar modules. *available online at http://www.solar.tel.com/fileadmin/solar/Contacts/Documents/LSS_TELSolar_RGB_-Dec13.pdf*, 2014. 123

[223] www.alibaba.com. 1200c industrial muffle furnace price for Annealing, Normalizing and brazing. *available online at http://www.alibaba.com/product-gs/1690560086/1200C_-Industrial_muffle_furnace_price_for.html*, 2014. 124

[224] W. R. Blischke and D. N. P Murthy. *Case Studies in Reliability and Maintenance*. John Wiley & Sons, 2003. 124

[225] L. A. Johnson. Laser diode burn-in and reliability testing. *Communications Magazine, IEEE*, 44(2):47, 2006. 124

[226] Eurostat. Half-yearly electricity and gas prices, second half of year, 2009-2011 (EUR per kWh). Technical report, Eurostat, 2012. 124

[227] M.I. Alonso, M. Garriga, C.A. Durante Rincón, E. Hernández, and M. León. Optical functions of chalcopyrite $CuGa_xIn_{1-x}Se_2$ alloys. *Applied Physics A: Materials Science & Processing*, 74(5):659–664, 2002. 151

[228] H. Lee, W. Lee, J. Y. Kim, M. J. Ko, K. Kim, K. Seo, D.-K. Lee, and H. Kim. Highly dense and crystalline $CuInSe_2$ thin films prepared by single bath electrochemical deposition. *Electrochimica Acta*, 87:450–456, 2013. 152

[229] M.E. Calixto, K.D. Dobson, B.E. McCandless, and R.W. Birkmire. Controlling growth chemistry and morphology of single-bath electrodeposited $Cu(In,Ga)Se_2$ thin films for photovoltaic application. *Journal of the Electrochemical Society*, 153(6):G521–G528, 2006. 155

12 Appendices

12.1 Deposition Baths

All deposition baths were made up with the chemicals specified below dissolved in deionised water (resistivity of 18.2 MΩ cm) to give 100 ml plating solution.

Unless specified, the depositions were carried out at room temperature, without a controlled atmosphere.

12.1.1 Cu/In/Se

Alkaline Cu deposition.

Full method given in [117].
Deposition at: -1.07 V (vs. Ag|AgCl)
Rotation Speed: 300 rpm
Film thickness: 50 nm (0.14 Ccm^{-2})

Chemical	Concentration [M]	Purity %	Supplier
$CuSO_4.7H_2O$	0.1	99.99	Alfa Aeser
NaOH	3	99.998	Sigma Aldrich
$C_6H_{14}O_6$ (Sorbitol)	0.2	99 +	Sigma Aldrich
$C_{16}H_{33}O_2N$ (Empigen BB)	9.32×10^{-4}	n/a	Sigma Aldrich

Acidic Cu deposition.

Full method given in [118]
Deposition at: 5 $mAcm^{-2}$ (Galvanostatic control)
Rotation Speed: 200 rpm
Film thickness: 75 nm (0.20 Ccm^{-2})

Chemical	Concentration	Purity %	Supplier
$CuSO_4.7H_2O$	0.3 [M]	99.99	Alfa Aeser
H_2SO_4	175 [gL^1]	95 - 97	Sigma Aldrich
$C_6H_{12}Na_2O_6S_4$ (SPS)	10 [ppm]	95	Hopax Fine Chemicals
$C_{2n}H_{4n+2}O_{n+1}$ (PEG)	0.3 [gL^1]	n/a	Sigma Aldrich
$C_5H_{10}N_2OS$ (HIT)	0.1 [ppm]	99	Matrix Scientific
HCl	50 [ppm]		Sigma Aldrich

In deposition.

Sulphamide In plating solution based on [119]. Method designed by M. Kurihara.
Deposition at: -0.97 V (-1.3 V, 0.1 s pulse for nucleation) (vs. Ag|AgCl)
Rotation Speed: 0 rpm
Film thickness: $\sim$175 nm (0.6 Ccm^{-2})

Chemical	Concentration [M]	Purity %	Supplier
$InCl_3$	0.261	99.99	Alfa Aeser
H_3NO_3S	2.3	95.99	Alfa Aeser
NaOH	2.0	99.99	Sigma Aldrich
$C_6H_{12}O_6$	8 [gL^1]	99.5	Sigma Aldrich
$C_6H_{15}NO_3$	2.29 [gL^1]	99	Sigma Aldrich

12.1.2 In_2Se_3 /$Cu_{2\text{-}x}Se$

Full method given in [25]

In_2Se_3 deposition.

Deposition at: -0.6 V (vs. Ag|AgCl)
Rotation Speed: 400 rpm
Film thickness: 800 nm (1.8 Ccm^{-2})
Temperature: 80 ^{o}C

Chemical	Concentration [mM]	Purity [%]	Supplier
$In_2(SO_4)_3.9H_2O$	2	99.9+	MaTeck
H_2SeO_3	1	99.999	Sigma Aldrich
H_3NSO_3	55 %	99.999	Sigma Aldrich
$C_8H_5KO_4$	45 %	99.95	Sigma Aldrich
K_2SO_4	100	99.999	MaTeck

$Cu_{2\text{-}x}Se$ deposition.

Deposition at: -0.3 V (vs. Ag|AgCl)
Rotation Speed: 100 rpm
Film thickness: 800 nm (1.55 Ccm^{-2})

Chemical	Concentration [mM]	Purity [%]	Supplier
$CuCl_2.H_2O$	2.6	99.999	Alfa Aesar
H_2SeO_3	5.9	99.999	Sigma Aldrich
$LiCl.H_2O$	232	99.99+	Sigma Aldrich
H_3NSO_3	55 %	99.999	Sigma Aldrich
$C_8H_5KO_4$	45 %	99.95	Sigma Aldrich

12.1.3 Codeposited $CuInSe_2$

Standard composition.

Deposition (vs. Ag|AgCl) at:
-0.5 V: 1200 s
-0.6 V: until charge passed for 1 μm thick film
Rotation Speed: 0 rpm
Film thickness: 1 μm (2.15 Ccm^{-2})
Glass frit positioned between counter and working electrode.
Small stirrer bar rotating at slowest speed, positioned below the counter electrode.
Maximum number of samples per deposition bath: 4

Chemical	Concentration [mM]	Purity [%]	Supplier
$InCl_3$	9.6	99.99	Alfa Aesar
$CuCl_2.2H_2O$	2.9	99.999	Alfa Aesar
H_2SeO_3	5.5	99.999	Sigma Aldrich
$LiCl.H_2O$	240	99.99+	Sigma Aldrich
Hydrion Buffer*			Sigma Aldrich

* Hydrion buffer is a commercial product containing sulfamic acid (H_3NSO_3) and potassium biphthalate ($C_8H_5KO_4$) which is used to stabilised the pH to pH: 3.

12.2 Transition State Theory

In order to explain the electrochemical rate constants, k_{ox} and k_{red}, transition state theory is used. In this theory, *e.g.* for the reaction: $[O^{+}] + ne^{-} \rightarrow [R]$, the $[O^{+}]$ species must pass through an activated (higher energy) transition state to reach $[R]$. The difference in free energy between the reactant and transition state is termed the 'activation energy', $\Delta G^{\ddagger}_{red}$. The magnitude of this energy barrier determines the magnitude of k$_{red}$, as given in equation 12.1.

$$k_{red} = A \exp\left(\frac{\Delta G^{\ddagger}_{red}}{RT}\right) \tag{12.1}$$

Where A is the frequency factor, giving the rate of collisions of the electroactive molecule with the electrode.

Eq.12.1 explains the equilibrium situation when$E = E_e$ and no current flows. Applying an overpotential, η adds a further term to the equation as given in Eq.12.2 for the reduction reaction.

$$k_{red} = A \exp\left(\frac{\Delta G^{\ddagger}_{red}}{RT}\right) \exp\left(\frac{\alpha F \eta}{RT}\right) \tag{12.2}$$

Where α is the 'transfer coefficient'and its importance is explained in detail in Section 6.1.2. If equation 12.2 is solved for k$_{ox}$ and k$_{red}$, their relative magnitude with respect to η, is determined. This is summarised in the Butler Volmer equation (Eq.6.4). Where k$_{ox}$ and k$_{red}$ from Eq.12.2 are input into the analytically derived equation for current generation, Eq.6.3.

12.3 The Effects of Pulsed Laser Annealing

In Fig.12.1 the results of laser annealing with the λ = 248 nm laser are presented. These observations similarly hold true for PLA with λ = 532 or 1064 nm lasers.

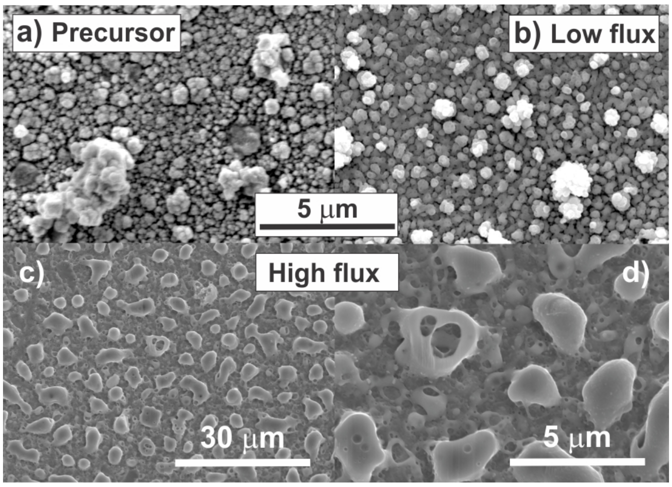

Figure 12.1: SEM micrographs showing a) codeposited CISe precursor and after PLA with KrF laser (λ = 248 nm) for 5 pulses at b) 2 x 10^6 Wcm^{-2}, c) and d) 2 x 10^7 Wcm^{-2}. d) has been magnified and tilted to show the height of the protusions.

Comparing the SEM micrographs of Fig.12.1 the differing effects of high and low flux PLA on the sample surface morphology are clear. At low flux, the appearance of the CISe absorber layer (b) matches that of its precursor (a) and XRD patterns (see Ref.[129]) indicate that the energy provided was insufficient bring about an increase in the crystal coherence length. However, using higher fluxes, (c) and (d), causes the film to dewet. This dewetting effect is due to the CISe film melting and forming droplets on the Mo substrate. Whilst XRD confirms that there is some crystal growth it is believed that this is only within the core of the droplet whilst the surface cools rapidly and thus remains amorphous [129]. Dewetted films are unsuitable for fabrication into photovoltaic devices due to the direct contact between the buffer layer and the Mo back contact leading to shunts. Therefore whilst crystal growth and atomic diffusion may be enhanced by the CISe film passing through a liquid phase during an annealing process, it is outweighed by the formation of droplets and hence this thesis only focuses on solid state annealing.

12.4 Calculating the Absorption Coefficient

In order to calculate the absorption coefficient, both the wavelength dependent reflection and transmission of the film must be measured as detailed in Section 5.1.4. The reflection spectra of CISe films is presented in Fig.7.3. In order to measure the transmission of a CISe film, it must be first removed from the optically opaque Mo back contact using a ‘rip off’ method. The transmission through the CISe film is then measured in a UV-Vis spectrometer, the results of such an analysis on a CISe precursor and laser annealed absorber layer are given in Fig.7.3a).

The transmission spectrum in Fig.7.3a) has the characteristic step between 1100 - 1300 nm close to the band gap of CISe that represents absorption of the incident radiation. The low

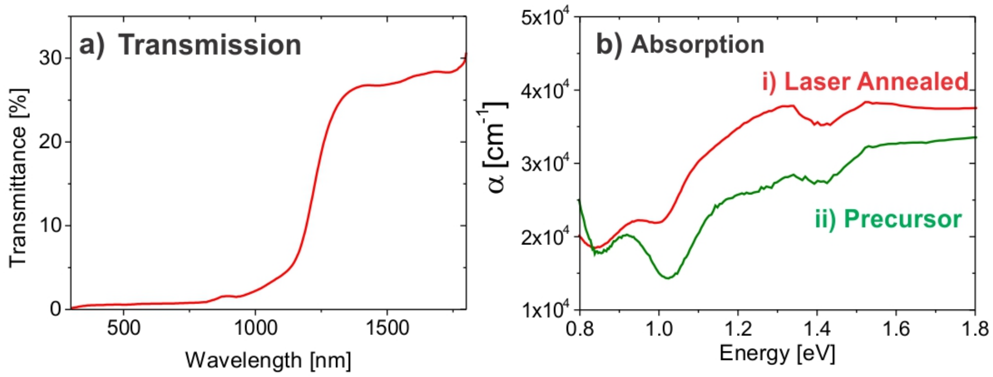

Figure 12.2: a) Transmission spectrum of a CISe electrodeposited film laser annealed at 150 Wcm^{-2}, 2 mms^{-1}, P_{Se} = 9 x 10^{-7} Pa. b) Calculated asorption coefficients for the laser annealed absorber layer of (a) and its precursor (using R data from Fig.7.3 and transmission data (not shown).

maximum transmission at higher wavelengths indicates strong free carrier absorption, which may be a result of the comparatively poor quality and defective nature of laser annealed absorber layers. In order to calculate α_λ from the measured transmission and reflection of a sample, Eq.12.3 is used.

$$\alpha_\lambda \approx -\frac{1}{x} ln \left[\frac{T}{(1-R)^2} \right] \tag{12.3}$$

Inputting the reflection and transmission data from Fig.7.3c) and Fig.12.2a) into Eq.12.3, α_λ is calculated as shown in Fig.12.2b). This analysis method yields a value of α_{1064nm} = 2.5 $\times$ 10^4 cm^{-1} for the precursor, and 3.3 $\times$ 10^4 cm^{-1} after laser annealing. The strange shape of this absorption spectra is likely due to the difficulties in using the ‘rip off’ method on co-electrodeposited samples which resulted a poor quality transmission spectrum. In order to corroborate this experimental value, a second laser annealed absorber layer was measured using Photothermal Deflection Spectroscopy (PDS) by Florian Köhler, Forschungszentrum Jülich GmbH. PDS measures the bending of light due to optical absorption. However, this technique also requires the film to be removed from the Mo substrate and so suffers the same difficulties as the transmission measurement. The PDS measurement gave α_{1064nm} = 2.0 $\times$ 10^4 cm^{-1}. These measured values are compared to those of literature given in Table 12.1.

Table 12.1 shows that α_{1064nm} only varies by 2.5 $\times$ 10^4 cm^{-1} even between different materials and analysis techniques. These results support the use of α_{1064nm} = 3.3 $\times$ 10^4 cm^{-1} used in the FEM. The effect of different values of α_{1064nm} on the temperature profile of the film is briefly examined in Section 9.2.2.

Material Type	α_{1064nm} [cm^{-1}]	Composition	Method [Reference]
Single crystal CISe	3.5×10^4	stoichiometric	Ellipsometry [227]
co-electrodeposited CISe	2.0×10^4 1.0×10^4	Cu-poor precursor Cu-poor furnace annealed	UV-Vis: R_λ, T_λ [136]
co-electrodeposited CISe	2.5×10^4 3.3×10^4	Cu-poor precursor Cu-poor laser annealed	UV-Vis: R_λ, T_λ [Lux]
co-electrodeposited CISe	2.0×10^4	Cu-poor laser annealed	PDS [Jülich]

Table 12.1: Comparison the values of α at a wavelength 1064 nm (1.16 eV) for different techniques. UV-Vis: R_λ, T_λ indicates measurement of reflection and transmission as detailed in section 5.1.4. Lux and Jülich indicate the measurements described above.

12.5 Codeposition of $CuInSe_2$ with elevated Se content

Precursors with an elevated Se content were deposited using the three electrode cell experimental set-up as depicted in Fig.6.1. In contrary to the standard co-deposition technique, there is no stirrer bar or a glass frit in the deposition bath. The parameters were as follows.

100 ml deposition bath
Deposition at: -0.5 V (vs. Ag|AgCl)
Rotation Speed: 0 rpm
Film thickness: 1 μm (2.15 Ccm^{-2})

Chemical	Concentration [mM]	Purity [%]	Supplier
$InCl_3$	2.4	99.99	Alfa Aesar
$CuCl_2.2H_2O$	2.56	99.999	Alfa Aesar
H_2SeO_3	4.8	99.999	Sigma Aldrich
KCl	240	99.995	Alfa Aesar
H_3NSO_3	10	99.999	Sigma Aldrich
$C_8H_5KO_4$	10	99.95	Sigma Aldrich

This deposition originated from that detailed in ref.[228].

12.6 Se-content of absorbers from precursors with no additional Se

In Section 8.3.1 it was shown that laser annealing precursors with an elevated Se content in the FTO annealing chamber lead to absorbers with Se/(Cu+In) $>$ 1. This indicates that excess Se vaporised during annealing forms a P_{Se} above the film, with a partial pressure corresponding to the temperature of the heated FTO window. When this P_{Se} exceeds the equilibrium vapour pressures, ρ, of the binary Se decomposition reactions (in Table 8.1), then CISe decomposition by this mechanism becomes unfavourable. However, when no excess Se is supplied to the precursor there is no elemental, excess Se available to form a background P_{Se}. Therefore Se is released from the film itself via the breakdown of CISe as detailed in Table 8.1. Thus it is hypothesised that these absorbers will have Se/(Cu+In) $<$ 1. To test this theory, a second set of electrodeposited precursors with similar composition to those which were subsequently Se capped were laser annealed under matching conditions. The Se/(Cu+In) of the resulting absorbers is given in Fig.12.3.

Comparing the Se/(Cu+In) of the uncapped absorbers to those which were Se capped prior to annealing, as shown in Fig.12.3, the importance of providing additional Se is clear. Whilst Se capped precursors all have a Se content above stoichiometry, only the uncapped precursor annealed at P_{Se} = (3) forms an absorber with Se/(Cu+In) $>$ 1. As the Se content has decreased from that of the precursor in all of the uncapped samples, it is clear that Se has been lost during annealing. This Se loss is expected to originate from the breakdown of the CISe lattice, which is favourable until the vaporised Se has $P_{Se} > \rho$ of the binary selenide decomposition. One could assume that this condition is attained during the annealing with P_{Se} = (3). However, the absorber annealed with the highest FTO temperature: Fig.12.3b4) has the lowest Se/(Cu+In) = 0.89 indicating that this P_{Se} created from sample decomposition does not prevent further CISe breakdown or that the Se can be reincorporated into the film during annealing. Absorbers with

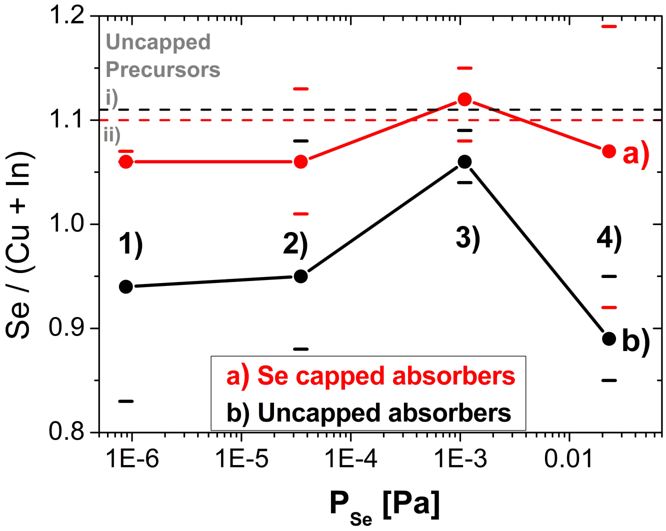

Figure 12.3: Se/(Cu+In) composition, determined from EDX measurements of absorbers layers produced by laser annealing at 50 Wcm^{-2}, 2 mms^{-1} under P_{Se} (1)-(4) from electrodeposited CISe precursors with a) Se cap and b) uncapped. Dotted lines give the composition of both precursors (before Se capping in the case of the capped precursor). Each composition is an average of three different measurement points on the same sample and error bars indicate the maximum and minimum measured values.

Se/(Cu+In) < 1 are expected to contain V_{Se} defects and secondary phases and therefore would show poor performance if completed into a device. This experiment shows the importance of generating an elevated background P_{Se} during annealing.

12.7 Experimental Evidence for Temperature Calculations

In Fig.9.12, it was shown that annealing with a laser flux of 375 Wcm^{-2} for 0.4 s (fluence = 150 Jcm^{-2}) led to an absorber layer with a crystal coherence length of 184 ±5 nm. Using the 2D FEM model the (spatially averaged) peak film temperature was calculated as > 1000 ^{o}C and the 3D model indicated that the peak temperature at the centre of the Gaussian reached > 1400 ^{o}C. As these values lie above the melting temperature for CISe (990 ^{o}C [169]), SEM micrographs of this absorber are analysed in Fig.12.4.

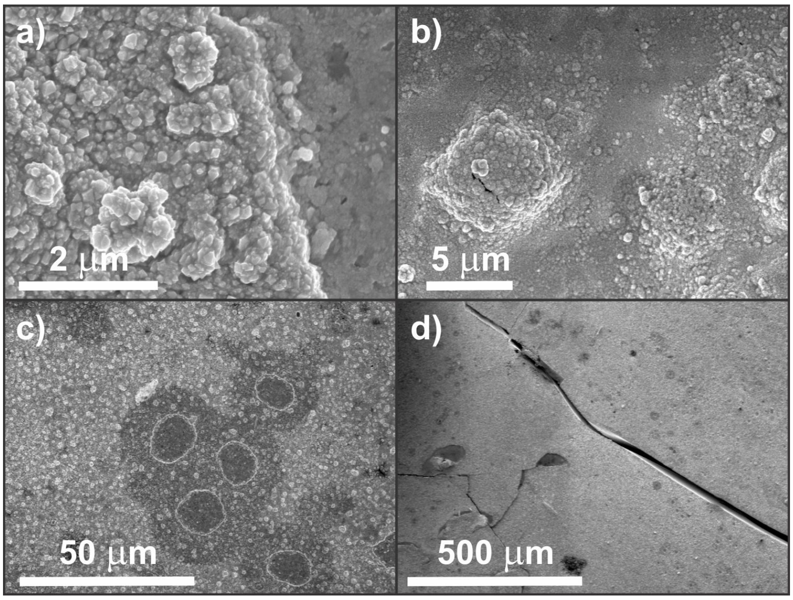

Figure 12.4: SEM micrographs of sample surface after irradiating with 375 Wcm^{-2}, 5 mms^{-1} scan rate, showing a) - d) different areas with different levels of magnification.

It is clear from the images of Fig.12.4 that the laser annealing process has caused significant damage to both the film and the underlying substrate. The film surface has changed from the microscale roughness of the precursor (for example Fig.7.8) to have large undulations in its height (a)-(b). This surface appearance may indicate that the film has partial melted or de-laminated from the substrate during the annealing process, which would corroborate the modelled temperatures. There are also areas where the CISe film has been damaged to the extent that there are holes through to the Mo substrate (Fig.7.8c). Finally, the poor thermal conductivity of the glass substrate leads to an extreme temperature gradient through its depth and causes the sample to crack.

12.8 Codeposition of Cu(In,Ga)Se_2

A three electrode cell experimental set up as depicted in Fig.6.1 was used. A small stirrer bar, rotating at minimum speed, was positioned below the counter electrode. The following conditions and plating solution were used:

Full method given in [229]
100 ml deposition bath
Deposition (vs. Ag|AgCl) at:
-0.55 V: 1200 s
-0.65 V: until charge passed for 1 μm thick film
Rotation Speed: 0 rpm
Film thickness: 1 μm (2.15 Ccm^{-2})

Chemical	Concentration [mM]	Purity [%]	Supplier
$InCl_3$	2.4	99.99	Alfa Aesar
GaCl	5.7	99.995	Alfa Aesar
$CuCl_2.2H_2O$	2.56	99.999	Alfa Aesar
H_2SeO_3	4.5	99.999	Sigma Aldrich
$LiCl.H_2O$	240	99.99+	Sigma Aldrich
Hydrion Buffer*			Sigma Aldrich

* Hydrion buffer is a commercial product containing sulfamic acid (H_3NSO_3) and potassium biphthalate ($C_8H_5KO_4$) which is used to stabilised the pH to pH: 3.

13 Abbreviations and Symbols

Abbreviations

AES	Auger Electron Spectroscopy
BSE	Back Scattered Electrons
CB	Conduction Band
CCD	Charge Coupled Device
CE	Counter Electrode
CISe	$CuInSe_2$
CIGSe	$Cu(In,Ga)Se_2$
CV	Cyclic Voltammogram
CW	Continuous Wave
EBIC	Electron Beam-Induced Current
ED	Electrochemical Deposition
EDX	Energy Dispersive X-ray Spectroscopy
EPBT	Energy Payback Time
EQE	External Quantum Efficiency
FEM	Finite Element Model
FF	Fill Factor
FTO	Fluorine Doped Tin Oxide
FWHM	Full Width at Half Maximum
GIXRD	Grazing Incidence X-ray Diffraction
HER	Hydrogen Evolution Reaction
IR	Infra-Red
IV	Current Voltage

LBIC	Light Beam Induced Current
Nd:YAG	Neodymium-doped Yttrium Aluminium Garnet
NIR	Near Infrared
OCP	Open Circuit Potential
OVC	Ordered Vacancy Compound
PEC	Photoelectrochemistry
PL	Photoluminescence
PLA	Pulsed Laser Annealing
PV	Photovoltaics
PVD	Physical Vapour Deposition
RDE	Rotating Disc Electrode
RTP	Rapid Thermal Processing
RT-PL	Room Temperature Photoluminescence
RE	Reference Electrode
SCR	Space Charge Region
SE	Secondary Electrons
SHE	Standard Hydrogen Electrode
SEM	Scanning Electron Microscopy
TC	Thermocouple
UV	Ultraviolet
VB	Valence Band
Vis	Visible (Electromagnetic Radiation)
WE	Working Electrode
XPS	X-ray Photoelectron Spectroscopy
XRD	X-ray Diffraction

Symbols

Symbols sorted according to chapter and are listed in alphabetical order. Each symbol is listed once, under the heading of the first chapter in which it appears.

Chapter 4

Ar^+	Ar-ion
$(In,Ga)_{Cu}$	In/Ga on Cu, antisite defect
λ	Wavelength
P_{Se}	Partial Pressure of Selenium
V_{Se}	Selenium Vacancy

Chapter 5

A	Diode Ideality Factor
α_λ	Absorption Coefficient
β_{instr}	Peak Broadening contributed by Instrument in X-ray Diffractogram
β_{obs}	Observed Peak Breadth in X-ray Diffractogram
β_{sample}	Integral Peak Breadth of Sample in X-ray Diffractogram
c_D	Charge Distribution of Atoms
D	Dimension of Coherently Scattering Crystallite Domains
d_{hlk}	Interplanar Crystal Spacing
$d\Phi$	Flux of Incident Photons
$\Delta\mu$	Quasi-Fermi Level Splitting
E_{bind}	Binding Energy of Auger Electron
E_{core}	Energy Level of Core Electron
E_g	Band Gap Energy
E_{upper}	Energy Level of non-Core Electron
E_v	Valence Band Energy
F_{hlk}	Structure Factor

f_n	Atomic Form Factor
I_0	Incident Beam Intensity
I_d	Current Density in the Dark
I_{ill}	Photocurrent Density
I_{max}	Maximum Current Density
I_{sat}	Saturation Current Density
I_{sc}	Short Circuit Current Density
η_{eff}	Power Conversion Efficiency
θ	Incident Angle of Impinging Electromagnetic Radiation
θ_c	Critical Angle
K	Scherrer Constant
κ	Extinction Coefficient
L	Minority Carrier Diffusion
n	Refractive Index
$\tilde{n}$	Complex Index of Refraction
n_i	Reflection Order
P_{in}	Input Power
P_{max}	Maximum Power
P_{out}	Output Power
R_λ	Reflection Coefficient
R_s	Series Resistance
R_{sh}	Parallel (Shunt) Resistance
T_λ	Transmission
τ	Charge Carrier Lifetime
V_{bi}	Built in Potential
V_{max}	Maximum Voltage
V_{oc}	Open Circuit Voltage
W	Space Charge Region

Y_{PL}	PL Yield
ω	Raman Shift
ω_1	Frequency of Irradiating Radiation in Raman Measurements
Ω	Phonon Frequency

Chapter 6

α	Transfer Coefficient
d	Thickness of Deposits
E_e	Equilibrium or Open Circuit Potential
E^0	Standard Electrode Potential
e^-	Electron
η	Overpotential
F	Faraday Constant
I_L	Current Density according to Levich Equation
I_{bv}	Current Density according to Butler-Volmer Equation
I_c	Deposition Current Density (given by Cotrell Equation)
I_{dep}	Deposition Current Density
I_{ex}	Exchange Current Density
k_{e-ox}	Rate Constant for Oxidative Electron Transfer
k_{e-red}	Rate Constant for Reductive Electron Transfer
M_w	Molecular Mass
n	Number of Electrons
O	Oxidised Species
$[O]_0$	Concentration of Oxidised Species at Electrode
$[O]_{bulk}$	Concentration of Oxidised Species in Bulk Solution
R	Reduced Species
$[R]_0$	Concentration of Reduced Species at Electrode

$[R]_{bulk}$	Concentration of Reduced Species in Bulk Solution
R_m	Molar Gas Constant
ρ	Density
v	Kinematic Viscosity
ω	Angular Viscosity

Chapter 7

$\bigtriangledown \times$	The Curl Operator
E	Electric Field Vector
E_{laser}	Energy of Laser
ϵ_{λ}	Wavelength Dependent Emission
ε_0	Relative Permittivity of a Wave in Free Space
ε_r	Relative Permittivity of a Wave in a Material
j	Current Density
k_0	Wavenumber
L_c	Cavity Length
λ	Wavelength
m	Integer
σ	Electrical Conductivity
ω	Angular Frequency of the Wave

Chapter 8

G	Gibbs Free Energy
G_r	Gibbs Free Energy of Reactants
G_p	Gibbs Free Energy of Products
ΔG_R	Gibbs Free Energy Change of Reaction

E_c	Conductance Band Energy
E_F	Fermi Level Energy
H	Enthalpy
I	Current Density
P	Pressure
P_r	Pressure of Reactants
P_p	Pressure of Products
p	Equilibrium Vapour Pressure
q	Elementary Charge
S	Entropy
T_m	Melting Temperature
U	Internal Energy
v	Volume

Chapter 9

<x>	Root Mean Squared Diffusion Distance
A_D	Diffusion Constant
a	Arbitrary Constant
A_{sys}	Exposed Area of System
C_i	Concentration of Interstitials
C_p	Specific Heat Capacity at Constant Pressure
C_v	Concentration of Vacancies
D	Diffusion Coefficient
D_i	Diffusivity of Interstitials
D_{self}	Self-Diffusion Coefficient
D_v	Diffusivity of Vacancies
E_a	Activation Energy of Atomic Diffusion

E_f	Formation Energy of Vacancies or Interstitials
E_m	Energy Barrier of Diffusion of Interstitials or Vacancies
E_L	Activation Energy of Grain Growth
$e(T)$	Flux of Energy Radiating from a Body
η	Power Conversion Efficiency [%]
h	Heat Transfer Coefficient
h_{air}	Heat Transfer Coefficient of Air
$I(x, y)$	Laser Beam Intensity at Location x,y
In_{Cu}	Indium on Copper Antisite Defect
In_i^{+3}	Indium Interstitial
J	Diffusional Flux
k	Thermal Conductivity
k_b	Boltzmann Constant
k_L	Rate Constant for Grain Growth
L_{crit}	Critical Grain Size
L_{max}	Limiting Grain Size
L_o	Initial Grain Size
L_t	Grain Size at Time t
M	Movement of Grain Boundaries
M_0	Grain Boundary Movement Constant
m	Mass
Na_{Cu}	Sodium on Copper Antisite Defect
O_{VSe}	Oxygen on Se Vacancy Defect
p	Equilibrium Vapour Pressure
p_{ext}	Pressure of Cooling Fluid
Q_{in}	Energy Supplied to Film by Laser Irradiation
Q_{rad}	Energy Change resulting from Thermal Radiation
Q_{conv}	Energy Change resulting from Convectional Cooling

Q_{out}	Net Heat Conduction Away from an Element
Σ_i	Sum of Interstitial Mechanisms
Σ_i	Sum of Vacancy Mechanisms
σ_B	Stefan-Boltzmann Constant
T_{CISe}	Temperature of CISe film
T_{ext}	Temperature of Cooling Fluid
T_f	Temperature of Cooling Fluid
T_m	Melting Temperature
T_{sys}	Temperature of System
t	Time
t^*	Effective Time
V	Volume
V_{In}	Indium Vacancy
V_{Cu}	Copper Vacancy
V_f	Volume of Cooling Fluid
v_{ext}	Velocity of Cooling Fluid
W_k	Work Transfer Rate
w	Gaussian Spreading Function
Φ	Concentration of Diffusing Species

Chapter 11

T_{vap}	Vaporisation Temperature